LAL 11-95
June 2011

THÈSE

Présentée le 5 juillet 2011

par

Henso ABREU

pour obtenir le grade de

Docteur ès Sciences
de l'Université Paris XI, Orsay

Measurement of the inclusive prompt photon cross section and preparation of the search of the Higgs boson decaying into two photons with the ATLAS detector at the LHC

CERN-THESIS-2011-157
05/07/2011

Soutenue devant la commission d'examen composée de :

M.	L.	Fayard	Directeur de thèse
Mme	S.	Gascon	Rapporteur
M.	J.	Ocariz	
M.	A.	Stocchi	Président
M.	G.	Unal	
M.	T.	Virdee	
Mme	M.	Wielers	Rapporteur

To my lovely wife Jeannilet.
To my parents.

Résumé

Ce travail présente les mesures de section efficace de production de photons isolés dans les collisions proton-proton avec l'experience ATLAS au LHC, à une énergie de 7 TeV dans le centre de masse. Les résultats sont d'abord obtenus pour une luminosité intégrée de 880 nb^{-1}, puis dans un deuxième temps pour une luminosité de 36 pb^{-1}. Les mesures faites avec 880 nb^{-1} et 36 pb^{-1} couvrent, respectivement, les intervalles en énergie transverse $15 \leq E_T^\gamma < 100$ GeV et $45 \leq E_T^\gamma < 400$ GeV. Les résultats sont comparés aux prédictions de la chromodynamique quantique perturbative à l'ordre NLO. Les premières études pour la recherche du Higgs dans le canal de désintégration en deux photons sont également présentées pour 38 pb^{-1} de données collectées par l'expérience ATLAS en 2010 (et plus récemment pour 210 pb^{-1} accumulés en 2011). Les limites d'exclusion observées sont citées en fonction d'une masse de Higgs se situant dans l'intervalle 110-140 GeV.

Abstract

This work presents the measurements with the ATLAS experiment of the cross section for inclusive production of isolated prompt photons in proton-proton collisions at a centre-of-mass energy $\sqrt{s} = 7$ TeV. The first results are based on an integrated luminosity of 880 nb^{-1} and the later results are based on 36 pb^{-1}, collected with the ATLAS detector at the Large Hadron Collider. The measurements performed with 880 nb^{-1} and 36 pb^{-1} cover the transverse energy range $15 \leq E_T^\gamma < 100$ GeV and $45 \leq E_T^\gamma < 400$ GeV, respectively. The results are compared to predictions from next-to-leading order perturbative QCD calculations. In addition, are also presented the first studies for the search for the Higgs boson in the decay channel into two photons with 38 pb^{-1} data collected by the ATLAS experiment in 2010 (and more recently with 210 pb^{-1} collected in 2011). Observed exclusion limits are quoted as a function of the Higgs mass in the range 110-140 GeV.

Contents

Introduction **9**

1 The Standard Electroweak Model and the Higgs Boson **11**
1.1 Elementary constituents . . . 11
1.2 Symmetries . . . 13
1.2.1 Quantum Electrodynamics (QED) . . . 13
1.2.2 Quantum Chromodynamics (QCD) . . . 13
1.2.3 Weak interaction . . . 14
1.3 The Higgs mechanism . . . 15
1.4 Constraints on the SM Higgs boson mass . . . 18
1.4.1 Theoretical limits . . . 18
1.4.2 Experimental limits . . . 20
1.5 SM Higgs boson at the LHC . . . 23
1.5.1 The Higgs production . . . 23
1.5.2 The Higgs decay modes . . . 24

2 QCD Prompt Photon Production **27**
2.1 The Factorization Theorem . . . 27
2.2 Prompt Photon Production . . . 30
2.3 Previous Measurements . . . 33

3 The Large Hadron Collider **36**
3.1 LHC Performance . . . 37
3.1.1 The Luminosity . . . 38

4 A Toroidal LHC ApparatuS **41**
4.1 Design overview . . . 42
4.2 Coordinate System and Basic Quantities . . . 42
4.3 Detectors . . . 43
4.3.1 Tracking . . . 43
4.3.2 Calorimetry . . . 45
4.3.3 Muon spectrometry . . . 49
4.3.4 Magnets . . . 51
4.3.5 Trigger System . . . 51

5 The EM Calorimeter of ATLAS **53**
5.1 Physics of the EM cascade . . . 53
5.2 Sampling Calorimeter . . . 55
5.3 Energy resolution . . . 56
5.4 Accordion geometry . . . 58
5.5 Cell energy reconstruction . . . 63
5.5.1 Triangular signal . . . 63
5.5.2 Readout electronic chain . . . 65
5.5.3 Energy reconstruction . . . 66

6 Photon Identification in ATLAS **68**
6.1 Photon reconstruction . . . 68
6.2 Characteristic variables and cut-based photon identification criteria . . . 70
6.2.1 Variables using calorimeter information . . . 70
6.2.2 Loose and Tight selections . . . 75
6.3 Photon isolation algorithm cuts . . . 75
6.3.1 Track isolation . . . 79
6.3.2 Calorimetric isolation . . . 80
6.4 Performance of the photon identification . . . 81
6.4.1 Signal photon efficiency . . . 81
6.4.2 Jet rejection . . . 83
6.4.3 Converted photon purity . . . 84
6.5 Identification with early data at $\sqrt{s} = 7$ TeV . . . 89
6.5.1 Efficiency estimation . . . 91

7 Measurement of the Purity of the Direct Photon Samples **99**
7.1 Two-dimensional sidebands method . . . 99
7.1.1 Description of the method . . . 99
7.1.2 Correction for signal and background correlation . . . 101
7.2 Purity results and systematic uncertainties . . . 107
7.2.1 Results from the 2D sidebands method . . . 107
7.2.2 Systematic uncertainties on the 2D sidebands method . . . 109
7.3 Background from mis-identified electrons . . . 112
7.3.1 Significance of electron contamination . . . 112

8 Inclusive Isolated Prompt Photon Cross Section Measurement **116**
8.1 The cross section . . . 116
8.2 Unfolding coefficients . . . 116
8.3 Cross section results and systematic uncertainties . . . 119
8.3.1 Results . . . 119
8.3.2 Systematic uncertainties . . . 120
8.4 Theoretical prediction . . . 123
8.5 Comparison between theory and data and Conclusion . . . 127

9 Prompt photons analysis with full 2010 data LHC runs and comparison with CMS **134**
9.1 Re-optimization of photon selection criteria . . . 134
9.2 Isolated prompt photon cross section with 34.6 pb^{-1} . . . 137
9.2.1 Collision data . . . 137
9.2.2 Efficiency results . . . 137
9.2.3 Purity results . . . 139
9.2.4 Cross section measurements . . . 141
9.2.5 Conclusion . . . 145
9.3 A short comparison between ATLAS and CMS results . . . 145
9.3.1 Photon identification and isolation . . . 145
9.3.2 Estimation of signal efficiency . . . 146
9.3.3 Signal extraction and background estimation . . . 148
9.3.4 Cross-sections comparison . . . 149

10 Contribution to the data analysis of the SM Higgs boson decaying into two photons **153**
10.1 Data and simulated samples . . . 153
10.1.1 Event selection and reconstruction . . . 153
10.1.2 Simulated samples . . . 154
10.2 Background composition . . . 154
10.3 Signal modelling . . . 155
10.4 Systematics . . . 157
10.5 Observed sensitivity . . . 159
10.6 Recent update on Higgs limit . . . 160
10.7 Future . . . 160

11 Conclusions **167**

Bibliography **170**

A Optimal Filtering Method **185**

B Selection cut thresholds **187**
B.1 Cut thresholds . . . 187
B.2 Data/MC discrepancies on Discriminating Varia-bles . . . 190

C Simulated samples and collision data **195**
C.1 Simulated events . . . 195
C.2 Collision Data . . . 197
C.3 Photon candidates preselection . . . 200
C.4 Reconstruction and trigger efficiencies . . . 202
C.4.1 Reconstruction and preselection efficiency . . . 202
C.4.2 Trigger efficiency . . . 203

Acknowlegements **204**

Introduction

In the year 2010, the Large Hadron Collider (LHC) at CERN started its operation. The first proton-proton collisions with a centre-of-mass energy of $\sqrt{s} = 7$ TeV and a luminosity up to $10^{32}\ cm^{-2}s^{-1}$ allowed to enter in a new era in high energy particle physics experiments. In the next years the LHC will probably multiply its integrated luminosity (the integrated luminosity recorded by ATLAS in 2010 was about 40 pb^{-1}) by more than a factor 100 and open new windows on physics. Therefore, the LHC is expected to answer the question whether the Higgs mechanism exist and is responsible for the electroweak symmetry breaking which explains how particles get masses. At the LHC are two general-purpose detectors: ATLAS (A Toroidal LHC AparatusS) and CMS (Compact Muon Solenoid). These detectors have been designed to discover the Higgs boson over its entire allowed mass range and to study a wide range of other physics subjects (which include the search of new physics and Standard Model precision measurements). In hadron colliders, there are a lot of QCD [1] backgrounds, however final states involving electrons and photons can provide clean signals in the detector, with a large rejection of the QCD background. The most promising decay channel for the discovery a low mass Standard Model Higgs boson, is the two photons final state, which, thanks to the very good energy resolution of the electromagnetic calorimeter, looks specially promising despite its small branching ratio of 0.002.

This thesis is dedicated to the first measurements of the prompt photon cross section with ATLAS at the LHC, which is a test for QCD predictions. Furthermore, the prompt photon analysis is the starting point for many Standard Model and Beyond Standard Model analyses. Prompt photons are the major backgrounds of $H \to \gamma\gamma$ searches. In addition, the first results of the search of the Higgs boson in the decay mode of two photons are given. Thus, this document is organized as follows:

Chapter 1, summarizes the theoretical foundations of the Standard Model of particle physics. In addition, a short discussion of the previous and current exclusion limits on the mass of the Higgs boson from other experiments is shown. The Higgs production and decay at the LHC are also described.

Chapter 2, provides an overview of the prompt photon production at high energy hadron collisions and of previous experimental measurements of prompt photons.

Chapter 3 describes quickly the LHC, with emphasis on the startup configuration and on the amount of data registered by the ATLAS experiment during the 2010 data-taking period.

[1] Quantum Chromodynamics

Chapter 4 contains general descriptions of the ATLAS experiment setup.

Chapter 5 is devoted to the Liquid-Argon ATLAS Electromagnetic calorimeter, which is one of the main detectors (together with the Inner Detector) used for the analyses presented in this document.

In chapter 6, the photon reconstruction procedure used by ATLAS is shortly described. In addition, the cut-based photon identification method is presented, as well as other studies. Results on selection efficiency obtained with early data (880 nb^{-1} of integrated luminosity) are given.

Chapter 7 describes the data-driven approach to estimate the signal fraction (the "purity") and the signal yield in the selected sample of photon candidates in different regions of pseudo-rapidity and transverse energy, for photon candidates satisfying tight identification criteria based on shower shapes and calorimetric isolation. The data set analysed amounts to an integrated luminosity of 880 nb^{-1}, collected up to August 2010.

Chapter 8 presents the inclusive cross section of isolated prompt photons measurements as well as the systematic uncertainties that affects this measurements, with an integrated luminosity of 880 nb^{-1} for a centre-of-mass energy collisions of $\sqrt{s} = 7$ TeV. The results obtained are compared with the theoretical predictions performed at full next-to-leading order pQCD calculations.

Chapter 9 shows an update of the measurements of the inclusive cross section analysis of Chapter 8. For this, an integrated luminosity of 36 pb^{-1} was used, corresponding the full 2010 data-taking period recorded by ATLAS. In this analysis, the transverse energy range is extended until 400 GeV and the pseudo-rapidity ranges include the whole acceptance. In addition, a comparison between ATLAS and CMS isolated photon cross sections is done.

Finally, chapter 10 reports the first studies on the search of the Standard Model Higgs boson in the diphoton decay channel with 2010 data and an integrated luminosity of 38 pb^{-1} (and also the very recent limit using 2011 data and 210 pb^{-1}). The observed exclusion is also provided.

Chapter 1

The Standard Electroweak Model and the Higgs Boson

Motivation

The Standard Model (SM) of particle physics is a successful theory, which describes matter and its interactions at the elementary scale. It is a relativistic quantum field theory based on a spontaneously broken local $SU(3)_C \otimes SU(2)_L \otimes U(1)_Y$ gauge group describing the strong, weak and electromagnetic interactions [1]. The spontaneous breaking of the SM electroweak symmetry part $(SU(2)_L \otimes U(1)_Y)$ generates mass terms for gauge bosons, and includes a new boson introduced by the scalar doublet that is the Higgs boson. The mass of the Higgs boson is the only unknown parameter in the theory, while all couplings are fixed by masses of the particles. However, the mass of the Higgs boson is constrained by theoretical predictions and experimental results.

A brief description of the SM and the Higgs mechanism is summarized in this chapter. In addition, an overview of production mechanisms, decay channels and the limits on the mass of SM Higgs boson from theory and experiments are presented.

1.1 Elementary constituents

As discussed above, the SM is the sum of:

- The Standard Electroweak Model (group $SU(2)_L \otimes U(1)_Y$) which was developed in the 60's, in particular by Glashow, Weinberg and Salam [145, 146, 194, 198–200, 212].
- The quantum chromodynamics (group $SU(3)_C$) describing strong interactions [142, 151, 152, 186, 187].

  A history of the Standard Model(s) can be found in [213].

[1] Gravity cannot be consistently described as a quantum field theory and is not included in the SM, but it is completely negligible on microscopic scales.

The elementary constituents are the matter fermions. Interactions between them are mediated by bosons and a "hypothetic" Higgs boson, which is responsible of the particles masses.

Fermions

The fermions can be separated in two categories: quarks, sensitive to all three interactions, and leptons, interacting only weakly and electromagnetically. All fermions can be organized in three families with identical properties except for their masses. The fermionic field have left chirality components transforming as $SU(2)_L$ doublets and right chirality components transforming as singlets. The charged weak interaction only acts on left chirality components.

$$\begin{array}{lccccc} \text{1st family} & \begin{pmatrix} \nu_e \\ e^- \end{pmatrix}_L, & e^-_R, & \begin{pmatrix} u \\ d \end{pmatrix}_L, & u_R, & d_R \\ \text{2st family} & \begin{pmatrix} \nu_\mu \\ \mu^- \end{pmatrix}_L, & \mu^-_R, & \begin{pmatrix} c \\ s \end{pmatrix}_L, & c_R, & s_R \\ \text{3rd family} & \begin{pmatrix} \nu_\tau \\ \tau^- \end{pmatrix}_L, & \tau^-_R, & \begin{pmatrix} t \\ b \end{pmatrix}_L, & t_R, & b_R \end{array}$$

This configuration assumes that neutrinos are massless [2].

Gauge bosons

There are twelve gauge mediators in the SM: the gluons, the mediators of the strong interaction, and the γ, $W^\pm$ and Z, which mediate the electromagnetic and weak interactions.

The gluons are massless, electrically neutral and carry color charge. There are eight gluons, corresponding to the number of $SU(3)_C$ generators.

The electromagnetic interaction is mediated by the photon, a massless particle that carries no electric charge and generates an interaction of infinite range.

The weak interaction boson, $W^\pm$ and Z, acquire mass trough spontaneous symmetry breaking. They can interact with each other through weak interaction couplings, and the $W^\pm$, due to its electric charge, couples with the photon.

The $W^\pm$ and Z boson were directly observed in 1983, by the UA1 and UA2 experiments at CERN's Super Proton Synchrotron (SPS) collider (with protons and antiprotons colliding). These experiments have observed that the weak bosons were massive and heavy [65, 66, 82, 88]

[2] The Super-Kamiokande, SNO and KamLAND experiments observed that neutrinos from one family can be transformed, by oscillation, to neutrinos of another family [67, 143] with frequencies proportional to their mass square differences. It is possible to extend the SM to take ν masses into account. However, this has no effect in the following discussion.

1.2 Symmetries

Symmetries play an important role in elementary particle physics, in part because of their relation to conservation laws (Noether's theorem) and in part because they allow theory to make progress when a complete dynamical theory is not yet available. Thus the invariance of translations in time ($t \rightarrow t + \Delta t$), translations in space ($x \rightarrow x + \Delta x$) and rotations generate conservation of energy, momentum and angular momentum, respectively. They in particular produce spin-1 bosons which correspond to the direct result of interaction symmetries and which are called *gauge* bosons. They are connected to the gauge transformations defined by applying an arbitrary phase to the state function of the system:

$$\psi(x) \rightarrow e^{i\alpha(x)}\psi(x) \tag{1.1}$$

where this transformation is called *local* if it changes in each point of the space.

1.2.1 Quantum Electrodynamics (QED)

The QED was the first theory that used this concept successfully. The Dirac lagrangian describes a massive spin 1/2 fermion, for example the electron, and includes solutions for anti-particles as well

$$\mathcal{L}_{Dirac} = \bar{\psi}\left(i\gamma_\mu\partial^\mu - m\right)\psi \tag{1.2}$$

It is not invariant under local gauge transformations 1.1, where α is a scalar. Indeed, the term $\partial^\mu\psi$ is not invariant under $U(1)$, but invariance is achieved by adding a compensating field to the covariant derivative A^μ, which changes according to the rule

$$\partial_\mu \rightarrow D_\mu = \partial_\mu - ieA^\mu \tag{1.3}$$

the A^μ field couples with the parameter e, the electrical charge, and it can be identified with the photon field. If A^μ associated to the photon would give an explicit mass term $\frac{1}{2}m_\gamma^2 A_\mu A^\mu$ then it would destroy the local gauge symmetry in the case where $m_\gamma^2 \neq 0$, but experiments show that indeed the photon mass is massless, with an experimental upper limit of $m_\gamma < 10^{-18}\ eV$ [134]. Adding a kinetic term leads to the following complete form of $\mathcal{L}$ for the QED

$$\mathcal{L}_{QED} = \bar{\psi}\left(i\gamma_\mu D^\mu - m\right)\psi + e\bar{\psi}\gamma^\mu\psi A_\mu - \frac{1}{4}F_{\mu\nu}F^{\mu\nu} \tag{1.4}$$

where $F_{\mu\nu} \equiv \partial_\mu A_\nu - \partial_\nu A_\mu$, corresponding to the electromagnetic field tensor.

1.2.2 Quantum Chromodynamics (QCD)

In an equivalent way, QCD can be described by the same procedure shown in the previous Subsection 1.2.1. The strong interaction is based under the gauge group of the transformations of phase $SU(3)_C$, where quarks form triplets and leptons are singlets.

$SU(3)_C$ describes the quark colors (three colors and their associated anti-colors). This color physics or chromodynamics is not unified with the others two forces. The gauge fields G^a_μ are introduced by each of the 8 group generators T_a, which are identified as gluons. These 8 fields appear in the theory as the mediators of the strong interaction between the quarks. Thus, the covariant derivative, $D_\mu = \partial_\mu - ig_s\frac{T_a}{2}G^a_\mu$ allow to write the QCD's lagrangian as

$$\mathcal{L}_{QCD} = \bar{q}\left(i\gamma_\mu D_\mu - m\right)q - \frac{1}{4}G^a_{\mu\nu}G^{\mu\nu}_a \tag{1.5}$$

with

$$G^a_{\mu\nu} = \partial_\mu G^a_\nu - \partial_\nu G^a_\mu + g_s f^{abc} G^b_\mu G^c_\nu \tag{1.6}$$

where f^{abc} are the structure constants of the group $SU(3)_C$. The third part of equation 1.6 makes QCD a non-abelian theory, which allows the interactions between the vectors bosons, gluons. In addition, QCD enjoys two peculiar properties:

- **Asymptotic freedom** [152, 186]**.** In analogy to QED, the vacuum polarization, introduces modifications to the coupling constant $\alpha_s = \frac{g_s^2}{4\pi}$ with energy. However, given the coupling previously mentioned, exchange corrections are described by quark-gluon loops. While the virtual quarks generate an increase of α_s with the energy (like in QED), the contribution of gluons goes in the opposite direction and is dominant: α_s decreases with the energy, meaning that at high energy, quarks can be described as almost free particles and a perturbative development can be used to make predictions.

- **Confinement.** At large distance of the order of 1 fm (low energy), the coupling constant α_s is around $\mathcal{O}(1)$. By consequence, one does not have anymore a perturbative theory. This phenomenon of confinement implies that color charged particles (such as quarks) cannot be isolated singularly, and therefore cannot be directly observed. High energy quarks and gluons radiate gluons until their energy is to the order of GeV. At this state, their products clump together (hadronisation) to form groups, or hadrons. The two types of hadrons are the mesons (one quark, one antiquark) and the baryons (three quarks). The final state found is a bundle of hadrons (jets) with the direction and the energy close to the initial quark or gluon direction and energy, which subsequently can be identified by the particle detectors.

1.2.3 Weak interaction

Weak interaction have been observed in the β radioactive decay, it was first described by Fermi in 1934, inspired by the structure of the electromagnetic interaction, as a contact term between fermions

$$-\frac{G_F}{\sqrt{2}}\bar{\psi}\gamma_\mu\left(1-\gamma_5\right)\psi\bar{\psi}\gamma^\nu\left(1-\gamma_5\right)\psi \tag{1.7}$$

Although violating the unitarity and non renormalizable, it is an effective theory at low energy of the SM. Weak interaction provides the following two properties that have been observed experimentally

- Weak interaction is propagated by neutral (Z) and charged ($W^{\pm}$) currents. These bosons are massive, so the weak interaction is a short range interaction ($< 10^{-18}\ m$).
- The charged weak interaction acts only on the left chirality fermions which appear as doublet $\begin{pmatrix} f_u \\ f_d \end{pmatrix}_L$ violating the parity symmetry P (and also the CP, where C is the charge conjugation).

1.3 The Higgs mechanism

As mentioned in the motivation, the SM is based on the direct product of three gauge theories

$$SU(3)_C \otimes SU(2)_L \otimes U(1)_Y \tag{1.8}$$

The idea consist in constructing a lagrangian for free massless fermions, which are able to distinguish between left chirality particles, organized in doublets, and right chirality one , organized in singlets, based under the group symmetry $SU(2)_L \otimes U(1)_Y$ where Y is the hypercharge [3]. In order to make this symmetry local, it is necessary to introduce the covariant derivative and therefore gauge bosons: one gauge boson B_μ for $U(1)_Y$ and 3 bosons W_μ for $SU(2)_L$, which have to satisfy the following equations

$$\begin{aligned}\mathcal{L}_{EW} = -\frac{1}{4}W^a_{\mu\nu}W^{\mu\nu}_a - \frac{1}{4}B_{\mu\nu}B^{\mu\nu} + \bar{f}_L i\gamma^\mu \left(\partial_\mu - ig\frac{\tau_a}{2}W^a_\mu - i\frac{g'}{2}B_\mu\right) f_L \\ + \bar{f}_R i\gamma^\mu \left(\partial_\mu - i\frac{g'}{2}B_\mu\right) f_R\end{aligned} \tag{1.9}$$

with

$$W^i_{\mu\nu} = \partial_\mu W^i_\nu - \partial_\nu W^i_\mu - g\epsilon_{ijk}W^j_\mu W^k_\nu \tag{1.10}$$

$$B_{\mu\nu} = \partial_\mu B_\nu - \partial_\mu B_\nu \tag{1.11}$$

Although this lagrangian describes fermions and gauge bosons massless, experimental observations show the short range of weak interaction, thus revealing that massive gauge bosons are necessary. The solution to the problem of massive gauge bosons was

[3] hypercharge is written $Y = 2(Q - T_3)$, where Q is the charge of the particle and T_3, the third component of the weak isospin

provided by the Higgs mechanism, in which massive gauge bosons can be accommodated by introducing a doublet complex scalar field of the form:

$$\Phi_H = \frac{1}{\sqrt{2}} \begin{pmatrix} \Phi^+ \\ \Phi^0 \end{pmatrix} \tag{1.12}$$

where Φ^0 and Φ^+ denote a neutral and a charged field respectively. In the beginning of the 60's the notion of spontaneous symmetry breaking was introduced in the relativistic theory in the context of approximate chiral symmetry and it implied the existence of massless particles (the Nambu-Goldstone bosons) [148, 149, 181–183]. This was consistent with the small pion mass.

The generation of mass for gauge fields through what is called the Higgs mechanism, was introduced by Brout, Englert [131] and Higgs [159], following a non relativistic treatment by Anderson [58]. It was followed by additional work by Guralnik, Hagen, Kibble and others [153, 157, 158, 168]. All this was done not having weak interactions in mind. It was applied to weak interactions by Weinberg [212] and Salam [194]. Some historical information on this can be found in [51, 218].

In the Higgs sector of the SM the Lagrangian of the theory is written as:

$$\mathcal{L}_H = (D_\mu \Phi_H)^\dagger (D^\mu \Phi_H) - V(\Phi_H) \tag{1.13}$$

where

$$\partial_\mu \rightarrow D_\mu = \partial_\mu - ig\frac{\tau_a}{2} W_\mu^a - i\frac{g'}{2} B_\mu \tag{1.14}$$

and

$$V(\Phi_H) = -\mu^2 \Phi^\dagger \Phi + \lambda \left(\Phi^\dagger \Phi\right)^2 \tag{1.15}$$

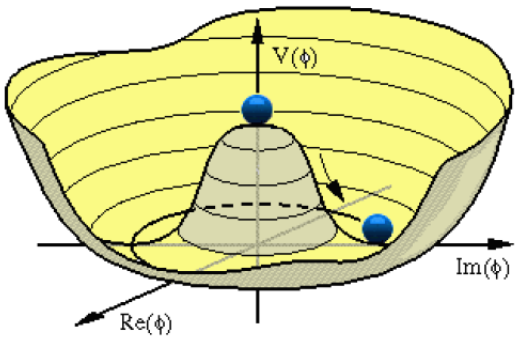


Figure 1.1: The Higgs potential V as a function of Φ_H in the plane $\mathcal{R}e(\Phi_H) - \mathcal{I}m(\Phi_H)$.

where μ and λ are positive free parameters. This minus sign before the μ^2 term ensures the spontaneous breakdown since it forces Φ_H to take a non-vanishing vacuum expectation

value. The Figure 1.1 shows the form that this potential takes in the plane $\mathcal{R}e(\Phi_H) - \mathcal{I}m(\Phi_H)$. The ground state of the Higgs field is given by the minimum of the potential which has an infinite number of values in that scenario. As the ground state is infinitely degenerated, one state is chosen as the reference for the local gauge transformation. It is commonly of the form:

$$\langle \Phi_H \rangle = \begin{pmatrix} 0 \\ \frac{v}{\sqrt{2}} \end{pmatrix} \qquad \text{with} \qquad v = \sqrt{\frac{-\mu^2}{\lambda}} \tag{1.16}$$

The choice of one particular direction of the space means that the system spontaneously breaks the symmetry [4]. The Higgs field fluctuations around the vacuum can be parametrized by four real fields $\theta_i (i = 1, 2, 3)$ and h

$$\Phi_H = e^{\frac{i}{v}\tau.\theta(x)} \begin{pmatrix} 0 \\ \frac{v+h(x)}{\sqrt{2}} \end{pmatrix} \tag{1.17}$$

The local invariance of the Lagrangian results in a cancellation of the three fields θ_i after one applies an unitary gauge transformation. The degrees of freedom of these that are not massive, are called Goldstone (or Nambu-Goldstone) bosons, which are absorbed by the three gauge fields W_i^μ. The broken symmetry provides masses to the gauge bosons $W^\pm$, Z, γ, which are defined as a combination of fields W_μ and B_μ via their coupling with the Higgs field.

$$W^{\mu\pm} = \frac{W_1^\mu \mp i W_2^\mu}{\sqrt{2}} \tag{1.18}$$

$$Z^\mu = \frac{g W_3^\mu - g' B^\mu}{\sqrt{g^2 + g'^2}} \tag{1.19}$$

$$A^\mu = \frac{g' W_3^\mu + g B^\mu}{\sqrt{g^2 + g'^2}} \tag{1.20}$$

$$M_{W^\pm} = \frac{gv}{2}, \quad M_{Z^0} = \frac{v}{2}\sqrt{g^2 + g'^2}, \quad M_\gamma = 0 \tag{1.21}$$

Fermions Masses: The electromagnetic gauge invariance allows the coupling between fermions and scalars and one can write the Lagrangian for the Yukawa interaction with the Higgs field:

$$\mathcal{L}_{Yukawa} = (\bar{e}, \bar{v})_L \Phi e_R + (\bar{u}, \bar{d})_L \Phi d_R + (\bar{u}, \bar{d})_L \tilde{\Phi} u_R + h.c. + \text{other generations} \tag{1.22}$$

where $\bar{\Phi} = i\sigma^2 \Phi^*$, and the terms corresponding to other generations have been included. Developing the new Lagrangian around its minimum results in the appearance of mass

[4] The choice in Equation 1.16 with $T = \frac{1}{2}$, $T_3 = -\frac{1}{2}$ and $Y = 1$ breaks the two symmetries simultaneously :$SU(2)_L$ and $U(1)_Y$

terms for fermions

$$\mathcal{L}_{Yukawa} = -\left(\frac{H}{v}\right)\left[m_e\bar{e}e + m_d\bar{d}d + m_u\bar{u}u\right] \tag{1.23}$$

where fermions interact with the Higgs field with a coupling λ_f proportional to their mass and to the average value of the vacuum ground state. However, the coupling terms must be added 'by hand' :

$$m_f = \frac{\lambda_f v}{\sqrt{2}} \quad \text{where} \quad v = \left(\sqrt{2}G_F\right)^{-1/2} = 246\ GeV \tag{1.24}$$

If all the couplings of Higgs to the other particles are well defined, its mass $\left(v\sqrt{2\lambda}\right)$ is a free parameter of the theory, defined by its self-coupling $\lambda(Q^2)$. However, several theoretical and experimental constraints limit the possible mass range, which will be discussed in the next section 1.4

1.4 Constraints on the SM Higgs boson mass

1.4.1 Theoretical limits

There are mainly three theoretical constraints that can be derived from assumptions on the energy range in which the SM is valid before pertubation theory breaks down and new phenomena should emerge. More details can be found in [128].

Unitarity

The Higgs boson has been introduced as a fundamental particle so that $2-2$ scattering amplitudes involving longitudinally polarized W bosons are compatible with unitarity. Based on the general principle of time-energy uncertainty, particles must decouple from a physical system if their mass grows indefinitely. The mass of the Higgs particle must therefore be bounded to restore unitarity in the perturbative regime. From the asymptotic expansion of the elastic W_LW_L S-wave scattering amplitude including W and Higgs exchanges, $A\left(W_LW_L \to W_LW_L\right) \to -G_FM_H^2/4\sqrt{2\pi}$, it follows [193] that

$$M_H^2 < 2\sqrt{2\pi}/G_F \sim (850\ GeV)^2 \tag{1.25}$$

Within the canonical formulation of the SM, consistency conditions therefore require a Higgs mass below 1 TeV [160].

Triviality

Higher order corrections to the Higgs self-couplings(λ) lead to the definition of the 'running' coupling constant [5]. With this consideration one can extract a limit on the Higgs

[5] the energy dependence of λ

boson mass [49, 195]. Thus, the behavior of the quadratic λ, as a function of a rising energy scale Q, follows from the renormalization group equation

$$\frac{d\lambda(Q^2)}{\lambda^2} = \frac{3}{4\pi^2}\frac{dQ}{Q} \Longrightarrow \lambda(Q^2) = \frac{\lambda(v^2)}{1 - \frac{3\lambda(v^2)}{4\pi^2}\ln\left(\frac{Q^2}{v^2}\right)} \tag{1.26}$$

where Q and v are respectively, the normalization and reference scales. $\lambda(Q^2)$ increases with Q and diverges at a critical scale [6]. The general triviality argument states that in order to remain perturbative at all scales one needs to have $\lambda = 0$ (which means that the Higgs boson remains massless), thus rendering the theory to be trivial, i.e non-interacting. One can choose different energy scales, for instance those below which assume that the SM is valid (Λ). The following upper limits have been obtained taking values from the superior curve shown in Figure 1.2.

- $m_H < 160\ GeV$, if $\Lambda = 10^{16}\ GeV$
- $m_H < 760\ GeV$, if $\Lambda = 1\ TeV$

Vaccum stability

The argument of vacuum stability is based on the requirement that the potential is always bounded from below. This means $\lambda(Q^2)$ has to remain positive throughout the history of renormalization group running. This gives rise to a lower bound on the Higgs mass [49, 166, 195].

The new solution of the Equation 1.26 (taking the scale of EW symmetry breaking as the energy reference) is :

$$\lambda(Q^2) = \lambda(v^2) + \frac{1}{16\pi^2}\left[-12\frac{m_t^4}{v^4} + \frac{3}{16}\left(2g^4 + \left(g^2 + g'^2\right)^2\right)\right]\ln\frac{Q^2}{v^2} \tag{1.27}$$

If the Higgs mass is too small (mainly top quark and weak boson loops arise) , i.e., λ is very small, then the top quark contribution dominates and could drive λ to a negative value. If it happens then the vacuum is not stable as it has no minimum.

To ensure that λ remains positive, the Higgs mass must satisfy

$$\lambda(Q^2) > 0 \Longrightarrow M_H^2 > \frac{v^2}{8\pi^2}\left[-12\frac{m_t^4}{v^4} + \frac{3}{16}\left(2g^4 + \left(g^2 + g'^2\right)^2\right)\right]\ln\frac{Q^2}{v^2} \tag{1.28}$$

At the energy scale of 1 TeV, it translates to a lower limit extremely restrictive $Q = \Lambda \sim 1\ TeV \Longrightarrow M_H \gtrsim 70\ GeV$. The combination of triviality and vacuum stability constraints is presented in Figure 1.2, as a function of the scale Λ beyond which the "new physics" should appear.

[6] the 'Landau pole', which moves towards lower values for increasing mass M_H

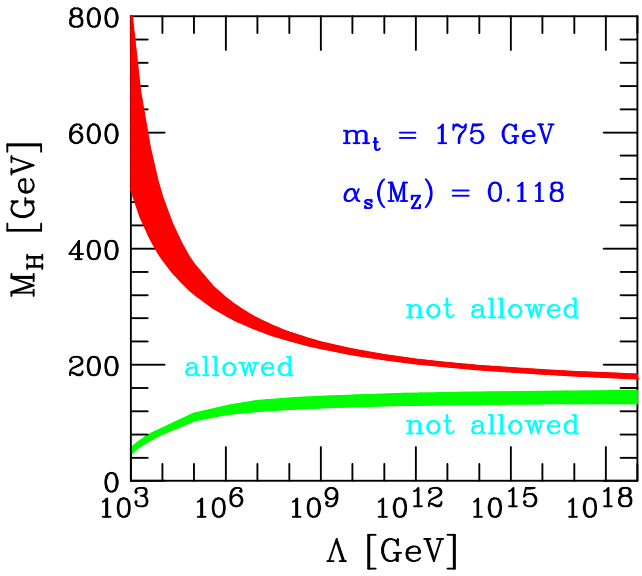


Figure 1.2: Theoretical limits on the SM Higgs boson mass from the absence of a Landau pole and from vacuum stability, the red and green bands correspondent to the uncertainties of the theory [160].

1.4.2 Experimental limits

Experimental constraints on the Higgs boson mass come from direct searches at colliders (e^+e^- at LEP, $p\bar{p}$ Tevatron), in which Higgs particles candidates were reconstructed in one of its final states. One can also use precision measurements of electroweak parameters from LEP, SLC ("Stanford Linear Collider") and Tevatron, in which predictions of the theory include loop corrections [7] where the Higgs boson enters [46]. Graphs corresponding to the some radiative corrections are shown in Figure 1.3.

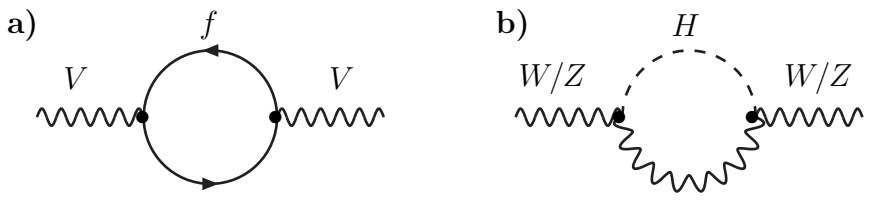


Figure 1.3: Some Feynman diagrams corresponding to electroweak radiative corrections: a) fermionic (quadratic) contributions, b) Higgs boson (logarithmic) contributions [128].

[7] for details see [128] for instance.

Direct searches

The Higgs boson has been searched at LEP [8], mainly in the Higgsstrahlung production mode ($e^+e^- \rightarrow Z^* \rightarrow ZH$), where the Higgs is expected to decay in the $b\bar{b}$ final state of mode. The absence of significant a signal on the combined data by the four LEP experiments (ALEPH, DELPHI, L3 and OPAL) has led to the lower limit $M_H > 114.4\ GeV$ at a 95% of Confidence Level (CL) [24].

At Tevatron [9], the dominant processes of Higgs production are:

- Higgs in association with a weak boson ($q\bar{q} \rightarrow W^{\pm}H$ and $q\bar{q} \rightarrow ZH$), at low Higgs mass range ($M_H < 135\ GeV$), with a final state $b\bar{b}$ for the Higgs.
- At higher Higgs masses: $M_H > 135\ GeV$, the gluon fusion process $gg \rightarrow H$ is used, where H is expected to decay into two W bosons. The experiments are reconstructed W's leptonic desintegrations, which lead to a very clean final state.

The Tevatron's experiments (CDF and DØ) combined results and exclusion limits on Higgs boson mass have been published for a integrated luminosity up to 6.7 fb^{-1} (and an average integrated luminosity of 5.9 fb^{-1}) [1]. The mass range of 158 GeV to 175 GeV has been excluded at 95% CL (see Figure 1.4 (**top**)). Very recently [203] an analysis of more data has been shown at the winter 2011 conferences by Tevatron for high mass Higgs searches. Although the expected exclusion is wider than in summer 2010, the observed mass range excluded at 95% now is between 158 GeV to 173 GeV (see Figure 1.4 (**bottom**)).

Indirect searches

As mentioned at the beginning of section 1.4.2, the Higgs boson mass is involved in radiative loops corrections of electroweak parameters of the SM. The principle of indirect searches consists of comparisons between electroweak precision data and theoretical predictions that dependent of M_H.

Two working groups, the LEP Electroweak Working Group [8] and the GFitter Collaboration [6] provide results about the possible values of M_H using global fit procedures of SM measured parameters.

The Higgs boson mass is constrained by fitting the SM using the set of SM parameters (G_F, M_t, M_Z, α_{QED}, α_{em}) measured in the different experiements. The LEP Eletroweak Working Group results are displayed in Figure 1.5, which shown the distribution of the global least-squares fit of the SM $\Delta\chi^2 = \chi^2 - \chi^2_{min}$ as a function of the Higgs mass. The preferred value for M_H at $\Delta\chi^2 = 0$ is found to be

$$M_H = 89^{+35}_{-26}\ \text{GeV} \tag{1.29}$$

The upper limit obtained for the Higgs boson mass is $M_H < 158$ GeV (with a CL of 95% obtained with $\Delta\chi^2 = 2.7$, which includes experimental and theoretical uncertainties).

[8] e^+e^- collisions at $\sqrt{s} = 90$ to 209 GeV were produced
[9] $p\bar{p}$ collisions are produced at $\sqrt{s} = 1.96\ TeV$

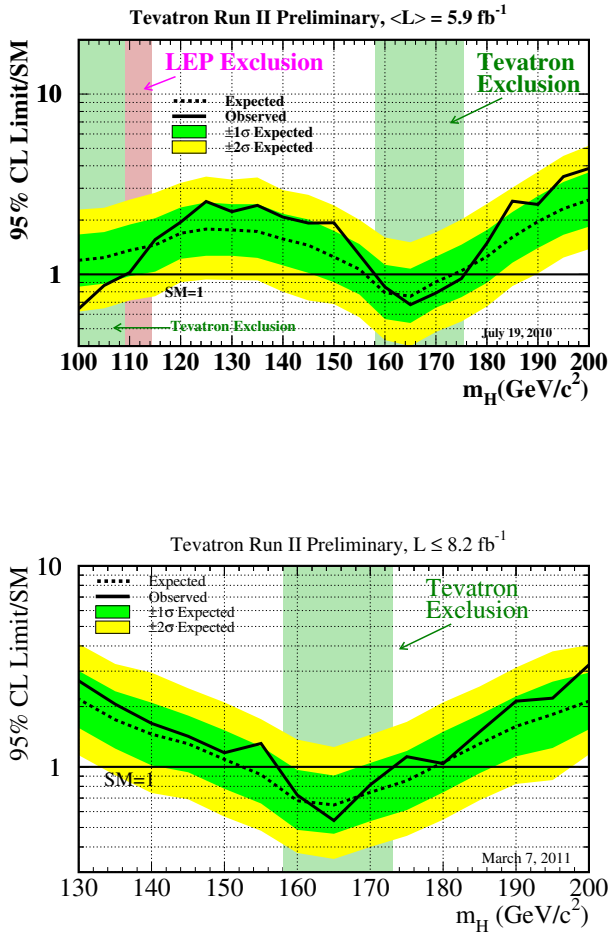


Figure 1.4: Observed and expected 95% C.L. upper limits on the ratios to the SM cross section, as functions of the Higgs boson mass for the combined CDF and DØ analyses. (**top**) summer 2010 [1], (**bottom**) spring 2011 [203].

The limit is $M_H < 185$ GeV if the results of direct searches of the Higgs boson at LEP are included.

Similar results are obtained by the GFitter collaboration when a standard fit is used with slightly different methods. This fit (see Figure 1.6(Left)) gives:

$$M_H = 95.7^{+30.6}_{-24.2} \text{ GeV} \tag{1.30}$$

And after using a complete fit (done in summer 2010, including last results of direct searches of the Higgs boson at LEP and Tevatron up to 5.9 fb^{-1} but not the direct Higgs search results shown in winter 2011 by Tevatron and LHC), see Figure 1.6 (**Right**) , the

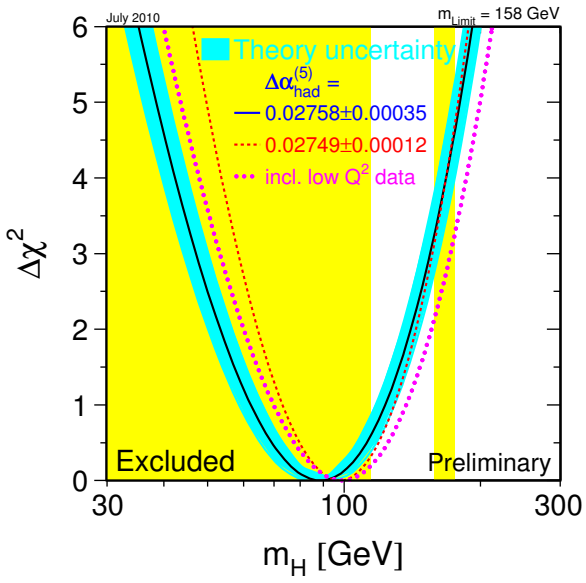


Figure 1.5: Global fit of the SM as a function of the Higgs mass. The direct limit established by LEP is represented by the yellow region, although not included in the fit. The theoretical errors are represented by the blue bands [8].

following results are found

$$M_H = 120.6^{+17.9}_{-5.2} \text{ GeV} \tag{1.31}$$

1.5 SM Higgs boson at the LHC

1.5.1 The Higgs production

In proton-proton collisions at the LHC the SM Higgs boson will be produced by the following processes, (for details see [174]) ordered by cross section (see Figure 1.7):

- Gluon fusion.
  The Higgs boson is produced by the fusion of two gluons via a heavy-quark loop. This process is also called direct production and it has the largest cross section over the allowed mass range. As displayed in the leading order diagram, the loop is dominated by top quarks. Important higher order processes are for example $gg \to H$, $gq \to Hq$ and $g\bar{q} \to Hg$. The NNLO cross section was computed in the last 10 years ([55, 155, 191]) and there is currently a large debate on the knowledge of the theoretical uncertainties (of the order of 15%).

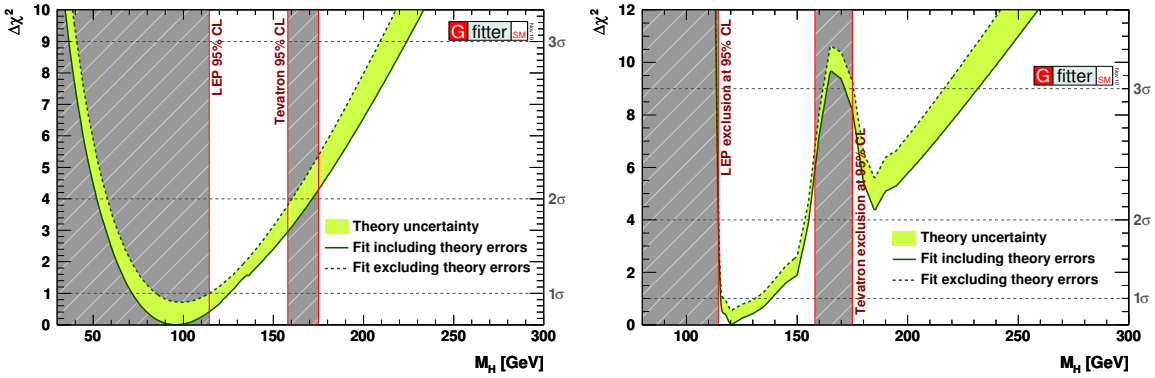


Figure 1.6: $\Delta\chi^2$ as a function of M_H.(**Left**) M_H with a standard fit and (**Right**) with a complete fit. The solid (dashed) line gives the results when including (ignoring) theoretical errors. The minimum χ^2 of the fit including theoretical errors is used for both curves to obtain the offset-corrected χ^2 [6].

- Vector-boson-fusion(VBF)
  In this channel the Higgs boson is produced by the fusion of two weak vector bosons (W or Z) which are radiated off quarks. This process leaves a special signature in the detector. The quarks hadronize to jets which will be detected in the forward region of the detector (close to the beam pipe). There is no color connection between the two quarks, hence between the two forward jets, little hadronic activity is expected in the signal process. This typical VBF signature is used to suppress the QCD background. This process has been computed recently at NNLO [96].

- Associated production $W^{\pm}H$, ZH
  In this process the Higgs boson is radiated off a weak vector boson (Higgstrahlung). Its cross section falls rapidly with an increasing value of M_H and has been computed at NNLO [101].

- Associated production $t\bar{t}H$
  The Higgs production in association with top-pairs is less important because the cross section is about five times smaller than the one for $W^{\pm}H$ or ZH for the low mass range M_H. It has been computed at NLO [91, 92, 122].

1.5.2 The Higgs decay modes

In the SM, the Higgs mass is a free parameter of the theory. It fixes the Higgs coupling to gauge bosons and fermions. In this section, the three main mass regions to be exploited at the LHC will be described (in Figure 1.8 is shown the variation of the braching ratios as a function of the Higgs boson mass):

- In the low mass range ($100 \leq M_H \lesssim 130$ GeV) the Higgs boson mainly decays into a $b\bar{b}$ pair, $BR_{b\bar{b}} > 70 - 75\%$, due to the Higgs coupling to fermions proportional

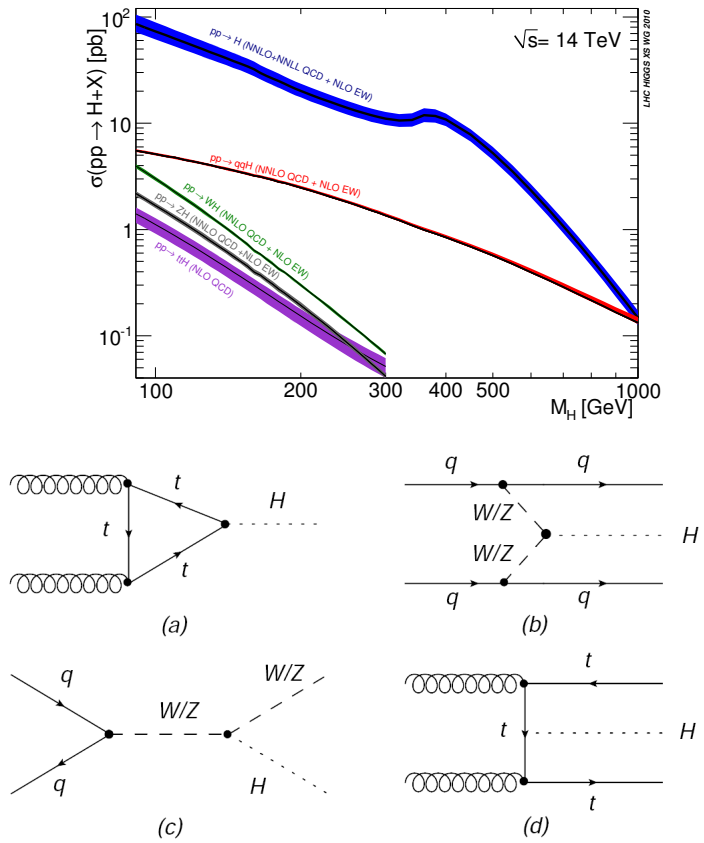


Figure 1.7: (**Top**) SM Higgs boson production cross section as a function of M_H at the LHC at $\sqrt{s} = 14\ TeV$ [174]. (**Bottom**) Leading order Feynman diagrams for the relevant SM Higgs boson production processes: (a) gluon fusion, (b) vector boson fusion, (c) W/Z associated and (d) $t\bar{t}$ associated production.

to their mass. The discovery potential of Higgs search in this channel at LHC is however small due to large QCD background.

The $H \rightarrow \tau\bar{\tau}$ channel has a smaller branching ratio, about 8%, and suffers from large background from the $Z \rightarrow \tau\bar{\tau}$ decay process. However, when searching the Higgs in the VBF production mode, this is a promising channel at low masses. Details can be found in [14].

The $\gamma\gamma$ and $Z\gamma$ decay modes also occur in the low mass range and are due to the indirect Higgs coupling to the photon. The Higgs decay into two photons is made through fermions, mainly top quark and W boson loops.

Despite its small branching ratio, the $H \rightarrow \gamma\gamma$ is a very important channel at low masses, ($100 < M_H < 150$ GeV) because it presents a very clean signature and has a narrow width which will provide sufficient discrimination against backgrounds. This channel was very important for physicists since the beginning of LHC. The

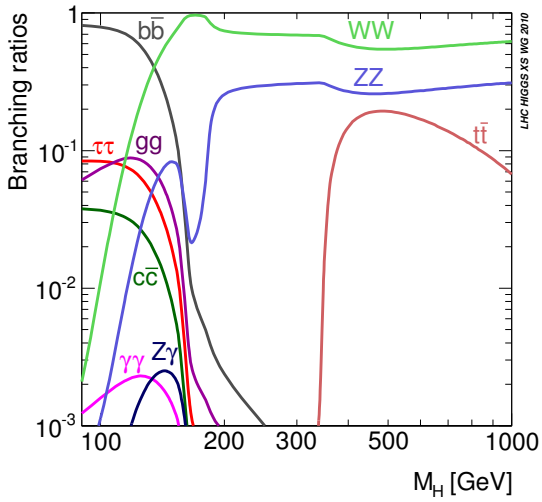


Figure 1.8: Branching ratios of the SM Higgs boson a function of M_H at the LHC at $\sqrt{s}$= 14 TeV [174].

first analysis [119] was done on Monte-Carlo by C. Seez and J. Virdee in 1990 in what will become CMS and was followed by several studies in ATLAS [140].

- In the intermediate mass range ($130 \leq M_H \lesssim 200\ GeV$). The WW and ZZ channels open and have a large branching ratio due to their stronger coupling to the Higgs. The decay to WW is the most promising channel, because this decay has a branching ratio close to 100% in this mass range.

  The $ZZ \rightarrow 4l$ is a very important channel at medium to high masses ($M_H \geq 200$ GeV), since the presence of four electrons or muons in one event is a very unique and therefore distinguishable signature at a hadron collider.

- At $M_H > 2M_{top} \sim 350\ GeV$, the top pair decay opens and increases rapidly due its very strong coupling to the Higgs. However large QCD background and background from the $t\bar{t}$ through this channel. There may be however some possibilities in the channels $H \rightarrow ZZ \rightarrow ll\nu\nu$ and $H \rightarrow ZZ \rightarrow llqq$ and $H \rightarrow WW \rightarrow l\nu qq$.

Chapter 2

QCD Prompt Photon Production

In this chapter, the prompt photon production with large transverse momentum in high energy hadron (proton at LHC) collisions is discussed. First, the QCD formalism for photon production and the different production mechanisms are presented. In addition, the main procedures used to compute their cross section are described. Finally, a short history about the experimental measurements of prompt photon is given.

2.1 The Factorization Theorem

The protons are composite objects of quarks and gluons, which are called *partons*. In a naive picture, the proton is made of three color quarks, two up quarks and one down quark, of respective electric charge 2/3 and $-1/3$. The proton is a colorless object of charge $+1$.

The proton is seen as a gas of partons each carrying a fraction x of the proton momentum. In addition to the three quarks of valence, the vacuum polarization generates gluons and sea-quarks (quark-antiquark pairs). Therefore, heavier quarks, charm and strange quarks (and also bottom quarks) arise in the proton. So, the proton structure is described by the parton distribution function (PDF) of valence quarks, gluons and sea-quarks.

QCD provides the formalism to calculate the cross section for interactions involving hadrons in the initial or the final state. The factorization theorem [130] says that the cross section of any QCD process can be written as the convolution of three basic building blocks; PDF, parton-parton cross section and parton fragmentation to hadrons.

$$\sigma(P_1,P_2)=\sum_{i,j,k}\int d_{x_1}d_{x_2}d_{z_3}f_{i/1}(x_1,\mu_F^2)f_{j/2}(x_2,\mu_F^2)D_{k/3}(z_k,\mu_f^2)\hat{\sigma}_{ijk}(p_1,p_2,p_3,\alpha(\mu_F^2),Q^2/\mu_F^2) \tag{2.1}$$

From equation 2.1, we have:

1. P_1 and P_2 are the momenta of the incoming hadrons. $p_{1,2}=x_{1,2}P_{1,2}$ correspond to

the momenta of the partons which belong to the hard scattering process.

2. $f_{m/n}(x_n, \mu_F^2)$, with $m = i, j$ corresponding to the parton type and $n = 1, 2$, corresponding to each of the incoming hadrons are probability densities for a parton to be found within the colliding hadron H_n. It is a function of the momentum fraction x_n of the hadron momentum carried by the parton at a given factorization scale μ_F (PDF), see an example in the Figure 2.1. The factorization scale is an arbitrary parameter introduced to handle singularities [1] in the calculation that cannot be treated perturbatively.

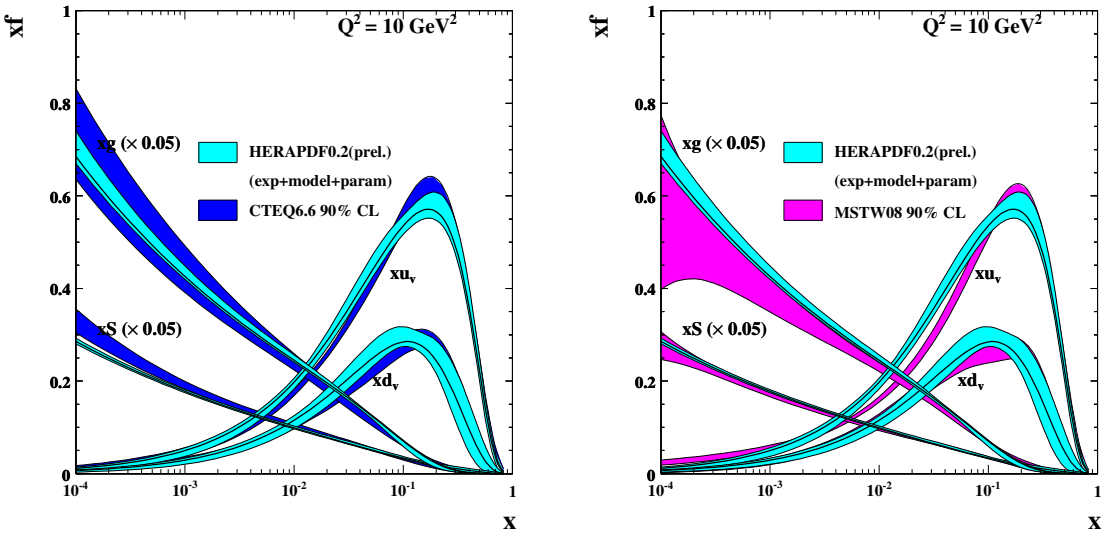


Figure 2.1: The HERA PDF compared to CTEQ (left) and MSTW (right) [125].

The PDFs cannot be determined by perturbative QCD calculations but its functional forms are parametrized from experimental data at a fixed scale Q_0^2. They are defined in a way that is universal and their evolution with the factorization scale is predicted by the DGLAP (Dokshitzer, Gribov, Lipatov, Altarelli, Parisi) equations [50, 129, 150, 175], so the PDFs measured at one scale can be used to predict the results of experiments at other scales. There are different sets of PDF parametrizations. Two mains groups have used HERA [127] data and different theoretical assumptions to predict the PDF at the LHC energy.

- The Coordinated Theoretical and Experimental Project on QCD (CTEQ) [3, 180].
- The Martin-Stirling-Thorne-Watt (MSTW) PDFs [10, 178].

They frequently publish updated tables of PDF's. At high energy and small x fraction of momenta, the gluon density dominates. The large gluonic activity in the

[1] These singularities are caused by soft physics effects such as collinear radiation, and are absorbed into the PDF at a given scale μ_F, usually chosen to be of the order of the hard scale Q^2.

LHC environment explains the large cross section of the Higgs boson production through the gluon fusion process despite the small (indirect) Higgs boson coupling to gluons.

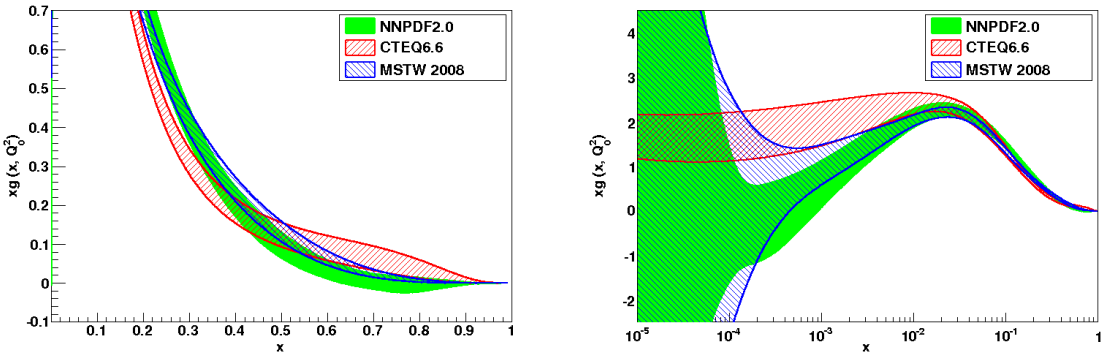


Figure 2.2: Gluon PDFs within the proton as a function of the fraction x of the proton momentum carried by the gluon. The scale used is $Q^2 = 5\ GeV^2$. The left plot, uses a linear scale and the right plot a logarithmic scale. A comparison is shown for three different teams that provide PDFs at Next-to-Leading Order [86].

3. $D_{k/3}(z_k, \mu_f^2)$ is the fragmentation function and gives the probability that the produced parton gives a final state particle H_k with momentum fraction z_k during the fragmentation process at some fragmentation scale μ_f. The fragmentation scale is introduced in the same way as the factorization scale and under similar prescription. It intends to absorb singularities due to final-state collinear radiation. Like the PDFs, the fragmentation functions are not calculable, but one can calculate their dependence with the scale. The fragmentation functions into hadrons (for instance π^0) appear in the calculation when the final state particle (π^0 in this case) is the result of the fragmentation process of the parton produced in the hard scattering in the hard interaction collision (in this case background to photons). One can have also the case of the fragmentation of a quark or a gluon into a photon (**fragmentation** photons). In this case the contribution to the cross section will depend on the quark and gluon fragmentation functions into photons $D_{\gamma/q}$ and $D_{\gamma/g}$ [99, 102].

4. Finally, the $\hat{\sigma}_{ijk}$ term corresponds to the parton cross section interaction. Its is normally computed at a given order of pQCD and at a renormalization scale μ_R. The renormalization scale is introduced to absorb the ultraviolet singularities that appear at higher than LO as in the perturbative calculations. It is usually chosen to have the same value of μ_F and μ_f. There is no reason for these three scales to be exactly the same, but they should not be chosen to be very different from each other because this would introduce an unphysical hierarchy into the calculation [2].

[2]Since they are totally arbitrary, any physical observable must be independent from their particular choice

If a calculation were carried out to all orders in perturbation theory, there would be no dependence left in the final result. However, most calculations are available at a fixed order, and therefore a residual dependence on the scales is left. The variation of the cross section with the scale reflects the size of the non computed terms in the perturbative expansion

$$\mu^2 \frac{d}{d\mu^2} \sum_{i=0}^{N} \alpha_s^i \sigma_i = \mathcal{O}\left(\alpha_s^{N+1}\right) \tag{2.2}$$

The choice of the PDFs and fragmentation functions used in the theory calculation also leaves some residual dependence in the predictions that must be taken into account when comparing to the experimental data.

2.2 Prompt Photon Production

The production and associated measurement of prompt photons provide a direct test of perturbative quantum chromodynamics (pQCD) predictions. Moreover, one of the main motivations for its measurements is their potential to constrain the gluon distribution of the proton [162, 169] since the dominant contribution to the cross section comes from gluon-quark interactions [see Figure 2.4(a),(c),(d),(e)]. In addition, its measurement offers some unique advantages over measurements with jets, because the process also gives access to lower transverse momenta (p_T) than jets, where the underlying event contamination reduces the sensitivity of the QCD measurements. The photon energies are measured in the Electromagnetic (EM) calorimeters, resulting in a better energy resolution. Furthermore, this process is also the starting point for the studies of many SM signatures, and constitutes a reducible background for important searches, such as $H \rightarrow \gamma\gamma$, or SUSY and extra-dimensions with energetic photons in the final state.

Prompt photons at a hadron collider, are produced, at leading order (LO), mainly by: Compton-like scattering [Figure 2.4(a)], or $q\bar{q}$ annihilation [Figure 2.4(b)]. At the LHC energies, the rate of the Compton-like process is much higher than that of the annihilation process, and effectively dominates the cross section at all transverse energies (E_T). This can be seen in Figure 2.3.

At next-to-leading order (NLO), diagrams with one-loop vertex corrections Figures 2.4(c) and 2.4(d) produce infrared divergences. To cancel them out, diagrams containing radiative corrections [Figures 2.4(e),(f),(g)] are required, in which photons are radiated off from an incoming or outgoing parton (ISR and FSR, respectively), or by intermediate propagators, giving the so-called "brem" diagrams. Additionally, "fragmentation" photons arise from final state partons which, during fragmentation, photons are produced [Figure 2.4(h)] [3].

[3]The distinction among ISR, FSR and fragmentation photons is only motivated by the way generators model these processes, but has no physical meaning, as the corresponding diagrams interfere.

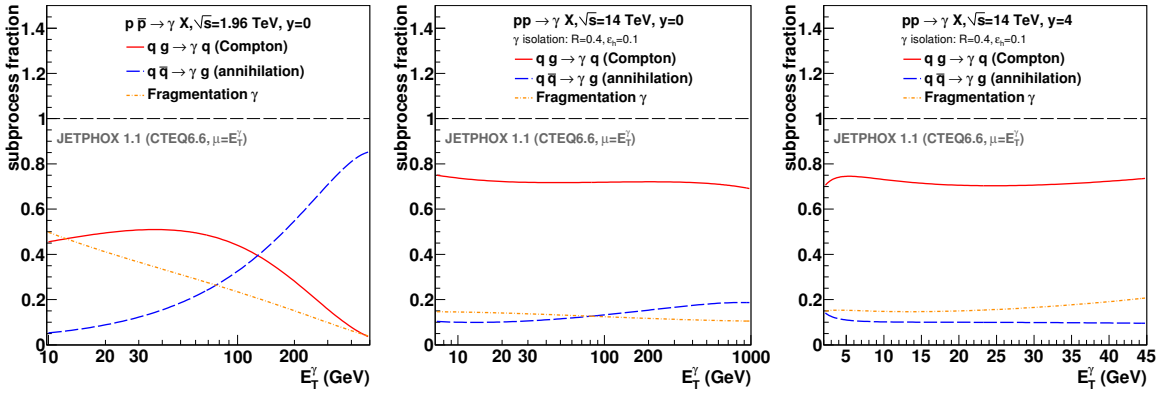


Figure 2.3: Relative contributions of the quark-gluon Compton, $q\bar{q}$ annihilation and fragmentation subprocesses in NLO *isolated* photon production at the Tevatron (left), LHC midrapidity (center) and LHC forward rapidity (right) obtained with JETPHOX (CTEQ6.6 PDF, $\mu = E_T^\gamma$, BFG-II FFs) for an isolation radius $R = 0.4$ and a hadron fraction of the photon energy of $\varepsilon_h = 0.1$ inside the cone [164].

At LO and NLO, the differential cross section as a function of the transverse momentum p_T and the pseudorapidity [4] η of the photon can be written as the sum of the direct and the fragmentation contributions [80, 104]:

$$\frac{d\sigma\left(\mu_R,\mu_F,\mu_f\right)}{dp_T d\eta} = \frac{d\sigma_D\left(\mu_R,\mu_F,\mu_f\right)}{dp_T d\eta} + \frac{d\sigma_f\left(\mu_R,\mu_F,\mu_f\right)}{dp_T d\eta} \tag{2.3}$$

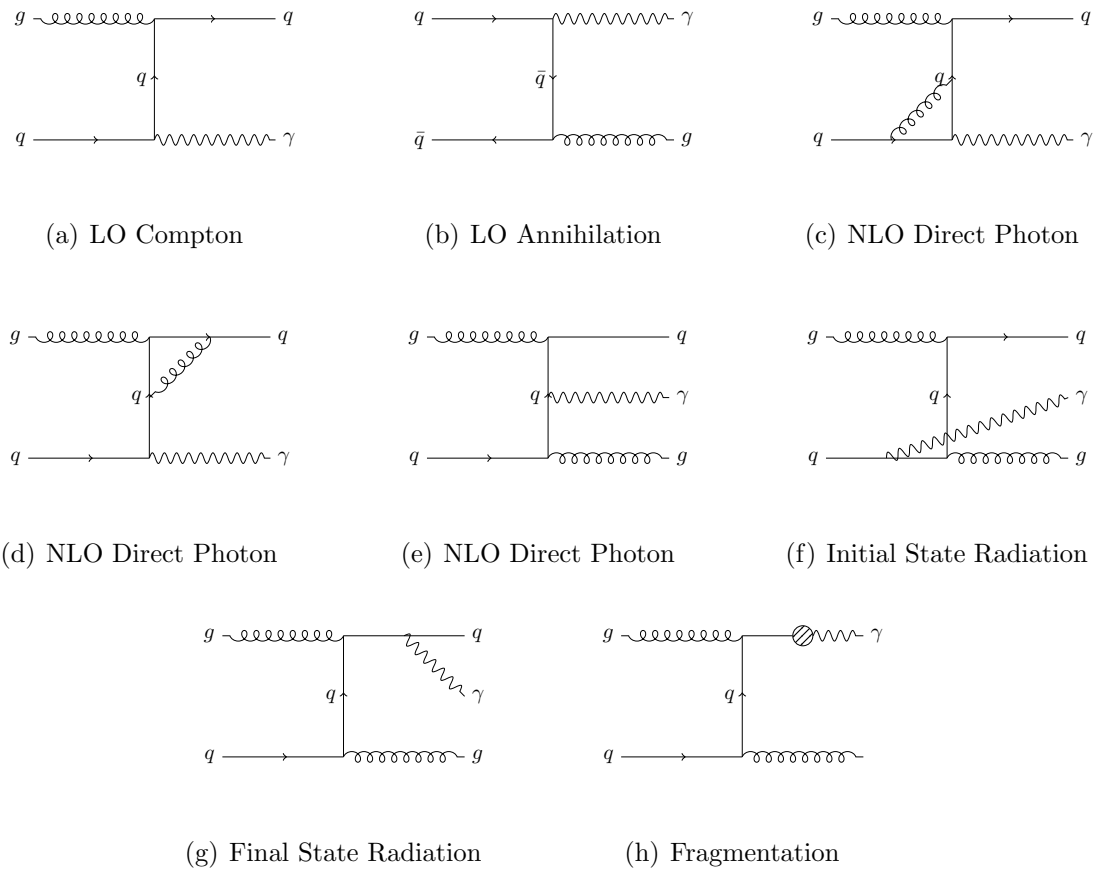
The distinction between these two mechanisms has no physical meaning [80] and one should note [93] that the fragmentation process shown in Figure 2.4(h) is of the same order than the LO Compton shown in Figure 2.4(a): if the fragmentation scale μ_f is large compared to the typical hadronic scale, the fragmentation functions behave roughly as $\alpha/\alpha_s(\mu_f^2)$. The separation between them in the theoretical calculations is arbitrary, and only their sum has physical meaning and can be compared to the experimental cross section. The fragmentation part can be expressed synthetically as:

$$\frac{d\sigma_f\left(\mu_R,\mu_F,\mu_f\right)}{dp_T d\eta} = \sum_{k=q,\bar{q},g} \frac{d\sigma_k^f\left(\mu_R,\mu_F,\mu_f\right)}{dp_T d\eta} \otimes D_{\gamma/k}(\mu_f) \tag{2.4}$$

σ_k^f describes the production of a parton k in the hard collision and $D_{\gamma/k}$ for the fragmentation function of the parton k into the photon.

Two alternative methods exist for the calculation and implementation of these functions. In both schemes the bremsstrahlung process is split into a perturbative and a non-perturbative part at some fragmentation scale, μ_f. In the first scheme, as outlined in [80] and implemented in the JETPHOX [7] Monte Carlo generator, the perturbative part (such as Figures 2.4(e),(f),(g)) is computed up to the desired order with contribu-

[4] The pseudorapidity is defined as a function of the polar angle of the photon θ as $\eta = -\ln\left(\tan\frac{\theta}{2}\right)$.



(a) LO Compton (b) LO Annihilation (c) NLO Direct Photon

(d) NLO Direct Photon (e) NLO Direct Photon (f) Initial State Radiation

(g) Final State Radiation (h) Fragmentation

Figure 2.4: Leading order (a,b) and next-to-leading order production diagrams of prompt photons in proton-proton collisions. In (h) one has the point-like fragmentation of a quark into a photon, which can be calculated perturbatively for asymptotically large scales.

tions containing μ_f being resummed. This resummation introduces a dependence on the factorisation scale. Photons produced during the soft QCD hadronisation (such as Figure 2.4(h)) are then described using the vector meson dominance (VMD) model [99]. Here the fragmentation of a quark or gluon is described via its fragmentation mainly into a linear combination of vector mesons which then decay into photons. Under the second scheme as outlined in [102, 147] the calculation of the perturbative part is not resummed and is performed to a fixed order in μ_f. The non-perturbative part is obtained through a fit to LEP data. Since the perturbative calculations are not resummed, there exist cancellations of terms involving μ_f factors and therefore, under this scheme, the calculations are not μ_f dependent.

Bremsstrahlung photons can provide a significant source of isolated photons. Clearly if the emission of a photon occurs at a shallow angle, these photons will be associated with the final state quark remnants and may be removed by a suitable isolation cut. However, in the cases where photons are radiated at large angles the isolation cuts will not remove such events. These events must therefore be included in the cross section calculation and somewhat "spoil" the simplicity of the direct photon formalism [161]. A

naive expectation of the rate of such events might be $\mathcal{O}(\alpha\alpha_s^2)$, since two strong and one electromagnetic vertices are involved in these processes. If this were the case then they should contribute little to the overall observed signal. However, as discussed above [81, 93, 184] the fragmentation component in fact scales as $\mathcal{O}(\alpha\alpha_s)$ and is therefore of the same order as the two LO processes. This then leads to the expectation that the cross section for fragmentation, in the absence of isolation, will be similar to that for the direct processes [104].

2.3 Previous Measurements

Many years of intense experimental and theoretical efforts have contributed to the understanding of inclusive prompt photon production in hadron collisions. A large variety of experiments have measured the photon cross section at both fixed target and collider energies (see Table 2.1 for a summary).

Fixed target experiments have traditionally provided data in the x range from 0.1 to 0.6. Indeed, data from WA70 and UA6 have been used in some parton distribution fits [170, 177]. However, inconsistencies between direct photon formalism and the more recent fixed target experiments carried out at the Tevatron (E706), together with the large theoretical uncertainties present implies that such data are now no longer included in the most standard fits. The high x gluon content is instead constrained using the high E_T jet data from CDF and DØ and momentum sum constraints from DIS ("Deep Inelastic Scattering") data.

The first hadron collider to measure direct photons cross section was the CERN ISR R806 experiment. Together with the UA1 and UA2 experiments at the S$p\bar{p}S$ they probed the gluon in the region $0.05 < x < 0.3$. These early data gave qualitative agreement with NLO calculations and it was the high statistic datasets of the Tevatron experiments, which made real precision measurements at high $\sqrt{s}$. The DØ and CDF experiments measured the gluon content down to 0.01 while the fixed target experiment (E706) made measurements in the region $0.01 < x < 0.7$. Data from these and other direct photon measurements are plotted in Figure 2.5 (left). The interpretation of these data and the completeness of current direct photon formalism has been the subject of much debate in last years. In particular, in the late 90's, some confusion was created by the fixed target experiment E706, whose experimental results are higher than the theoretical predictions; the data showing a steeper dependency on x_T than suggested by the theory. This situation motivated the introduction of an extra non-perturbative parameter to account for the effects of multiple soft gluon emissions associated to the hard partonic scattering [62, 170], so the colliding partons would posses a small amount of transverse momentum (k_T) due to the recoil of the system, and the smearing of the initial-state center-of-mass energy would increase the cross section because of its steep slope as a function of p_T.

It should be noted that this k_T hypothesis is not universally accepted. Authors of [80] show that good agreement between NLO theory and data is possible over a wide range of data sets without the need for additional k_T. This is reproduced in Figure 2.5 (right), showing data over eight orders of magnitude in the cross section and two orders of mag-

Experiment	Accelerator	Initial state	$\sqrt{s}$ or E [GeV]	year	Ref.
SFM	ISR	pp	45, 53	1976	[121]
R108	ISR	pp	62.4	1980	[59]
R806	ISR	pp	63	1982	[54]
R807	ISR	pp, $\bar{p}p$	53	1985	[44]
NA24	SPS fixed target	$\pi^{\pm}p$, pp	E =300	1987	[124]
WA70	SPS	pp	280	1988	[97]
UA1	S$p\bar{p}$S	$p\bar{p}$	546, 630	1988	[45]
UA2	S$p\bar{p}$S	$p\bar{p}$	630	1988	[61]
R110	ISR	pp	63	1989	[60]
UA2	S$p\bar{p}$S	$p\bar{p}$	630	1992	[48]
E706	Tevatron fixed target	$\pi^{-}Be$, pBe	E =500	1992	[52]
UA6	SPS	$p\bar{p}$, pp	24.3	1993	[144]
E704	Tevatron fixed target	p-liquid hydrogen	E =200	1995	[39]
CDF	Tevatron	$p\bar{p}$	1800	1995	[26]
DØ	Tevatron	$p\bar{p}$	1800	1996	[21]
UA6	SPS	$p\bar{p}$, pp	24.3	1998	[87]
E706	Tevatron fixed target	pBe	38.8, 31.6	1998	[63]
DØ	Tevatron	$p\bar{p}$	1800	2000	[25]
DØ	Tevatron	$p\bar{p}$	1800, 630	2001	[23]
CDF	Tevatron	$p\bar{p}$	1800, 630	2002	[37]
CDF	Tevatron	$p\bar{p}$	1800	2004	[38]
E706	Tevatron fixed target	$\pi^{-}Be$, pBe	38.8, 31.6	2004	[64]
PHENIX	RHIC	pp	200	2005	[40]
DØ	Tevatron	$p\bar{p}$	1960	2006	[22]
PHENIX	RHIC	pp	200	2007	[41]
CDF	Tevatron	$p\bar{p}$	1960	2009	[20]

Table 2.1: Summary of the direct photon measurements at the different accelerators (fixed targets or colliders). The name of the experiment is given in the first column, in the second column the name of the accelerator is indicated. The third column provides the particles in the initial state. The next columns detail the centre-of-mass of fixed target energy, the year when the experiment published their results and their references [126, 163].

nitude in energy in agreement with the NLO `JETPHOX` Monte-Carlo program. The clear exception to this is shown by the E706 data, on the bottom left of the Figure 2.5 (right). In addition, they also point out that the introduction of k_T smearing has an opposite effect on the agreement of other data sets with NLO theory. The first results from LHC will be shown later. One will expect at the end of 2012 to have measurements up to a transverse momentum close to 1 TeV.

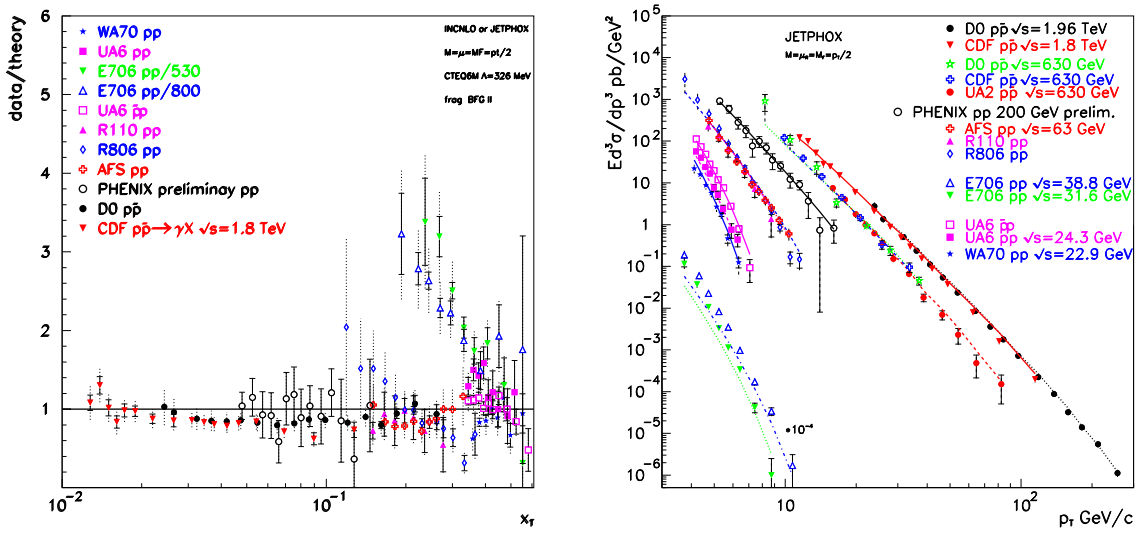


Figure 2.5: The left plot shows the ratios data/theory (NLO pQCD calculations) for collider and fixed target data with the scale $\mu = p_T/2$. In the right plot is shown, the world inclusive and isolated direct photon productions cross sections measured in pp and $p\bar{p}$ collisions compared with `JETPHOX` NLO predictions using BFG II (CTEQ6M) for fragmentation (structure) functions and a common scale $p_T/2$. The plots and captions have been taken from [80].

Chapter 3

The Large Hadron Collider

The Large Hadron Collider (LHC) [137] is a proton-proton collider with a nominal centre-of-mass energy of 14 TeV and a design luminosity of $10^{34}\ cm^{-2}s^{-1}$. It is installed in the LEP (Large Electron Positron Collider) circular tunnel under the French-Swiss border. It is 27 Km in circumference and lies between 50 and 175 meters below the surface.

At the LHC, the beam trajectory is bent by 1232 14.3 meters long 35 tons superconducting dipole magnets which contain the two beam pipes. The dipoles generate for the nominal centre-of-mass energy a magnetic field of 8.4 T at a current of around 11.7 kA. 392 quadrupoles magnets are used to focus the beams. The magnets are cooled to the temperature of the superfluid Helium T = 1.9 K (at atmospheric pressure).

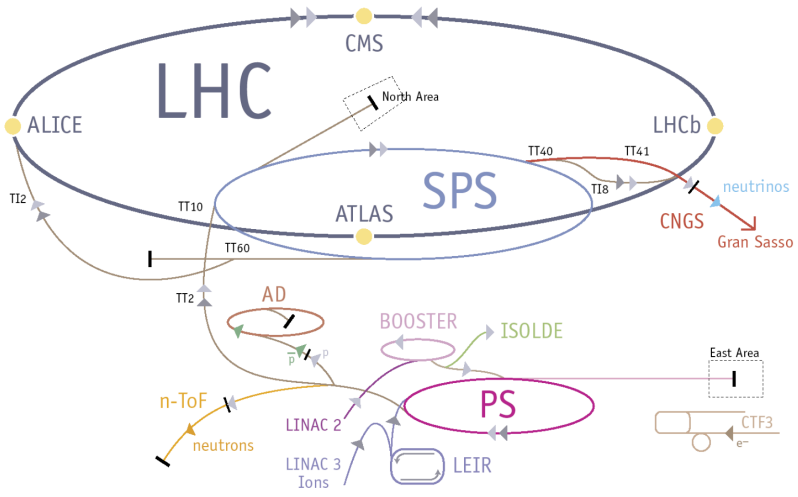


Figure 3.1: The LHC accelerator complex

The accelerator complex comprises several steps. The protons are produced from a source of hydrogen [133] and then injected in the linear proton accelerator LINAC2, which generates 50 MeV proton beams. The Proton Synchrotron booster (BOOSTER) increases the energy up to 1.4 GeV and the protons are injected into the two proton synchrotrons,

the Proton Synchroton (PS) and the Super Proton Synchrotron (SPS), where the beam energy will be increased to 25 and 450 GeV respectively and finally will be ready to be injected into the LHC accelerator where beams will be accelerated to the collision energy (nominally 7 TeV).

Figure 3.1 shows the beams interaction points around which the different physics experiments are installed and the accelerator system.

- Two multi-purpose experiments, ATLAS (A Toroidal LHC ApparatuS) [111] and CMS (Compact Muon Solenoid) [112] whose experimental techniques are complementary while the physics goals are the same. In CMS for example the electromagnetic (EM) calorimeter is made by scintillating lead-tungsten crystal located within a solenoid coil, while ATLAS has chosen liquid argon as sampling material and lead and stainless steel as absorbers (see chapter 5) situated outside of the solenoid coil.

- The Large Hadron Collider beauty (LHCb) experiment [113] is a one-side forward detector designed to study *b-physics* and aiming at measuring the parameters of CP violation.

- A Large Ion Collider Experiment [202] (ALICE) is a heavy ion experiment. For this physics, the LHC collides lead ions (^{206}Pb). The main goal is to study the quark-gluon plasma in order to understand the matter confinement at the early time of Universe. The first heavy collisions in the LHC happened in 2010. One may have $p-Pb$ collisions in 2012, and lighter ions (Ar, Xe, ...) could be available later [165].

- The TOTEM [115], for "TOTal cross section, Elastic scattering and diffraction dissociation Measurement at the LHC". Like its name indicates it will measure the total cross section of the proton and the absolute luminosity at LHC. TOTEM is installed near of the interaction point used by CMS.

- The Large Hadron Collider forward [114] (LHCf) Detector will measure particles produced very close to the direction of the beams in the proton-proton collisions at the LHC. The motivation is to test models used to estimate the primary energy of ultra high-energy cosmic rays. It consists of two small detectors located at 140 m on each side of the interaction point of the ATLAS detector.

3.1 LHC Performance

The main parameters that determine the performance of the LHC are its *instantaneous Luminosity* ($\mathcal{L}$) and its centre-of-mass energy ($\sqrt{s}$). The rate R (the number of events per second) of any given particle interaction is governed by the instantaneous luminosity, such that

$$R = \mathcal{L} \cdot \sigma_{int} \tag{3.1}$$

were σ_{int} is the interaction cross section. Tables 3.1 list some of the typical cross-sections expected for SM processes as well as possible new physics. Table 3.2 summarizes the

parameter values for the end of the 2010 data-taking and for the nominal running at $10^{34}\ cm^{-2}.\ s^{-1}$ of instantaneous luminosity.

and the beam characteristics for two scenarios at the LHC, respectively.

Final state	Cross-section
$b\bar{b}$	$\mathcal{O}(100\ \mu b)$
High p_T Jets	$\mathcal{O}(1\ \mu b)$
$t\bar{t}$	$\mathcal{O}(1\ nb)$
Higgs	$\mathcal{O}(1\ pb)$
Supersymetry	$\mathcal{O}(10\ pb)$

Table 3.1: Typical cross-sections at the LHC.

3.1.1 The Luminosity

The luminosity can be written as [9]:

$$\mathcal{L} = \frac{N_p^2 k_b f_{rev} \gamma}{4\pi\beta^* \epsilon_n} F \tag{3.2}$$

It only depends on the beams and collisions parameters:

- N_p : is the number of protons per bunch.

- k_b : the number of bunches per beam.

- f_{rev} : is the frequency of revolution (11245 Hz, corresponding the circumference of 26.7 km).

- γ : relativistic factor= E/m_p.

- F : the geometric reduction factor, related to the angle of beam crossing (nominally 285 μrad). The beam crossing angle (angle between the two beams) was 340 μrad during injection and 200 μrad during collisions at the end of the 2010 data taking period.

- ϵ_n : is the normalized emittance.

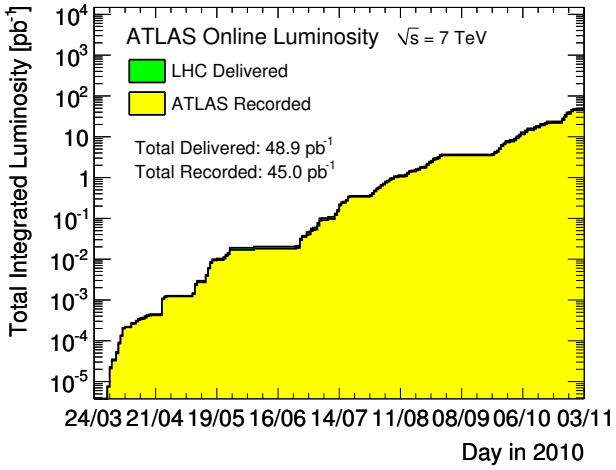
- β^* : is the amplitude function and represents the beam focalization at the collision point (nominally 0.55 m).

LHC characteristics	Typical values	
	Low Luminosity	Nominal Luminosity
Circumference	27 km	
Injection energy	450 GeV	
Beam energy	3.5 TeV	7 TeV
Magnetic field		8.4 Tesla
Luminosity	$10^{32} cm^{-2}.s^{-1}$	$10^{34} cm^{-2}.s^{-1}$
Luminosity-beam life-time	$\sim 10 - 22$ h	
Number of bunches	348	2808
Number of protons per bunch	$\sim 10^{11}$	$\sim 10^{11}$
Time interval between two bunches	150 ns	25 ns
Space interval between two bunches	45 m	7.5 m
Bunch length	7.55 cm	
Transverse beam size at the interaction point		16.7 μm

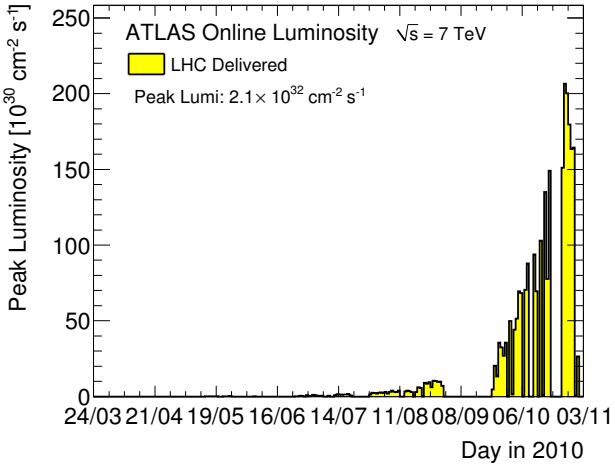
Table 3.2: LHC characteristics: "low luminosity" means the working point of the LHC at the end of 2010 data taking.

The luminosity road at the LHC

In December 2009, first collisions happened at 900 GeV centre-of-mass energy. There were 5×10^{10} protons per bunch, two bunches per beam and no crossing angle between the beams. Collected data during it first low energy collisions were used to study the perfomance of the ATLAS detector [17]. At the end of March 2010 first collisions at 7 TeV centre-of-mass energy were recorded with the same numbers of protons per bunch and bunches per beam than at 900 GeV collisions. The number of protons per bunch increased to a peak value of $\sim 1.2 \times 10^{11}$ and the number of bunches per beam progressively evolved to 368 (348 colliding in ATLAS) corresponding to a time interval between two bunches of 150 ns inside 46 bunch trains. Thus, an instantaneous luminosity peak of 2.1×10^{32} $cm^{-2}s^{-1}$ was registered. The total integrated luminosity and instantaneous luminosity by day of the 2010 data-taking period at 7 TeV collisions are shown xin Figure 3.2. In 2011 there is an increase of the number of the bunches and a decrease of β^* such that the current luminosity is larger than 10^{33} $cm^{-2}s^{-1}$.



(a)



(b)

Figure 3.2: **(a):** Total integrated luminosity and **(b):** instantaneous luminosity by day during data-taking period between 24^{th} March and 03^{rd} November 2010 with 7 TeV collisions. The systematic uncertainty on the luminosity was estimated to be 11% [18] and then was decreased to 3.4% [75] (with a central value found to be 3.6% smaller than the previous result).

Chapter 4

A Toroidal LHC ApparatuS

The ATLAS detector is a general purpose detector designed to cover the widest possible range of physics at the LHC, from the search for the Higgs boson to supersymmetry (SUSY), extra dimensions and other possible new physics. It is 44 m long, 25 m high and weighs approximately 7000 *tons*, the largest-volume collider-detector ever constructed. The ATLAS collaboration includes more than 3000 signing authors in more than 180 institutes in 39 countries (February 2011).

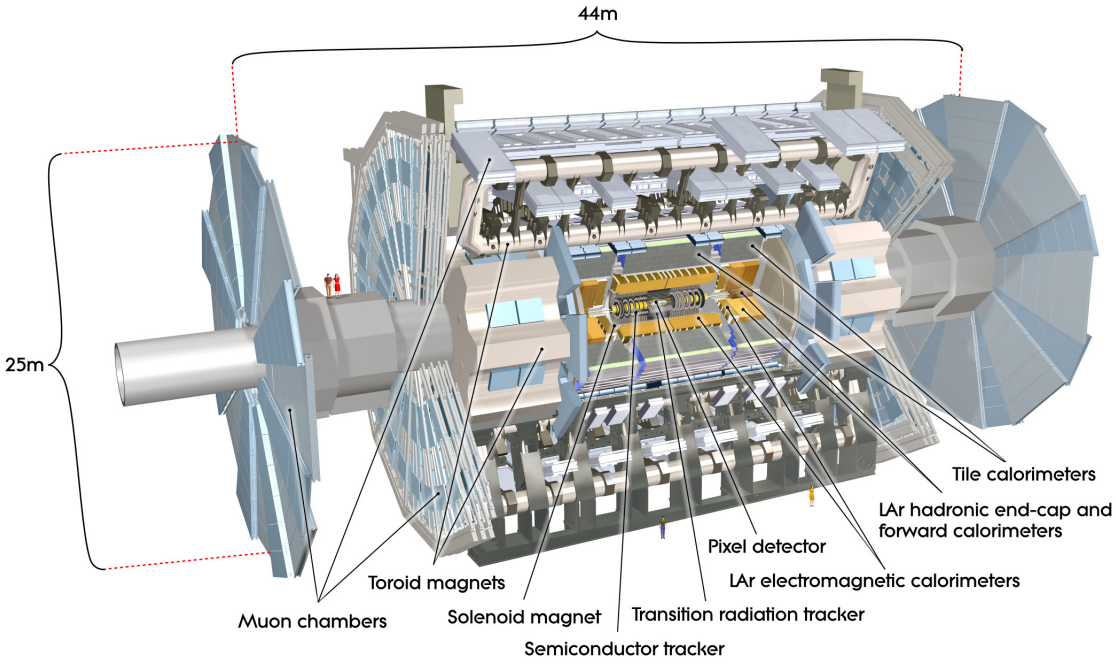


Figure 4.1: The ATLAS detectors and its sub-systems.

4.1 Design overview

The high energy and luminosity of the LHC offer a large range of physics opportunities. The requirements for the ATLAS detector system were driven by some of the most important signals for possible new physics which might be observed. ATLAS will be able to detect hadrons due to the large cross-sections of QCD interactions and all the range of the known particles in order to perform studies in electroweak interactions and flavor physics. The top quark will be produced at the LHC at a rate of a few tens of Hz, providing the opportunity to test its couplings and spin. The search for the Higgs Boson and supersymmetry have been used as benchmarks to establish the performance of ATLAS.

The promising channels for the search of the Higgs Boson at low mass (m_H <130 GeV) are the $H \to \gamma\gamma$, $H \to b\bar{b}$ and $H \to \tau\tau$. Above 130 GeV, $H \to ZZ^* \to 4l$ is the golden channel and there also $H \to WW$ and $H \to ZZ$ channels. Supersymmetry production (at low scalar mass m_0 <1 TeV) is dominated by gluinos and squarks, generating final states with many jets and isolated leptons and others Lightest Supersymmetry Particles(LSP) which will escape the detector leading to large missing transverse energy ($\not\!\!E_T$). New heavy gauge bosons (Z' and W') predicted by other models of new physics will produce leptons or jet pairs with very high transverse momenta(p_T). So, mentioned physics searches produce events featuring multi-jets, isolated leptons and photons and $\not\!\!E_T$ in a very busy multi-interaction environment driving the fundamental requirements of the detector design:

- fast, radiation resistant electronics and sensor elements,
- good charged-particle momentum resolution and reconstruction efficiency in the tracking detector and secondary vertex detection close to the interaction point for τ-leptons and b-tagging,
- very good electromagnetic calorimetry for electron and photon measurements,
- full-coverage hadronic calorimetry for accurate jet and missing transverse energy measurements,
- good muon identification and momentum resolution over a wide range of momenta,
- highly efficient triggering on low-p_T objects with sufficient background rejection.

4.2 Coordinate System and Basic Quantities

The nominal interaction point is defined as the origin of the coordinate system, while the beam direction defines the (longitudinal) z-axis, the x-y plane is transversal to the beam direction. The positive x- axis is defined as pointing from the interaction point to the centre of the LHC ring and positive y-axis is defined as pointing upwards from the interaction point. The side-A of the detector is defined to have positive z values and side-C negative z values. The azimuthal angle ϕ in the plane x-y is measured around the beam axis, and the polar angle θ is the angle from the beam axis.

In proton-proton collision, a large fraction of the longitudinal (z-axis) momentum of a partonic system giving rise to *hard processes* cannot be fully measured (undetected particles near the beam pipe). On the other hand, transverse momentum (x-y plane) is null [1]. Therefore one will use Lorentz invariant (along the z-axis) kinematic quantities

Thus, the polar angle is replaced by the rapidity

$$y = \frac{1}{2} \ln \left(\frac{E + p_z}{E - p_z} \right) \tag{4.1}$$

or rather the pseudorapidity, which is equal to the rapidity in the ultra-relativistic approximation:

$$\eta = -\ln \left(\tan \frac{\theta}{2} \right) \tag{4.2}$$

where $\eta = 0$ correspond to $\theta = 90°$ and $\eta = 5$ (typical limit on acceptance for detectors at the LHC) to $\theta \sim 0.8°$. So in hadron colliders in general and in ATLAS in particular the usual coordinate system, instead of E_x, E_y, E_z will be E_T, η, ϕ.

The transverse momentum p_T and the transverse energy E_T and the missing transverse E_T^{miss} (or $\not{E}_T$) are defined in the (x-y) plane. The ΔR cone in the pseudorapidity-azimuthal angle plane is defined as

$$\Delta R = \sqrt{\Delta\eta^2 + \Delta\phi^2} \tag{4.3}$$

4.3 Detectors

The detectors are symmetrical around the interaction point in ϕ. They will be described going from the inside to the outside.

4.3.1 Tracking

The inner detector (ID) is the component of ATLAS installed closest to the beam axis, it is used to the charge-track reconstruction of particles inside $|\eta| < 2.5$. It is contained within a cylinder 6.2 m in length, with radius 1.15 m. It consists of three disjoints and complementaries subsystems (pixel, SCT and TRT) that play an important role for the particle identification. The silicium detectors (pixel, SCT) provides an excellent position resolution and the transition radiation tracker generates trajectory points and a signal of transition radiation used for identification of electrons/pions. This detector system is surrounded by a solenoid which provides a magnetic field of 2 T.

Pixel Detector

The pixel detector is the innermost detector and aims to provide high granularity precision tracking as close to the interaction point as possible. The detector is made of three layers

[1] Supposing that transverse momentum of the partons inside protons is negligible

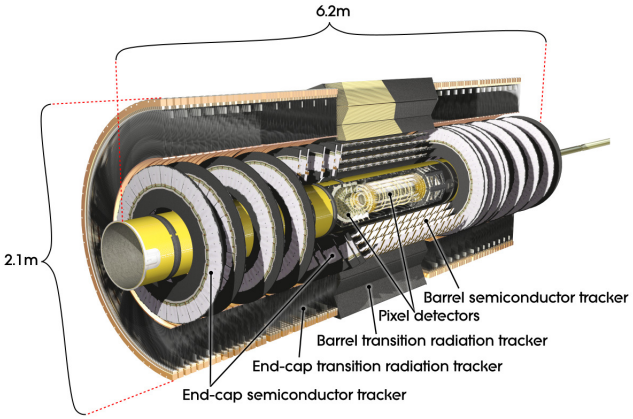


Figure 4.2: The ATLAS inner detector

in the central region (barrel) of silicon pixels located 50.5, 88.5 and 122.5 mm away from the beam axis, together with three end-cap disks installed at z position between 49 and 65 cm from the interaction point with a radius ranging from 90 to 150 mm. Each layer is paved with $\Delta(R\phi) \times \Delta z = 50 \times 400\ \mu m^2$ pixels amounting to a total of 80.4 million readout channels. The first layer starting from the beam axis is called the vertexing-layer, also called B-layer [2]. It allows for a very precise determination of primary and secondary vertices, hence useful for the tagging of b-jets. The vertexing-layer is also used to distinguish electrons (leaving in general a hit in this layer) and converted photons (if the photon is converted after the B-layer the tracks of the conversion will not leave hits in the B-layer). The accuracies in the barrel are 10 μm in $(R\phi)$ and 115 μm in z and 10 μm $(R\phi)$ and 115μm (R) for the end-cap wheels.

Semiconductor Tracker (SCT)

The SCT system is located after the pixel detector, it consists of silicon microstrip detectors providing four precision measurements per track. The detector is arranged into four concentric layers (r = 299, 371, 443 and 514 mm) and nine end-cap wheels (z = 854 to 2720 mm). The microstrip sensor installed in SCT modules consists of 126 mm long chained sensors with a strip pitch of 80μm. Each module is made of two detectors slightly tilted by 40 $mrad$ stereo angle to measure both z and $R\phi$ position with a resolution in the barrel of 580 μm and 17 μm respectively. In total, there are approximatively 6.3 millions of readout channels in the SCT. The combination of hits from strips in the same layer constitutes a so-called space-point.

[2]The B-layer will be strongly exposed to radiations, justifying its replacement after about 4-5 years of ATLAS run-periods. The IBL (Insertable B-layer) will be installed in 2013 (phase I of SuperLHC project) if it is possible. A range of new pixel sensor technologies are under study to build $250 \times 50\ \mu m^2$ pixel modules with increased radiation hardness.

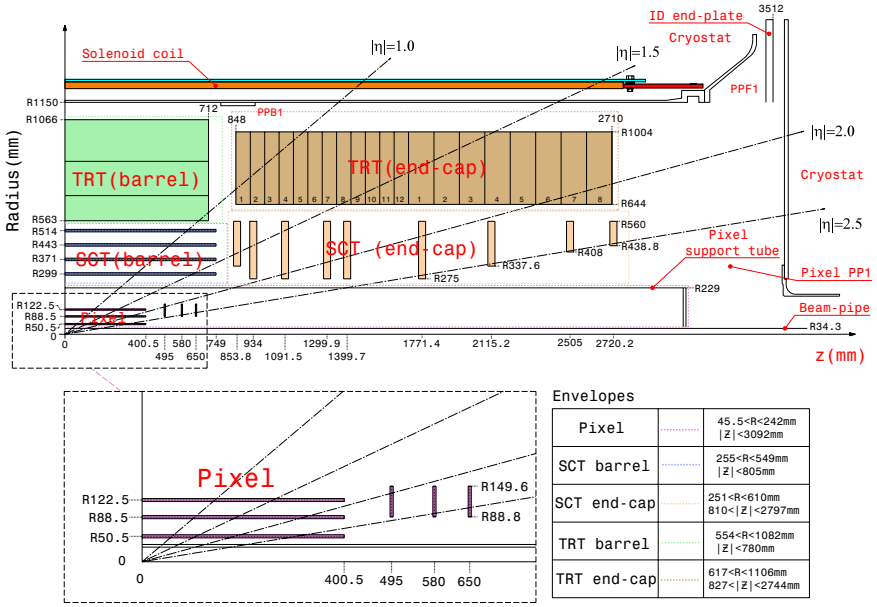


Figure 4.3: Plan view of a quarter of the ATLAS tracking detector.

Transition Radiation Tracker (TRT)

The outermost of the ATLAS tracking detectors, the TRT is a combination of a straw tracker and transition radiation detector. It is made of 4 mm diameter straw tubes filled with 70% Xenon, 20% methane and 10% CO_2. In the centre of each straw runs a gold tungsten wire(30 μm) diameter, the anode of the system that collects electrons after the gas is ionized by the passage of a charged particle, while the tube plays the role of the cathode. In the barrel, straws are aligned parallel to the beam pipe. End-cap straws are arranged in a fan shape, projecting outwardly from the beam pipe. The TRT coverage enables track trajectory reconstruction up to $|\eta| \sim 2.0 - 2.1$, as shown in Figure 4.3. This subsystem solely provides a measurement of $R\phi$ (in the barrel part) the resolution of which is 130 μm per straw. It provides a measurement of the charge particle trajectory with typically $30 - 36$ hits per track.

The transition radiation (TR) is provided by radiator foils (polyethylene and polypropylene) between the straws and two independent thresholds to distinguish between tracking hits (the lower threshold) and TR (the higher threshold). The energy in transition radiation for signals from electrons is larger than the signal deposited by particles at their minimum of ionization (MIP) which allows an efficient discrimination between electrons and $\pi^{\pm}$ (see Figure 4.4). There are in total 351000 readout channels in the TRT.

4.3.2 Calorimetry

The calorimeter's purpose is to measure the energy of the particles, together with their direction from energy deposits. In addition it will provide a measurement of the missing

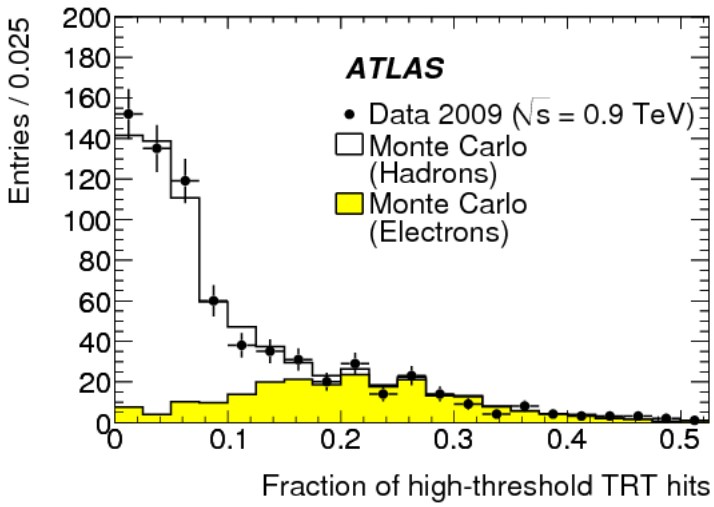


Figure 4.4: The fraction of high-threshold TRT hits for candidates within the detector acceptance of $|\eta| < 2.0$ and with a total number of TRT hits larger than ten. This results is obtained from the first LHC collisions at $\sqrt{s} = 900$ GeV [17].

transverse energy (missing E_T) of electromagnetic and hadronic particles (not muons). The calorimeter is divided into an electromagnetic (EM) compartment, dedicated to the measurement of electrons and photons, and a hadronic compartment, behind the EM calorimeter , suited for hadronic jets reconstruction and missing transverse energy measurements. It is preceded by the presampler.

The general layout of the calorimetric system is shown in Figure 4.5 and their characteristics (coverage and cells $\Delta\eta \times \Delta\phi$) are listed in Figure 4.6.

Presampler

The presampler is a 11 mm thick liquid argon layer located (inside the barrel cryostat) in front of calorimeters, covering a pseudorapidity zone of $|\eta| < 1.8$ and has a granularity of $\Delta\eta \times \Delta\phi = 0.025 \times 0.098$. It provides an estimation of the energy loss by particles in the tracking detector and solenoid in order to correct the measurements of the barrel and end-cap(at low rapidity) calorimeters.

Electromagnetic Calorimeter

The EM calorimeter is a lead / liquid-argon (LAr) ionization chamber detector covering the pseudorapidity region $\eta < 3.2$. It is divided into two half-barrels (covering the $|\eta| < 1.5$ and two end-caps $1.4 < |\eta| < 3.2$) each subdivided into two coaxial wheels. The region between the barrel and end-cap EM calorimeters, $1.37 < |\eta| < 1.52$, is expected to have poorer performance because of the large presence of matter (cables, services, ...) in front of the instrumented material. It is often referred to as the crack region. The EM calorimeter was designed to optimize the resolution and efficiency for the measurement of photons in the $H \rightarrow \gamma\gamma$ channel and electrons in the $H \rightarrow 4l$ channel as well as in supersymmetric

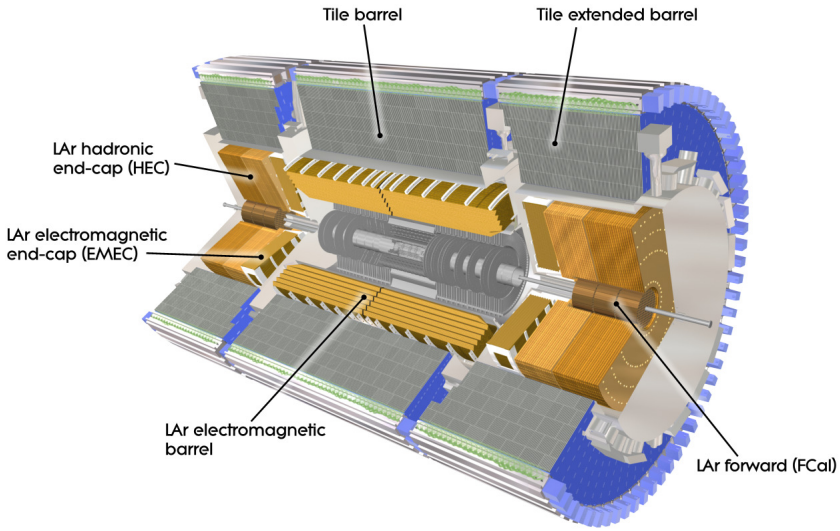


Figure 4.5: View of the ATLAS calorimeter system.

cascades. To ensure maximum azimuthal coverage the EM calorimeter was designed with an accordion geometry, its conception being due to D. Fournier [108, 141]: readout electrodes and lead absorbers are laid out radially and folded so that particles cannot cross the calorimeter without being detected. The electrodes work as transmission lines as well, so that no dead regions are introduced. The EM calorimeter will be described with further details in the next chapter.

Hadronic Calorimeter

The Hadronic calorimeter is realised with a variety of techniques depending on the region: central, end-cap or forward.

The central region is instrumented with the *Tile Calorimeter* (Tiles) [16], a sampling steel-scintillator detector. It is divided into a barrel ($|\eta| < 1.0$) and two extended barrels ($0.8 < |\eta| < 1.7$). There are three segmentations in depth, for a total depth of 7.4 interaction length (at $\eta = 0$). The readout cells in pseudorapidity are pseudo-projective towers towards the interaction region. The *hadronic End-cap* (HEC) is a LAr-copper detector and covers the region, $1.5 < |\eta| < 3.1$, overlapping both with the Tiles and Forward Calorimeter.

The *Forward Calorimeter* (FCal) covers the $3.1 < |\eta| < 4.9$ region and is a LAr detector. The absorber material is copper, optimal for EM measurements, in the first module in depth, and tungsten for the remaining two modules, aiming at the energy measurements of hadrons. Due to the high radiation dose expected in this region a design with very small LAr gaps has been done. These small gaps are obtained using an electrode structure of small-diameter rods centered in tubes oriented parallel to the beam axis. The total depth of this subdetector is 10 interaction lengths.

	Barrel		End-cap	
EM calorimeter				
Number of layers and $\|\eta\|$ coverage				
Presampler	1	$\|\eta\| < 1.52$	1	$1.5 < \|\eta\| < 1.8$
Calorimeter	3	$\|\eta\| < 1.35$	2	$1.375 < \|\eta\| < 1.5$
	2	$1.35 < \|\eta\| < 1.475$	3	$1.5 < \|\eta\| < 2.5$
			2	$2.5 < \|\eta\| < 3.2$
Granularity $\Delta\eta \times \Delta\phi$ versus $\|\eta\|$				
Presampler	0.025×0.1	$\|\eta\| < 1.52$	0.025×0.1	$1.5 < \|\eta\| < 1.8$
Calorimeter 1st layer	$0.025/8 \times 0.1$	$\|\eta\| < 1.40$	0.050×0.1	$1.375 < \|\eta\| < 1.425$
	0.025×0.025	$1.40 < \|\eta\| < 1.475$	0.025×0.1	$1.425 < \|\eta\| < 1.5$
			$0.025/8 \times 0.1$	$1.5 < \|\eta\| < 1.8$
			$0.025/6 \times 0.1$	$1.8 < \|\eta\| < 2.0$
			$0.025/4 \times 0.1$	$2.0 < \|\eta\| < 2.4$
			0.025×0.1	$2.4 < \|\eta\| < 2.5$
			0.1×0.1	$2.5 < \|\eta\| < 3.2$
Calorimeter 2nd layer	0.025×0.025	$\|\eta\| < 1.40$	0.050×0.025	$1.375 < \|\eta\| < 1.425$
	0.075×0.025	$1.40 < \|\eta\| < 1.475$	0.025×0.025	$1.425 < \|\eta\| < 2.5$
			0.1×0.1	$2.5 < \|\eta\| < 3.2$
Calorimeter 3rd layer	0.050×0.025	$\|\eta\| < 1.35$	0.050×0.025	$1.5 < \|\eta\| < 2.5$
Number of readout channels				
Presampler	7808		1536 (both sides)	
Calorimeter	101760		62208 (both sides)	
LAr hadronic end-cap				
$\|\eta\|$ coverage			$1.5 < \|\eta\| < 3.2$	
Number of layers			4	
Granularity $\Delta\eta \times \Delta\phi$			0.1×0.1	$1.5 < \|\eta\| < 2.5$
			0.2×0.2	$2.5 < \|\eta\| < 3.2$
Readout channels			5632 (both sides)	
LAr forward calorimeter				
$\|\eta\|$ coverage			$3.1 < \|\eta\| < 4.9$	
Number of layers			3	
Granularity $\Delta x \times \Delta y$ (cm)			FCal1: 3.0×2.6	$3.15 < \|\eta\| < 4.30$
			FCal1: $\sim$ four times finer	$3.10 < \|\eta\| < 3.15$,
				$4.30 < \|\eta\| < 4.83$
			FCal2: 3.3×4.2	$3.24 < \|\eta\| < 4.50$
			FCal2: $\sim$ four times finer	$3.20 < \|\eta\| < 3.24$,
				$4.50 < \|\eta\| < 4.81$
			FCal3: 5.4×4.7	$3.32 < \|\eta\| < 4.60$
			FCal3: $\sim$ four times finer	$3.29 < \|\eta\| < 3.32$,
				$4.60 < \|\eta\| < 4.75$
Readout channels			3524 (both sides)	
Scintillator tile calorimeter				
	Barrel		Extended barrel	
$\|\eta\|$ coverage	$\|\eta\| < 1.0$		$0.8 < \|\eta\| < 1.7$	
Number of layers	3		3	
Granularity $\Delta\eta \times \Delta\phi$	0.1×0.1		0.1×0.1	
Last layer	0.2×0.1		0.2×0.1	
Readout channels	5760		4092 (both sides)	

Figure 4.6: Main parameters of the calorimeter system [111].

4.3.3 Muon spectrometry

The muon spectrometer is based on the magnetic deflection of muon tracks in the large superconducting air-core toroid magnets [15], whose layout is shown in Figure 4.7, in order to mimimize the effect of multiple scattering. The large volume magnetic field necessary to bend the particle trajectories is provided by the large barrel toroid in the region $|\eta| < 1.4$, by two smaller smaller end-cap magnets in the $1.6 < |\eta| < 2.7$ region and by a combination of the two in the transition region ($1.4 < |\eta| < 1.6$). This magnet configuration provides a field which is mostly orthogonal to the muon trajectories.
In the barrel region, tracks are measured in chambers arranged in three cylindrical layers around the beam axis at radii of approximately 5, 7.5 and 10 m. In the two end-cap regions, the chambers are installed in planes perpendicular to the beam (larges wheels) at distances of 7.4, 10.8, 14 and 21.5 m from the interaction point.

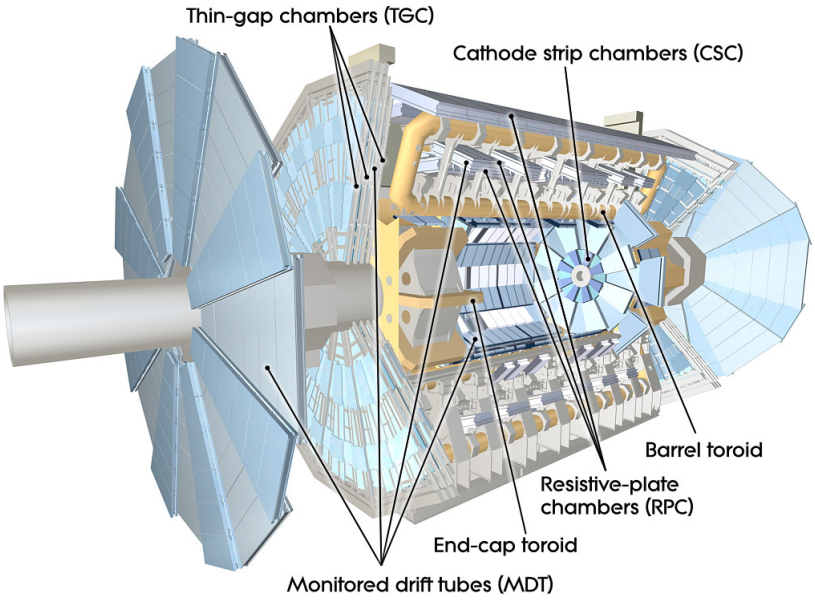


Figure 4.7: ATLAS muon system.

There are two different functions that muon chambers must accomplish:

High Precision Tracking

The tracking is performed by the *Monitored Drift Tubes* (MDT's) and by *Cathode Strips Chambers* (CSC's). MDT chambers are used in the barrel covering the region $|\eta| < 2.0$, for the measurement of the muons momentum. The basic element of the MDT chambers is a 0.9 to 6.2 m long pressurized drift tube with a diameter of 30 mm operating with argon (93%) and CO_2 (7%) gas at 3 bars. Electrons resulting from the ionisation are collected at the central tungsten-rhenium wire. MDT's allow for a very good track reconstruction with a resolution of $300\mu m$

CSC's are used in the area where MDT's cannot stand the particle flux, that is $|\eta| > 2$. They are located in the innermost end-cap wheels, at $|z| = 7.4\ m$. The CSC system consists of two disks with eight chambers each. Each chamber contains four CSC planes providing independent measurements in η and ϕ along each track.
The CSC's are multi-wire proportional chambers with the wires oriented in the radial direction. Both cathodes are segmented, one with the strips perpendicular to the wires, providing the precision coordinate. The position of the track is obtained by the interpolation between the charges induced on neighbouring cathode strips. Strips are 5.08 mm apart and the gas mixture is made of argon (30%), CO_2(50%) and CH_4(20%). The CSC's provide a resolution of 50 to 70 μm.
High precision mechanical assembly techniques and optical alignment systems provide the essential alignment of the chambers.

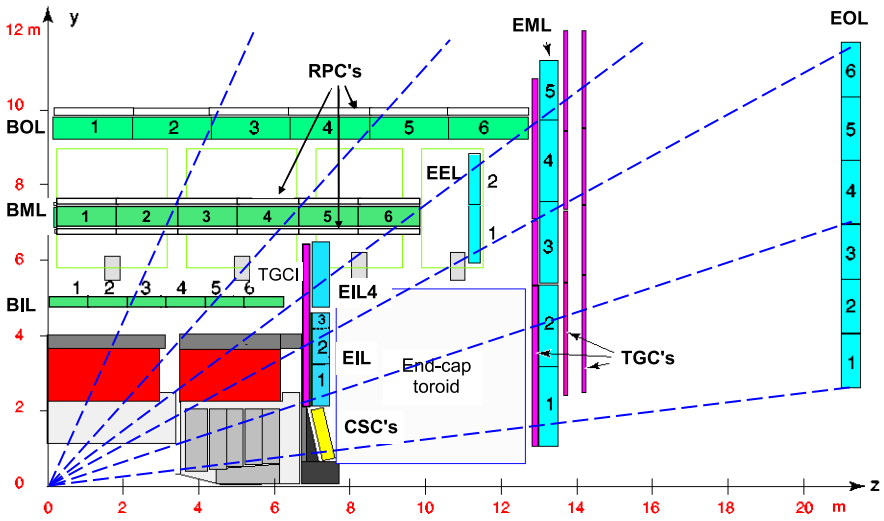


Figure 4.8: Plan view of a quarter of the ATLAS muon spectrometer. Monitored drift tubes are shown in green in the barrel and blue in the end-cap, cathode strips chambers in yellow, resistive plate chambers in white and thin gap chambers in magenta.

Trigger chambers

The trigger system covers the region up to $|\eta| < 2.4$, and is composed by *Resistive Plate Chambers* (RPCs) in the barrel and *Thin Gap Chamber* (TGC) in the end-caps.
The RPC is a gaseous parallel electrode-plate (i.e no wire) detector. Two resistive plates, made of phenolic-melaminic plastic laminate, are kept parallel to each other at a distance of 2 mm by insulating spacers. The electric field between the plates allows avalanches to form along the ionising tracks towards the anode. The gas used a mixture of $C_2H_2F_4$(94.7%), Iso$-C_4H_{10}$(5%) and SF_6(0.3%). A RPC trigger chamber is made of two rectangular detectors, contiguous to each other called units. Each unit consists of

two independent detector layers readout by two orthogonal sets of pick-up strips. RPC's provide resolutions of 1 cm and smaller than 10 ns.
TGC's are similar in design to CSC's with 1.8 mm anode separation and 2.4 mm cathode separation. The gas is a mixture of $CO_2(55\%)$ and $n - C_5H_{12}$. TGC's provide level one trigger signal (with a beam crossing identification efficiency larger than 99%) as well as η and ϕ information for the offline reconstruction.

4.3.4 Magnets

ATLAS features a unique hybrid system of four large superconducting magnets. This magnetic system is 22 m in diameter and 26 m in length, with a stored energy of 16.6 GJ and provides a magnetic field over a volume or approximately 12.000 m^3. The ATLAS magnet system consist of :

- a solenoid which is aligned on the beam axis and provides a 2 T axial magnetic field for the tracking detector. It is incorporated into the cryostat in order to minimize the radiative thickness in front of the barrel EM calorimeter,

- a barrel toroid and two end-cap toroids which produce a toroidal magnetic field of approximately 0.5 T and 1 T on average for the muon detectors in the central and end-cap regions, respectively, but with large variations: in the barrel it varies, depending of R and ϕ between 0.15 T and 2.15 T, and in the end-cap between 0.2 T and 3.5 T.

4.3.5 Trigger System

The proton-proton interaction rate at the design luminosity of $10^{34}cm^{-2}s^{-1}$ is approximately 1 GHz, while the event data recording which limitation is the processing capacity at `Tier0`, is limited to about 200 Hz. This requires an overall rejection factor of 5×10^6 against minimum-bias processes while maintaining maximum efficiency for keeping interesting events which might lead to discovery of new physics. This rejection is achieved by the ATLAS trigger system. The trigger system has three distinct levels. Each trigger level refines the decisions made at the previous level and, where necessary, applies additional selection criteria.

1. The Level 1 (L1) operates at the beam-crossing frequency and is aimed at reducing the output rate to 100 kHz. It searches for high transverse-momentum muons, electrons, photons, jets, and τ decaying into hadrons, as well as large missing and total transverse energy using the calorimeter and muon detector information. High tranverse-momentum muons are identified using trigger chambers in the barrel and end-cap regions of the spectrometer. Calorimeter selections are based on reduced granularity ($\Delta\eta \times \Delta\phi = 0.1 \times 0.1$) information from all the calorimeters. The Level 1 defines one or more so called Regions-of-Interest (RoI's), that is the geographical coordinates in η and ϕ, of those regions within the detector where its selection process has identified interesting features. The RoI data include information on the

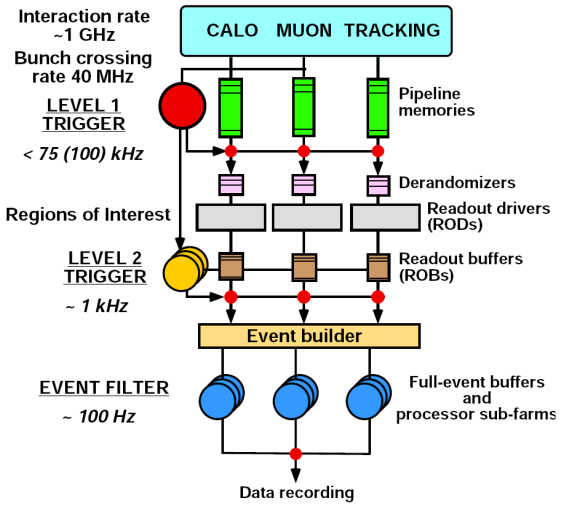


Figure 4.9: The three levels of the ATLAS trigger system

type of particle identified and the criteria passed. This information is subsequently used by the high-level-trigger. The L1 decision must reach the front-end electronics within 2.5μs after the beam-crossing with which it is associated.

2. The Level 2 selection is seeded by the RoI information provided by the L1 trigger. Level 2 selections use, at full granularity and precision, all the available detector data within the RoI's (approximately 2% of the total event data). The Level 2 menus are designed to reduce the trigger rate to approximately 3.5 kHz, with an event processing time of about 40 ms, averaged over all events.

3. The Event Filter corresponds to the final event selection, which reduces the event rate to about 200 Hz (again the RoI concept is used). Its selections are implementing offline analysis procedures. The average event processing time is of the order of four seconds.

Chapter 5

The EM Calorimeter of ATLAS

Electromagnetic (EM) calorimeters are blocks of instrumented material in which the electrons and photons to be measured are fully absorbed and their energy transformed into a measured quantity [134, 138, 139]. The EM interaction of the incident particle with the detector produces a shower of secondary particles with progressively reduced energy (the electrons emit bremsstrahlung photons in presence of material and the photons convert in an e^+e^- pair, the pair can then emit bremsstrahlung, ... etc ...). In this chapter is reviewed the physics of the EM shower as well as the characteristics and performance of the ATLAS EM calorimeter.

5.1 Physics of the EM cascade

The average energy lost by electrons in lead and the photon interaction cross section are shown in Figure 5.1 as a function of energy. Two main regimes can be identified. For energies larger than $\sim$ 10 MeV, the main source of electron energy loss is bremsstrahlung. In this energy range, photon interactions produce mainly electron-positron pairs. For energies above 1 GeV both these processes become roughly energy independent. At low energies, on the other hand, electrons loose their energy mainly trough collisions with atoms and molecules of the material via ionization and thermal excitation; photons lose their energy through Compton scattering and the photoelectric effect.

As a consequence, electrons and photons of sufficiently high energy ($\geq$ 1 GeV) incident on a block of material produce secondary photons by bremsstrahlung and secondary particles in turn produce other particles by the same mechanisms, thus giving rise to a cascade (shower) of particles with progressively reduced energies. The number of particles in the shower increases until the energy of the electron component falls below a critical energy ϵ [1], where energy is dissipated mainly by ionization and excitation and not in the generation of other particles.

The main features of electromagnetic showers (e.g., their longitudinal and lateral sizes) can be described in terms of one parameter, the radiation length X_0, which depends on

[1] $\epsilon = \frac{610(710)\ MeV}{Z+1.24(0.92)}$, for solids(gases)

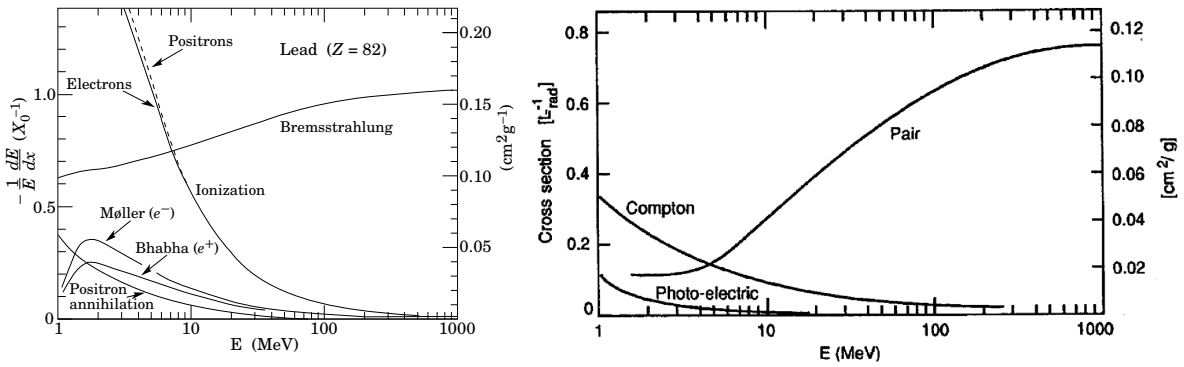


Figure 5.1: **Right:** Fractional energy lost in lead by electrons and positrons as a function of energy [134]. **Left:** Photon interaction cross section in lead as a function of energy [139].

the characteristics of the material [134].

$$X_0(g/cm^2) \simeq \frac{716.4\ g.cm^{-2}A}{Z\,(Z+1)\ln\left(\frac{287}{\sqrt{Z}}\right)} \tag{5.1}$$

where Z and A are the atomic number and weight of the material, respectively. The radiation length governs the rate at which electrons lose energy by bremsstrahlung, since it represents the average distance x that an electron needs to travel in a material to reduce its energy to $1/e$ of its original energy E_0,

$$\langle E(x)\rangle = E_0 e^{-\frac{x}{X_0}} \tag{5.2}$$

Similary, a photon beam of initial intensity I_0 traversing a block of material is absorbed mainly through pair production. After traveling a distance $x = \frac{9}{7}X_0$, its intensity is reduced to $1/e$ of the original intensity,

$$\langle I(x)\rangle = I_0 e^{-\frac{7}{9}\frac{x}{X_0}} \tag{5.3}$$

Equations 5.2 and 5.3 show that the electromagnetic showers can be described in a universal way by using simple functions of the radiation length.

The distribution of energy lost per unit of X_0 in the electromagnetic cascade is given by the empirical formula

$$\frac{dE}{dt} = E_0 b \frac{(bt)^{a-1}e^{-bt}}{\Gamma(a)} \tag{5.4}$$

where $t = x/X_0$ is the depth inside the material in radiation lengths and a and b are parameters related to material characteristics. This gives as mean position the distribution of the shower maximun, i.e. the depth at which the largest number of secondary particles

is produced,

$$t_{max} = \frac{a-1}{b} = \ln\left(\frac{E_0}{\epsilon}\right) + C \ , \ (C_{\gamma,e^{\pm}} = 0.5, -0.5) \tag{5.5}$$

Thus, in lead $X_0(Pb) = 5.6\ mm$ and $\epsilon = 7.3\ MeV$, and the electromagnetic shower generated by a photon with a initial energy of 100 GeV has a maximum development position at $\sim 10X_0$. On average, 98% of the EM shower is contained in $20-25\ X_0$, which fixes the EM calorimeter longitudinal size.

The transverse size of an electromagnetic shower is mainly due to multiple scattering of electrons and positrons away from the shower axis. Bremsstrahlung photons emitted by these electrons and positrons can also contribute to the shower spread. A measurement of the transverse size, integrated over the full shower depth, is given by the Molière radius (R_M), which can be written as

$$R_M(g/cm^2) = 21.2\ MeV \times \frac{X_0}{\epsilon_{[MeV]}} \tag{5.6}$$

on average, about 90% of the shower energy in contained in a cylinder of radius $\sim 1R_M$, 95% in $2R_M$ and 99% in $3.5R_M$, which allow to fix the cells size of the calorimeter.

5.2 Sampling Calorimeter

The principle of a sampling calorimeter such as the EM calorimeter of ATLAS consists in alternating layers of an *absorber* [2] (lead), a dense material used to degrade the energy of incident particles (in addition to reduce the size of the calorimeter) and an *active medium* (LAr) that provides the detectable signal (collected in the form of electric charge from the induced current produced by the ionisation of the medium while particles are crossing it, for instance electrons ionizing the LAr and creating Ar^+e^- pairs). LAr allows a good resistance to radiations and a high drift velocity of the electrons [3].

In a sampling calorimeter only a fraction of the energy is deposited in the active part, thus the total energy deposited (E^{tot}) can be estimated from the energy deposited in the active medium (E^{act}) divided by the sampling fraction f^e_{samp},

$$E^{tot} = \frac{1}{f^e_{samp}} E^{act}, \text{ with } f^e_{samp} = \frac{E^{act}}{E^{act} + E^{pas}} \tag{5.7}$$

where E^{pass} is the energy deposited in the passive material.

For a minimum ionising particle the sampling fraction is a fixed number which can be calculated from the known energy deposited in the active and passive materials due to ionisations. Since the energy loss of electrons is different from that of muons in the active and in the Pb part, their sampling fraction is lower (by a factor ~ 0.75).

[2] also called *passive medium*

[3] while the ions drift slowly due to the high density of the liquid

In Figure 5.2 (*Top*) is shown the shape of the deposited energy distribution of an EM shower along the shower axis(l) for electrons with $E = 10,\ 100$ and 500 GeV, and for muons with $E = 10$ GeV in ATLAS. The *accordion calorimeter* [4] starts at 1500 mm. The sampling structure of the calorimeter ends at about 1960 mm. The energy depositions before and behind the calorimeter are not shown.

Particles produced in the EM shower interact differently with the detector at the beginning and at the end of the shower development. At the end of the shower a large number of low-energetic photons are produced, which have a higher probability to produce low energy electrons (via e.g., the photo-electric effect and Compton scattering) in the lead absorber than in the LAr. Since the range of these electrons is typically smaller than the lead absorber thickness, the energy deposited in the active material towards the end of the shower and the sampling fraction decrease as shown in Figure 5.2 (*Bottom*).

5.3 Energy resolution

The numbers of electrons and positrons in a shower produced by a particle with a given energy fluctuate statistically. Since the total ionization signal is proportional to the number of secondary charged particles the reconstruction energy fluctuates in the same way. The relative width of the distribution of the number of charged particles is proportional to $\sqrt{n}/n = 1/\sqrt{n}$ where n is the number of secondary charged particles, proportional to the energy of the initial particle. Therefore the relative precision of the energy measurement with a calorimeter can be expressed as

$$\frac{\Delta E}{E} \propto \frac{1}{\sqrt{E}} \tag{5.8}$$

From equation 5.8, the relative energy resolution of a calorimeter improves with the energy. To account for more effects than statistical fluctuations like mechanical imprecisions, or electronic noise for instance, the energy resolution can be written as

$$\frac{\sigma(E)}{E} = \frac{a}{\sqrt{E}} \oplus \frac{b}{E} \oplus c \tag{5.9}$$

where the symbol $\oplus$ indicates a quadratic sum. The first term on the right-hand side is called the *stochastic term*, the second term is the *noise term*, and the third term is the *constant term*. The relative importance of the various terms depends on the energy of the incident particle, since the energy resolution is dominated by different contributions. These contributions are discussed in turn below:

- The stochastic term corresponds to the statistical fluctuactions associated to the EM shower development. The a coefficient is expected to be $\approx 10\%$ in the ATLAS LAr EM calorimeter. In the hadronic end-cap and forward calorimeter it is expected to be about 50% and 100% respectively. The sampling fraction has a major contribution to a.

[4] discussed with further details in section 5.4

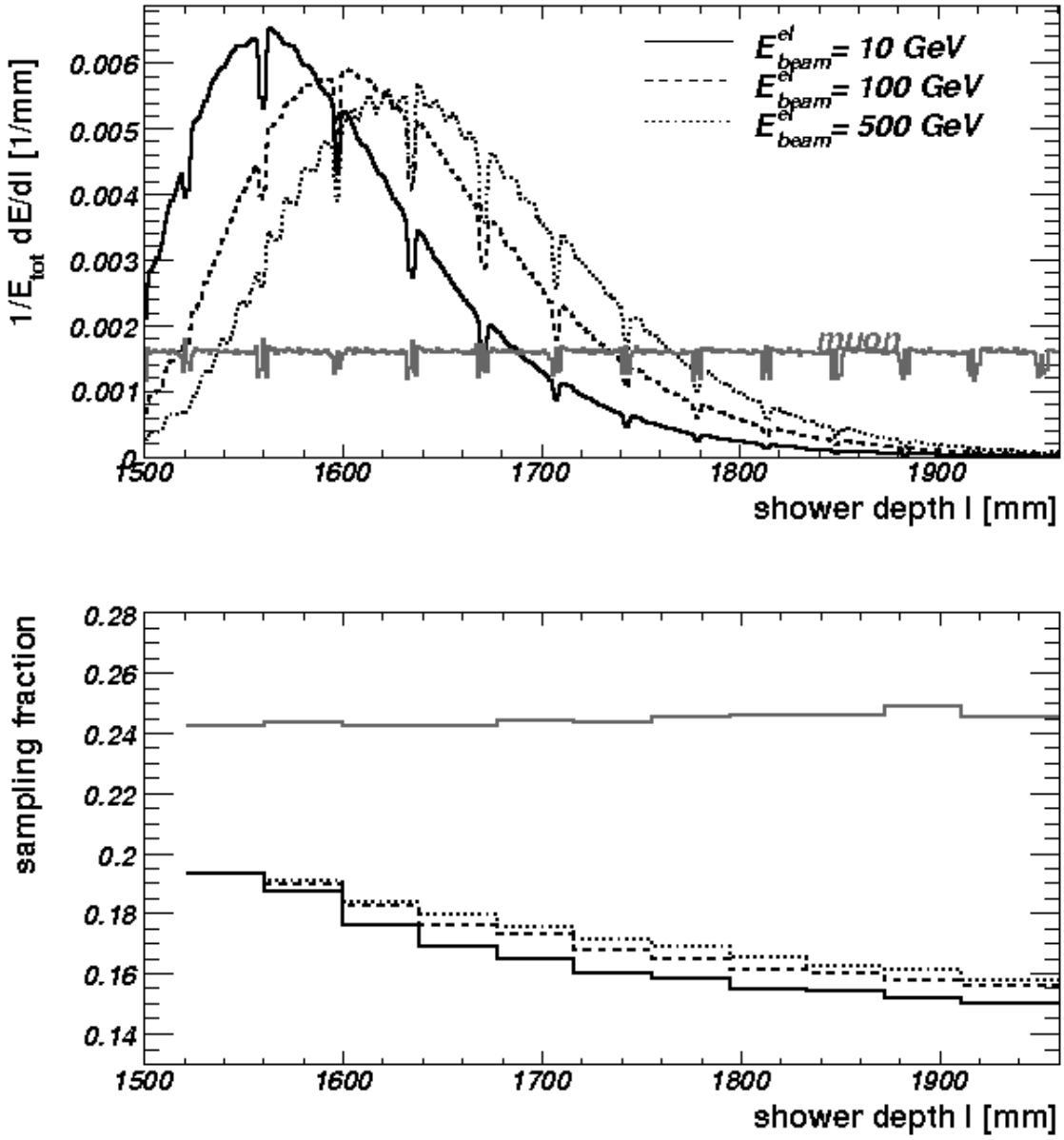


Figure 5.2: **Top:** Shape of the energy deposited along the shower axis, **Bottom:** Sampling fraction along the shower axis [135], both for the barrel EM calorimeter respectivily.

- The noise term is the sum of the electronic readout chain and of the pile-up noises (the pile-up noise is the signal produced by other interactions than the high p_T interaction we are looking at. There is in-time pile-up produced by the same bunches that have produced the high p_T interaction, and out-of-time pile-up produced by other bunches. The effect of this pile-up adds to the electronic noise). Techniques like a signal shaping and *optimal filtering* are used to reduce the noise [211]. The $1/E$ dependence implies that this contribution becomes important (and dominates) at low energies.

- The constant term c summarizes all contributions to the non-uniformity of the calorimeter response, that do not depend on the particle energy: material non-uniformity (gaps and absorbers thickness), imperfections in mechanical structures, temperature gradient, radiation damage, energy reconstruction scheme and stability in time... . In the EM barrel calorimeter it is expected not to exceed 0.7% while in the hadronic and forward calorimeter it is respectively expected to be below 3 and 10%. During the test-beam [136], the response uniformity of the EM calorimeter of ATLAS was measured in four barrel and three end-cap modules and a global constant term of $\sim 0.6\%$ was found.

- There are additional effects causing a dispersion in the energy measurement:

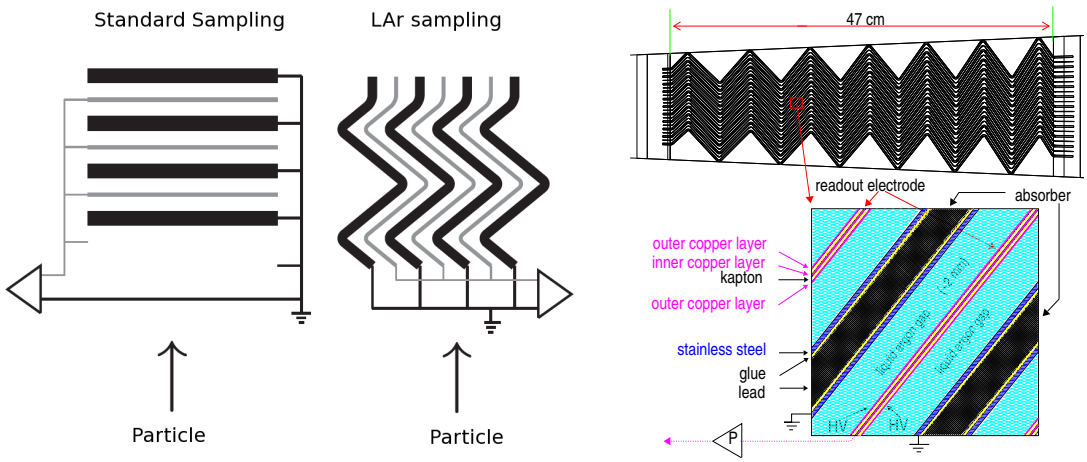
  – The longitudinal leakage corresponding to showers which are exceeding in length that of the calorimeter, thus leaking outside.

  – The lateral leakage at the beginning of the EM shower and at the end of the shower where low energy photons are more sensitive to Coulomb interaction and Compton scattering, deflecting their trajectory.

  – The amount of matter in front of and in the calorimeter, coming from the cryostat, inner detector (ID), the cables, services and support structures. Also accurately referred, fluctuations in the upstream material induces a degradation of the energy. The presampler is a dedicated small detector installed between the ID and the calorimeter, that aims in estimating the energy lost by electrons and photons before arriving in the calorimeter.

5.4 Accordion geometry

In standard LAr sampling calorimeters, the alternating absorber and active layer are disposed perpendicular to the direction of the incident particle, as illustrated in Figure 5.3(a)*(Left)*. The ionization signal produced by the shower in the LAr gaps is collected by electrodes located in the middle of the gaps. These electrodes carry the high voltage, whereas the absorbers are at ground. For a typical LAr gap of 2 mm on each side of the collecting electrode and a high voltage of $\simeq 2\ kV$ across the gap, the electron drift time to the electrode is $\simeq 400\ ns$. This time, which is needed to collect the total ionization charge, is too slow for the operation at the LHC, where detector responses



(a) (b)

Figure 5.3: (a) Schematic views of a traditional sampling calorimeter **Left**, and of the accordion calorimeter geometry **Right**. (b) Schematic view of the electrode structure of the ATLAS EM calorimeter. In the top picture particles enter the calorimeter from the left.

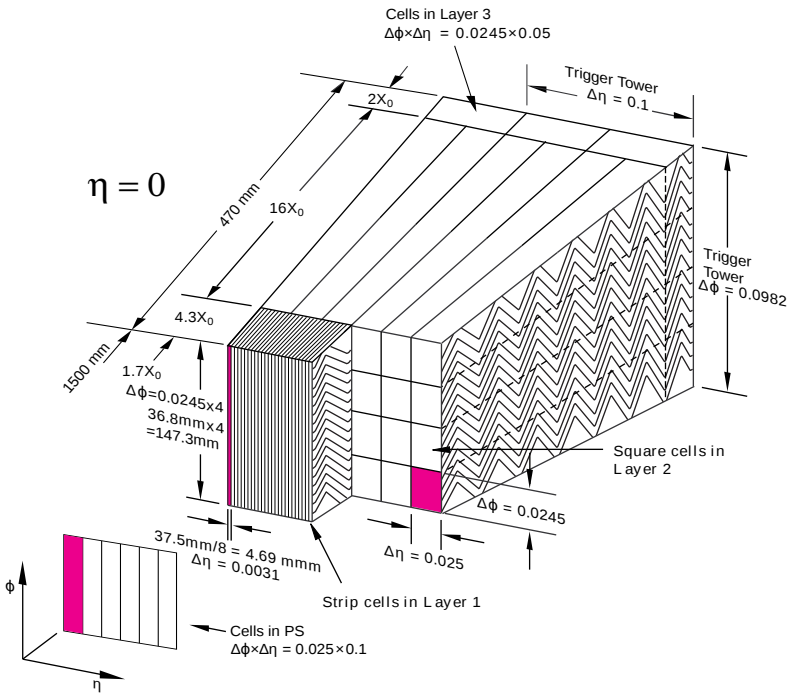


Figure 5.4: Schematic view of the segmentation of the ATLAS EM calorimeter.

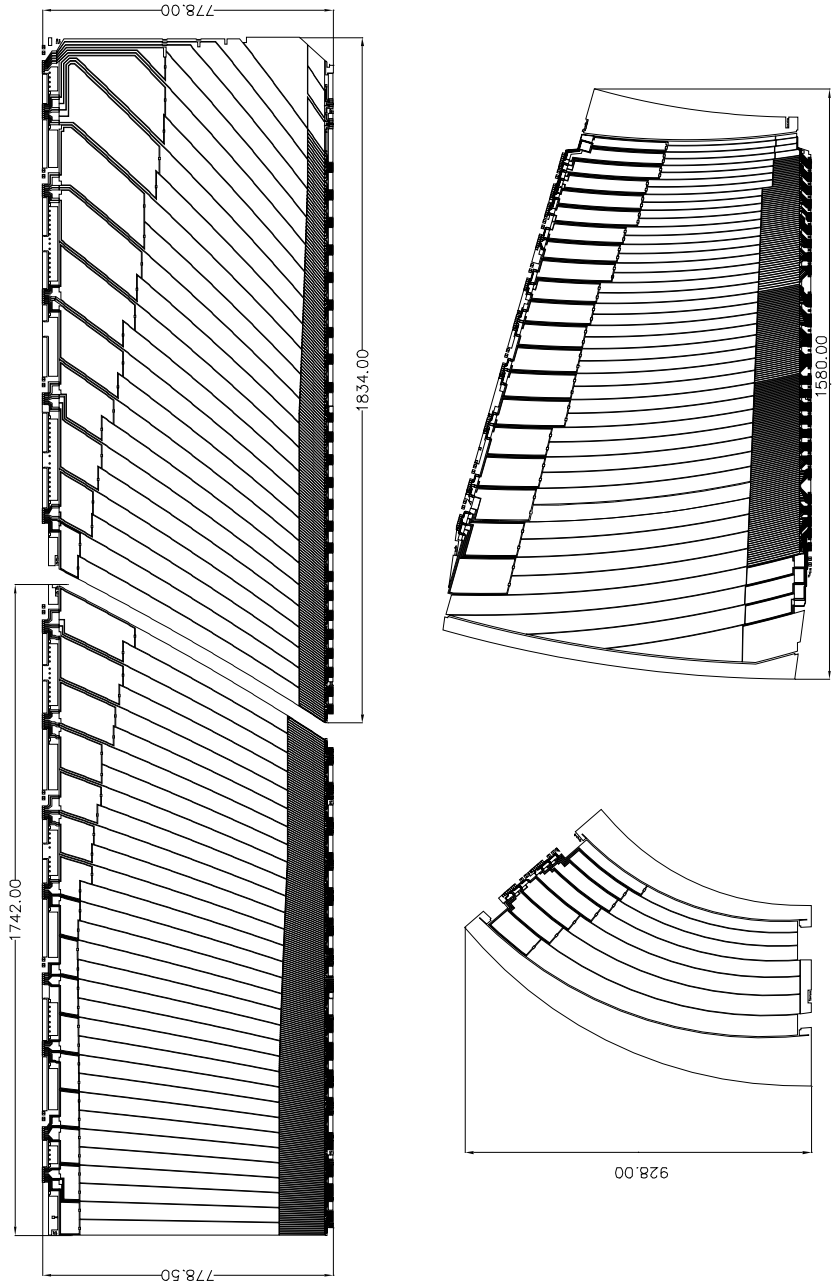


Figure 5.5: Layout of the signal layer for the four different types of electrodes before folding. The two top electrodes are for the LAr EM barrel and the two bottom electrodes are for the LAr EM end-cap inner (left) and outer (right) wheels. Dimensions are in millimeters. The two or three different layers in depth are clearly visible.

of 50 ns or smaller are needed (since several collisions are expected each 25 ns during nominal operation). The solution is to integrate the ionization current over a time (t_p) of only 40-50 ns, thus collecting only a fraction of the total charge. This solution has the drawback that the signal-to-noise ratio is degraded, and can only work if the signal transfer time from the electrodes to the readout chain is much smaller that t_p, i.e., if cables and connections (which introduce capacitance and inductance and therefore give rise to long time constant of the circuit) are minimized. With the standard electrode geometry shown in Figure 5.3(a)*(Left)*, long cables are needed to gang together successive longitudinal layers to form calorimeter towers and to transfer the signal from these towers to end of one calorimeter module. As a consequence, the charge-transfer time from the electrodes to the first element of the readout chain (usually a preamplifier) is several tens of nanoseconds, i.e., comparable to t_p, and a smaller signal is collected if t_p = 40-50 ns. In addition, these cables introduce dead spaces between calorimeter towers at the expense of the detector hermeticity.

These problems can be solved by placing the absorber and gap layers with an accordion geometry following an original idea of D. Fournier [108, 138] In this way the signal from the front and back faces of the calorimeter and sent to the readout chain with a minimum number of cables and connections. Dead spaces inside the detector active volume are also minimized with this geometry: in order to prevent the incident particles from escaping trough the LAr gaps without crossing the absorber, the electrodes must be bent into an accordion shape, as illustrated in Figure 5.3(a)*(Right)*.

This is the technique developed for the ATLAS EM calorimeter [138](which was tested, in a preliminary way already 20 years ago [78]). The structure of this calorimeter is shown in Figure 5.3(b). The calorimeter covers the rapidity region $|\eta| < 3.2$ and is divided longitudinally into three compartements (plus a presampler layer) as shown in Figure 5.4 and 5.5. A high voltage (nominal) of 2 kV is applied to the electrodes, whereas the absorbers are connected to ground, for the LAr electromagnetic barrel, while a varying high voltage is applied to the LAr electromagnetic end-cap electrodes, depending on the radius. The reason is that the gap size between LAr and absorbers in end-caps, varies according to the radius resulting in a varying sampling fraction. This effect is thus compensated to first order by the application of a respectively varing high voltage.

As already mentioned, the absorbers are made of lead plates, to which two stainless-steel sheets (0.2 mm thick) are glued to provide mechanical strength. The lead plates in the barrel have a thickness of 1.53 mm for $|\eta| < 0.8$ and of 1.13 mm for $|\eta| > 0.8$. The change in lead thickness at $|\eta| = 0.8$ limits the decrease of the sampling frequency [5], as $|\eta|$ increases. In the end-cap calorimeters, the plates have a thickness of 1.7 mm for $|\eta| < 2.5$ and of 2.2 mm for $|\eta| > 2.5$. The readout electrodes are located in the gaps between the absorbers and consist of three conductive copper layers separated by insulating polyimide sheets (Figure(b) 5.3(right)). The two outer layers are at high-voltage potential and the inner one is used for the reading out the signal via capacitive coupling. The segmentation of the calorimeter in $|\eta|$ and in depth is obtained by etched patterns with two electrodes, one type for $|\eta| < 0.8$ and another one for $|\eta| > 0.8$. Similarly, each end-cap gap between

[5]the number of sucessive layers of the LAr and absorber crossed by an EM shower

two absorbers is equipped with one type of electrode for $|\eta| < 2.5$ and with another for $|\eta| > 2.5$. One can note, since the tracker works for $|\eta| < 2.5$, that this region is for precision physics.

- The presampler, as already presented in the subsection 4.3.2, is a thin layer of LAr of 1.1 *cm* thickness in the barrel and 0.5 *cm* in the end-cap. It is located between the cryostat-coil assembly and the calorimeter. The main purpose of this detector is to improve the energy resolution of the EM calorimeter correcting the energy lost by electrons and photons in the upstream material (see figure 5.6).

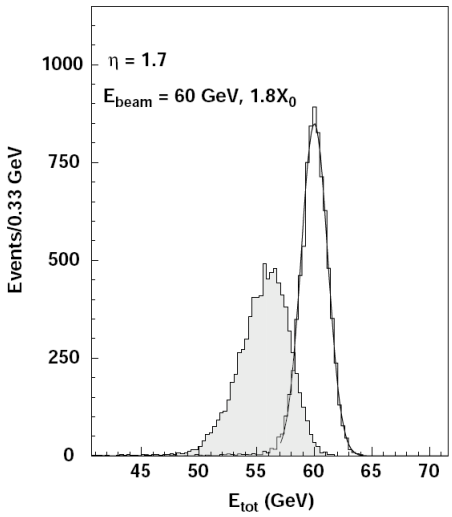


Figure 5.6: Energy distribution with no presampler (solid histogram) and with the optimal presampler weight (open histogram) [79].

- The first layer of the ATLAS EM calorimeter, commonly named the *strip* or *front*, is made of narrow strips, as show in Figure 5.4 (in the barrel part). In the central region ($|\eta| < 1.4$) the cells size is $\Delta\eta \times \Delta\phi = 0.0025/8 \times 0.1$. The fine longitudinal segmentation provides an accurate η direction measurement and allows for an efficient π^0/γ separation.

- The second layer, commonly called the *Middle*, contains most of the e/γ EM shower energy. It is segmented in squared cells of size $\Delta\eta \times \Delta\phi = 0.025 \times 0.025$, except near the barrel-end-cap transition where cells are larger. Typically, the shower of an unconverted photon is contained in a cluster of size 3×5 in the barrel part and that of a converted photon (in the inner detector) in a cluster of size 3×7. the spread in ϕ is due to the electron and positron (from conversion) curvature under the electric field (In the end-caps, the photons are typically defined in a cluster of size 5×5).

- The third layer, or *Back* sampling, has the same ϕ granularity that middle but has twice a coarser granularity in $|\eta|$. It is used to measure the end of the EM

shower, therefore it is used to separate the e/γ from jets and estimate the EM shower leakage which is approximately proportional to the energy deposited in the barrel. This layer is not really used for e/γ identification.

The distributions of the radiation length in front and in each of the EM calorimeter layers are shown in Figure 5.7. At the transition region between the barrel and the end-cap there are a large fraction of material mainly due to cables and services which causes a important degradation in the measurement of the energy.

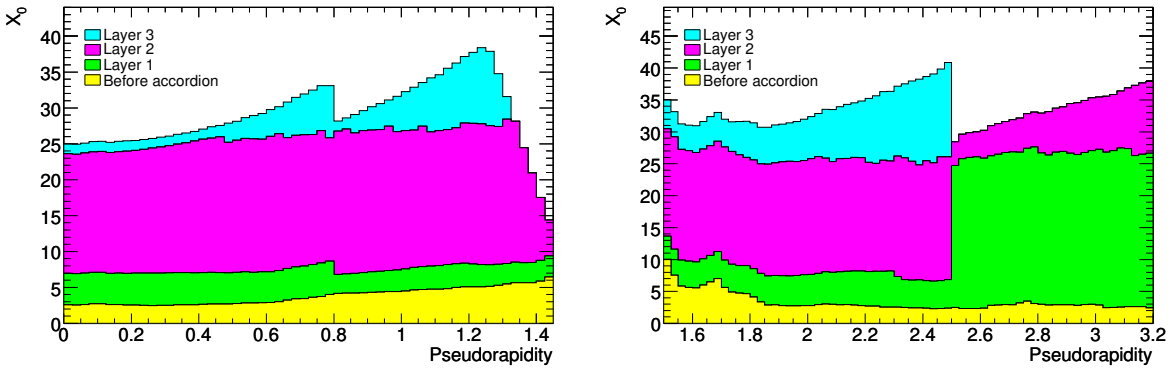


Figure 5.7: Cumulative amounts of material, in units of radiation length X_0 as a function of $|\eta|$ for the barrel (*Left*) and end-cap (*Right*). The thicknesses of each accordion layer as well as the amount of the material in front of the accordion is given [111].

5.5 Cell energy reconstruction

As described in the section 5.2, the electrons and photons interact with the calorimeter matter which are the absorbers and the active medium. On the active medium (LAr in ATLAS) the signal is generated and is collected by the readout electrodes. The overall readout architecture of the LAr calorimeters is sketched out in Figure 5.8 and described in the following.

5.5.1 Triangular signal

The electrical field applied between a read-out electrode and the absorber, collects the electrical charges produced by the ionization of Argon. The induced current has a triangular form as a function of time

$$I(t) = \frac{Q_0}{t_d}\left(1 - \frac{t}{t_d}\right) \tag{5.10}$$

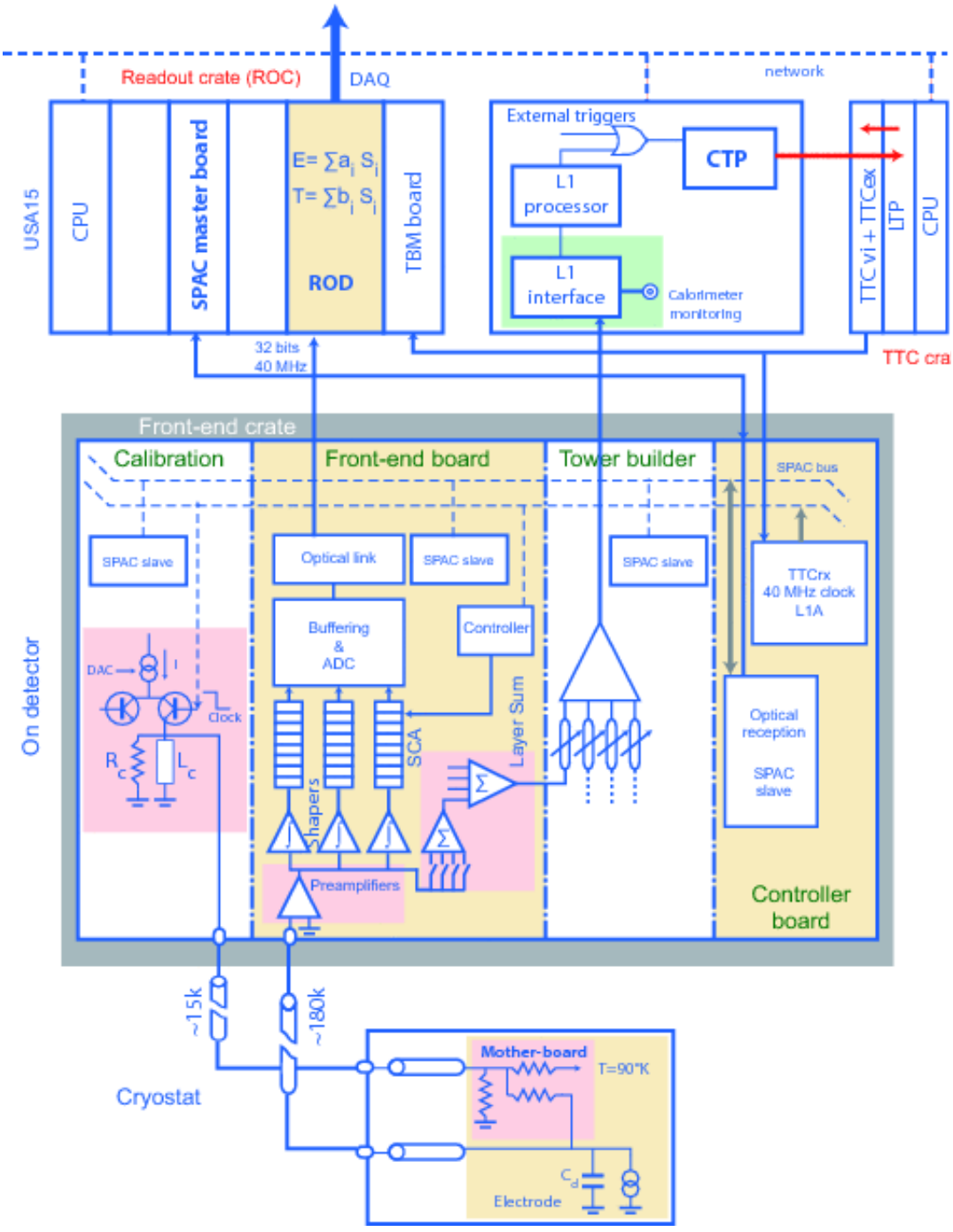


Figure 5.8: Block diagram depicting the architecture of the overall LAr readout electronics [111].

where t_d is the average time of electrons in the LAr, approximately 450 ns in the EM calorimeter barrel, and Q_0 is the total charge deposited in the LAr [6]. This signal passes afterwards through an electronic card in the *Front End Board* (FEB). which are close to the feed throughs coming out of the cryostat.

5.5.2 Readout electronic chain

Passing through the FEB's, the triangular signal is amplified by the pre-amplifiers to obtain a signal above the electronics noise level. Afterwards, the signal is being transported to special shapers which are bipolar filters like $CR - RC^2$ which give the bipolar pulse shape of Figure 5.9. The main advantage of this procedure is to make the whole time integral to be zero. The pile-up noise will then peak at zero and contributes as a 'noise' and will not produce an 'offset'. The bipolar shape is sampled every 25 ns (every bunch crossing in the nominal LHC configuration). The maximal amplitude of the shaped signal is proportional to the initial current and arises at around 40-50 ns, between the second and third samplings. During the physics runs, 5 samples will be recorded (centered around the sampling with the maximum of amplitude) in nominal configuration, but for special studies more samplings can be recorded.

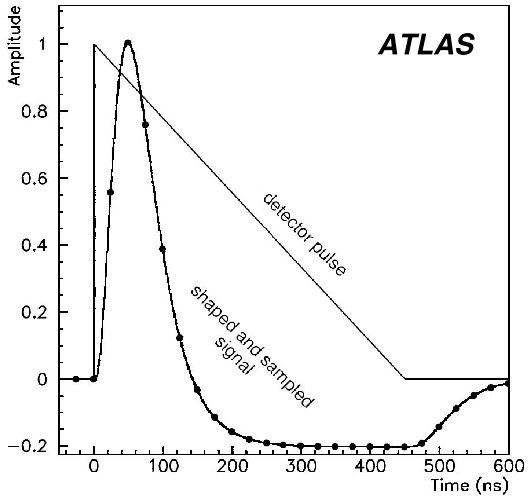


Figure 5.9: Example of ionization current and bipolar shaped sampled signal in time.

The samples are digitized by an *Analogical-to-Digital Converter* (ADC). The large dynamic range in energy covered by the EM calorimeter(between 50 MeV until some few TeV) needs a signal coding corresponding to 16 bits, while the ADC is limited to 12 bits. To provide an accurate and uniform signal reconstruction the shaper uses three different gains (*high, medium and low*), which amplify the signal by a factor of 93/9.3/1. The gain

[6] In a first approximation the current signal depends only on the initial current and the drift time t_d. Impurities in the Argon(such as O_2), recombination of the Ar^+e^- pairs can however create deformations of the triangular shape [53].

is applied to the signal according the ADC thresholds, then the signal samples are stored in SCA (*Switched Capacitor Array*) pipelines.

To properly achieve the correspondence between ADC and current a calibration signal is generated by the calibration board [106] transformed by *Digital-to-Analogical Converters* (DAC). The calibration signal is converted through an inductance into a continuous current whose discharge induces an exponential signal. The calibration current is written as:

$$I^{cali}(t) = I_0^{cali}\left[f_{step} + (1 - f_{step})\, e^{-t/\tau_{cali}}\right] \tag{5.11}$$

where τ_{cali} is the constant time, of about 430 ns, and f_{step} is a shift of about 7% introduced to compensate the resistive component of the inductance. The calibration current is then injected to the electrode and passes through the complete read-out electronic chain followed by the ionization signal, until it reaches the ADC.

When an event candidate is triggered, the samples are routed via optical fibers to *Read Out Drivers* (ROD) [89]. The ROD's receive the signal samples from the ADC and information from the calibration board. They perform the *Optimal Filtering* [7] procedure (see Appendix A) on DSPs (*Digital Signal Processors*) and send the signal to *Read Out Buffer*(ROB) in the form of a triplet: energy, time, and data quality. ROB's are the input of the *Data Acquisition System* (DAQ).

5.5.3 Energy reconstruction

To reconstruct the energy deposited in the LAr gap from the signal samples amplitude s_i measured in ADC counts, correspondence factors are used that translate the electronic chain crossed by the ionization and calibration signals, as illustrated through the following equation [33]:

$$E_{reco} = C_{\mu A \leftrightarrow MeV} \cdot C_{DAC \leftrightarrow \mu A} \left(\frac{M_{phys}}{M_{cali}}\right)^{-1} \left[\Sigma^i \left(s_i - p_i\right) OFC_i\{a_i, b_i\}\right] \tag{5.12}$$

the reconstructed energy relies on the correspondence factors from the electronic chain and on the signal samples amplitude.

- $C_{\mu A \leftrightarrow MeV}$ is the correspondence factor between the current collected by the readout electrode and the energy deposited in the LAr. It can be affected by different effects such as: temperature, variation of the High Voltages, pollution and space charge saturation.

- $C_{DAC \leftrightarrow \mu A}$ converts the Digital-to-Analog Converter(DAC) setting of the calibration board to the injected current. It is calculated at the calibration level and is corrected by effects like the crosstalk [33].

[7] further information in appendix A

- $\left(\frac{M_{phys}}{M_{cali}}\right)^{-1}$ is the correction factor accounting for the difference between the responses to a calibration pulse and to an ionization pulse corresponding to the same input current.

- The last term is the signal amplitude, obtained with the OF (see Appendix A) procedure, after the *pedestal subtraction* (see Appendix A). The OFC_i are computed for each cell and stored in a database.

Chapter 6

Photon Identification in ATLAS

Isolated photons with large transverse momentum, p_T, in the final state are important signatures for many physics analyses at the LHC, in particular, in the search for the $H \to \gamma\gamma$ channel, where isolated high-p_T photons may play a significant role in discovering the Higgs particle in the low mass region (see Section 1.5.2). In addition, very high-p_T photons are also signatures of more exotic particles, such as the Randall-Sundrum's gravitons [74, 190], which are expected to have a mass larger than 500 GeV. One should note that at transverse energies above 20 GeV, neutral hadron decay $\pi^0 \to \gamma\gamma$, are responsible for the majority of the background photons.

Since the ATLAS electromagnetic calorimeter (shown in Section 5.4) is highly segmented with a three-fold granularity in depth and with a $\eta \times \phi$ granularity in the barrel of 0.003×0.1, 0.025×0.025, and 0.05×0.025, respectively, in the front, middle and back compartments complemented by a pre-sampler in front of the calorimeter, photon identification in ATLAS should be much more powerful that those used in past experiments as the ATLAS electromagnetic calorimeter provides excellent γ/jet separation capabilities. The experiment also employs an elaborate trigger systems that select electron and photon candidates efficiently, as described in detail in [14].

In this chapter we discuss the ATLAS photon identification and its performance for isolated photons from physics processes.

6.1 Photon reconstruction

The "sliding window" [1] algorithm [172] is used to reconstruct electromagnetic clusters. Rectangular clusters with a fixed size are formed, positioned in order to maximise the amount of energy within the cluster. Electromagnetic objects are considered as the rectangular clusters seeded with tranverse energies exceeding 2.5 GeV, measured in projective towers of 3×5 cells in the second layer of the calorimeter. These energy clusters are then matched to tracks that are reconstructed in the inner detector and extrapolated to the calorimeter. Clusters without matching tracks are directly classified as *unconverted pho-*

[1] Based on a grid using towers of size 0.025×0.0025, sliding window does cluster seed finding. Then one look at the 2^{nd} layer to start building the clusters followed by looking into the others layers.

ton candidates. Clusters with matched tracks from reconstructed conversions vertices by the ID software can be considered as *converted photons* and/or as electrons.

The detailed description of photons (converted and unconverted) reconstruction and its interplay with electron reconstruction can be found in [31] and only a schematic description will be discussed below. The reconstruction of converted photons includes the initial reconstruction of conversion vertices inside the tracker (see [14] p.122) which uses both standard inside-out tracking and more recent outside-in tracking.

The conversion vertices are classified in two main categories. Conversion vertices with two electron tracks, called *double-track* conversions and the so-called *single-track* conversions. In the last case, one of the two produced electron tracks fail to be reconstructed either because it is very soft (asymmetric conversions where one of the two tracks has $p_T < 0.5$ GeV), or because the two tracks are very close to each other (for instance in the case of symmetric conversions that happen late inside the tracker). Besides, single-track conversions can be distiguished from electrons because they do not have any hit in the first layer of the pixel (B-layer) subdetector. There are also conversions on beam pipe but not distinguishable from "match" tracks from ID.

Double-track conversions are efficiently reconstructed at low values of the conversion radius (see Figure 6.1). On the other hand, single-track conversions are mainly reconstructed for large vertices radius. If one combine the two conversion categories a high efficiency can be achieved. The efficiency of reconstruction for converted photon is show in Figure 6.1 as a function of the conversion radius.

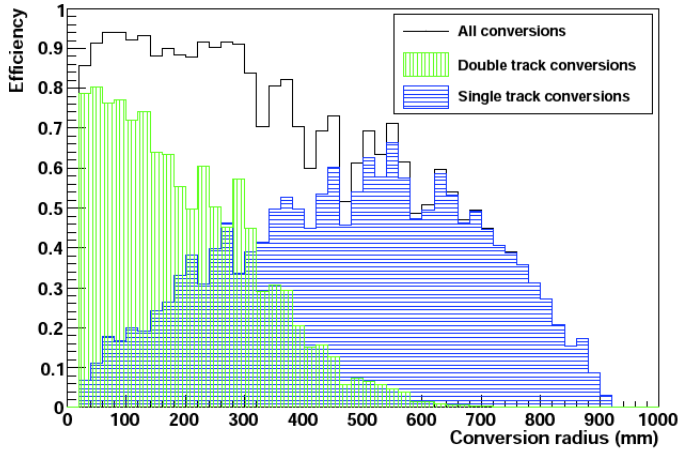


Figure 6.1: Efficiency for conversion reconstruction [176].

A large fraction of single-track conversion candidates arise from to a track reconstructed only in the TRT detector. Such tracks have no associated silicon detector information and have therefore poorer momentum resolution and almost no η information.

The final energy measurement, for both converted and unconverted photons, is made using only the calorimeter, with a cluster size that depends on the photon classification. In the barrel, a cluster corresponding to 3×5 cells in the second layer is used for unconverted photons, while the cluster for converted photon candidates is 3×7 cells (to compensate

for the opening between the conversion products in the ϕ direction due to the magnetic field). In the end-cap, a cluster size of 5×5 is used for all candidates. A dedicated energy calibration [14] is then applied to account for upstream energy lost, lateral leakage, and longitudinal leakage. (The calibration is applied separately for converted and unconverted candidates.)

6.2 Characteristic variables and cut-based photon identification criteria

In order to separate real photons from fake photons coming from jets, several discriminating variables are defined using the information from both the calorimeters and the inner tracking system. Cuts on these variables have been developed in order to maintain high photon efficiency even in the presence of pile-up resulting from the overlapping minimum bias events due to high instantaneous luminosity at the LHC. A detailed description of these variables and the cuts applied can be found in [31] following the previous works of [14, 215, 216].

6.2.1 Variables using calorimeter information

Photons are narrow objects, well contained in the electromagnetic calorimeter, while fake photons induced from jets tend to have a broader profile and can deposit a substantial fraction of their energy in the hadronic calorimeter. Hence, longitudinal and transverse shower-shape variables are used to reject jets.

- **Hadronic leakage**

  – *Normalized hadronic leakage*

$$R_{\mathrm{had_1}} = \frac{E_T^{\mathrm{had1}}}{E_T} \tag{6.1}$$

  is the transverse energy E_T^{had1} deposited in the first compartment of the hadronic calorimeter behind the electromagnetic cluster, normalized to the transverse energy E_T of the photon candidate, computed from the cluster energy E and the cluster pseudorapidity η reconstructed in the second longitudinal compartment of the electromagnetic calorimeter (EMC) through the relation $E_T = E/\cosh(\eta)$. This variable is used over the ranges $|\eta| < 0.8$ and $|\eta| > 1.37$. For the rest the variable $R_{\mathrm{had}} = \frac{E_T^{\mathrm{had}}}{E_T}$ is used, where E_T^{had} is the total transverse energy seen by the hadronic calorimeter [2].

[2] In this pseudo-rapidity region, there is no first compartiment of the hadronic calorimeter able to catch the tail of the shower.

- **Variables using the second compartment of the EMC (Middle):** Electromagnetic showers deposit most of their energy in the second layer of the electromagnetic calorimeter. For this reason several variables that measure the shape of the shower are calculated as follows:

  – *Middle η energy ratio*

  $$R_\eta = \frac{E^{S2}_{3\times7}}{E^{S2}_{7\times7}} \tag{6.2}$$

  is the ratio between the sum $E^{S2}_{3\times7}$ of the energies of the EMC Middle cells contained in a 3×7 $\eta\times\phi$ rectangle (measured in cell units), and the sum $E^{S2}_{7\times7}$ of the Middle cell energies in a 7×7 rectangle, both centered around the cluster seed. Since electrons and photons have a small transversal shower shape, most of it is in a 3×7 rectangle and this variable is very useful for discriminating against jets, much broader.

  – *Middle ϕ energy ratio*

  $$R_\phi = \frac{E^{S2}_{3\times3}}{E^{S2}_{3\times7}} \tag{6.3}$$

  is the ratio between the sum $E^{S2}_{3\times3}$ of the energies of the EMC Middle cells contained in a 3×3 $\eta\times\phi$ rectangle (measured in cell units), and the sum $E^{S2}_{3\times7}$ of the Middle cell energies in a 3×7 rectangle, both centered around the cluster seed.

  – *Middle lateral width*

  $$w_{\eta 2} = \sqrt{\frac{\sum E_i\eta_i^2}{\sum E_i} - \left(\frac{\sum E_i\eta_i}{\sum E_i}\right)^2} \tag{6.4}$$

  measures the shower lateral width in the EMC Middle, using all cells in a window $\eta\times\phi = 3\times5$ measured in cell units.

- **Variables using the first longitudinal compartment of the EMC (Front):** Cuts applied on the variables in the hadronic calorimeter and the second layer of the electromagnetic calorimeter reject jets which contain high-energy hadrons and broad showers. After cuts on the second compartment (sampling) jets containing single or multiple neutral hadron such as η and π^0, provide the main contribution which can fake photons. The readout of the first layer of the calorimeter uses strips and provides a very fine granularity in pseudorapidity. Thus, the information from this layer can be used to identify substructures in the showers an distinguish isolated photons from the hard scatter and photon from π^0 decays efficiently.

  – *Front side energy ratio*

  $$F_{\text{side}} = \frac{E(\pm3) - E(\pm1)}{E(\pm1)} \tag{6.5}$$

measures the containment of the shower in the EMC front compartment, where $E(\pm n)$ is the energy in the $\pm n$ strip cells around the one with the largest energy.

– *Front lateral width (3 strips)*

$$w_{s3} = \sqrt{\frac{\sum E_i (i - i_{\max})^2}{\sum E_i}} \tag{6.6}$$

measures the shower width in the EMC front compartment, using 2 strip cells around the maximal energy deposit. The index i is the strip identification number, $i_{\max}$ identifies the strip cells with the greatest energy, E_i is the energy deposit in each strip cell.

– *Front lateral width (total)* w_{stot} measures the shower width in the EMC front using all cells in a window $\Delta\eta \times \Delta\phi = 0.0625 \times 0.2$, corresponding to approximately 20 strip cells in η and 2 in ϕ, and is computed as w_{s3}.

– *Front second maximum difference*

$$\Delta E = E^{S1}_{2^{\text{nd}}\text{max}} - E^{S1}_{\text{min}} \tag{6.7}$$

is the difference between the energy of the strips cell with the second greatest energy $E^{S1}_{2^{\text{nd}}\text{max}}$, and the energy in the strip cell with the least energy found between the greatest and the second greatest energy E^{S1}_{min}.

– *Front maxima relative ratio*:

$$E_{ratio} = \frac{E^{S1}_{1^{st}max} - E^{S1}_{2^{nd}max}}{E^{S1}_{1^{st}max} + E^{S1}_{2^{nd}max}} \tag{6.8}$$

measured the relative difference between the energy of the strips cell with the greatest energy $E^{S1}_{1^{st}max}$ and the energy in the strip cell with second greatest energy $E^{S1}_{2^{nd}max}$. This variable was not used in Ref. [14], and is introduced here to replace the *rescaled front second maximun:*

$$R^{S1}_{2^{\text{nd}}max} = \frac{E^{S1}_{2^{\text{nd}}\text{max}}}{1000 + 0.009 E_T/\text{MeV}} \tag{6.9}$$

used there, since it proved to be more discriminating.

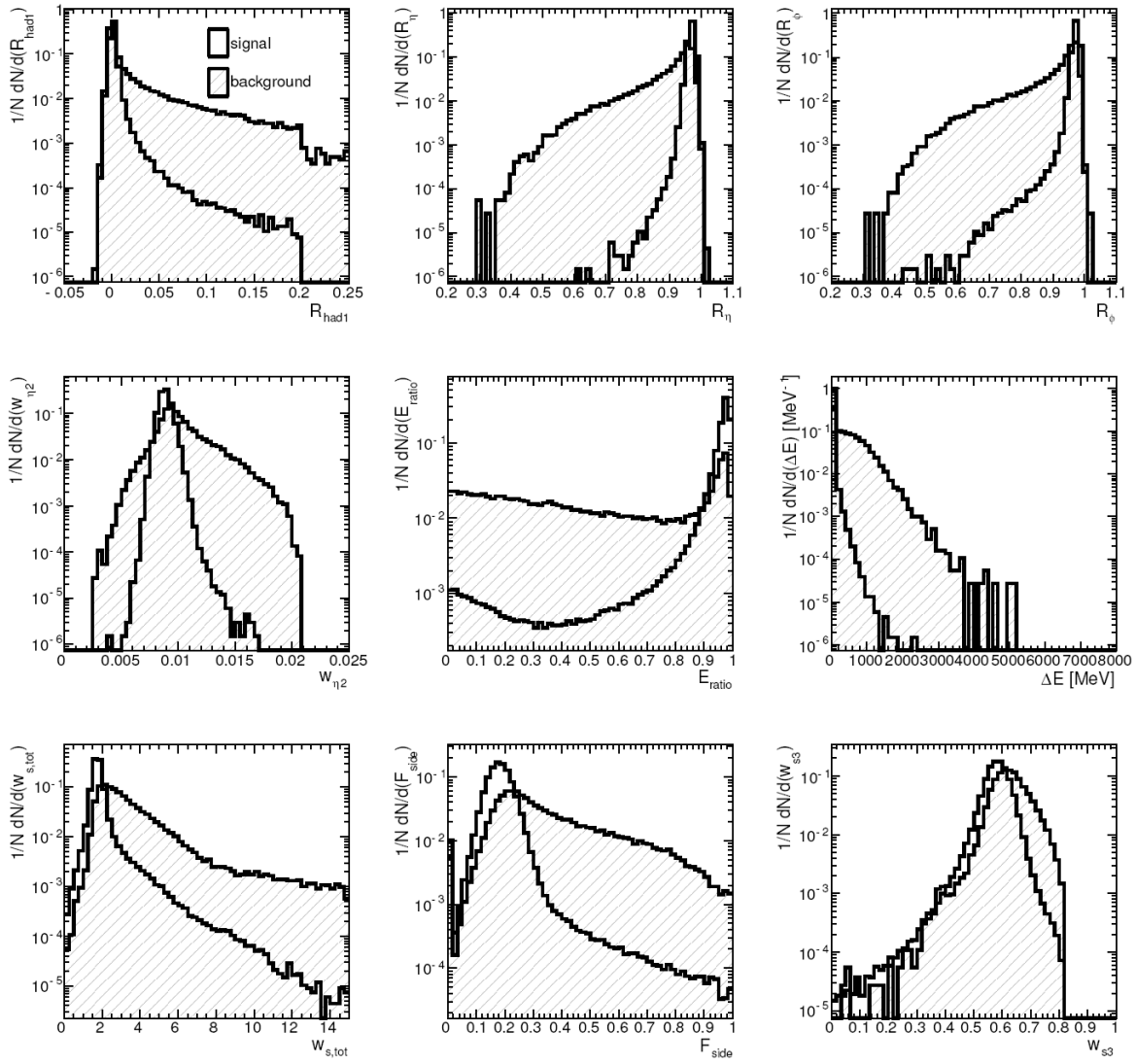


Figure 6.2: Normalized distributions of the calorimetric discriminating variables in the region $|\eta| < 0.6$ for $E_T > 20\ GeV$. for true and fake photons reconstructed as unconverted before any selection [31].

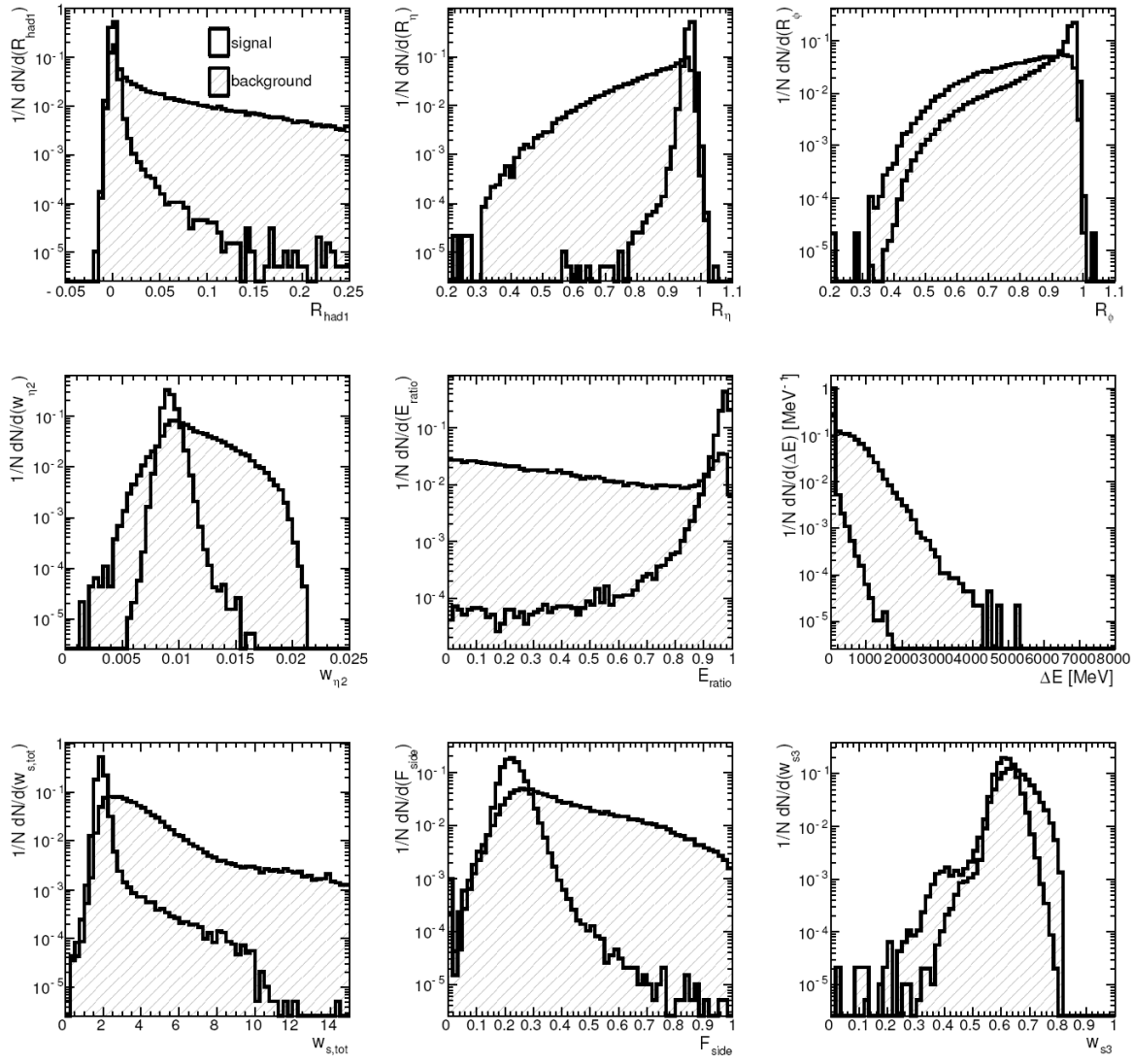


Figure 6.3: Normalized distributions of the calorimetric discriminating variables in the region $|\eta| < 0.6$ for $E_T > 20\ GeV$. for true and fake photons reconstructed as converted before any selection [31].

6.2.2 Loose and Tight selections

Two photon identification criteria menu have been built using the discriminating variables (DV) that are just defined (Table 6.1 summarizes the DV used by each photon selection):

- The *loose* selection, which is harmonized with the corresponding electron one and used for triggering purposes [3]. Numerical values cut thresholds for this selection are shown in tables in Appendix B.

- The *tight* photon identification criteria have been optimized based on simulated samples of true photons from photon-jet (γj) QCD processes and of fake photon candidates reconstructed in dijet (jj) QCD events. A multivariate tool, TMVA [11], has been used in order to find - taking into account the correlations among the discriminating variables - the optimal set of rectangular cuts that gives the lowest fake photon efficiency ε_B for a fixed true photon efficiency ε_S. One should note that for tight electrons there are no cuts on the following variables of the first sampling that are used for tight photons: F_{side}, w_{s3} and ΔE. In addition there is also no cut applied on R_ϕ.

  A separate optimization has been performed for converted and unconverted photon candidates, in order to take into account their different shower shapes [31] (for instance, the electrons from a photon conversion are bent in opposite directions in ϕ from the solenoid magnetic field and thus the shower is wider). Numerical values cut thresholds for this selection are shown in Appendix B. Due to some differences between data and Monte Carlo some variables were loosened during the 2010 data-taking period [103] and new values of cut thresholds were deduced for the first photon cross section measurement [19]. Other changes were done later and are described in Appendix B.

The importance of the calorimeter variables and in particular of the first sample of the ATLAS calorimeter can be seen below on the two displays 6.4 and 6.5 of data events. At least for these two examples, the discriminating power of the calorimeter is therefore obvious.

6.3 Photon isolation algorithm cuts

After calorimeter cuts are applied, the contamination of the inclusive signal from charged hadrons is greatly reduced. The remaining background is dominated by low multiplicity jets containing high-p_T π^0 mesons.

The left plot in Figure 6.6, shows the ratio between the energy of the leading π^0 in a cone of 0.2 around the cluster and the cluster energy after tight photon identification cuts. In 70% of the cases the cluster is dominated by a single π^0 . After the application of the cuts on the shower-shape in the first section of the electromagnetic calorimeter, this

[3] Which are also used in the *Event Filter* trigger.

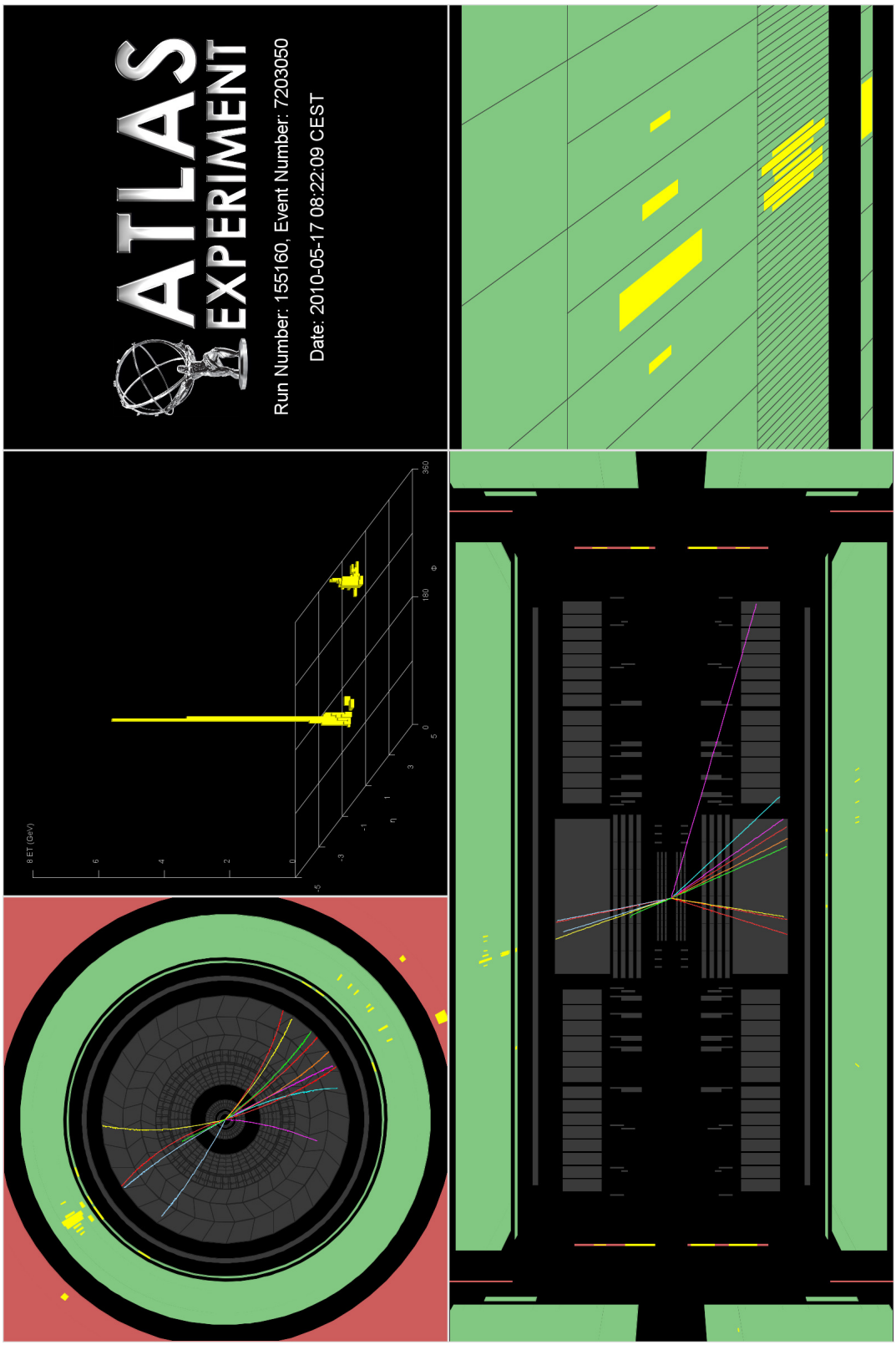


Figure 6.4: π^0 candidate passing "loose" selection criteria, falling "tight" selection.

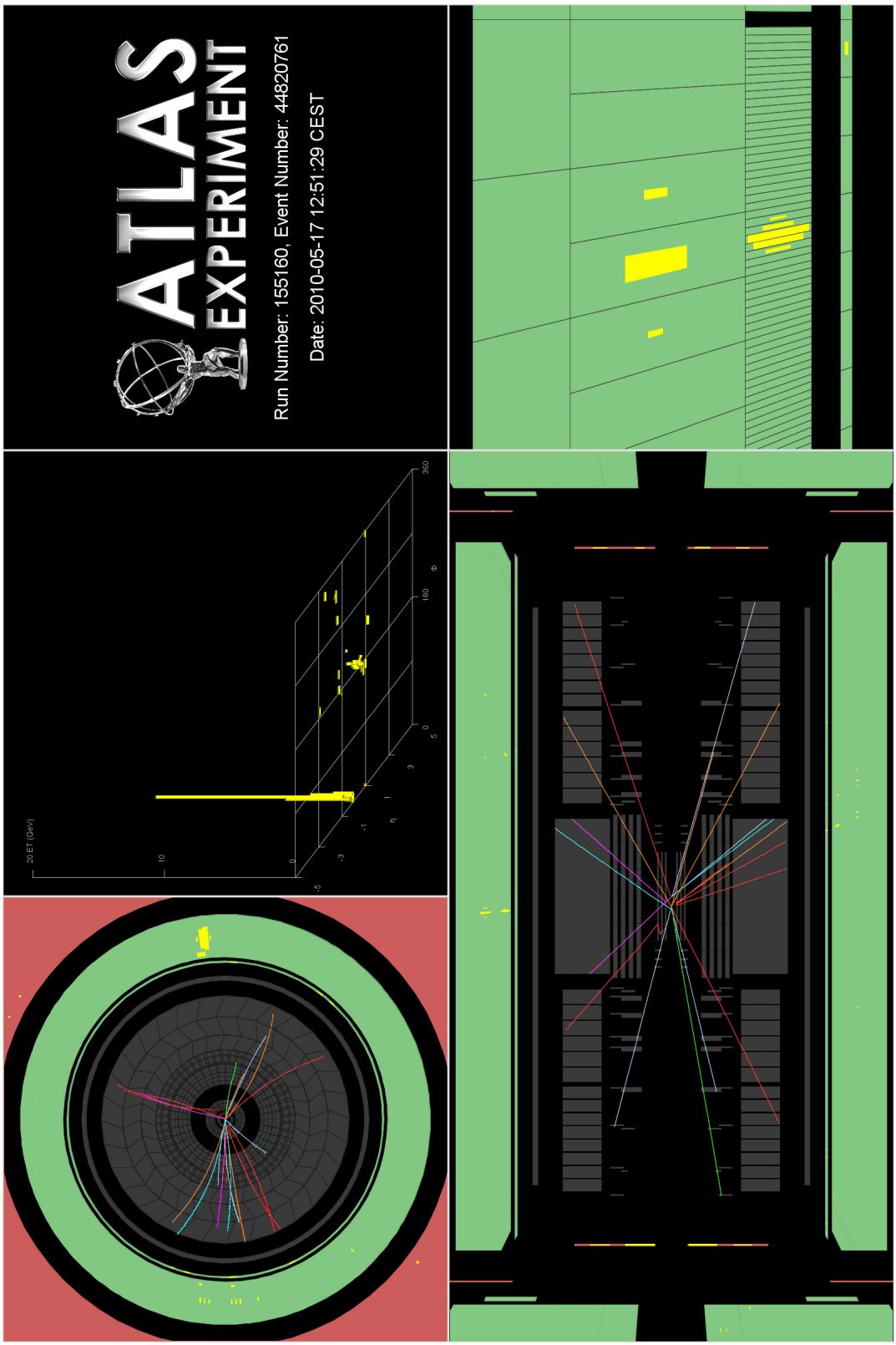


Figure 6.5: Photon candidate passing "tight" selection.

Category	Description	DV	Loose	Tight
Acceptance	$\|\eta\| < 2.37$, $1.37 < \|\eta\| < 1.52$ excluded	–		✓
Hadronic leakage	Ratio of E_T in the first sampling of the hadronic calorimeter to E_T of the EM cluster (used over the ranges $\|\eta\| < 0.8$ and $\|\eta\| > 1.37$)	R_{had_1}	✓	✓
	Ratio of E_T in all the hadronic calorimeter to E_T of the EM cluster (used over the range $0.8 < \|\eta\| < 1.37$)	R_{had}	✓	✓
EM Middle layer	Ratio in η of cell energies in 3×7 versus 7×7 cells	R_η	✓	✓
	Lateral width of the shower in the η direction	w_{η_2}	✓	✓
	Ratio in ϕ of cell energies in 3×3 and 3×7 cells	R_ϕ		✓
EM Strip layer	Shower width for three strips around maximum strip	$w_{s\,3}$		✓
	Total lateral shower width	$w_{s\,\mathrm{tot}}$		✓
	Fraction of energy outside core of three central strips but within seven strips	F_{side}		✓
	Difference between the energy associated with the second maximum in the strip layer, and the energy reconstructed in the strip with the minimal value found between the first and second maxima	ΔE		✓
	Ratio of the energy difference associated with the largest and second largest energy deposits over the sum of these energies	E_{ratio}		✓

Table 6.1: Discriminating variables used for loose and tight photon identification cuts [31].

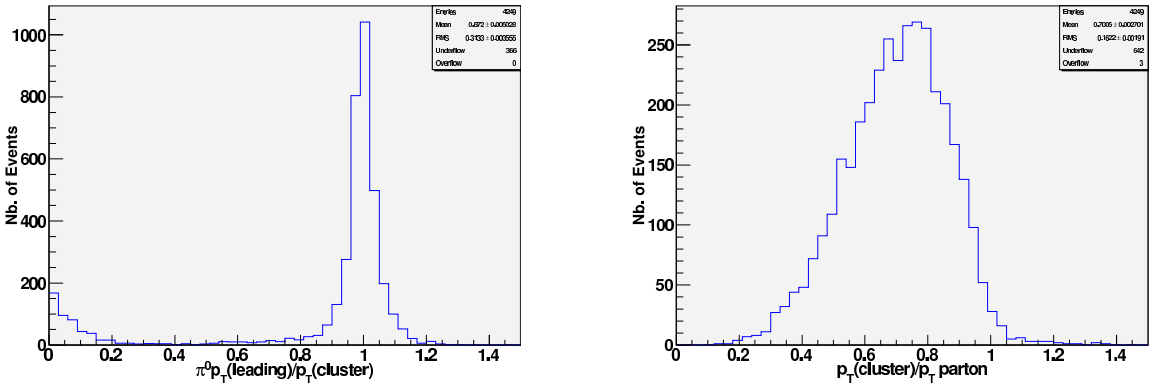


Figure 6.6: MC comparison between the cluster p_T and the leading π^0 (**left**) and the ratio between the cluster p_T and the parton transverse energy (**right**) for clusters fulfilling all calorimeter shower-shape cuts.

background cannot be further reduced using only the cluster shower shape information. Indeed most of the surviving π^0 are either very asymmetric decays, or decays with a small opening in η (less than one strip). On the other hand, the plot on the right of Figure 6.6 shows that the cluster does not take the full energy of the original parton which produced it (defined as the leading quark or gluon in the `PYTHIA` event record within ΔR of 0.4 around the cluster). Typically, only 70% of the parton energy is found in the cluster energy. There is thus a non negligible amount of hadronic activity around the cluster which can be used to increase the rejection.

Various analyses may require different isolation criteria of different tightness and therefore the isolation cuts are applied on top of the photon identification. Different calorimeter and tracking based isolation variables have been studied and optimized.

6.3.1 Track isolation

To further reduce the dijet and $\gamma-$jet background, a track-based isolation requirement can be applied. For each candidate photon that passes the selection described in Section 6.2, one computes the sum of the transverse momenta $\sum_{tracks} p_T$ of the charged particles around the candidate. The tracks must:

- lie within a cone of $\Delta R = \sqrt{(\Delta\phi)^2 + (\Delta\eta)^2} = 0.3$
- have a transverse momentum $p_T > 1\ GeV$
- leave at least one B-layer and 7 Si (Pixel + SCT) hits
- have an impact parameter smaller than $1 \sim mm$.

In the smaller cone of $\Delta R = 0.1$, an additional requirement is to exclude converted tracks. With these cuts, one have, for the moment, the optimal track isolation for photons. This was used in [14] and in the prospects of exclusion in the $H \to \gamma\gamma$ channel using 10 TeV Monte Carlo samples [27–29].

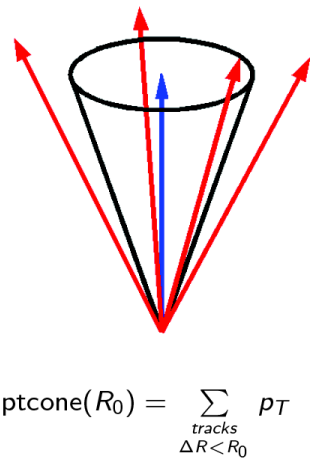


Figure 6.7: Sketch to ilustrate the track-isolation.

6.3.2 Calorimetric isolation

With the calorimetric isolation one can estimate the activity in the calorimeters close to the candidate. As we did mention in the Section 2.2, the treatment of the photon isolation provides some experimental and theoretical issues. So it is very important to define an experimental approach for the isolation. It should be compared with their theoretical equivalent, which was used when the cross section was computed.

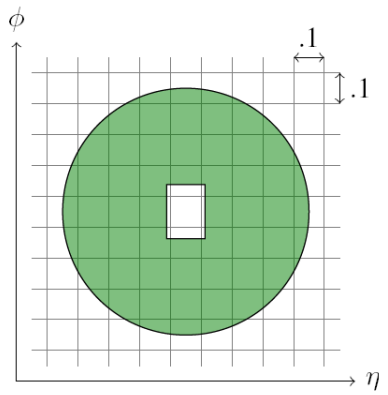


Figure 6.8: Construction of the isolation variable in a cone of $\Delta R = 0.4$.

The isolation variable is computed as the energy sum over all the calorimeter cells from both the electromagnetic and hadronic calorimeters, within a cone of $\Delta R = 0.4$. The contributions from 5×7 electromagnetic calorimeter cells in the $\eta - \phi$ space around the photon barycenter are not included in the calculation, as is shown in the Figure 6.8.

Thus, the resulting energy includes contributions from the following three sources:

(a) Leakage from the photon outside this region.

(b) Contribution of the underlying event.

(c) Hadronic activity close the photon cluster.

The small leakage from the photon outside the electromagnetic cluster (a), evaluated and parametrized as a function of photon transverse energy on simulated samples of single photons, is then subtracted from the isolation variable. After this correction, the isolation energy of truly isolated photons is independent of the photon transverse energy.

To reduce uncertainties from underlying event modeling (b), the isolation is then further corrected [32, 154] using a method suggested in Ref [179]. It is based on a technique for measuring an ambient energy density event-by-event, using low energy jets, which is then multiplied by the area of the isolation cone and subtracted from the isolation energy. The typical correction for an event with one *pp* interaction is 500 MeV. Thus, the isolation energy represents only the hadronic and electromagnetic activity near the photon candidate.

6.4 Performance of the photon identification

In this section, the performance of the cuts described in Section 6.2 and the track-isolation algorithm mentioned in Section 6.3 in terms of signal efficiency and the jet rejection power are discussed. In addition, a dedicated analysis, which allows to estimate the quality of the reconstructed conversions is presented.

For this task, a group of simulated samples (see Table 6.2) have been produced using the MC generators, `PYTHIA` [197] and `HERWIG` [116] [4] with an energy of the centre of mass of 10 TeV. Then, these samples are reconstructed with the same algorithms used for data.

Data Set	Process	σ [pb]	Filter type	Filter threshold [GeV]	Filter eff [%]	Nevts	Eq. luminosity [pb^{-1}]	Generator
106384	$H \rightarrow \gamma\gamma$ (gg+VBF), $m_H = 120\ GeV$	3.536E-2	2 prompt γ	20	78.0	99873	3.62E+6	`PYTHIA`
108086	γ-jet	2.893E+5	2 prompt γ	17	7.073	3976508	1.94E+2	`PYTHIA`
105802	QCD(jet-jet)	1.461E+9	1 prompt γ	17	7.060	9849209	9.55E-2	`PYTHIA`
105830	QCD(jet-jet)	1.166E+9	1 prompt γ	17	8.480	4398206	4.45E-2	`HERWIG`

Table 6.2: Monte Carlo samples used in the photon performance studies produced at $\sqrt{s} = 10$ TeV. The physics process, size of samples, corresponding equivalent luminosity, filter efficiency and cross-section are shown.

6.4.1 Signal photon efficiency

The photon identification efficiency for photons originated in the $H \rightarrow \gamma\gamma$ decay as well as for those from direct production in the γj QCD processes has been evaluated using the `PYTHIA` datasets previously described in Table 6.2.

[4] A brief description of these generators is given in the Appendix C

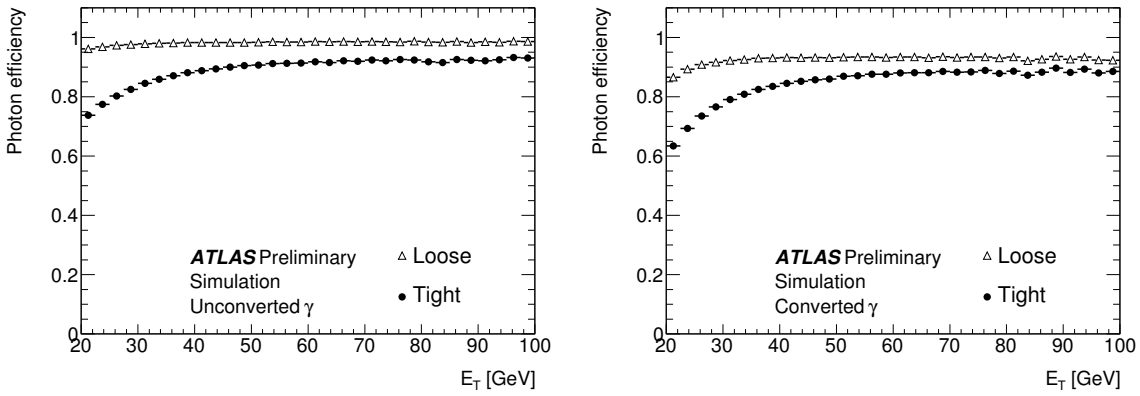


Figure 6.9: Expected total photon efficiency (reconstruction + identification) for true photons with $E_T > 20$ GeV in a MC sample of γj events in the region $0 < |\eta| < 1.37$ and $1.52 < |\eta| < 2.37$, as a function of transverse energy for loose and tight selection criteria and for unconverted (**right**) and converted (**left**) photons [31].

To evaluate the identification efficiency, it is necessary to provide an association between reconstructed candidates and true particles. Thus, for each photon candidate, the position $(\eta^{clus}, \phi^{clus})$ of the barycenter in the EMS2 layer is compared to the coordinates $(\eta^{extr}, \phi^{extr})$ obtained for all the final state particles; depending on $\Delta\eta = \eta^{extr} - \eta^{clus}$ and $\Delta\phi = \phi^{extr} - \phi^{clus}$, the best association between a candidate and a true particle is defined as follows:

- inside an elliptical cone $(\Delta\eta/0.025)^2 + (\Delta\phi/0.05)^2 < 1$, corresponding roughly to a 3×5 cluster, the true photon with highest p_T is associated to the candidate. If no photons are present one choose the highest pt truth particle in the elliptical cone is chosen. In this way about 87% of candidates are associated to a true particle in a typical filtered-jet dataset.

- to account for possible tails of the extrapolation result and to increase the efficiency of the association, in case the previous criterion fails, the true particle with the smallest $\Delta R = \sqrt{\Delta\eta^2 + \Delta\phi^2}$ inside a cone $\Delta R < 0.1$ is associated. After this the matching is close to 100% for $H \to \gamma\gamma$.

The photon identification efficiency with respect to the reconstructed candidates is defined as:

$$\epsilon_{wrt\ reco} = \frac{N_\gamma^{reco,\ pass\ cut}}{N_\gamma^{truth,\ reco}} \tag{6.10}$$

where $N_\gamma^{truth,\ reco}$ is the total number of true photons associated to a reconstructed candidate, having true E_T greater than a given threshold (20, 25 and 40 GeV). Table 6.3 summarizes the average efficiencies for loose and tight selections, as defined in Equation 6.10.

		loose selection efficiency (%)			*tight* selection efficiency (%)		
		all	unconverted	converted	all	unconverted	converted
γj	$E_T > 20\ GeV$	95.45 ± 0.01	97.80 ± 0.01	91.73 ± 0.01	82.88 ± 0.02	85.04 ± 0.03	79.44 ± 0.04
	$E_T > 25\ GeV$	95.96 ± 0.01	98.08 ± 0.01	92.58 ± 0.03	85.31 ± 0.02	87.16 ± 0.03	82.35 ± 0.04
	$E_T > 40\ GeV$	96.37 ± 0.02	98.40 ± 0.02	93.17 ± 0.04	89.21 ± 0.03	90.76 ± 0.04	86.76 ± 0.05
$H \to \gamma\gamma$	$E_T > 20\ GeV$	96.15 ± 0.05	97.93 ± 0.04	93.00 ± 0.10	88.45 ± 0.08	89.81 ± 0.09	86.05 ± 0.14
	$E_T > 25\ GeV$	96.25 ± 0.05	97.99 ± 0.04	93.16 ± 0.10	88.92 ± 0.08	90.22 ± 0.09	86.61 ± 0.14
	$E_T > 40\ GeV$	96.46 ± 0.05	98.16 ± 0.04	93.42 ± 0.11	90.06 ± 0.08	91.27 ± 0.09	87.92 ± 0.14

Table 6.3: Expected total photon identification efficiencies (reconstruction + identification for loose and tight selections). The errors are statistical only [31].

6.4.2 Jet rejection

The rejection of jets is defined by the following equation:

$$R = \frac{N_{jet}}{N_{fake\gamma}} \tag{6.11}$$

where N_{jet} is the total number of jets and $N_{fake\gamma}$ the number of jets that pass the selection cuts. The difficulty arises from the fact that N_{jet} must reflect the initial number of jets, before any cut, and therefore must be measured from the high statistics generator level unfiltered samples described in Table 6.2, whereas $N_{fake\gamma}$ can be measured only on fully reconstructed filtered MC samples (since the rejection is high, one has to make some particle filter on the Monte Carlo event in order to have a reasonable number of events that will be fully simulated in `GEANT4`). Therefore, one must normalize N_{jets}^{unfilt} and $N_{fake\gamma}^{filt}$ to the generated number of events in the relevant sample: N_{evts}^{unfilt} in the unfiltered samples and $N_{evts}^{filt}/\epsilon_{filt}$ in the filtered ones. [5] The rejection factor then reads:

$$R = \frac{N_{jet}^{unfilt}}{N_{fake\gamma}^{filt}} \frac{N_{evts}^{filt}}{N_{evts}^{unfilt}} \frac{1}{\epsilon_{filt}} \tag{6.12}$$

Table 6.4 shows the rejection factors for the `PYTHIA` dijet sample, whereas Tables 6.5 and 6.6 show the rejection factor after application of the tight selection criteria and the track-isolation requirement (which was chosen to be < 4 GeV) in the dijet and γ-jet datasets produced with `PYTHIA` and `HERWIG`. The rejections are given separately for quark and gluon jets. This is calculated after matching the candidate photon with the original parton by requiring that the particle four-momenta at generator level lie within a cone of size $\Delta R = 0.4$. The fraction $N_{jets}^{unfilt}/N_{evts}^{unfilt}$ for the γ-jet sample has to be modified since the filter is applied on two objects, including the photon from matrix element. In this case N_{jets}^{unflit} is the number of jets in the unfiltered sample asking in addition that the photon from the matrix element passes the filter. One observes that the rejection for gluon-jets is larger than for quark-jets which is in agreement with Ref. [132]. One find some differences between the rejection factors depending on the generator and the physical process, due

[5] Numerical values for parameters in Equation 6.12 are available at https://twiki.cern.ch/twiki/bin/view/Main/HggExercice10TeV.

to different parton fragmentation functions. An extended study is discussed in Ref. [201]. Therefore, from Tables 6.5 and 6.6 we can see easily how the rejection increase when the track-isolation requeriment is applied, which allow us to have a more pure sample.

	loose rejection			*tight* rejection		
	all jets	quark jets	gluon jets	all jets	quark jets	gluon jets
$E_T > 20\ GeV$	898 ± 4	323 ± 2	2224 ± 16	4780 ± 43	1626 ± 17	13688 ± 238
$E_T > 25\ GeV$	1030 ± 6	365 ± 3	2674 ± 30	5288 ± 71	1743 ± 27	16765 ± 458
$E_T > 40\ GeV$	944 ± 13	368 ± 6	2211 ± 55	5098 ± 165	1675 ± 60	20110 ± 1504

Table 6.4: Expected jet rejection for loose and tight selections for a jet-jet MC sample.

Figure 6.10 shows the E_T spectra of the photon candidates in the `PYTHIA` background dijet sample (see Table 6.2 for more details) passing the loose (left) and tight (right) selections. The sample is sub-divided into five components of decreasing importance: after the loose (tight) selection approximately 69.9 ± 0.2 $(47.6 \pm 0.3)\%$ of the candidates with $E_T > 20$ GeV correspond to photons from π^0 decay, whereas $\sim 9.7 \pm 0.1$ $(7.8 \pm 0.1)\%$ are from η, η' or ω decay into two photons, and 6.0 ± 0.1 $(2.7 \pm 0.1)\%$ are from other hadrons with complex decay processes and particles interacting in the tracker material. A fraction of $\sim 8.4 \pm 0.1$ $(25.5 \pm 0.3)\%$ of all photon candidates after the loose (tight) selections, in this sample, are expected to be produced directly by *hard scattering* at these energies, and $\sim 5.9 \pm 0.1$ $(16.7 \pm 0.3)\%$ from initial or final state radiation of quarks (ISR/FSR).

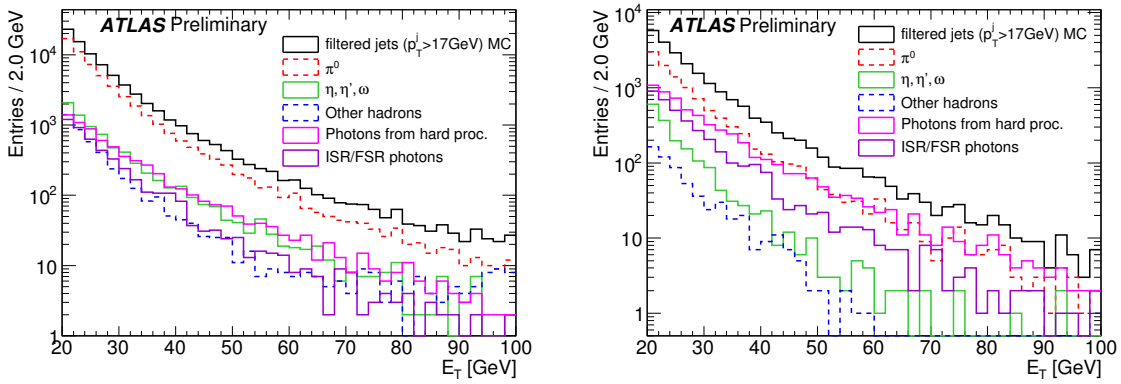


Figure 6.10: E_T spectra for the photon candidates in the background `PHYTIA` jet sample passing the loose (**left**) and tight (**right**) selections. The different components are shown [31].

6.4.3 Converted photon purity

In this subsection, the quality of reconstructed conversions was checked. The idea is to compute the purity in a $H \rightarrow \gamma\gamma$ simulated data sample using only converted photons. In

	sample	generator	all	quark-jet	gluon-jet
Rejection factor	jj	PYTHIA	7777 ± 122	2517 ± 50	27218 ± 941
		HERWIG	3398 ± 79	933 ± 25	16092 ± 940
	γj	PYTHIA	1929 ± 44	1657 ± 38	25846 ± 4361

Table 6.5: Jet rejections expected for the dijet and $\gamma-$jet samples for $E_T > 25\ GeV$. The results are shown after tight selection and track isolation cuts for all jets and separately for quark and gluon jets. The errors are statistical only.

	sample	generator	all	quark-jet	gluon-jet
Rejection Factor	jj	PYTHIA	8659 ± 362	2894 ± 141	40008 ± 3850
		HERWIG	3323 ± 190	959 ± 61	24983 ± 4544
	γj	PHYTIA	2321 ± 106	2048 ± 96	38768 ± 17484

Table 6.6: Jet rejections expected for the dijet and $\gamma-$jet samples for $E_T > 40\ GeV$. The results are shown after tight selection and track isolation cuts for all jets and separately for quark and gluon jets. The errors are statistical only.

order to know how many of these reconstructed conversions are coming from a correctly identified truth conversion.

The main purpose is to identify the origin of the converted photon in the ATLAS detector. It is indeed possible to have photons with multiple interations before arriving to EM calorimeter due to the considerable amount of material situated in front of this, see Figure 6.11(and Figure 5.7).

For this, an ID track classification has been performed. It is based on a method which establishes links between reconstructed track and truth track which is provided by the standard simulation infrastructure used in the ATLAS collaboration [13]. This method is able to make an association from a (truth) reconstructed track to a truth particle, measuring the probability of track association with the truth particle.

Photon pre-selection

For this study, pairs of photons are required to have a reconstruted pseudo-rapidity in the ranges $|\eta| < 1.37$ and $1.52 < |\eta| < 2.37$. Moreover, they have to pass the tight selection criteria. The leading and subleading photons are defined as those with a reconstructed transverse momentum of $p_{T_{\gamma 1}} > 40$ GeV and $p_{T_{\gamma 2}} > 25$ GeV, respectively.

Current conversion definitions

Reconstructed converted photons are classified in the following three categories:

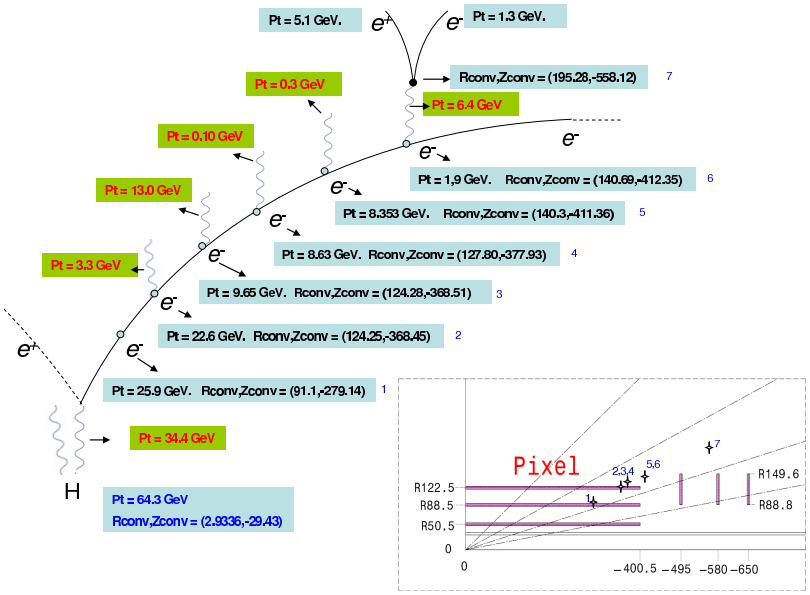


Figure 6.11: Example of secondary converted photon from Higgs. Here are shown, the coordinates where the conversions and the bremsstrahlung occur. They are represented by little stars in the sketch of the innermost pixel subdetector (inside the square with dashed line). This event was extracted from the simulated data set described in Table 6.2.

- **Signal :** Converted photons coming directly from Higgs with an associated conversion found in the MC truth.

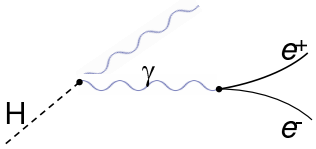


Figure 6.12: Sketch of a signal converted photon .

- **Secondary :** True converted photon from Higgs decay (after single or multiple Bremsstrahlung) or false conversion but at least one track is coming from Higgs. A example is shown in Figure 6.11 (a badly reconstructed converted γ for which one of the electrons comes from a conversion from the Higgs decay).

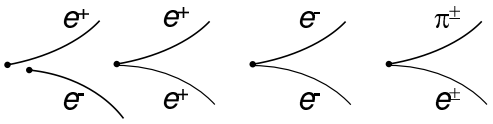


Figure 6.13: Sketch some of the possible vertices for secondary converted photon .

- **Fakes :** False converted photon not coming from Higgs decay (small fraction, in particular charged pion) or a true converted photon not coming from the Higgs decay.

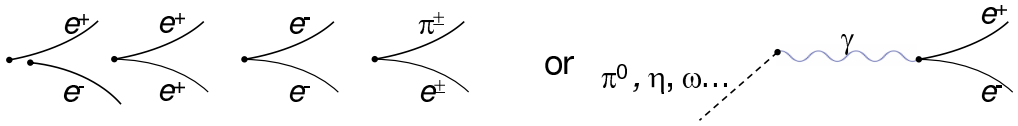


Figure 6.14: Sketch of the fake converted photon .

Results of the converted photon classification

The results of this classification are summarized in Table 6.7. The table is splitted into two parts, which correspond to the results obtained for single-track and double-tracks conversions respectively. In general, conversions are highly efficiently identified for both cases. Signal efficiency is greater for single-track than for double-tracks conversions. This is the same for the fake percentage. On the other hand, the percentage of secondaries is higher in double-tracks conversions. One sees that the application of the isolation requirement in addition to the tight selection criterion, does not change significantly the results. It is due to the fact that photons from Higgs decay are expected to be well isolated.

Futhermore, a detailed study was carried out, which reproduces the analysis showed in Table 6.7. Results are shown in Tables 6.8 and 6.9. This study exploits the characteristics of reconstructed tracks in the ID system of the ATLAS detector. The main idea is to determinate where the most of the fakes conversions comes from. So, in this spirit, tracks are classified as following:

- *TRT-Standalone tracks*, They are reconstructed tracks only with hits associated in the TRT ID subsystem.

- *NON TRT-Standalone tracks*, these correspond to tracks with hits associated in the Silicium ID subdetector.

In Tables 6.8, 6.9 is shown that for single-track and double-track conversions the majority of fakes are found when tracks are TRT-Standalone (reconstructed only with the TRT detector). On the other hand, a very pure converted signal is achieved when the tracks have associated hits in the Silicium ID subsystem. This is very promising for the analysis with collision data if one want to work with a very pure sample of converted photon.

		after tight		tight+track-isolation	
	Origin of converted photon	Ncand.	Summary %	Ncand.	Summary %
Single-track	photon's mother is a Higgs	15827		15602	
	photon's mother is a e^-/e^+ (indirectly from Higgs)	229 (226)	93.62 ± 0.19	222 (220)	93.72 ± 0.19
	photon's mother is $(\pi^0, \eta, \omega, ...)$	189	1.34 ± 0.09	182	1.32 ± 0.09
	truth track-particle found non coming from truth conversion (indirectly from Higgs)	190 (0)	5.03 ± 0.17	181 (0)	4.95 ± 0.17
	don't truth track particle found	486		459	
Double-tracks	photon's mother is a Higgs	19201		18920	
	photon's mother is a e^-/e^+ (indirectly from Higgs)	88 (84)		87 (83)	
	photon's mother is $(\pi^0, \eta, \omega, ...)$	59		54	
	pair e^-/e^+ (no true conversion) (indirectly from Higgs)	1421 (1395)	86.67 ± 0.23	1390 (1365)	86.85 ± 0.23
	pair e^-/e^- or e^+/e^+ (indirectly from Higgs)	370 (338)	11.88 ± 0.22 1.44 ± 0.08	361 (331)	11.76 ± 0.22 1.39 ± 0.08
	pair e^- or e^+ with other partcile (indirectly from Higgs)	771 (724)		738 (694)	
	pair of particles $\neq e^-$ and $\neq e^+$	67		61	
	don't truth track particle found at least for one track (indirectly from Higgs)	177 (92)		174 (90)	

Table 6.7: Converted photon clasification according the truth association - Signal, Secondary or Fakes for object photons reconstructed from a $H \to \gamma\gamma$ simulated sample at $\sqrt{s} = 7$ TeV. Results are separated for single-track and double-tracks conversions.

Single-track	TRT-Standalone tracks	NON TRT-Standalone tracks
Signal	(92.58 ± 0.22) %	(99.07 ± 0.18) %
Secondary	(1.52 ± 0.10) %	(0.38 ± 0.11) %
Fakes	(5.88 ± 0.20) %	(0.55 ± 0.14) %

Table 6.8: Converted photon classification according to the truth association - Signal, Secondary or Fakes efficiencies (relative percentage) for object photons reconstructed from a $H \to \gamma\gamma$ simulated sample at $\sqrt{s} = 7$ TeV. Results for single-track conversions are shown according the characteristics of her track.

Double-tracks	TRT-Standalone tracks	at least a TRT-Standalone track	NON TRT-Standalone tracks
Signal	(53.87 ± 0.95) %	(66.81 ± 0.90) %	(95.90 ± 0.16) %
Secondary	(36.14 ± 0.91) %	(32.90 ± 0.89) %	(4.00 ± 0.15) %
Fakes	(10.00 ± 0.57) %	(0.29 ± 0.10) %	(0.10 ± 0.02) %

Table 6.9: Converted photon classification according to the truth association - Signal, Secondary or Fakes efficiencies (relative percentage) for object photons reconstructed from a $H \to \gamma\gamma$ simulated sample at $\sqrt{s} = 7$ TeV. Results for double-tracks conversions a shown according the characteristics of their tracks.

6.5 Identification with early data at $\sqrt{s} = 7$ TeV

The following measurements presented here, are based on proton-proton collision data collected at a centre-of-mass energy $\sqrt{s} = 7$ TeV with the ATLAS detector at the LHC between April and August 2010. Data taken between ATLAS run periods A and E4 have been included in the analysis [19]. The total integrated luminosity of the sample, as used in the measurement, is $880 \pm 100\ nb^{-1}$. The photon event selection for data and simulated samples are further explained in the Appendix C.2.

Photon candidates pre-selection

Photon candidates with calibrated transverse energies in the range $15 < E_T < 100\ GeV$ and reconstructed pseudorapidity in the detector intervals $\eta < 1.37$, or $1.52 < \eta < 2.37$ are retained for the successive analysis steps. In addition, candidates are separated in the following pseudorapidy regions:

$$\eta \in [0.00; 0.60), \quad \eta \in [0.60; 1.37), \quad \eta \in [1.52; 1.81), \quad \eta \in [1.81; 2.37)$$

and regrouped in several E_T intervals [GeV]:

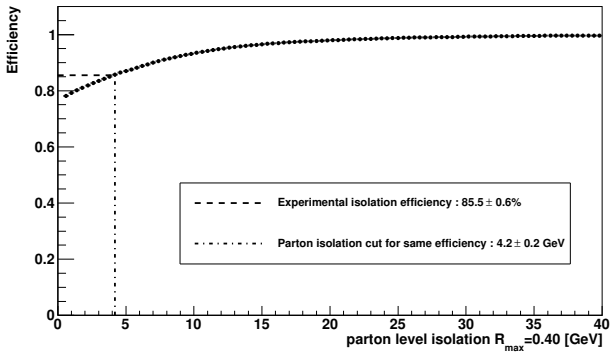
$$[15; 20), \quad [20; 25), \quad [25; 30), \quad [30; 35), \quad [35; 40), \quad [40; 50), \quad [50; 60), \quad [60; 100)$$

where the increase of the interval width at higher E_T values is motivated by the lower candidate statistics.

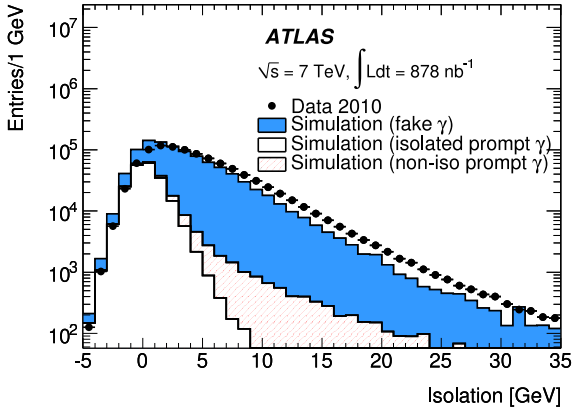
All the details of preselection are explained in the Appendix C, Section C.3.

Energy isolation

A study was performed in [95] to determine the correspondence between the parton-level and reconstruction-level isolation criteria which is a very delicate issue. The efficiency of a parton-level isolation cut on `PYTHIA` photons originating in a Bremsstrahlung process was compared to the efficiency of the reconstruction-level cut at 3 GeV. Figure 6.15(**top**) shows the efficiency as a function of the isolation cut for such photons. In a bremsstrahlung process $q \rightarrow \gamma q_1 \dots q_n$ the q_1 to q_n within a cone of $R = 0.4$ around the photon direction are added together to form a single quadri-vector, and the transverse momentum of this quadri-vector is taken as the partonic isolation transverse energy associated to the photon (note that all partons produced by the generator are not added in the cone, for more details see [95]). The parton-level cut chosen was that which best matched the efficiency of the reconstruction-level cut at 3 GeV. Since the parton cut value that matches the 3 GeV cut at experimental level varies across different pseudo-rapidity bins, a sensitive mean value of 4 GeV was used [19] to compute the NLO cross section.



(a)



(b)

Figure 6.15: In the top plot [95], the efficiency as a function of different parton level isolation cuts, with comparison to the experimental isolation efficiency. In the bottom plot [32] is shown the distribution of the isolation energy of reconstructed photon candidates passing the preselection and the loose identification criteria. The data are represented by dots and the colored histograms represent the expectations from Monte Carlo simulations using `PYTHIA`.

The isolation distributions for prompt and fake photon candidates from simulation, as well as the distribution of selected candidates in data, are shown in Figure 6.15(**bottom**) for reconstructed photon candidates passing the preselection and the loose identification criteria. The signal distribution is separated into two components: true isolated prompt photons ($E_T^{\text{iso}} < 4$ GeV), and prompt photons that fail the true isolation cut ($E_T^{\text{iso}} > 4$ GeV). The true isolation energy E_T^{iso} is determined in the signal MC samples by looping over the MC truth block and computing the total transverse energy of all partons inside a (η, ϕ) cone of radius 0.4 around the photon direction. These figures serve to illustrate the differences in the isolation energy distributions between signal and background in simulation. It's important to note, however, that possible differences between simulated and collision data imply that data-driven models of the isolation energy distributions for both signal and background are critical components of this analysis.

The efficiency that the reconstructed isolation energy is less than 3 GeV is around 96 % for true isolated prompt photons that pass tight identification criteria, both for photons from hard scattering (96.5%) and from fragmentation(95.6%). The criterion is slightly less efficient for photons from parton bremsstrahlung and fragmentation because they have, on average, more nearby hadronic activity that gives rise to the asymmetry positive tail of the prompt photon signal distribution in Figure 6.15(**bottom**). The same criterion is expected to reject about 50% of background candidates with transverse energy above 15 GeV.

6.5.1 Efficiency estimation

Robust tight selection criteria

The photon showers in collision data are wider in η than expected from simulation (seen in early electron studies with data [43]). While the exact cause of the difference between data and simulation is still under investigation, the result is a loss in efficiency for photons in collision data, due primarily to cuts on R_η and w_{η_2} which reject more signal photons than anticipated.

To reduce this inefficiency, the tight cuts on R_η and w_{η_2} were relaxed, with the constraint that the new "tight" cut cannot be weaker than the loose cut on the same variable. The new modified cut values for R_η and w_{η_2} can be found in Appendix B, Table B.3. In the next section the implications of these relaxed cuts are discussed.

Data/MC discrepancies of discriminating variables

Distributions of the DV's listed in Table 6.1 are built from all photon candidates in the data and in the MC samples passing the pre-selection described at the beginning of the Section 6.5.

The data and MC DV distributions corresponding to a given selection level in a given E_T and η are compared; two representative examples are shown for R_η and w_{η_2} in Figure 6.16(left) and 6.16(right) respectively, from which the discrepancies mentioned above can be qualitatively appreciated.

The discrepancy between the DV distributions in data and MC can be at first order approximated by a small shift, that can be evaluated as the difference between the means of the DV distributions in data and MC:

$$\Delta\mu^s_{\mathrm{DV}} = \langle \mathrm{DV}^s_{\mathrm{data}} \rangle - \langle \mathrm{DV}^s_{\mathrm{MC}} \rangle \tag{6.13}$$

where the index s indicates the candidates sub-samples used to built the reference distributions. Meanwhile in Appendix B, Section B.2 are shown the values of $\Delta\mu^{loose}$ and $\Delta\mu^{tight}$ for each DV, computed from the data and MC comparison in the different E_T and η regions. For instance, in Figures 6.17 and 6.18 are shown how these $\Delta\mu^s$ plots look like for the R_η and w_{η_2} variables.

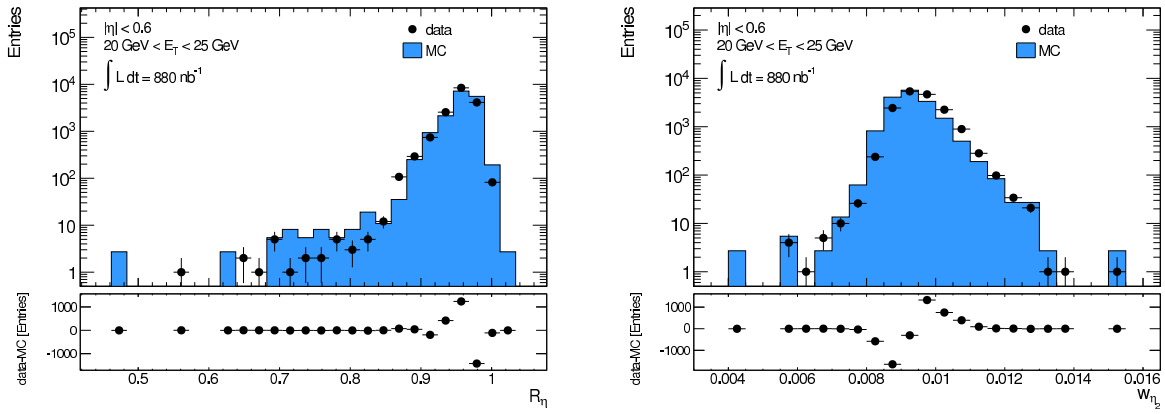
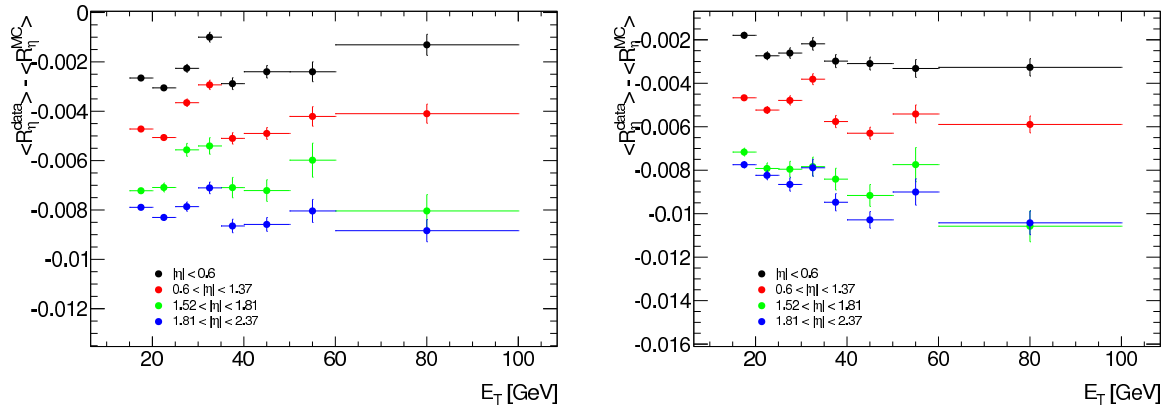


Figure 6.16: Examples [103] of distribution of R_η (left) and w_{η_2} (right) in data and MC for photon candidates with $|\eta| < 0.6$ and $E_T \in [20, 25)\ GeV$ passing a tight modified selection (corresponding to all tight cuts but without cutting on R_η nor w_{η_2}). The MC distributions are normalized to the corresponding number of entries in data.



(a) (b)

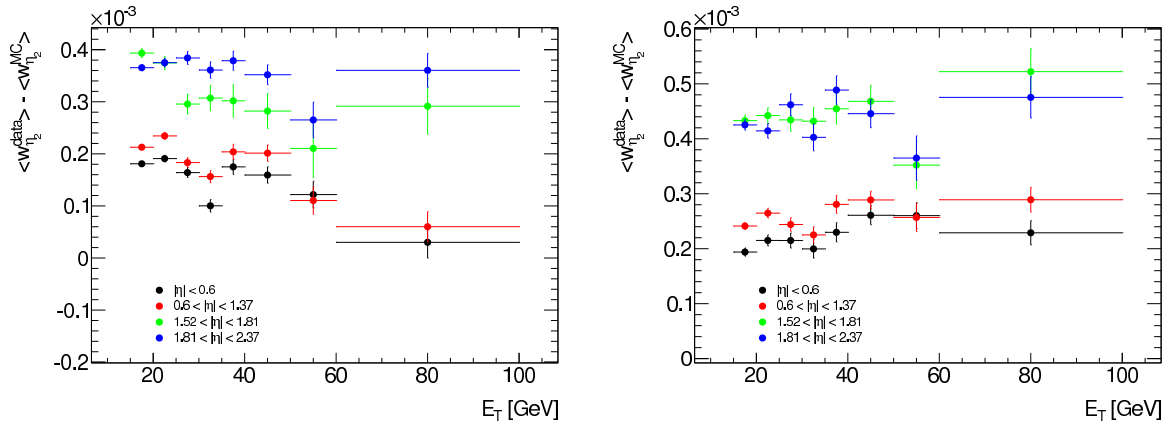
Figure 6.17: Differences $\Delta\mu_{R_\eta}$ between the means of the R_η distributions in data and MC for photon candidates passing the loose (a) and tight (b) selections [103]. Errors are statistical only.

Photon efficiency estimation using a candidate-by-candidate data-driven MC correction

In order to quantitatively estimate these effects, the $\Delta\mu^s_{DV}\,(E_T, \eta)$ values are applied as corrective factors [6] on a candidate-by-candidate basis to the DV of photon candidates matched to true direct and fragmentation photons in the MC sampled:

$$DV_k^{corr} = DV_k + \Delta\mu^s_{DV}\,(E_T, \eta) \tag{6.14}$$

[6] In order to take into account MC/Data discrepancies.



(a) (b)

Figure 6.18: Differences $\Delta\mu_{w_{\eta_2}}$ between the means of the w_{η_2} distributions in data and MC for photon candidates passing the loose (a) and tight (b) selections [103].

where the index k runs over all photon candidates, and E_T and η measure the actual reconstructed momentum and pseudorapidity position of the candidate. The tight selection is then applied on the corrected DV values DV_k^{corr} for the k-th candidate, and from the global behavior of all candidate of all candidate sample after the corrections a corrected identification efficiency is computed according to:

$$\epsilon^{\mathrm{offl,k}}(E^{\gamma}_{T,\mathrm{reco}}) \equiv \frac{dN^{\gamma}(\eta_{k,1} \leq |\eta^{\gamma}_{\mathrm{reco}}| < \eta_{k,2}, E^{\mathrm{iso}}_{T,\mathrm{reco}} < 3\ GeV, \mathrm{tight-ID})/dE^{\gamma}_{T,\mathrm{reco}}}{dN^{\gamma}(\eta_{k,1} \leq |\eta^{\gamma}_{\mathrm{reco}}| < \eta_{k,2}, E^{\mathrm{iso}}_{T,\mathrm{reco}} < 3\ GeV)/dE^{\gamma}_{T,\mathrm{reco}}} \quad (6.15)$$

In Equation 6.15 we have the offline photon efficiency, which is computed as a function of the reconstructed photon transverse energy and for a certain bin k of pseudorapidity. It is defined as the efficiency for reconstructed true prompt photons, with reconstructed isolation lower than 3 GeV, to pass the tight photon identification criteria (tight ID).

Results and systematics on photon efficiency

The offline efficiencies are determined after the shower shape corrections, and are listed in Table 6.10 as a function of the reconstructed photon transverse energy in the four pseudorapidity intervals under study. The corresponding distributions are shown in Figure 6.19 (including both uncorrected and corrected computed efficiencies, respectively). These central values are computed for a mixture of direct and fragmentation photons, weighted according to the respective and MC sample sizes and production cross sections predicted by `PYTHIA`.

In the following list the sources of systematic uncertainties are shortly described [32, 103]

- **Corrected photon efficiency central value**, here is taking into account the effect

E_T range $[GeV]$	$0.00 \leq \lvert\eta^\gamma\rvert < 0.60$ [%]	$0.60 \leq \lvert\eta^\gamma\rvert < 1.37$ [%]	$1.52 \leq \lvert\eta^\gamma\rvert < 1.81$ [%]	$1.81 \leq \lvert\eta^\gamma\rvert < 2.37$ [%]
$[15-20)$	63.3 ± 6.6	63.5 ± 6.9	72.2 ± 8.4	69.9 ± 8.2
$[20-25)$	73.5 ± 6.1	73.5 ± 6.8	81.6 ± 8.3	75.7 ± 9.0
$[25-30)$	80.2 ± 5.4	80.8 ± 5.7	86.7 ± 6.6	78.9 ± 9.0
$[30-35)$	85.5 ± 4.5	85.3 ± 4.8	90.4 ± 5.9	82.3 ± 7.8
$[35-40)$	85.2 ± 3.9	89.3 ± 4.3	92.3 ± 5.0	84.4 ± 6.8
$[40-50)$	89.2 ± 3.3	92.1 ± 3.6	93.5 ± 4.6	85.4 ± 6.2
$[50-60)$	91.3 ± 3.1	94.1 ± 2.8	93.9 ± 3.6	87.3 ± 5.3
$[60-100)$	92.2 ± 2.6	94.8 ± 2.6	94.2 ± 2.9	89.3 ± 4.2

Table 6.10: Isolated prompt photon selection efficiency $\epsilon_k^{\text{offl}}(E_T{}^\gamma)$, defined as the fraction of true prompt photons reconstructed in a certain interval k of pseudorapidity, passing γ object quality criteria, with reconstructed isolation transverse energy lower than 3 GeV, that pass tight photon identification criteria. The overall errors shown (excluding the systematics associated with the comparision of the nominal results with those of the electron extrapolation method) systematic uncertainties are shown [32, 103].

of correction factors $\Delta\mu^s_{DV}$ on the computed efficiencies.

- **LAr cell gain corruption**, the problem is that the gain information for channels 0 (rep 64) from a FEB is overwritten at the input of the ROD to be the one of channel 63 (resp 127). So channels 0 and 64 can thus be miscalibrated by a factor of 10 (or 1/10) depending on the original gain configuration of the pair of channels. The 'most' dangerous case is probably when channel 0 (or 64) are Medium gain originally but 63 (or 127) are high Gain. Channel 0 (or 64) are then calibrated (ADC $\rightarrow$ energy) as if they were high gain resulting to an energy too low by a factor 10. This problem affected both the DSP online calibration and the offline energy computation.

- **Hard-process/fragmentation photons relative composition**, which is the effect of the different composition of the photon inclusive signal. For this, the hard-process photons ("direct") and fragmentation photons ("brem") [7] were variated in a range between 80% - 20% . In addition, this procedure was evaluated with the MC generators `PYTHIA` and `HERWIG`.

- **Upstream material uncertainty**, the impact of upstream material uncertainty is assessed by comparing photon efficiencies from nominal photon Monte Carlo samples with those obtained with Monte Carlo samples simulated with additional material in different detector geometries [8]. In addition a detector geometry with extra material in the inner detector only was considered [9], which affects mainly the PID efficiencies

[7] See Section 2.2.

[8] +5%: Increase of whole Inner Detector (excluding sensitive detectors)

[9] ID material changes: +10% whole ID, +20% Pixel services, +20% SCT services, +15% X_0 at end of SCT/TRT endcap, +15% X_0 at ID endplate. LAr material changes: +0.1 X_0 radial in the barrel

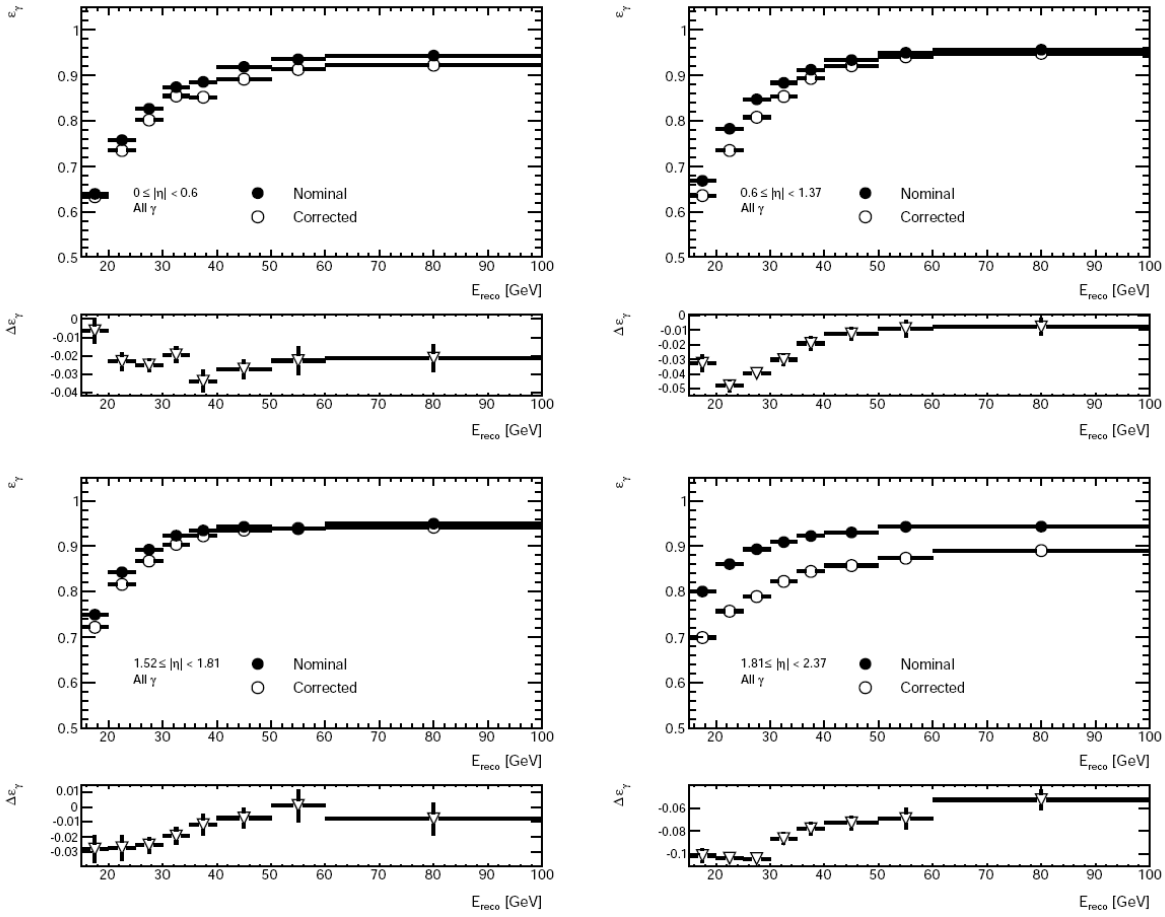


Figure 6.19: MC photon efficiencies for tight isolated photons as a function of E_T in different pseudorapidity regions. The figures below show efficiency differences between the uncorrected values ("nominal" close circle) and the corrected values ("corrected by $\Delta\mu^s_{\rm DV}$: *Fudge Factors*" open circles) .

of converted photons.

- **Object quality**, here is evaluated the acceptance loss due to the object quality cut on data and on different MC samples. The configuration of the disabled readout regions at reconstruction level on MC samples reflects the dead OTx configuration present at the beginning of the data taking (OQ map made with run 152166 [10]). Due to this fact, the systematic error was estimated only by comparing data and MC with this map.

- **Pileup**, there is a significant fraction of events with additional soft interactions in the same bunch crossing as the hard scatter event, called *in-time pile-up*. The

cryostat region before the presampler, +0.05 X_0 radial between the presampler and the layer 1 of the calorimeter.

[10] it is shown in the Table C.4 first line, third row of the Appendix C

average number of additional interactions changes over time with the instantaneous luminosity and it is hard to know exactly but it is in average smaller than 2. The best estimator for the number of additional interactions in one event is the number of reconstructed primary vertices. To quantify the pile-up effect, a dedicated MC sample of γ-jet events ($p_T > 17$ GeV) is used, which has been generated with a mean number of extra pile-up events of 2. Since it is known that the mean number of extra pile-up events in data is less than that, a re-weighting of the MC events depending on the number of PV was done in order to get a good agreement between data and MC.

- **Classification between converted and unconverted photons**, a worse conversion reconstruction efficiency in data with respect to MC would lead to global loss in the total identification efficiency, since the selection cuts for unconverted photons are generally tighter than the corresponding ones for converted photons. This effect was studied changing the converted photons efficiency by 10%.

- **EM scale uncertainty**, the impact of the EM scale uncertainty was addressed by varying $\pm 3\%$ all the selection variables affected. The cluster energy, the isolation energy and the shower shapes affected by this re-scaling(e.g. ΔE and R_{had}) were shifted by these values and the PID efficiency was then re-computed. This effect was found to be negligible.

The systematic uncertainties described above on the offline photon identification are shown in the Table 6.11.

Considerations about the $|\eta| \geq 1.81$ region

As shown in the Table 6.11, the offline identification efficiency values in the region at $|\eta| \geq 1.81$ suffers of the largest impact of the data-driven candidate-by-candidate MC correction, because of a larger data/MC discrepancies due to non optimal cut values applied to the identification variables in this pseudorapidity region (as an example, some trigger cuts were too tight and we could not have the offline correct cuts).

The large value of the correction (about 10 %) as compared to the region $|\eta| < 1.81$ (about $3 - 5\%$), associated with the larger systematic uncertainty associated to the correction itself, suggest to avoid the use of the region $|\eta| \geq 1.81$ for the inclusive cross section measurement at the time of this analysis, and to postpone it to when one will have a more reliable estimate of the offline identification efficiency. Another check done [103] showing a larger uncertainty in this last η region was to compare the predicted converted photons efficiencies from electrons from $W's$ and the nominal modified tight efficiency computed for converted photons. The results are shown in Figure 6.20 and one sees that in the last bin there are larger differences.

E_T GeV	$\sigma^{\text{MC corr}}$	$\sigma^{\text{material}}_{\text{PID}}$	$\sigma^{\text{LAr gain}}_{\text{PID}}$	$\sigma^{\text{hard/brem}}_{\text{PID}}$	$\sigma^{\text{Pythia/Herwig}}_{\text{PID}}$	$\sigma^{\text{pile-up}}_{\text{PID}}$	$\sigma^{\text{worse conv reco}}$
$\lvert\eta\rvert < 0.6$							
$[15, 20)$	4.5 %	4.4 %	0.5 %	1.5 %	1.0 %	0.4 %	0.6 %
$[20, 25)$	3.6 %	4.4 %	0.5 %	1.5 %	1.0 %	0.4 %	1.0 %
$[25, 30)$	3.5 %	3.4 %	0.5 %	1.5 %	1.0 %	0.4 %	1.1 %
$[30, 35)$	2.9 %	2.7 %	0.5 %	1.5 %	1.0 %	0.4 %	1.1 %
$[35, 40)$	2.4 %	2.2 %	0.5 %	1.5 %	1.0 %	0.4 %	1.0 %
$[40, 50)$	1.9 %	1.5 %	0.5 %	1.5 %	1.0 %	0.4 %	1.2 %
$[50, 60)$	2.1 %	0.2 %	0.5 %	1.5 %	1.0 %	0.4 %	1.3 %
$[60, 100)$	1.1 %	0.1 %	0.5 %	1.5 %	1.0 %	0.4 %	1.3 %
$0.6 < \lvert\eta\rvert < 1.37$							
$[15, 20)$	4.8 %	4.4 %	0.5 %	1.5 %	1.0 %	0.4 %	1.2 %
$[20, 25)$	4.7 %	4.4 %	0.5 %	1.5 %	1.0 %	0.4 %	1.3 %
$[25, 30)$	4.0 %	3.4 %	0.5 %	1.5 %	1.0 %	0.4 %	1.2 %
$[30, 35)$	3.2 %	2.7 %	0.5 %	1.5 %	1.0 %	0.4 %	1.3 %
$[35, 40)$	3.0 %	2.2 %	0.5 %	1.5 %	1.0 %	0.4 %	1.1 %
$[40, 50)$	2.5 %	1.5 %	0.5 %	1.5 %	1.0 %	0.4 %	0.9 %
$[50, 60)$	1.9 %	0.2 %	0.5 %	1.5 %	1.0 %	0.4 %	0.8 %
$[60, 100)$	1.7 %	0.1 %	0.5 %	1.5 %	1.0 %	0.4 %	0.5 %
$1.52 < \lvert\eta\rvert < 1.81$							
$[15, 20)$	4.6 %	6.3 %	1.0 %	1.5 %	1.0 %	1.2 %	2.0 %
$[20, 25)$	4.5 %	6.4 %	1.0 %	1.5 %	1.0 %	1.2 %	1.7 %
$[25, 30)$	2.7 %	5.3 %	1.0 %	1.5 %	1.0 %	1.2 %	1.6 %
$[30, 35)$	2.4 %	4.5 %	1.0 %	1.5 %	1.0 %	1.2 %	1.7 %
$[35, 40)$	2.1 %	3.5 %	1.0 %	1.5 %	1.0 %	1.2 %	1.5 %
$[40, 50)$	1.5 %	3.4 %	1.0 %	1.5 %	1.0 %	1.2 %	1.2 %
$[50, 60)$	0.8 %	2.2 %	1.0 %	1.5 %	1.0 %	1.2 %	1.2 %
$[60, 100)$	1.3 %	1.0 %	1.0 %	1.5 %	1.0 %	1.2 %	0.1 %
$1.81 < \lvert\eta\rvert < 2.37$							
$[15, 20)$	4.3 %	6.3 %	1.0 %	1.5 %	1.0 %	1.2 %	1.8 %
$[20, 25)$	5.5 %	6.4 %	1.0 %	1.5 %	1.0 %	1.2 %	2.1 %
$[25, 30)$	6.5 %	5.3 %	1.0 %	1.5 %	1.0 %	1.2 %	2.3 %
$[30, 35)$	5.4 %	4.5 %	1.0 %	1.5 %	1.0 %	1.2 %	2.3 %
$[35, 40)$	4.9 %	3.5 %	1.0 %	1.5 %	1.0 %	1.2 %	2.2 %
$[40, 50)$	4.2 %	3.4 %	1.0 %	1.5 %	1.0 %	1.2 %	1.8 %
$[50, 60)$	3.6 %	2.2 %	1.0 %	1.5 %	1.0 %	1.2 %	2.1 %
$[60, 100)$	3.2 %	1.0 %	1.0 %	1.5 %	1.0 %	1.2 %	0.9 %

Table 6.11: Contributions to the overall systematic uncertainty on the offline photon identification efficiency used for the inclusive photon cross section measurement, and total systematic uncertainty in the different η and p_T bins used in the study [32, 103].

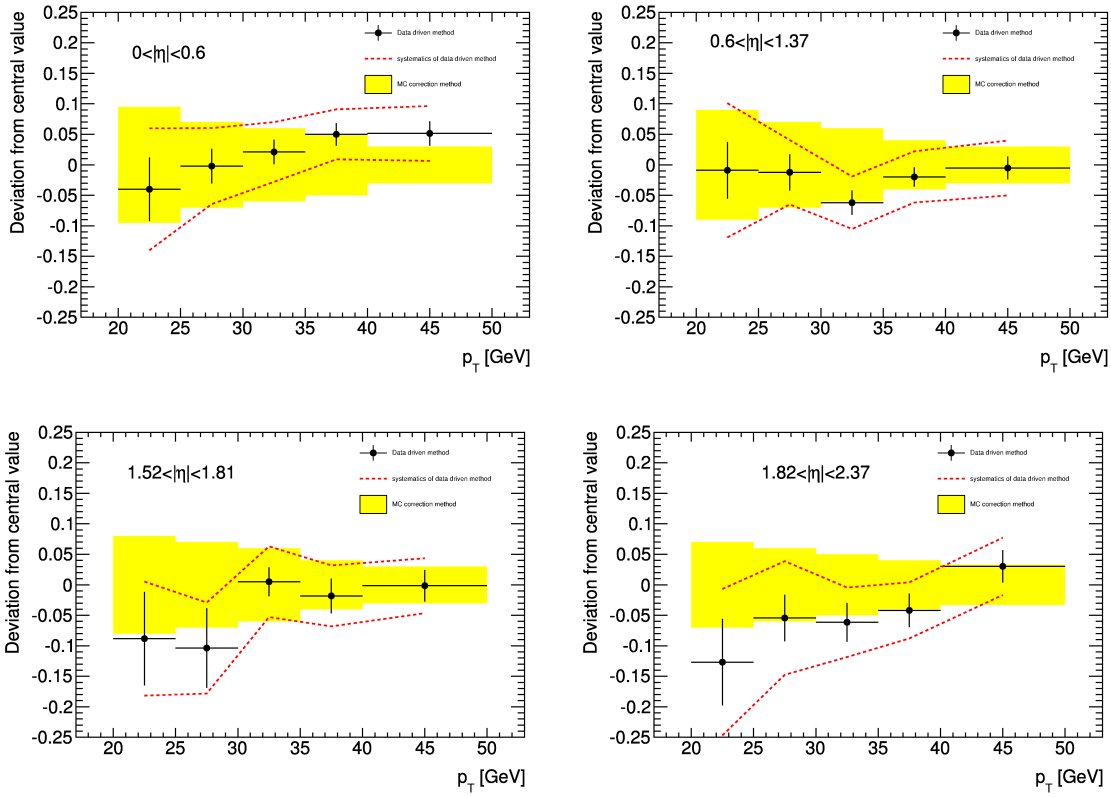


Figure 6.20: Comparison between the predicted converted photons efficiencies from electrons and the nominal modified tight efficiency discussed at the beginning of Section 6.5.1 for converted photons. The yellow bands account for the sum of the systematic errors discussed in this Section. The errors on the black points are statistical only, while the red lines represent the quadratic sum of statistical and systematic errors on the efficiency extrapolated from the W electrons [103].

Chapter 7

Measurement of the Purity of the Direct Photon Samples

The photon identification strategy, already discussed in the Section 6.5, is optimized to provide a high efficiency for signal photons. However, these selection criteria do not reject all the background. In addition, as the simulation cannot be trusted to predict accurately the fake rate, a data driven method is used to estimate the background and extract the prompt photon signal. The method employed to compute the fraction of signal [1] (2D sidebands method) relies on the use of the isolation variable and of the shower shape variables based on the energy measurement in the first layer of the electromagnetic calorimeter. A variant of this method based on isolation templates has also been developped. It will not be described here but can be found in [19].

7.1 Two-dimensional sidebands method

The main features of the two-dimensional (2D) sidebands method are that no precise knowledge of the signal is required, and that the background properties are deduced from observed data, where one can use simulation only for second-order corrections to the results. A detailed discussion of this method is presented in the followings Subsections.

7.1.1 Description of the method

This method extrapolates the background rate from "control regions", dominated by background, into a "signal region", which contains a mixture of signal and background. In this case, the two dimensions are defined by the isolation on one axis, and the "tightness" of the photon candidate on the other axis (see Figure 7.1). One defines the signal region as the region with isolated candidates (isolation energy lower than 3 GeV) passing the tight identification criteria, called N_A, and three background enriched regions, N_B non-isolated candidates (isolation energy greater than 5 GeV) passing the shower shape

[1] In a data sample for a centre-of-mass energy collision of $\sqrt{s} = 7$ TeV and 0.88 pb^{-1} of integrated luminosity of 2010 LHC runs.

requirements [2], N_C and N_D (candidates failing the shower shape criteria and which are respectively isolated or non-isolated (the criterion that defined the ID cuts choice of N_C and N_D background control regions is explained in the Subsection 7.1.2). A two dimensional plane is illustrated in Figure 7.1. The intermediate region ($3 <$ isolation < 5 GeV) is ignored.

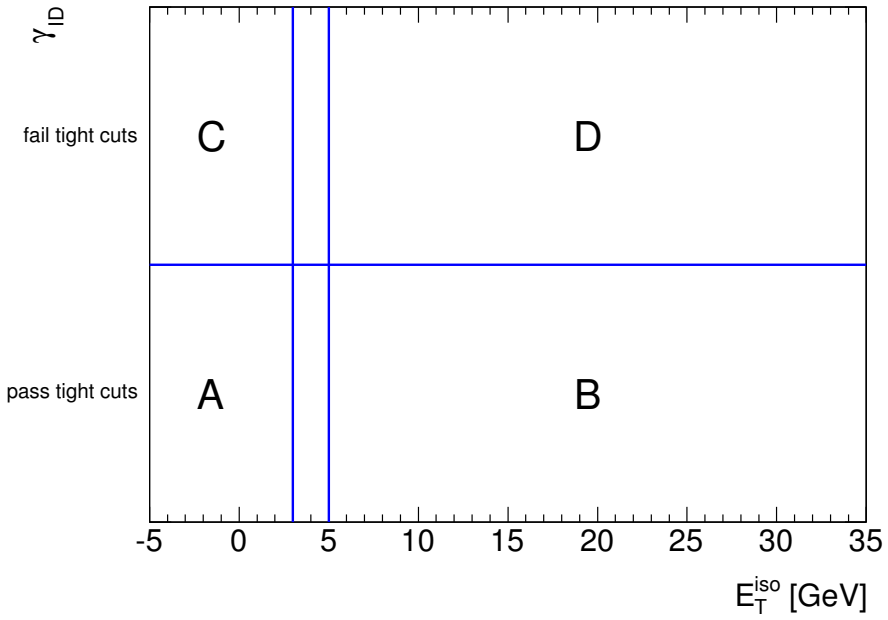


Figure 7.1: Illustration of the two-dimensional plane, defined by means of the isolation and a subset of the photon identification (ID) variables, from the observed yields N_B, N_C and N_D in the three control regions, the background yield in the signal region were the observed total signal yield is N_A. Sketch and caption are taken from [19].

This technique relies on two assumptions:

- The signal contamination in the three background regions is negligible.
- The ratio of isolated to non-isolated background candidates in the non-tight bin $\left(\frac{N_D^{\text{bkg}}}{N_C^{\text{bkg}}}\right)$ is equal to the same ratio in the tight bin $\left(\frac{N_B^{\text{bkg}}}{N_A^{\text{bkg}}}\right)$. (i.e. no correlation between the background isolation and the shape of the DVs of photon ID in the cells of the first layer).

Using these two assumptions, the signal yield (N_A^{sig}) and purity (P) can be calculated with only those four numbers:

$$N_A^{\text{sig}} = N_A - N_B \frac{N_C}{N_D} \tag{7.1}$$

[2] it means, passing the tight selection criteria

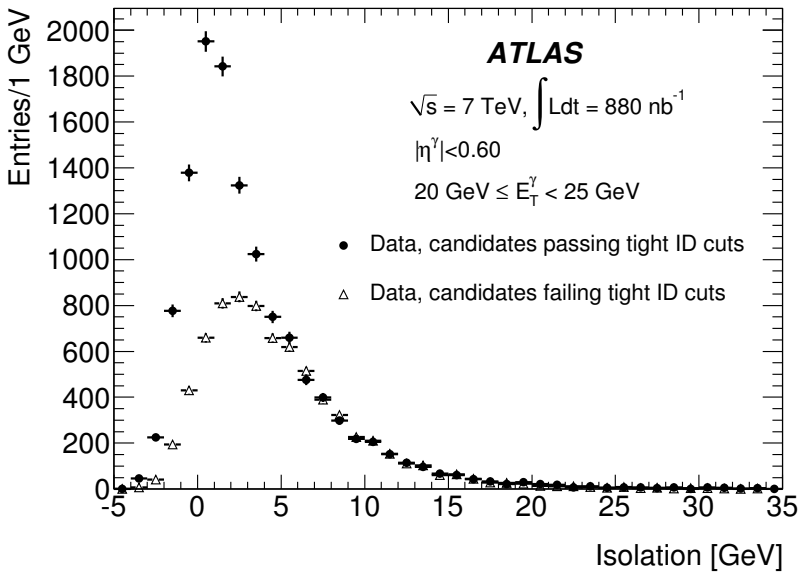


Figure 7.2: The distributions for the calorimetric isolation variable $E_T^{(R<0.4)}$, for tight (solid dots) and non-tight (open triangles) candidates. The latter is normalized to the former in the non-isolated region $E_T^{(R<0.4)} > 5$ GeV. The excess of tight candidates over the normalized non-tight candidates in the isolated region $E_T^{(R<0.4)} < 3$ GeV proves the evidence of a signal. [30]

$$P = 1 - \frac{N_B}{N_A}\frac{N_C}{N_D} \tag{7.2}$$

Figure 7.2 shows the application of this method. The distribution of $E_T^{(R<0.4)}$ for the non-tight candidates is normalized to that of tight candidates, in the non-isolated region ${E_T}^{(R<0.4)} > 5$GeV (i.e. it is scaled by the N_B/N_D factor): the agreement between the two shapes reinforce the two assumptions that a good background estimation can be obtained from the non-tight sample, and that the non-isolated regions are fairly free of signal. In the isolated region ${E_T}^{(R<0.4)} < 3$GeV, a clear excess of tight over normalized non-tight candidates puts in evidence the presence of a photon signal. The difference between tight and normalized non-tight candidates is considered as a measurement of the signal yield in the signal region.

7.1.2 Correction for signal and background correlation

Signal leakage in the control regions

The presence of signal in the control regions is not completely negligible. However, it is small and this was checked using the prompt photon Monte Carlo sample produced with `PYTHIA`: the ratio between the signal in each control region **B, C, D** and the one in the

signal region **A**,

$$c_{\mathbf{i}} = \frac{N_{\mathbf{i}}^{\mathrm{sig}}}{N_{\mathbf{A}}^{\mathrm{sig}}} \qquad \text{with} \qquad \mathbf{i} = \mathbf{B}, \mathbf{C}, \mathbf{D}. \tag{7.3}$$

may be as large as $\approx 5\%$ [68]. The complete set of values are displayed in Table 7.1. As was already mentioned this is then a small correction to the background extraction, which can anyway be taken into account explicity in the formula for the estimated signal yield and purity.

E_T range	$\eta_{s2} \in [0.00, 0.60)$			$\eta_{s2} \in [0.60, 1.37)$			$\eta_{s2} \in [1.52, 1.81)$			$\eta_{s2} \in [1.81, 2.37)$		
[GeV]	$c_{\mathbf{B}}$	$c_{\mathbf{C}}$	$c_{\mathbf{D}}$	$c_{\mathbf{B}}$	$c_{\mathbf{C}}$	$c_{\mathbf{D}}$	$c_{\mathbf{B}}$	$c_{\mathbf{C}}$	$c_{\mathbf{D}}$	$c_{\mathbf{B}}$	$c_{\mathbf{C}}$	$c_{\mathbf{D}}$
$[15; 20)$	0.03	0.12	0.00	0.03	0.14	0.00	0.04	0.07	0.01	0.03	0.14	0.01
$[20; 25)$	0.04	0.08	0.00	0.05	0.09	0.01	0.06	0.06	0.01	0.04	0.10	0.01
$[25; 30)$	0.05	0.06	0.00	0.05	0.06	0.01	0.08	0.05	0.01	0.05	0.08	0.01
$[30; 35)$	0.06	0.04	0.00	0.06	0.05	0.01	0.08	0.04	0.01	0.07	0.07	0.01
$[35; 40)$	0.07	0.04	0.01	0.08	0.04	0.01	0.10	0.04	0.01	0.07	0.06	0.01
$[40; 50)$	0.08	0.03	0.00	0.10	0.03	0.01	0.11	0.03	0.02	0.08	0.05	0.01
$[50; 60)$	0.10	0.03	0.01	0.12	0.03	0.01	0.17	0.05	0.01	0.11	0.05	0.01
$[60; 100)$	0.14	0.02	0.01	0.14	0.03	0.01	0.17	0.03	0.05	0.14	0.04	0.02

$c_{\mathbf{B}}$: leakage to tight, non-isolated region,
$c_{\mathbf{C}}$: leakage to non-tight, isolated region,
$c_{\mathbf{D}}$: leakage to non-tight, non-isolated region.

Table 7.1: Fractions of signal leaking into the three control regions, as predicted by `PYTHIA`, for all η_{s2} and E_T regions. Errors are always < 0.01 [30].

The choice of the non-tight region

The choice of the shower shape variable to be used for the definition of the background control regions is driven by the main criteria of minimize correlations between the isolation variable and the first layer variables. One would prefer to apply a cut reversal [3] only using the cuts on a small subset of shower shape variables that are less correlated with isolation in the background enriched samples. The better choice would therefore be to revert the selection criteria on the two variables F_{side} and $w_{s\,3}$, which are evaluated in a narrower η region. Reversing the cuts on these two only would be too similar to the one of the signal, and suffering from statistics. Conversely, $w_{s\,\mathrm{tot}}$ makes use of the largest η region, therefore showing more residual correlation with $E_T^{R<0.4}$. A reasonable tradeoff has been found by reverting the requirements on four of the five shower shape variables (all except $w_{s\,\mathrm{tot}}$) for defining the background control regions.

[3] By "cut reversal" it is intended the following: a photon candidate must pass the `Photon Loose` selection, but fail the `Photon RobustTight` selection for at least one of the chosen variables. Several examples are shown in Figure 7.3

Even with this configuration, Monte Carlo studies suggest the presence of a residual correlation of the background, which manifests itself as a difference in the background $E_T^{R<0.4}$ distributions for the tight and non-tight regions. As a consequence, the quantity

$$R = \frac{N_A^{\text{bkg}}}{N_B^{\text{bkg}}} \frac{N_D^{\text{bkg}}}{N_C^{\text{bkg}}} \tag{7.4}$$

may show substantial deviations from 1. The predicted values from 50 million PYTHIA JF17 ("jet-jet filtered at $p_T > 17$ GeV") events, are shown as an example in the Figure 7.3(blue dots) in different E_T bins and integrated over the full pseudorapidity range. In addition, the R quantity (Equation 7.4) was also computed for the four different pseudorapidities regions considered in this study as a function of E_T in Figure 7.6(blue dots).

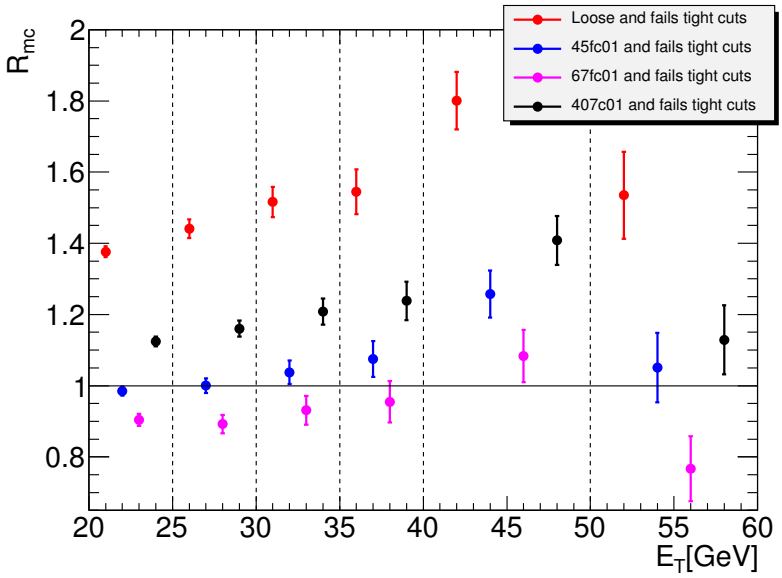


Figure 7.3: The pseudo-correlation factor (R_{mc}) for background between isolation and the chosen non-tight region are shown for different configurations of cut reversal (*see footnote 3 of the preceding page*) in the first layer shower shapes, computed as a function of E_T for photon candidates in the full pseudorapidity range. In this plot the background photon identification control region is the standard loose selection (represented by a red point) or obtained by reversing the tight identification criteria on two strip variables($F_{\text{side}}, w_{s\,3}$), or four strip variables ($F_{\text{side}}, w_{s\,3}, \Delta E, E_{\text{ratio}}$) or on the five strip variables shown in magenta, blue and black points respectively.

2D sidebands formula taking into account both signal leakage and background correlations

Since both the background correlation from the simulation and the signal leakage in the background control regions are found to be small but not negligible, they are taken

into account in the background determination. The signal leakage in the three control regions is included by replacing, in Equation 7.1, the observed data yields with the yields corrected for the expected signal contribution, $N_B \to N_B - c_{\mathbf{B}} N_A^{sig}$, $N_C \to N_C - c_{\mathbf{C}} N_C^{sig}$, $N_D \to N_D - c_{\mathbf{D}} N_D^{sig}$, and solving the resulting second order polynomial equation for N_A^{sig}. The correlations between the isolation and the shower shape variables are taken into account by correcting the estimated background yield in the signal region by the ratio between the true ($N_A^{\rm bkg}$) and the estimated $\left(N_B^{\rm bkg}\frac{N_C^{\rm bkg}}{N_D^{\rm bkg}}\right)$ background yield, obtained from simulated background events. The two corrections can be applied simultaneously in order to obtain the final measurement of the signal yield and purity in the signal region. Thus, Equations 7.1 and 7.2 become

$$N_A^{\rm sig} = N_A - \left[\left(N_B - c_{\mathbf{B}} N_A^{\rm sig}\right)\frac{\left(N_C - c_{\mathbf{C}} N_A^{\rm sig}\right)}{\left(N_D - c_{\mathbf{D}} N_A^{\rm sig}\right)}\right]\left(\frac{N_A^{\rm bkg}}{N_B^{\rm bkg}}\frac{N_D^{\rm bkg}}{N_C^{\rm bkg}}\right) \tag{7.5}$$

$$P = \frac{N_A^{\rm sig}}{N} \tag{7.6}$$

The usefulness of the correlation deduced from Monte Carlo can be hinted [90] from a study of differences of purity relaxing the cuts, either going to loose or relaxing four strip variables: the difference is smaller if the Monte Carlo correlation factor is taken into account as seen in Figure 7.4.

The background correlation in the used data sample

The Monte Carlo prediction for the $R^{\rm bkg}$ (from Equation 7.4) does not show a clear trend as a function of E_T, which does not help in diagnosing what to do.

In addition, there is no way to get a handle on the measure of $R^{\rm bkg}$ from data, where it is impossible to disentangle the signal component in region **A**. Therefore a similiar quantity is defined across the four regions **A', B', C'** and **D'**, located in a very non-isolated region, which is assumed to be completely *signal-free* (see Figure 7.5). The quantity:

$$R' = \frac{N_{\mathbf{A'}}^{\rm obs}}{N_{\mathbf{B'}}^{\rm obs}}\frac{N_{\mathbf{D'}}^{\rm obs}}{N_{\mathbf{C'}}^{\rm obs}} \tag{7.7}$$

which can be measured both on data and Monte Carlo samples, thus having a check on the reliability of the simulation. The R' values are displayed in Figure 7.6, for Monte Carlo (red dots) and data (black triangles). The statistical errors are large, making it difficult to draw concrete conclusions. One may observe that:

- R' shows compatibility between data and Monte Carlo (black triangles vs red dots), apart maybe for the region $0.60 \leq |\eta_{s2}| < 1.37$.
- R' for data (black triangles) do not show strong evidence of deviation from 1, apart maybe for the region $0.60 \leq |\eta_{s2}| < 1.37$. For Monte Carlo (red dots) the deviations seem only a little bit more evident.

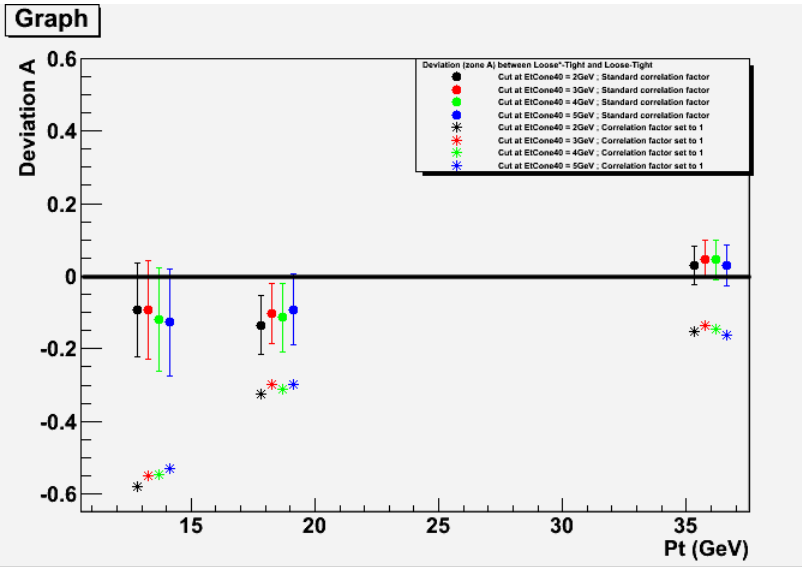


Figure 7.4: Differences in photon purity in data between cases where the background photon identification control region is taken from: the standard loose and if it is obtained by reversing the tight identification criteria on four strip variables ($F_{side}, w_{s3}, \Delta E, E_{ratio}$). The isolation transverse energy cut have been varied between 2, 3, 4 and 5 GeV, indicated by black, red, green and blue colors respectively. Points corresponds to the deviation considering the pseudo-correlation factor different to one in Equation 7.6, whereas stars mean the deviations assuming no correlation hypothesis, pseudo-correlation factor equal to one. For these computations a simulated `PYTHIA` Minimum Bias sample was used.

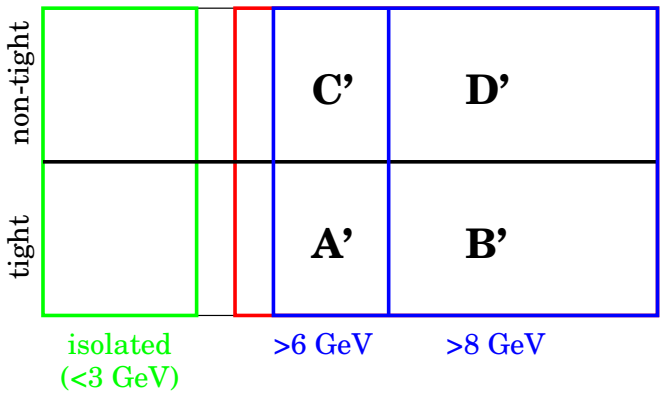
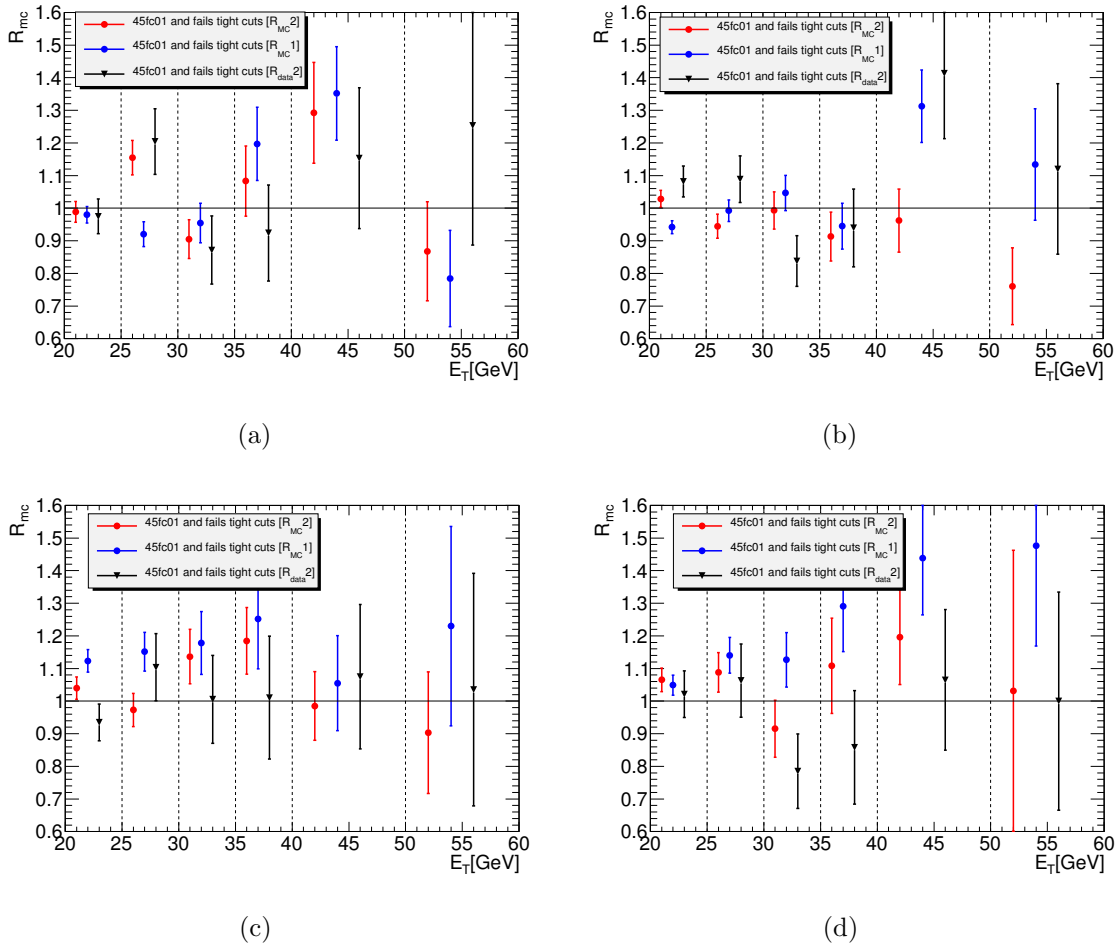


Figure 7.5: The four zones **A',B',C'** and **D'** in a very non-isolated region are used to validate the Monte Carlo prediction on possible distortions of the background isolation, between the tight and non-tight samples.

- On Monte Carlo, R^{bkg} (blue dots) values are a little bit larger than R' values (but there is a clear lack of statistics), therefore there is no way to infer R^{bkg} from data.



(a) (b)

(c) (d)

Figure 7.6: R-factors as functions of E_T, for each $|\eta_{s2}|$ zone. The blue dots are the values of R^{bkg} (computed with Equation 7.4), as predicted by 50 millions `PYTHIA` JF17 Monte Carlo events. The red dots are the R' values (see Equation 7.7) on the same Monte Carlo sample, while the black dots are the R' values are evaluated from data. The figures (a), (b), (c) and (d) are corresponding to the pseudoradidity regions $|\eta_{s2}| < 0.6$, $0.6 \leq |\eta_{s2}| < 1.37$, $1.52 \leq |\eta_{s2}| < 1.81$ and $1.81 \leq |\eta_{s2}| < 2.37$ respectively. Errors are statistical.

A simple correction for R^{bkg} on observed data would produce scattering in the purity profiles due to the too small statistics of the Monte Carlo when η bins are done. Therefore it has been chosen to evaluate N_A^{sig} assuming $R^{\text{bkg}} = 1$ in Equation 7.5, and the deviations from such values are accounted for as systematic errors.

7.2 Purity results and systematic uncertainties

This section summarizes how the various contributions to the signal yield systematic uncertainties and central values for the photon signal fraction have been evaluated, when the photon data sample satisfies the preselection described at the beginning of the Section 6.5.

7.2.1 Results from the 2D sidebands method

The isolated prompt photon purity measured, as a function of the photon reconstructed transverse energy, is shown in Figure 7.7. The purity and the estimated signal yield in each pseudorapidity and E_T bin are also summarized in Table 7.2. Both Figure 7.7 and Table 7.2 include also the systematic uncertainties on the measured purity and signal yields. The evaluation of these uncertainties is described in detail in the next Subsection 7.2.2.

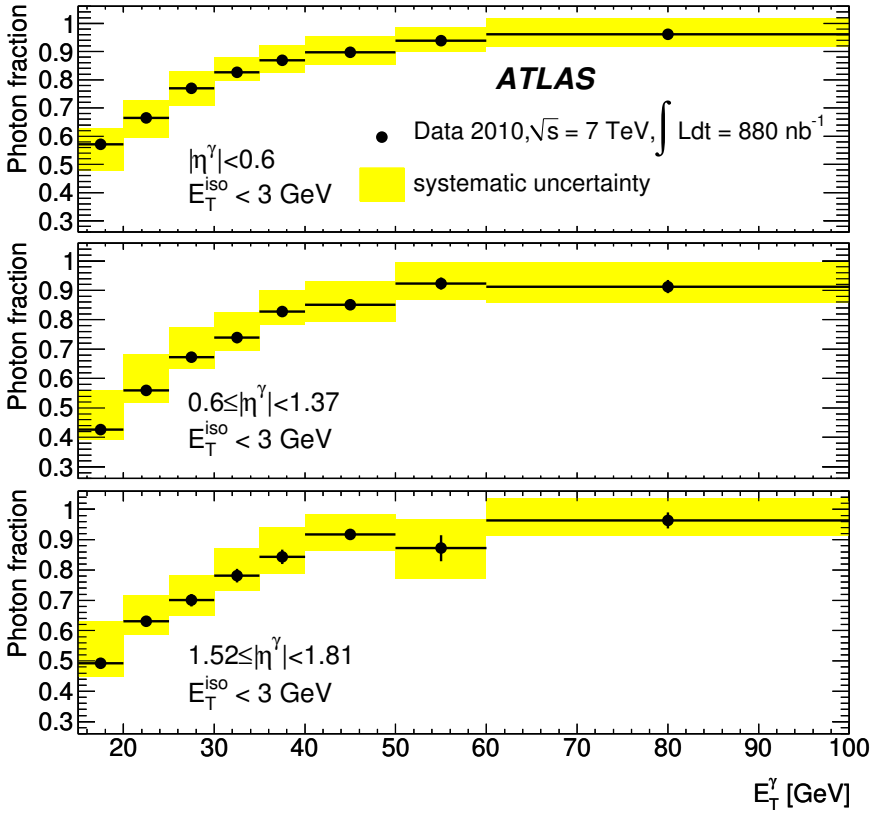


Figure 7.7: Fraction of isolated prompt photons as a function of the photon transverse energy, as obtained with the 2D sideband method [19].

E_T [GeV]	N_{sig}	stat	syst	*Purity* [%]	stat [%]	syst [%]
			$\|\eta\| < 0.6$			
[15, 20)	11964	±254	$^{+1180}_{-1979}$	57.1	±1.0	$^{+5.6}_{-9.5}$
[20, 25)	5014	±125	$^{+468}_{-530}$	66.5	±1.2	$^{+6.2}_{-7.1}$
[25, 30)	2577	±73	$^{+202}_{-205}$	76.9	±1.2	$^{+6.1}_{-6.1}$
[30, 35)	1461	±50	$^{+88}_{-57}$	82.7	±1.4	$^{+5.0}_{-3.2}$
[35, 40)	815	±35	$^{+49}_{-41}$	86.9	±1.5	$^{+5.3}_{-4.4}$
[40, 50)	767	±33	$^{+49}_{-37}$	89.7	±1.4	$^{+5.7}_{-4.2}$
[50, 60)	329	±20	$^{+17}_{-14}$	93.8	±1.6	$^{+4.8}_{-3.9}$
[60, 100)	329	±20	$^{+19}_{-15}$	96.2	±1.7	$^{+5.7}_{-4.4}$
			$0.6 < \|\eta\| < 1.37$			
[15, 20)	12989	±395	$^{+4017}_{-1079}$	42.7	±1.2	$^{+13.1}_{-3.6}$
[20, 25)	5782	±175	$^{+1252}_{-453}$	55.9	±1.4	$^{+12.2}_{-4.3}$
[25, 30)	3057	±98	$^{+459}_{-180}$	67.3	±1.5	$^{+10.1}_{-4.0}$
[30, 35)	1605	±63	$^{+188}_{-94}$	73.9	±1.8	$^{+8.6}_{-4.3}$
[35, 40)	1024	±43	$^{+86}_{-59}$	82.8	±1.9	$^{+7.0}_{-4.7}$
[40, 50)	982	±41	$^{+93}_{-67}$	85.2	±1.8	$^{+8.0}_{-5.9}$
[50, 60)	420	±24	$^{+33}_{-25}$	92.3	±2.0	$^{+7.1}_{-5.5}$
[60, 100)	373	±23	$^{+34}_{-23}$	91.2	±2.2	$^{+8.3}_{-5.6}$
			$1.52 < \|\eta\| < 1.81$			
[15, 20)	7224	±221	$^{+2010}_{-660}$	49.3	±1.3	$^{+13.7}_{-4.6}$
[20, 25)	3038	±101	$^{+400}_{-228}$	63.1	±1.5	$^{+8.4}_{-4.7}$
[25, 30)	1345	±59	$^{+159}_{-100}$	70.0	±2.0	$^{+8.3}_{-5.1}$
[30, 35)	731	±38	$^{+83}_{-46}$	78.1	±2.3	$^{+9.0}_{-4.9}$
[35, 40)	441	±27	$^{+51}_{-28}$	84.4	±2.4	$^{+9.6}_{-5.5}$
[40, 50)	378	±22	$^{+27}_{-21}$	91.7	±1.8	$^{+6.7}_{-5.1}$
[50, 60)	147	±16	$^{+16}_{-17}$	97.2	±4.3	$^{+9.5}_{-10.0}$
[60, 100)	154	±12	$^{+12}_{-8}$	96.4	±2.6	$^{+7.3}_{-5.0}$
			$1.81 < \|\eta\| < 2.37$			
[15, 20)	8568	±276	$^{+1347}_{-1431}$	49.2	±1.4	$^{+7.8}_{-8.2}$
[20, 25)	3926	±132	$^{+579}_{-484}$	61.7	±1.6	$^{+9.2}_{-7.6}$
[25, 30)	2058	±71	$^{+224}_{-159}$	75.2	±1.6	$^{+8.2}_{-5.7}$
[30, 35)	1093	±48	$^{+117}_{-87}$	79.1	±2.0	$^{+8.4}_{-6.4}$
[35, 40)	615	±34	$^{+61}_{-49}$	81.0	±2.5	$^{+8.0}_{-6.4}$
[40, 50)	619	±35	$^{+70}_{-53}$	81.3	±2.6	$^{+9.2}_{-6.9}$
[50, 60)	277	±20	$^{+27}_{-22}$	90.7	±2.7	$^{+8.8}_{-7.3}$
[60, 100)	264	±19	$^{+31}_{-24}$	91.7	±2.8	$^{+10.7}_{-8.2}$

Table 7.2: Observed signal yields and purities as obtained from the 2D sidebands counting method. The photons are required to be reconstructed in the pseudorapidity range shown in the Table. The statistical uncertainty on the signal yield includes the contribution from Poisson fluctuations of the various components of Equations 7.5 and 7.6 [32].

7.2.2 Systematic uncertainties on the 2D sidebands method

The main sources of systematic uncertainties are listed below [30]:

- **Background non-tight control regions**: the non-tight definition may be varied, by reversing `RobustTight` cuts on two variables only ($w_{s\,3}, F_{\rm side}$) or on five variables ($w_{s\,3}, F_{\rm side}, \Delta E, E_{\rm ratio}, w_{s\,\rm tot}$) — instead of the four standard variables. The systematic effect on the purity is typically around ±3%.
- **Background in non-isolated control region**: the lower boundary for $E_T^{R<0.4}$ may be varied from the standard 5 GeV value to 4 GeV or 6 GeV. An upper boundary may also be introduced, equal to 10 or 15 GeV (by default no upper boundary is used). The effects of these variations on the purity are usually less than ±1%.
- **Signal leakage into control regions**: this amount is estimated from Monte Carlo, for both the non-tight and non-isolated regions. However, it is a known issue that the Monte Carlo does not model correctly the shower shape, being generally broader in the real data. For this reason, the nominal efficiency of `RobustTight` cuts is lowered by 5% (absolute), making the leakage to the non-tight region larger. Moreover, the mixture of hard/fragmentation photons is changed, up to the extreme conditions of pure hard photons and pure fragmentation photons. The overall effect of these changes on the purity ranges from ±3% to ±5%.
- **Signal event simulation**: the purity measurement has been repeated using samples simulated with `HERWIG` and `PYTHIA` to estimate the fraction of signal leaking into the three background control regions.
- **Background correlations**: The introduction of $R^{\rm bkg}$ correction into Equation 7.6 would yield higher/lower purity values, whether $R^{\rm bkg}$ be lower/higher than 1. Since the values of $R^{\rm bkg}$ oscillate significantly and have large errors, it has been chosen to quote only average effects in each η_{s2} region, by averaging through the full E_T interval. Calling P_0 and $P_R \pm \sigma_{P_R}$ the purities evaluated without and with the $R^{\rm bkg}$ correction (where σ_{P_R} comes from the uncertainty of $R^{\rm bkg}$), a weighted average is evaluated for all $\Delta P = (P_R - P_0) \pm \sigma_{P_R}$ in the same η_{s2} region, and the sum of this average and its uncertainty is quoted as systematic. The effect is $< 0.5\%$ for each of the Barrel regions, and $\sim 3.5\%$ for each of the Endcap regions.

The various systematic uncertainty sources and the corresponding uncertainties on the signal yield are summarized in the Table 7.3 (the values for last η bin are only illustrative and have not been used in the paper [19]). One can note that for converted photons there is another method to study purity, looking at p_T/E_T of conversion. Figure 7.8 shows [4, 56] the distribution of the data (for double track conversions starting in the Silicium detector and an integrated luminosity of 62 nb^{-1}) superimposed to Monte Carlo for direct photon signal and background. One sees that the purity is very large. However this method was not used in a quantitative way here.

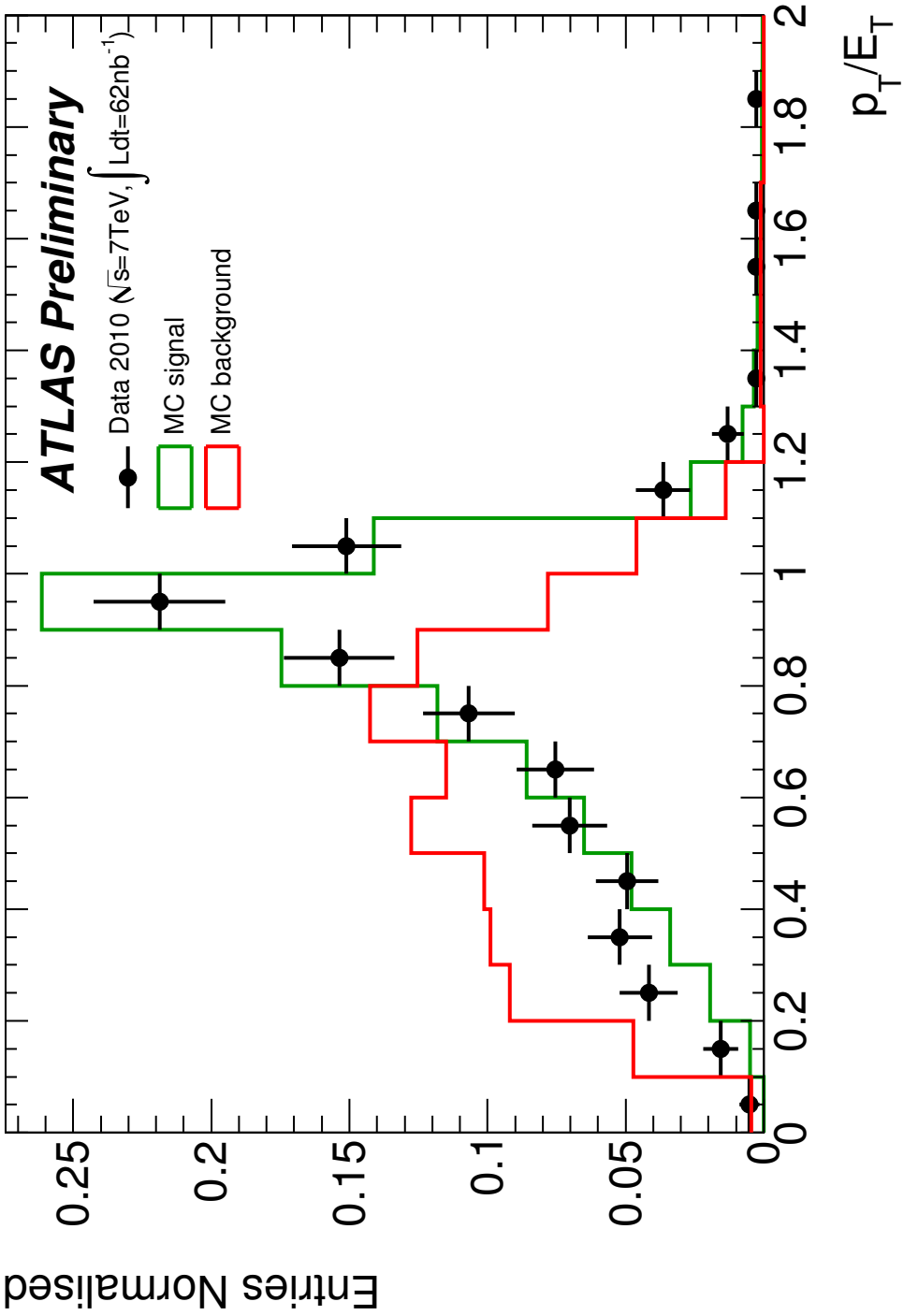


Figure 7.8: p_T/E_T for converted photon candidates. Signal and background MC are represented in lines green and red respectively, while data is shown in black points. This plot was performed with 62 nb^{-1} of integrated luminosity. Converted photons candidates were required to pass the following selection: two-tracks reconstructed conversions (having hits in the Silicium detector), p_T bigger than 20 GeV, $E_T^{R<0.4} < 3$ GeV. This plot was taken from [4].

E_T [GeV]	tight-ID ctrl-region	isolation ctrl-region	leakage in non-iso region	HERWIG vs PYTHIA	leakage in non-ID region	Background correlation
			$\lvert\eta\rvert < 0.6$			
[15, 20)	$^{+766}_{-1842}$	$^{+282}_{-348}$	$^{+587}_{-364}$	± 156	$^{+592}_{-489}$	± 84
[20, 25)	$^{+306}_{-465}$	$^{+39}_{-43}$	$^{+286}_{-175}$	± 76	$^{+189}_{-159}$	± 30
[25, 30)	$^{+118}_{-164}$	$^{+20}_{-55}$	$^{+142}_{-87}$	± 10	$^{+76}_{-65}$	± 13
[30, 35)	$^{+37}_{-6}$	$^{+9}_{-7}$	$^{+65}_{-39}$	± 0	$^{+46}_{-39}$	± 7
[35, 40)	$^{+15}_{-24}$	$^{+5}_{-6}$	$^{+39}_{-25}$	± 6	$^{+24}_{-20}$	± 4
[40, 50)	$^{+10}_{-13}$	$^{+11}_{-10}$	$^{+39}_{-24}$	± 12	$^{+22}_{-19}$	± 3
[50, 60)	$^{+5}_{-4}$	$^{+2}_{-4}$	$^{+12}_{-8}$	± 4	$^{+9}_{-8}$	± 1
[60, 100)	$^{+1}_{-1}$	$^{+2}_{-1}$	$^{+12}_{-7}$	± 6	$^{+14}_{-11}$	± 1
			$0.6 < \lvert\eta\rvert < 1.37$			
[15, 20)	$^{+3762}_{-198}$	$^{+172}_{-158}$	$^{+769}_{-469}$	± 322	$^{+1108}_{-862}$	± 183
[20, 25)	$^{+1144}_{-250}$	$^{+5}_{-53}$	$^{+323}_{-198}$	± 58	$^{+381}_{-306}$	± 62
[25, 30)	$^{+396}_{-2}$	$^{+21}_{-45}$	$^{+136}_{-84}$	± 20	$^{+183}_{-149}$	± 27
[30, 35)	$^{+141}_{0}$	$^{0}_{-10}$	$^{+76}_{-48}$	± 10	$^{+96}_{-78}$	± 13
[35, 40)	$^{+42}_{0}$	$^{+13}_{-9}$	$^{+36}_{-23}$	± 12	$^{+63}_{-51}$	± 7
[40, 50)	$^{+53}_{-1}$	$^{+5}_{-34}$	$^{+44}_{-27}$	± 13	$^{+60}_{-49}$	± 7
[50, 60)	$^{+9}_{0}$	$^{+1}_{-6}$	$^{+10}_{-6}$	± 4	$^{+29}_{-23}$	± 3
[60, 100)	$^{+18}_{0}$	$^{+2}_{-7}$	$^{+14}_{-9}$	± 7	$^{+23}_{-19}$	± 2
			$1.52 < \lvert\eta\rvert < 1.81$			
[15, 20)	$^{+1854}_{0}$	$^{+75}_{-135}$	$^{+437}_{-266}$	± 84	$^{+426}_{-346}$	± 469
[20, 25)	$^{+301}_{0}$	$^{+3}_{-50}$	$^{+147}_{-90}$	± 60	$^{+143}_{-118}$	± 154
[25, 30)	$^{+109}_{-28}$	$^{+24}_{-27}$	$^{+69}_{-42}$	± 2	$^{+65}_{-53}$	± 61
[30, 35)	$^{+63}_{0}$	$^{+2}_{-4}$	$^{+26}_{-16}$	± 3	$^{+37}_{-30}$	± 30
[35, 40)	$^{+38}_{0}$	$^{+1}_{-6}$	$^{+19}_{-13}$	± 5	$^{+21}_{-17}$	± 17
[40, 50)	$^{+15}_{0}$	$^{+3}_{-7}$	$^{+8}_{-5}$	± 2	$^{+17}_{-14}$	± 13
[50, 60)	$^{+2}_{-10}$	$^{+1}_{-3}$	$^{+10}_{-7}$	± 6	$^{+9}_{-7}$	± 5
[60, 100)	$^{+7}_{0}$	$^{0}_{0}$	$^{+2}_{-1}$	± 0	$^{+7}_{-6}$	± 5
			$1.81 < \lvert\eta\rvert < 2.37$			
[15, 20)	$^{+915}_{-1193}$	$^{+276}_{-69}$	$^{+606}_{-354}$	± 92	$^{+364}_{-304}$	± 627
[20, 25)	$^{+328}_{-327}$	$^{+34}_{-26}$	$^{+373}_{-212}$	± 130	$^{+130}_{-111}$	± 229
[25, 30)	$^{+81}_{-51}$	$^{+10}_{-18}$	$^{+174}_{-101}$	± 23	$^{+53}_{-45}$	± 99
[30, 35)	$^{+19}_{-30}$	$^{+7}_{-14}$	$^{+99}_{-57}$	± 12	$^{+29}_{-25}$	± 50
[35, 40)	$^{+10}_{-18}$	$^{+7}_{-16}$	$^{+49}_{-28}$	± 6	$^{+17}_{-15}$	± 27
[40, 50)	$^{+23}_{-20}$	$^{+1}_{-12}$	$^{+53}_{-30}$	± 14	$^{+24}_{-20}$	± 27
[50, 60)	$^{+5}_{-8}$	$^{+2}_{-3}$	$^{+20}_{-12}$	± 8	$^{+11}_{-9}$	± 11
[60, 100)	$^{+4}_{-4}$	$^{0}_{-8}$	$^{+25}_{-14}$	± 11	$^{+9}_{-8}$	± 10

Table 7.3: Systematic uncertainties, for the different E_T and η_{s2} intervals, on the estimated number of signal photons [32].

7.3 Background from mis-identified electrons

The contamination of the photon sample from isolated electrons is estimated in this section. Prompt electrons with low isolation energy and passing the calorimeter-based `Robust tight` identification criteria may bias the selected photon sample has been evaluated using a purely Monte Carlo based method, which involved counting the number of photon candidates passing the analysis cuts that are matched to true electrons.

7.3.1 Significance of electron contamination

Electrons are produced by two main processes: the dominant one is from hadron decays (mostly from *Heavy Flavors*, called (e_{HF})), the second is from decays of *Electroweak* particles (labelled as (e_{EW}), mainly W, secondarily Z, τ decays). While electrons from the HF are often associated with jets, and are therefore characterized by large $E_T^{R<0.4}$ values, as is shown in the Figure 7.9, those from the latter process are more isolated and therefore more similar to signal photons.

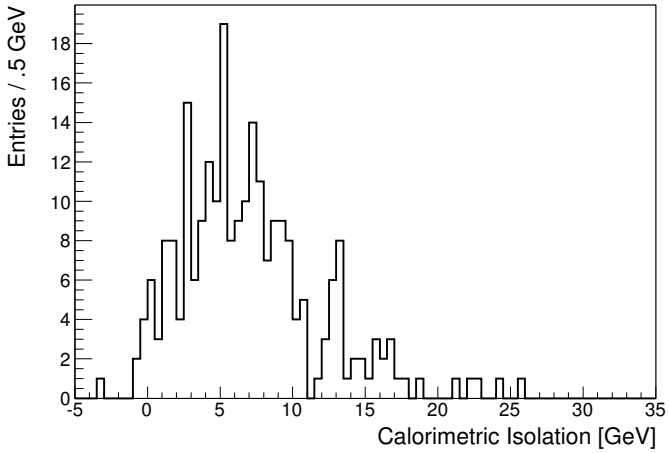


Figure 7.9: Calorimetric isolation for electrons produced in hadron decays, as predicted by the `PYTHIA` JF17 Monte Carlo sample.

The 2D sidebands method discussed in Section 7.1 has been designed to reject jet background and is therefore expected to account for most electrons from hadron decays. To check this, several Monte Carlo tests have been carried out, based on JF17 and JF35 `PYTHIA` samples. First, the existence of a correlation across the four regions A, B, C and D (Figure 7.1), has been checked, by evaluating:

$$R^{e_{\mathrm{HF}}} = \frac{N_A^{e_{\mathrm{HF}}}}{N_B^{e_{\mathrm{HF}}}} \frac{N_D^{e_{\mathrm{HF}}}}{N_C^{e_{\mathrm{HF}}}} \tag{7.8}$$

which has a value compatible with 1 meaning that the heavy flavor background across the four regions is uncorrelated.

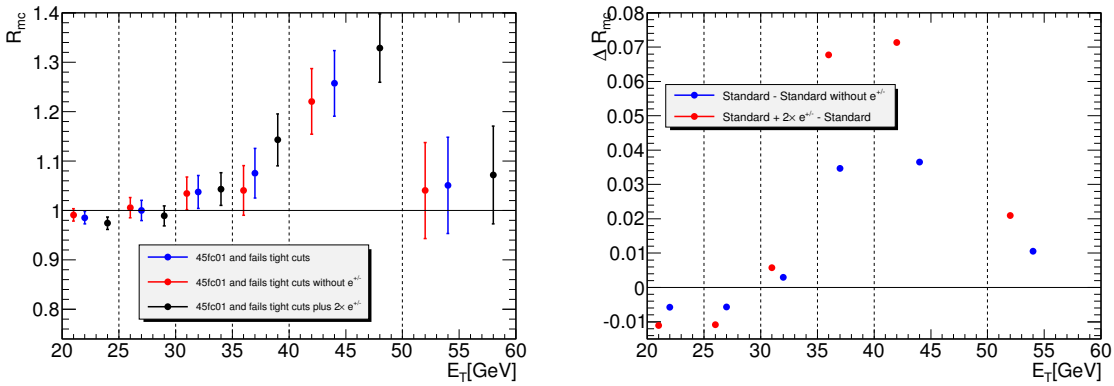


Figure 7.10: Significance of electron contamination on R_{MC} for the Monte Carlo JF17 as a function of p_T with different configurations of electron fractions. In the left plot are shown the R_{MC} with and without electrons, and a configuration where the fraction of electrons was multiplied by a factor 2, in blue, red and black respectively. In the right plot are shown the ΔR_{MC} values of some of the configurations used in the left plot are shown. Errors are statistical only.

One can see in Figure 7.10(**left**) the R_{MC} values for the Monte Carlo JF17 ("jet-jet filtered at $p_T > 17$ GeV") as a function of p_T with and without the electrons, and also multiplying the fraction of electrons by a factor 2 (for heavy flavours it may take into account in a pessimistic way systematic uncertainties).

In Figure 7.10(**right**), one sees the difference of the R_{MC} between a comparition with the default Monte Carlo and without any electron (and also with twice the number of electrons). One sees at low p_T, where the electrons are mainly coming from heavy flavors a systematic negative trend, in agreement with the fact that photon candidates which are electrons coming from heavy flavors are less isolated than normal photon candidates. At high p_T one sees the opposite trend (because photons which are electrons from Z and W are more isolated than normal photon candidates).

In the following Subsection, the characteristics of electrons from both sources are shown, and a contamination from isolated electrons is provided.

Counting Monte Carlo method

In the Table 7.4 the number of photon candidates passing the analysis cuts are shown as well as their contribution from misidentified electrons, for the three `PYTHIA` Monte Carlo samples (JF17, JF35 and JF70. "jet-jet filtered at $p_T > 17$, 35 and 70 GeV, respectively"). One sees a larger fraction for JF35 due to the importance of $W's$ and $Z's$ in this sample.

Meanwhile, in Table 7.5 one of the main characteristic related to the isolation of the electrons faking photons is displayed.

Process	Number of events	N_γ	N_{γ_e}	N_{γ_e}/N_γ
JF17 ("jet-jet filtered at p_T >17 GeV")	10 millions	21655	97	$(0.45 \pm 0.05)\%$
JF35 ("jet-jet filtered at p_T >35 GeV")	5 millions	7627	96	$(1.3 \pm 0.1)\%$
JF70 ("jet-jet filtered at p_T >70 GeV")	100 thousands	1306	4	$(0.3 \pm 0.1)\%$

Table 7.4: Electron contribution to photon impurity on each Monte Carlo sample. N_γ is the total number of photon candidates passing the adopted selection, N_{γ_e} are those due to misidentified electrons. The errors on N_{γ_e}/N_γ are statistical.

	isolated ($E_T^{R<0.4} < 3$ GeV)		non-isolated ($E_T^{R<0.4} > 5$ GeV)	
electron origin	JF17	JF35	JF17	JF35
$W^\pm$	40.2%	66.7%	0.6%	5.9%
B^0	12.4%	2.1%	34.6%	41.2%
$B^\pm$	12.4%	—	29.5%	23.5%
J/ψ	11.3%	—	5.8%	8.8%
Z^0	4.1%	24.0%	0.6%	—
π^0	4.1%	1.0%	2.6%	2.9%
Υ	4.1%	1.0%	0.6%	5.9%
$\tau^\pm$	3.1%	1.0%	0.6%	—
$D^\pm$	2.1%	—	—	—
B_s^0	2.1%	—	7.0%	8.8%
η	1.0%	1.0%	2.6%	—
D^0	1.0%	—	5.8%	—
$D_s^\pm$	—	—	1.9%	—

Table 7.5: Parent particles of electrons faking photons, passing tight cuts. In the 2nd and 3rd columns, the isolation cut is also satisfied, while in 4th and 5th column the non-isolation cut is applied.

Data-driven method

In addition, a data-driven method which involves the measurement of the electron-photon fake rate from collision data was performed. It consists in looking at $e\gamma$ pairs reconstructed with an invariant mass close to the Z-mass, an $e \to \gamma$ fake rate is inferred at the level of $\sim 8\%$. This value, applied to the inclusive production cross-section of isolated electrons (originated mainly by W decays, secondarily by Z, τ decays), implies an average contamination of $\sim 0.5\%$ in the photon selected sample. Due to the different p_T spectra of electrons from W (peaked around 40 GeV) and of prompt photons (exponentially decreasing as p_T increases), the electron contamination is not uniform over the E_T range, exhibiting its maximum value of 2.5% between 40 and 50 GeV. Electrons from hadron decays would produce a relatively higher contamination, but since they are not isolated,

they are removed by the 2D sidebands method (at the percent level described in the beginning of the paragraph). Further details about this data driven method presented in this subsection are outline in [30, 123].

Chapter 8

Inclusive Isolated Prompt Photon Cross Section Measurement

In this chapter, the inclusive isolated prompt photon cross section measurement [19] is presented, as well as the systematic uncertainties that affects this measurement, for a centre-of-mass energy collision of $\sqrt{s} = 7$ TeV and 0.88 pb^{-1} of integrated luminosity [1]. Moreover, the measured photon cross section is then compared with theoretical predictions performed at full NLO pQCD.

8.1 The cross section

The inclusive photon cross section is defined as a function of the E_T of the photon according to the following equation:

$$\frac{d\sigma}{dE_T^\gamma} = \frac{N_{\text{yield}}\ U}{\left(\int \mathcal{L}dt\right)\ \Delta E_T^\gamma\ \epsilon_{\text{trigger}}\ \epsilon_{\text{reco}}\ \epsilon_{\text{ID}}} \tag{8.1}$$

where N_{yield} is the observed signal yield, which is divided by the widths of the E_T-intervals (ΔE_T^γ) and by the product of the photon identification efficiency (ϵ_{ID}, determined in Section 6.5) and of trigger efficiency relative to photon candidates passing the identification criteria ($\epsilon_{\text{trigger}}$, discussed in Section C.4.2). The spectrum obtained this way, is then corrected using bin-by-bin correction factors (the "unfolding coefficients", see next Section 8.2), and is divided by the photon reconstruction efficiency ϵ_{reco} (Section C.4.1) and by the integrated luminosity of the data sample, $\int \mathcal{L}dt$.

8.2 Unfolding coefficients

The measured photon p_T spectrum shape depends on the efficiency of the photon identification cuts, and on the detector acceptance and resolution. These dependencies must

[1] For a data sample collected by the ATLAS detector with LHC 2010 runs up to August 2010.

be removed from the measurement, in order to compare the result to the theoretical predictions (Section 8.4). This procedure is called "unfolding" of the cross section.

The unfolding coefficients are evaluated from the ratio of the true to reconstructed E_T distributions of the photon candidates, using simulated isolated prompt photon samples produced with `PYTHIA LO`. The unfolding coefficients are computed bin by bin in p_T and pseudorapidity as is defined in Equation 8.2. This procedure is justified by the small bin-to-bin migrations (typically of the order of a few %) that are expected. One can note that the standard deviation of the transverse energy smearing is smaller than the bin size, given the electromagnetic calorimeter energy resolution and the width of the bins in this analysis (5 to 40 GeV).

Bin-by-bin unfolding matrices

The bin-by-bin unfolding matrices are the diagonal matrices of the inverse of the generalized efficiencies, $U_{ij}^k = u_i^k \delta_{ij}$.

$$u_i^k = \frac{N^\gamma \left(\eta_{k,1} \leq |\eta^\gamma_{\text{reco}}| < \eta_{k,2}, E^{\text{iso}}_{T,\text{reco}} < 3\text{GeV}, E_{T,i,1} \leq E_{T,\text{true}} < E_{T,i,2}\right)}{N^\gamma \left(\eta_{k,1} \leq |\eta^\gamma_{\text{reco}}| < \eta_{k,2}, E^{\text{iso}}_{T,\text{reco}} < 3\text{GeV}, E_{T,i,1} \leq E_{T,\text{reco}} < E_{T,i,2}\right)} \tag{8.2}$$

The unfolding coefficients u_i^k values for all the E_T and pseudorapidity ranges are summarized in Table 8.1 and displayed in Figure 8.1. One can note that the unfolding coefficients are larger than 1, due to the low p_T tails in the photon energy reconstruction (if we had a gaussian distribution for the uncertainty the unfolding coefficients would be slightly smaller than 1) see Subsection 8.3.2.

E_T [GeV]	$0.00 \leq \lvert\eta^\gamma\rvert < 0.60$	$0.60 \leq \lvert\eta^\gamma\rvert < 1.37$	$1.52 \leq \lvert\eta^\gamma\rvert < 1.81$	$1.81 \leq \lvert\eta^\gamma\rvert < 2.37$
$[15-20)$	1.021 ± 0.003	1.066 ± 0.004	1.031 ± 0.007	1.055 ± 0.004
$[20-25)$	1.018 ± 0.001	1.052 ± 0.002	1.046 ± 0.003	1.035 ± 0.001
$[25-30)$	1.016 ± 0.002	1.046 ± 0.002	1.054 ± 0.005	1.028 ± 0.002
$[30-35)$	1.009 ± 0.003	1.051 ± 0.004	1.035 ± 0.007	1.028 ± 0.004
$[35-40)$	1.007 ± 0.005	1.037 ± 0.005	1.049 ± 0.011	1.019 ± 0.005
$[40-50)$	1.004 ± 0.004	1.029 ± 0.004	1.043 ± 0.008	1.013 ± 0.004
$[50-60)$	1.006 ± 0.007	1.017 ± 0.007	1.017 ± 0.012	1.022 ± 0.008
$[60-100)$	0.991 ± 0.006	1.017 ± 0.006	1.037 ± 0.011	1.009 ± 0.006

Table 8.1: The bin-by-bin unfolding coefficients as defined in Equation 8.2.

Parton vs. particle isolation

In order to check the impact of applying the isolation requirement at the parton- or particle-level, the cross section was computed separately for each case. Figure 8.2 shows the ratio of the measured differential cross section computed using a particle-level isolation requirement to that using a parton-level isolation requirement. The differences in all

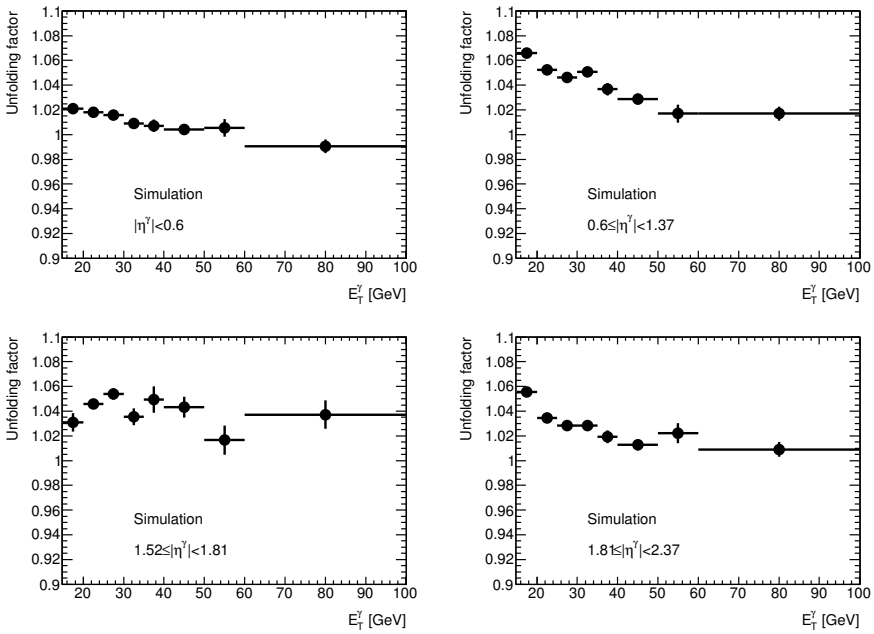
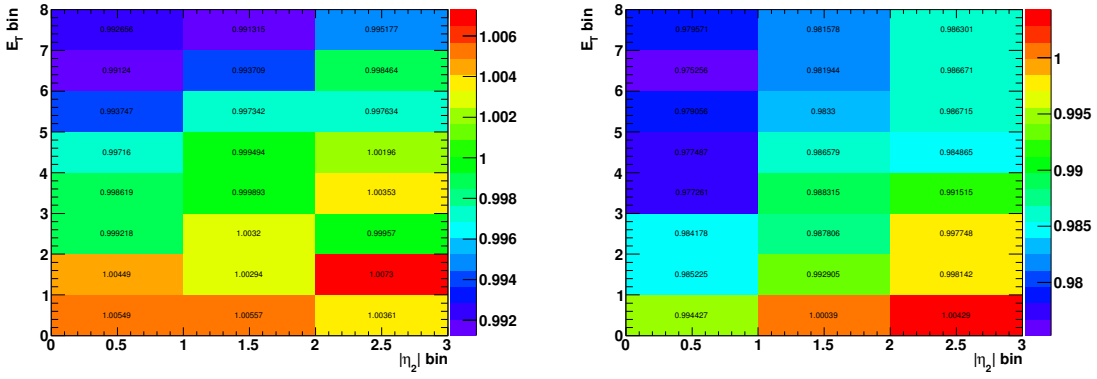


Figure 8.1: Bin-by-bin transverse energy unfolding coefficients as determined from a simulation of prompt photons. Top left: $|\eta^\gamma| < 0.6$. Top right: $0.6 \leq |\eta^\gamma| < 1.37$. Bottom: $1.52 \leq |\eta^\gamma| < 1.81$ Bottom left: $1.52 \leq |\eta^\gamma| < 1.81$ Bottom right: $1.81 \leq |\eta^\gamma| < 2.37$.

regions of transverse energy and pseudorapidity are small, at the 1% level, indicating the robustness of the isolation prescription to the effects of hadronization.



(a) PYTHIA (b) HERWIG

Figure 8.2: Ratio of the measured differential cross section using a parton-level isolation requirement of 4 GeV to that using a particle-level isolation cut at 4 GeV, with unfolding factors computed using prompt photons from PYTHIA (left) and HERWIG (right). In all cases the differences are less than 1% for PYTHIA, and less than 3% for HERWIG. Figures and caption taken from [32].

8.3 Cross section results and systematic uncertainties

8.3.1 Results

The cross sections measured using the 2D sidebands method technique are listed in Table 8.2. Correlated systematic uncertainties have been added linearly, uncorrelated uncertainties have been added in quadrature.

E_T^γ	$\frac{d\sigma}{dE_T^\gamma}$	stat	syst (purity)	syst (efficiency)	syst (en. scale)	syst (unfolding)	syst (luminosity)	total uncertainty
[GeV]	[nb/GeV]	[nb/GeV]	[nb/GeV]	[nb/GeV]	[nb/GeV]	[nb/GeV]	[nb/GeV]	[nb/GeV]
				$\lvert\eta^\gamma\rvert < 0.6$				
[15, 20)	5.24	±0.11	$^{+0.52}_{-0.88}$	±0.81	$^{+0.51}_{-0.46}$	±0.11	±0.58	$^{+1.3}_{-1.4}$
[20, 25)	1.88	±0.05	$^{+0.18}_{-0.20}$	±0.21	$^{+0.14}_{-0.14}$	±0.04	±0.21	±0.36
[25, 30)	0.88	±0.03	±0.07	±0.08	$^{+0.09}_{-0.08}$	±0.02	±0.10	$^{+0.16}_{-0.15}$
[30, 35)	0.461	±0.016	$^{+0.029}_{-0.019}$	±0.035	$^{+0.045}_{-0.046}$	±0.009	±0.05	±0.07
[35, 40)	0.254	±0.011	$^{+0.017}_{-0.015}$	±0.019	$^{+0.027}_{-0.025}$	±0.005	±0.028	±0.04
[40, 50)	0.115	±0.005	$^{+0.008}_{-0.006}$	±0.007	$^{+0.009}_{-0.009}$	±0.0023	±0.013	$^{+0.017}_{-0.016}$
[50, 60)	0.050	±0.003	$^{+0.003}_{-0.002}$	±0.003	$^{+0.006}_{-0.005}$	±0.001	±0.005	$^{+0.008}_{-0.007}$
[60, 100)	0.0120	±0.0007	$^{+0.0007}_{-0.0005}$	±0.0006	$^{+0.0013}_{-0.0012}$	±0.0002	±0.0013	$^{+0.0019}_{-0.0018}$
				$0.6 \leq \lvert\eta^\gamma\rvert < 1.37$				
[15, 20)	5.9	±0.2	$^{+1.8}_{-0.5}$	±1.0	$^{+0.6}_{-0.5}$	±0.1	±0.6	$^{+2.3}_{-1.4}$
[20, 25)	2.23	±0.07	$^{+0.49}_{-0.18}$	±0.28	$^{+0.16}_{-0.16}$	±0.04	±0.24	$^{+0.6}_{-0.4}$
[25, 30)	1.05	±0.03	$^{+0.16}_{-0.06}$	±0.10	$^{+0.10}_{-0.10}$	±0.021	±0.12	$^{+0.24}_{-0.19}$
[30, 35)	0.52	±0.02	$^{+0.06}_{-0.03}$	±0.04	$^{+0.05}_{-0.05}$	±0.011	±0.06	$^{+0.11}_{-0.09}$
[35, 40)	0.313	±0.014	$^{+0.029}_{-0.021}$	±0.024	$^{+0.035}_{-0.032}$	±0.006	±0.034	$^{+0.06}_{-0.05}$
[40, 50)	0.146	±0.006	$^{+0.014}_{-0.011}$	±0.009	$^{+0.013}_{-0.013}$	±0.003	±0.016	$^{+0.025}_{-0.022}$
[50, 60)	0.062	±0.004	$^{+0.005}_{-0.004}$	±0.003	$^{+0.006}_{-0.006}$	±0.001	±0.007	$^{+0.010}_{-0.009}$
[60, 100)	0.0138	±0.0008	$^{+0.0013}_{-0.0009}$	±0.0007	$^{+0.0016}_{-0.0014}$	±0.0003	±0.0015	$^{+0.0025}_{-0.0022}$
				$1.52 \leq \lvert\eta^\gamma\rvert < 1.81$				
[15, 20)	2.9	±0.1	$^{+0.8}_{-0.3}$	±0.5	$^{+0.3}_{-0.3}$	±0.1	±0.3	$^{+1.1}_{-0.7}$
[20, 25)	1.12	±0.04	$^{+0.15}_{-0.08}$	±0.16	$^{+0.08}_{-0.08}$	±0.02	±0.12	$^{+0.27}_{-0.24}$
[25, 30)	0.47	±0.02	$^{+0.06}_{-0.04}$	±0.05	$^{+0.05}_{-0.04}$	±0.01	±0.05	$^{+0.11}_{-0.09}$
[30, 35)	0.240	±0.013	$^{+0.028}_{-0.016}$	±0.023	$^{+0.025}_{-0.026}$	±0.005	±0.026	$^{+0.052}_{-0.045}$
[35, 40)	0.142	±0.009	$^{+0.018}_{-0.010}$	±0.012	$^{+0.014}_{-0.013}$	±0.0032	±0.016	$^{+0.030}_{-0.026}$
[40, 50)	0.062	±0.004	$^{+0.005}_{-0.004}$	±0.005	$^{+0.006}_{-0.006}$	±0.0013	±0.007	$^{+0.011}_{-0.010}$
[50, 60)	0.0237	±0.0025	$^{+0.0026}_{-0.0028}$	±0.0019	$^{+0.0024}_{-0.0022}$	±0.0005	±0.003	±0.005
[60, 100)	0.0066	±0.0005	$^{+0.0005}_{-0.0003}$	±0.0005	$^{+0.0008}_{-0.0007}$	±0.0002	±0.0007	$^{+0.0013}_{-0.0012}$

Table 8.2: The measured isolated prompt photon production cross section. The systematic uncertainties originating from the purity measurement, the photon selection, the photon energy scale, the unfolding procedure and the luminosity are shown. The total uncertainty includes both the statistical and all systematic uncertainties, except for the uncertainty on the luminosity [19].

8.3.2 Systematic uncertainties

Purity

Uncertainties associated to the estimation of the number of signal events are described in detail in Section 7.2.2, and its values are listed in Table 7.3. The uncertainty from the electron contamination was also taken into account and added in quadrature to the uncertainty on the signal photon yield. In addition, the potential bias introduced by the PYTHIA fragmentation model was evaluated by varying the background rates of neutral hadrons (like π^0's, η 's and ω's) by 50%; the effects found are covered by systematics associated with the construction of the background control-region from the reverse-cuts procedure. Total signal yield relative uncertainties are propagated into the cross-section measurement assuming no correlation between them and the uncertainties related to the unfolding procedure, efficiency, energy scale, or luminosity.

Reconstruction, identification, trigger

Uncertainties on the reconstruction and identification efficiencies are evaluated together, as is outlined in detail in [103]. Uncertainty values are shown in Section 6.5. Between the uncertainties which contribute to this measurement, the largest effects are due to material effects (ranging from 1-8% absolute uncertainties, largest at low E_T^γ) and the uncertainty associated with the shower-shape-corrected efficiency estimates from simulation (ranging from 1-5% absolute uncertainties, largest at low E_T^γ).

The uncertainty on the trigger efficiency (0.5%) is very small.

Luminosity

The integrated luminosities are calculated during runs by measuring interaction rates using several ATLAS devices (LUCID $\equiv$ LUminosity using Cherenkov Integrating Detector and the BCM $\equiv$ Beam Conditions Monitor - see [156] for more descriptions) at small angles to the beam direction, with the absolute calibration obtained from Van der Meer scans. The relative systematic uncertainty on the luminosity measurement is estimated to be 11% [2] [18] and translates into a 11% of relative uncertainty on the cross-section.

Unfolding coefficients

The unfolding coefficients used to correct the measured cross-section for E_T bin-by-bin migrations are taken from the simulations. There are three sources of uncertainties on these corrections.

- *Energy scale uncertainty.*
  The energy-scale uncertainty is taken from test beams studies, which quoted a 3% error [47]. It is below this value from the comparison of the $Z \rightarrow e^-e^+$ invariant mass peak in data and Monte Carlo. The unfolding coefficients are thus recomputed using

[2] At the time of this 1^{st} γ analysis

simulated signal events where the true photon energy is shifted by ±3% (shown in Figure 8.3). The coefficients change by ±10%. This uncertainty introduces a relative uncertainty of about 10% on the measured cross section which is fully correlated between the different E_T intervals within each pseudorapidity range.

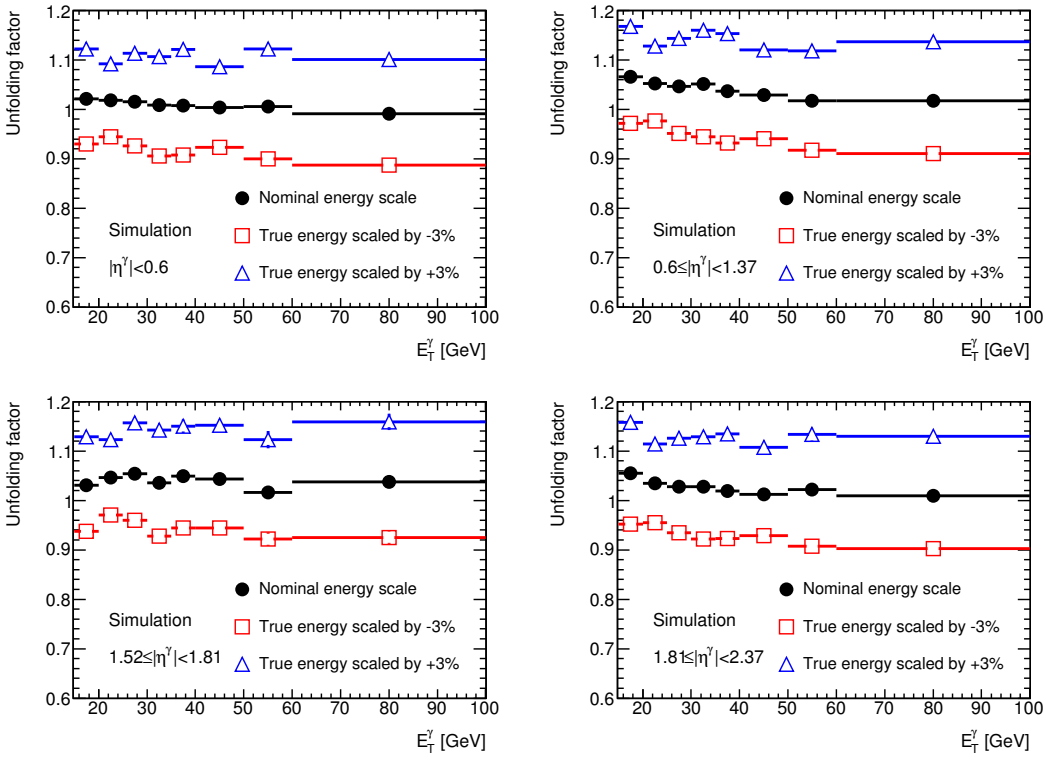


Figure 8.3: Bin-by-bin transverse energy unfolding factors as determined from a simulation of prompt photons: nominal energy scale (full black dots), and after shifting the true photon energy by −3% (red open squares) or +3% (blue open triangles).

- *Energy resolution uncertainty.*
  The uncertainty on the energy resolution may affect bin-by-bin migrations between adjacent E_T bins. Test beam studies indicated that the sampling term of the resolution agreement between data and MC lies within 10-20% relative. $Z \rightarrow e^+e^-$ invariant mass resolution studies in data seems to indicate that a constant term of the calorimeter energy resolution is below 1.5% in the barrel and 3.0% in the end-cap (it is 0.7% in the simulation). The unfolding coefficients are thus recomputed after the reconstructed energy of simulated photon smearing to take into account a 20% relative increase of the sampling term and a constant term of 1.5% in the barrel and 3.0% in the end-cap. The resulting variation of the unfolding coefficients is always less than 1%. The uncertainty arising from non-gaussian tails of the energy resolution function is estimated by recomputing the coefficients using a prompt photon simulation where a significant amount of material is added to the detector

model [3]. As is shown in Figure 8.4, the variations of the unfolding coefficients are smaller than 1% in all the pseudorapidity and transverse energy intervals under study. When combined with the energy scale uncertainty, the uncertainty from the energy resolution therefore is negligible.

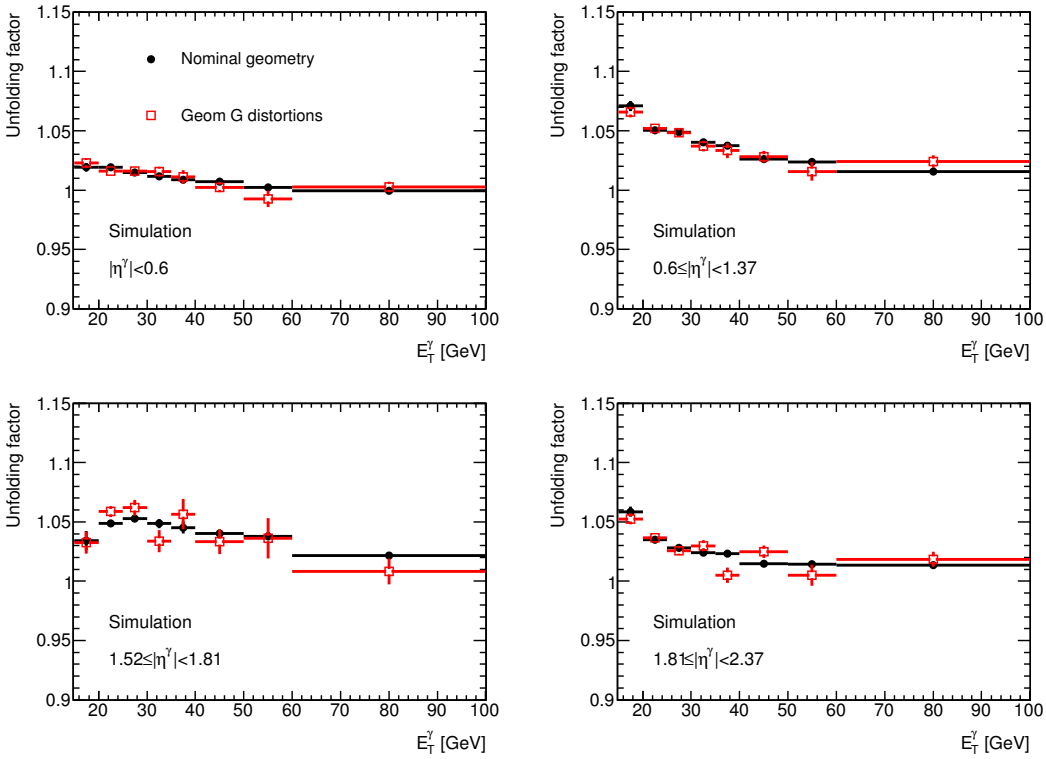


Figure 8.4: Bin-by-bin transverse energy unfolding factors as determined from a simulation of direct photons, after correcting the energy scale for the average energy loss in upstream material: nominal geometry (full black dots), and alternative geometry with additional material in the inner detector, the calorimeter cryostat, and several services.

- *Simulated photon transverse energy distribution.*
  The uncertainty from the `PYTHIA` E_T distribution is estimated by repeating the cross-section measurement with an alternative unfolding technique outlined in Reference [120], which relies on the repeated application of Bayes' theorem to iteratively obtain an improved estimate of the unfolded spectrum. This technique relies less on the simulated original E_T distribution of the prompt photons. The differences between the cross-sections estimated using the bin-by-bin unfolding and the iterative Bayesian unfolding are within 2%. In Figure 8.5, one sees that differences between the two results are small.

[3] We use the same geometry to study material-related systematic uncertainties on the photon efficiency, already discussed in Section 6.5.

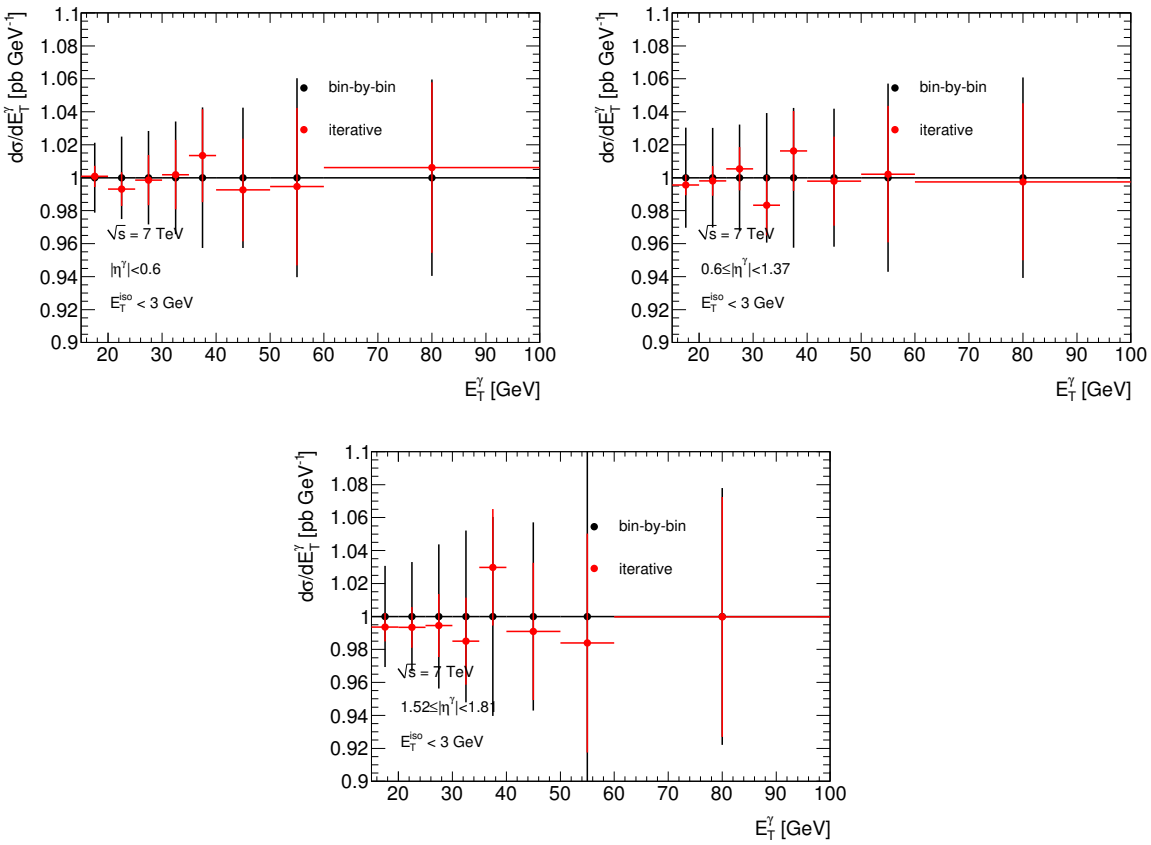


Figure 8.5: Measured cross sections, with the iterative and the bin-by-bin unfolding approaches, normalized to the central values obtained with the bin-by-bin unfolding. Uncertainties are purely statistical. Top left: $|\eta^{\gamma}| < 0.6$. Top right: $0.6 \leq |\eta^{\gamma}| < 1.37$. Bottom: $1.52 \leq |\eta^{\gamma}| < 1.81$.

8.4 Theoretical prediction

The NLO pQCD predictions to the isolated prompt photon production cross section were determined using the JETPHOX [4] Monte Carlo Program [7, 104]. This is written as a partonic event generator and calculates predictions including both direct and fragmentation processes (already discussed in Section 2.2). JETPHOX calculations are done in two parts. The first is the full NLO γj, matrix element (including therefore γjj). The second part is a NLO matrix element for jj final states (including therefore jjj), followed by a jet fragmenting into photon. The code allows the specification of several parameters like kinematics range, isolation settings, PDFs and fragmentation functions.

The choice of parameters and uncertainties are listed below:

- **Isolation criterion** used in these calculations is described as the following:
  A photon is isolated if, inside a cone centered around the photon direction in the rapidity and azimuthal angle plane, the amount of hadronic transverse momentum

[4] code version 1.2.2

$p_T^{\rm had}$ *deposited is smaller than some value:*

$$\text{for } (\eta-\eta_\gamma)^2+(\phi-\phi_\gamma)^2 \leq R^2, \qquad p_T^{\rm had} \leq E_T^{\rm cut} \tag{8.3}$$

The parton cut value that matches the 3 GeV cut at experimental level varies across different pseudorapidity bins. A sensitive mean value of 4 GeV in a cone of $R = 0.4$ has been chosen to compute the NLO cross section. The uncertainty on the parton level isolation cut has been evaluated by varing the cut between ± 2 GeV. This changes the predicted cross section by 2% at most.

- **Scales**: the changes in the theoretical cross section due to the variation of the scales provide an estimation of the size of the higher order terms which have not been considered in the fixed-order calculation. In order to measure the dependence of the prediction with the renormalization, factorization and fragmentation scales, the scale uncertainty has been evaluated by varying these three scales independently between 0.5 and 2.0 times the nominal scale. This leads to a change of the predicted cross section between 20% at low E_T and 10% at high E_T.

- **PDF**: the predicted cross section depends on the particular PDFs employed in the calculation. The uncertainty on the cross section has been obtained by varing the PDFs within the 68% C.L. intervals. The corresponding uncertainty on the cross section varies between 5% and 2% as E_T increases between 15 and 100 GeV. NLO photon fragmentation [100] and the CTEQ 6.6 parton density functions [188] provided by the LHAPDF package [214] are used. The MSTW 2008 PDFs [177] are used as a cross-check of the choice of PDF. The central values obtained with the MSTW 2008 PDFs are between 3% and 5% higher than those predicted using the CTEQ 6.6. PDFs.

The results obtained are listed in Tables 8.3 and 8.4.

E_T^γ [GeV]	$\frac{d\sigma}{dE_T^\gamma}$ [nb/GeV]	stat [nb/GeV]	scale [nb/GeV]	PDF [nb/GeV]	isolation [nb/GeV]	tot [nb/GeV]
			$\lvert\eta^\gamma\rvert < 0.6$			
$[15, 20)$	6.7797	± 0.0143	$^{+1.3020}_{-0.9094}$	$^{+0.3463}_{-0.1881}$	± 0.1356	$^{+1.3540}_{-0.9385}$
$[20, 25)$	2.3839	± 0.0086	$^{+0.4329}_{-0.2930}$	$^{+0.0992}_{-0.0587}$	± 0.0477	$^{+0.4466}_{-0.3026}$
$[25, 30)$	1.0109	± 0.0057	$^{+0.1666}_{-0.1229}$	$^{+0.0493}_{-0.0390}$	± 0.0202	$^{+0.1749}_{-0.1305}$
$[30, 35)$	0.5045	± 0.0040	$^{+0.0841}_{-0.0441}$	$^{+0.0558}_{-0.0045}$	± 0.0101	$^{+0.1015}_{-0.0455}$
$[35, 40)$	0.2774	± 0.0008	$^{+0.0405}_{-0.0306}$	$^{+0.0068}_{-0.0112}$	± 0.0055	$^{+0.0414}_{-0.0330}$
$[40, 50)$	0.1273	± 0.0008	$^{+0.0167}_{-0.0133}$	$^{+0.0047}_{-0.0035}$	± 0.0025	$^{+0.0175}_{-0.0140}$
$[50, 60)$	0.0515	± 0.0005	$^{+0.0065}_{-0.0052}$	$^{+0.0013}_{-0.0013}$	± 0.0010	$^{+0.0067}_{-0.0055}$
$[60, 100)$	0.0121	± 0.0002	$^{+0.0014}_{-0.0011}$	$^{+0.0003}_{-0.0003}$	± 0.0002	$^{+0.0014}_{-0.0012}$
			$0.6 \leq \lvert\eta^\gamma\rvert < 1.37$			
$[15, 20)$	8.5265	± 0.0179	$^{+1.6483}_{-1.2427}$	$^{+0.2593}_{-0.3297}$	± 0.1705	$^{+1.6773}_{-1.2969}$
$[20, 25)$	3.0013	± 0.0107	$^{+0.5360}_{-0.3827}$	$^{+0.0980}_{-0.0882}$	± 0.0600	$^{+0.5481}_{-0.3973}$
$[25, 30)$	1.2768	± 0.0071	$^{+0.1768}_{-0.1536}$	$^{+0.0349}_{-0.0540}$	± 0.0255	$^{+0.1820}_{-0.1648}$
$[30, 35)$	0.6409	± 0.0050	$^{+0.1058}_{-0.0815}$	$^{+0.0216}_{-0.0213}$	± 0.0128	$^{+0.1088}_{-0.0852}$
$[35, 40)$	0.3443	± 0.0010	$^{+0.0510}_{-0.0380}$	$^{+0.0102}_{-0.0081}$	± 0.0069	$^{+0.0525}_{-0.0394}$
$[40, 50)$	0.1609	± 0.0009	$^{+0.0213}_{-0.0179}$	$^{+0.0023}_{-0.0062}$	± 0.0032	$^{+0.0217}_{-0.0193}$
$[50, 60)$	0.0653	± 0.0006	$^{+0.0090}_{-0.0065}$	$^{+0.0020}_{-0.0009}$	± 0.0013	$^{+0.0094}_{-0.0067}$
$[60, 100)$	0.0154	± 0.0003	$^{+0.0018}_{-0.0015}$	$^{+0.0003}_{-0.0003}$	± 0.0003	$^{+0.0019}_{-0.0015}$
			$1.52 \leq \lvert\eta^\gamma\rvert < 1.81$			
$[15, 20)$	3.0809	± 0.0064	$^{+0.6079}_{-0.4352}$	$^{+0.0898}_{-0.1037}$	± 0.0616	$^{+0.6176}_{-0.4515}$
$[20, 25)$	1.0974	± 0.0039	$^{+0.1922}_{-0.1430}$	$^{+0.0290}_{-0.0293}$	± 0.0219	$^{+0.1957}_{-0.1476}$
$[25, 30)$	0.4609	± 0.0026	$^{+0.0727}_{-0.0583}$	$^{+0.0121}_{-0.0110}$	± 0.0092	$^{+0.0742}_{-0.0600}$
$[30, 35)$	0.2330	± 0.0018	$^{+0.0355}_{-0.0294}$	$^{+0.0077}_{-0.0060}$	± 0.0047	$^{+0.0367}_{-0.0304}$
$[35, 40)$	0.1259	± 0.0003	$^{+0.0193}_{-0.0148}$	$^{+0.0030}_{-0.0031}$	± 0.0025	$^{+0.0197}_{-0.0153}$
$[40, 50)$	0.0582	± 0.0003	$^{+0.0083}_{-0.0063}$	$^{+0.0012}_{-0.0006}$	± 0.0012	$^{+0.0085}_{-0.0065}$
$[50, 60)$	0.0243	± 0.0002	$^{+0.0032}_{-0.0025}$	$^{+0.0002}_{-0.0007}$	± 0.0005	$^{+0.0033}_{-0.0027}$
$[60, 100)$	0.0057	± 0.0001	$^{+0.0007}_{-0.0006}$	$^{+0.0001}_{-0.0001}$	± 0.0001	$^{+0.0007}_{-0.0006}$

Table 8.3: NLO pQCD isolated prompt photon production cross section computed with `JETPHOX` 1.2.2 using CTEQ 6.6 PDFs. The nominal factorization, fragmentation and renormalization scales are set to the photon transverse energy ($\mu_f = \mu_F = \mu_R = E_T^\gamma$). Scale errors are evaluated by varying the three scales independently between $0.5 \times E_T^\gamma$ and $2 \times E_T^\gamma$. PDF errors correspond to 68% CL PDF uncertainties [32].

E_T^γ [GeV]	$\frac{d\sigma}{dE_T^\gamma}$ [nb/GeV]	stat [nb/GeV]	scale [nb/GeV]	PDF [nb/GeV]	isolation [nb/GeV]	tot [nb/GeV]
			$\lvert\eta^\gamma\rvert < 0.6$			
$[15, 20)$	6.9598	± 0.0148	$^{+1.3689}_{-1.0857}$	$^{+0.1898}_{-0.1162}$	± 0.1392	$^{+1.3890}_{-1.1007}$
$[20, 25)$	2.4806	± 0.0090	$^{+0.4436}_{-0.3413}$	$^{+0.0243}_{-0.1082}$	± 0.0496	$^{+0.4470}_{-0.3615}$
$[25, 30)$	1.0568	± 0.0059	$^{+0.1617}_{-0.1412}$	$^{+0.0247}_{-0.0494}$	± 0.0211	$^{+0.1650}_{-0.1511}$
$[30, 35)$	0.5365	± 0.0042	$^{+0.1069}_{-0.0729}$	$^{+0.0309}_{-0.0157}$	± 0.0107	$^{+0.1118}_{-0.0753}$
$[35, 40)$	0.2870	± 0.0008	$^{+0.0448}_{-0.0332}$	$^{+0.0053}_{-0.0065}$	± 0.0057	$^{+0.0454}_{-0.0343}$
$[40, 50)$	0.1341	± 0.0008	$^{+0.0175}_{-0.0148}$	$^{+0.0013}_{-0.0041}$	± 0.0027	$^{+0.0178}_{-0.0156}$
$[50, 60)$	0.0542	± 0.0005	$^{+0.0079}_{-0.0055}$	$^{+0.0024}_{-0.0003}$	± 0.0011	$^{+0.0083}_{-0.0056}$
$[60, 100)$	0.0128	± 0.0002	$^{+0.0015}_{-0.0012}$	$^{+0.0001}_{-0.0002}$	± 0.0003	$^{+0.0015}_{-0.0013}$
			$0.6 \leq \lvert\eta^\gamma\rvert < 1.37$			
$[15, 20)$	8.7278	± 0.0185	$^{+1.7323}_{-1.3498}$	$^{+0.1824}_{-0.2107}$	± 0.1746	$^{+1.7506}_{-1.3772}$
$[20, 25)$	3.1223	± 0.0112	$^{+0.5681}_{-0.4068}$	$^{+0.0414}_{-0.0695}$	± 0.0624	$^{+0.5731}_{-0.4174}$
$[25, 30)$	1.3412	± 0.0074	$^{+0.2178}_{-0.1746}$	$^{+0.0395}_{-0.0575}$	± 0.0268	$^{+0.2230}_{-0.1858}$
$[30, 35)$	0.6733	± 0.0053	$^{+0.1132}_{-0.0871}$	$^{+0.0412}_{-0.0177}$	± 0.0135	$^{+0.1212}_{-0.0899}$
$[35, 40)$	0.3606	± 0.0010	$^{+0.0578}_{-0.0412}$	$^{+0.0087}_{-0.0043}$	± 0.0072	$^{+0.0589}_{-0.0421}$
$[40, 50)$	0.1680	± 0.0010	$^{+0.0228}_{-0.0192}$	$^{+0.0011}_{-0.0052}$	± 0.0034	$^{+0.0231}_{-0.0201}$
$[50, 60)$	0.0689	± 0.0006	$^{+0.0093}_{-0.0069}$	$^{+0.0025}_{-0.0002}$	± 0.0014	$^{+0.0097}_{-0.0071}$
$[60, 100)$	0.0162	± 0.0003	$^{+0.0020}_{-0.0016}$	$^{+0.0001}_{-0.0002}$	± 0.0003	$^{+0.0020}_{-0.0016}$
			$1.52 \leq \lvert\eta^\gamma\rvert < 1.81$			
$[15, 20)$	3.1519	± 0.0066	$^{+0.6359}_{-0.4486}$	$^{+0.0720}_{-0.0505}$	± 0.0630	$^{+0.6430}_{-0.4558}$
$[20, 25)$	1.1332	± 0.0040	$^{+0.2095}_{-0.1567}$	$^{+0.0213}_{-0.0259}$	± 0.0227	$^{+0.2118}_{-0.1604}$
$[25, 30)$	0.4811	± 0.0027	$^{+0.0837}_{-0.0706}$	$^{+0.0053}_{-0.0199}$	± 0.0096	$^{+0.0844}_{-0.0740}$
$[30, 35)$	0.2446	± 0.0019	$^{+0.0460}_{-0.0319}$	$^{+0.0083}_{-0.0058}$	± 0.0049	$^{+0.0470}_{-0.0327}$
$[35, 40)$	0.1316	± 0.0004	$^{+0.0209}_{-0.0155}$	$^{+0.0018}_{-0.0015}$	± 0.0026	$^{+0.0211}_{-0.0158}$
$[40, 50)$	0.0611	± 0.0004	$^{+0.0091}_{-0.0073}$	$^{+0.0005}_{-0.0013}$	± 0.0012	$^{+0.0092}_{-0.0075}$
$[50, 60)$	0.0251	± 0.0002	$^{+0.0032}_{-0.0026}$	$^{+0.0008}_{-0.0005}$	± 0.0005	$^{+0.0034}_{-0.0027}$
$[60, 100)$	0.0059	± 0.0001	$^{+0.0008}_{-0.0006}$	$^{+0.0001}_{-0.0000}$	± 0.0001	$^{+0.0008}_{-0.0006}$

Table 8.4: NLO pQCD isolated prompt photon production cross section computed with `JETPHOX` 1.2.2 using MSTW 2008 PDFs. The nominal factorization, fragmentation and renormalization scales are set to the photon transverse energy ($\mu_f = \mu_F = \mu_R = E_T^\gamma$). Scale errors are evaluated by varying the three scales independently between $0.5 \times E_T^\gamma$ and $2.0 \times E_T^\gamma$. PDF errors correspond to 68% CL PDF uncertainties [32].

8.5 Comparison between theory and data and Conclusion

The measured differential cross-section are plotted, with the theoretical cross-sections overlaid in different η regions. In Figures 8.6, 8.7 and 8.8 the CTEQ66 PDFs have been used to compute the theoretical cross sections. In Figures 8.11, 8.10 and 8.11 similar plots are shown by using the MSTW08 PDFs. The ratio of data to theory is also plotted, showing the relative deviation of the measured cross section from the predicted one across the full E_T range on a linear scale. The error bars represent the combination of statistical and systematic uncertainties, but are dominated by systematic uncertainties in all regions. The luminosity uncertainty is plotted separately.

The NLO pQCD predictions agree with the observed cross sections for transverse energies greater than 25 GeV, while for transverse energies below 25 GeV the cross sections predicted by `JETPHOX` are higher than measured. However, the precision of this comparison below 25 GeV is limited by large systematic uncertainties on the measurement and on the theoretical predictions at such low values of $x_T = 2E_T^{\gamma}/\sqrt{s}$.

The measured prompt photon production cross section is more than a factor of 30 larger than that measured at the Tevatron, and a factor 10^4 larger than photoproduction at HERA, assuming a similar kinematic range in transverse energy and pseudorapidity. This will allow the extension of the measurement up to energies in the TeV range after only few years of data-taking at the LHC.

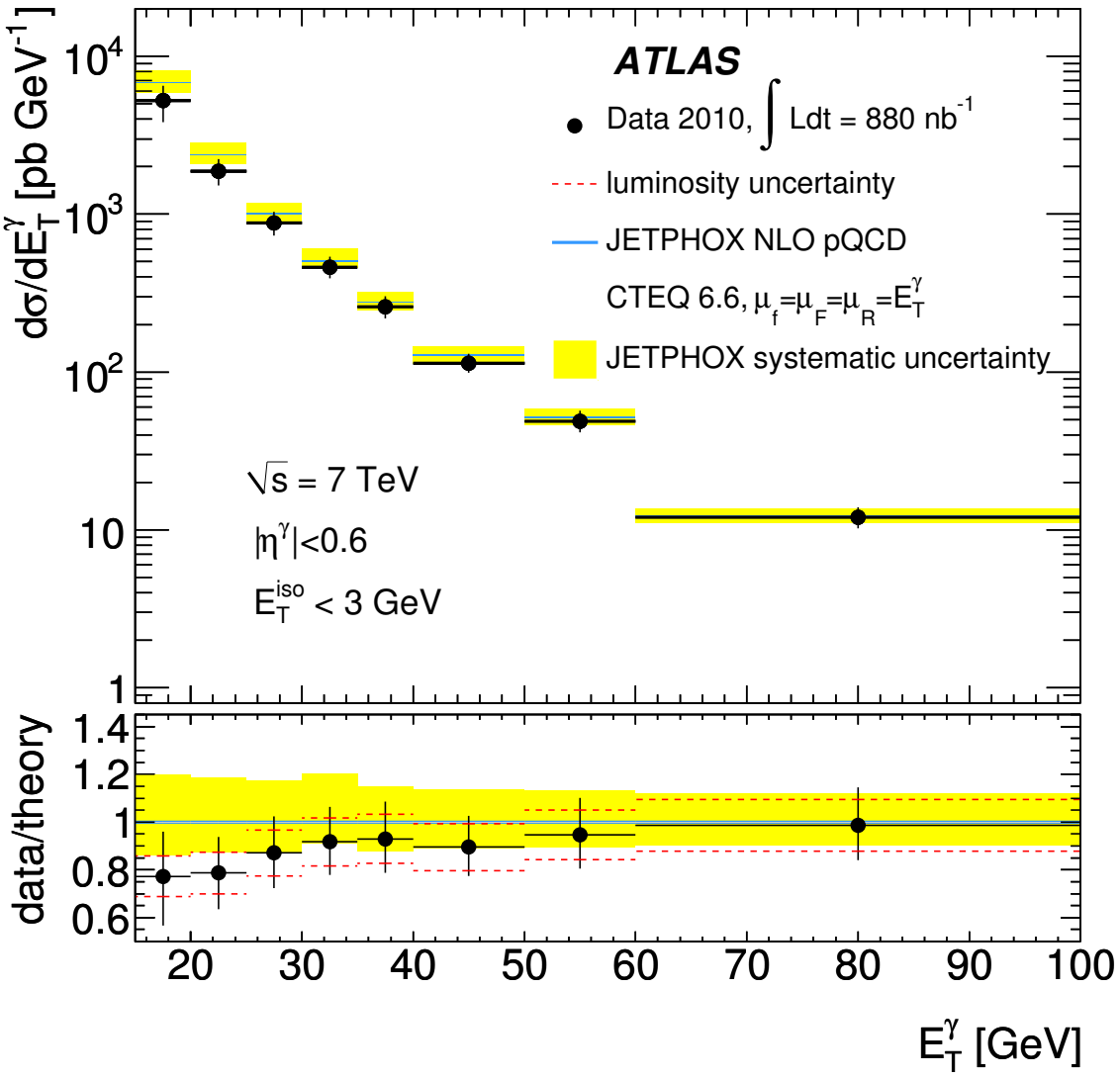


Figure 8.6: Measured vs expected inclusive prompt photon production cross section, for photons with transverse energies above 15 GeV and in the pseudorapidity range $|\eta^{\gamma}| < 0.6$. Results with the 2D sideband method. The CTEQ6.6 PDFs are used in the theoretical computation [19].

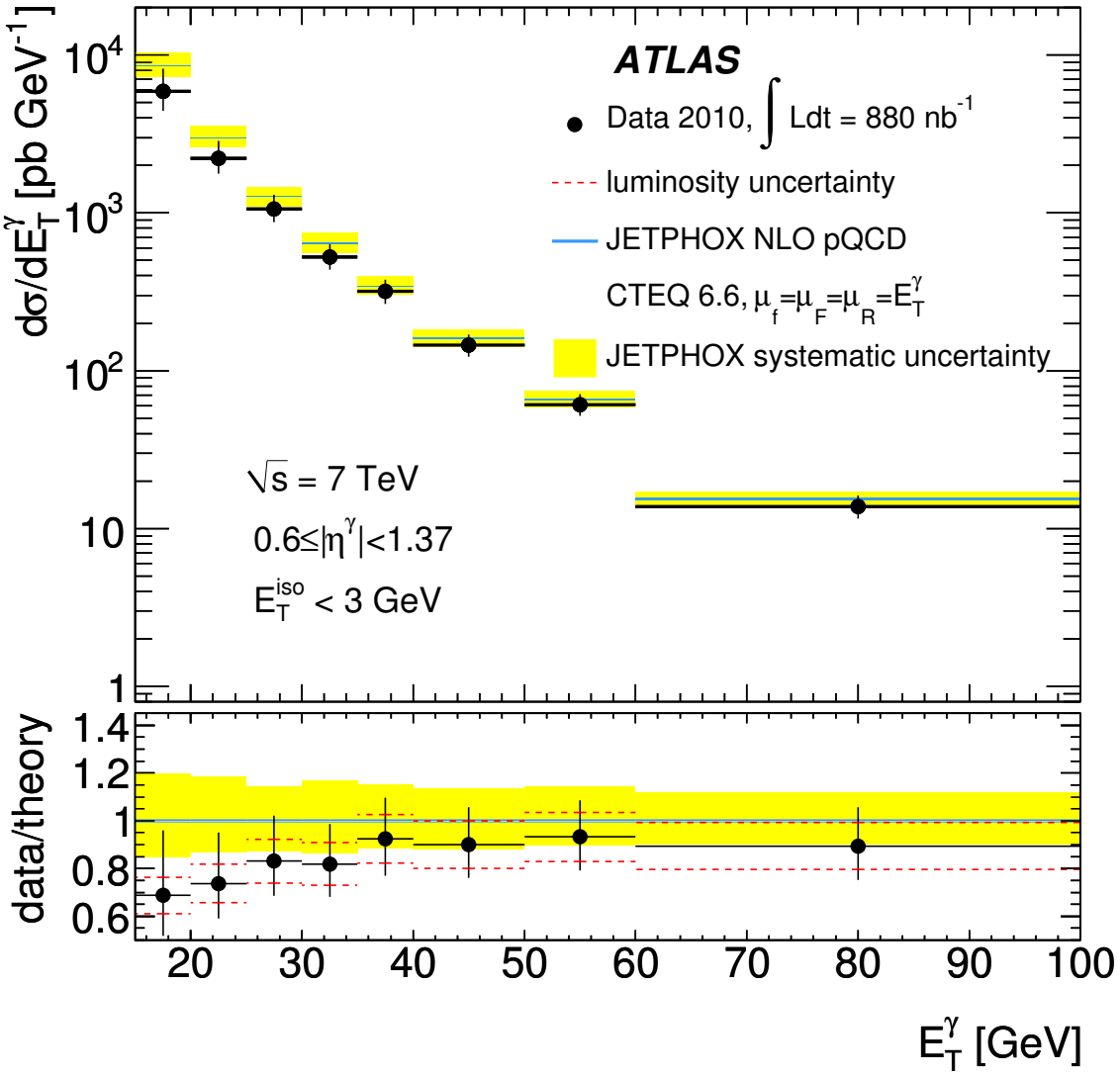


Figure 8.7: Measured vs expected inclusive prompt photon production cross section, for photons with transverse energies above 15 GeV and in the pseudorapidity range $0.6 \leq |\eta^{\gamma}| < 1.37$. Results with the 2D sideband method. The CTEQ6.6 PDFs are used in the theoretical computation [19].

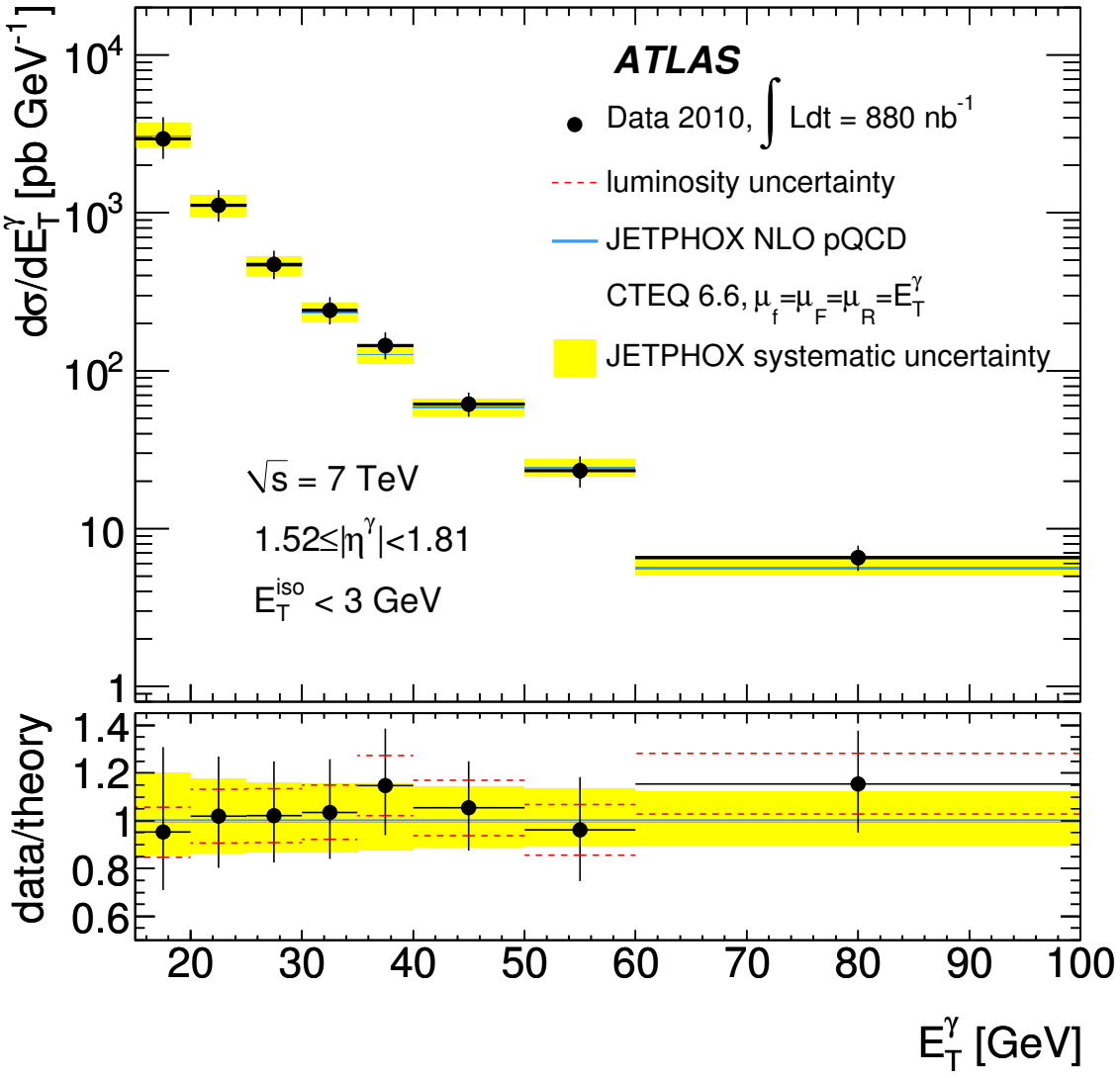


Figure 8.8: Measured vs expected inclusive prompt photon production cross section, for photons with transverse energies above 15 GeV and in the pseudorapidity range $1.52 \leq |\eta^{\gamma}| < 1.81$. Results with the 2D sideband method. The CTEQ6.6 PDFs are used in the theoretical computation [19].

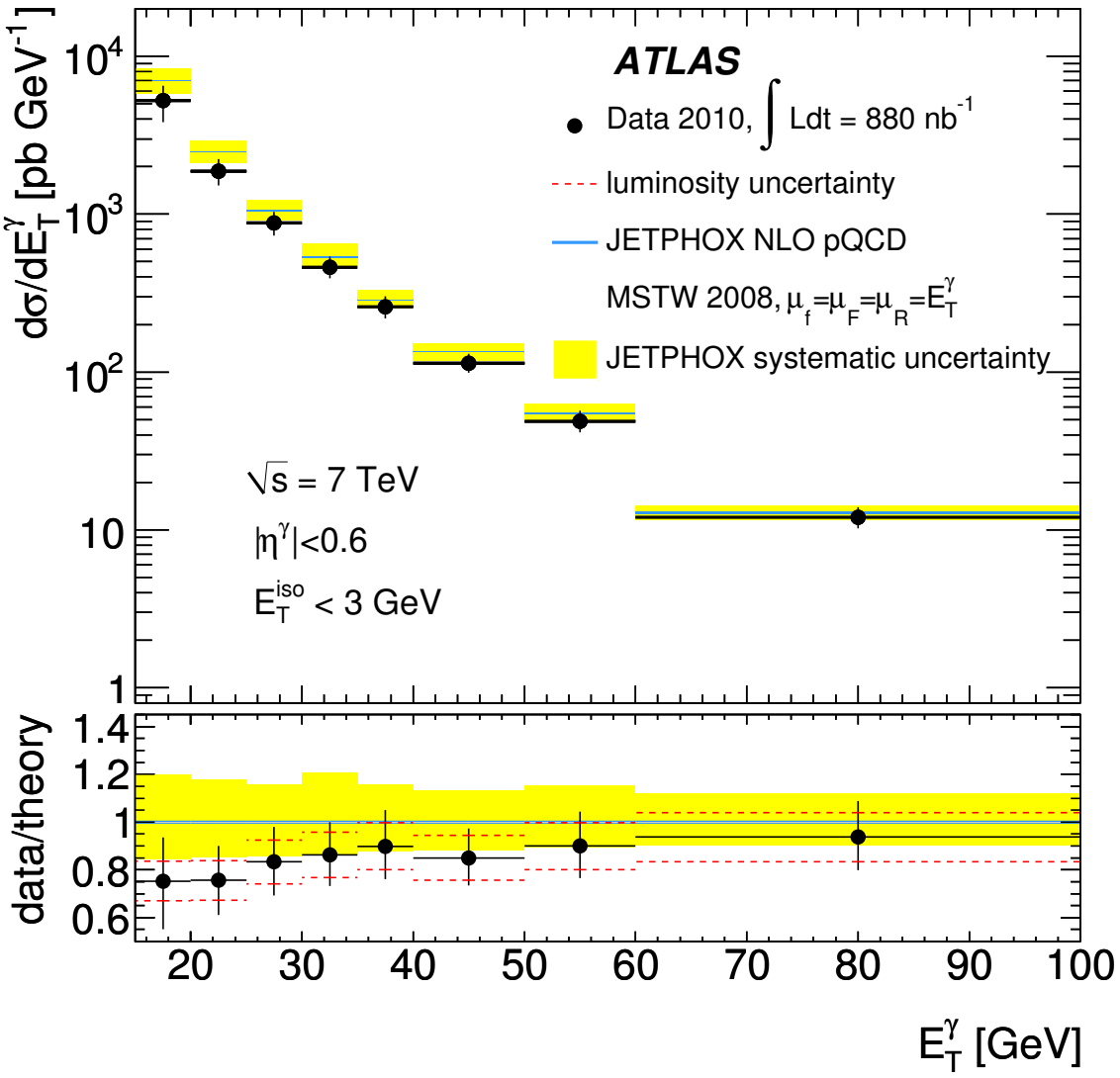


Figure 8.9: Measured vs expected inclusive prompt photon production cross section, for photons with transverse energies above 15 GeV and in the pseudorapidity range $|\eta^{\gamma}| < 0.6$. Results with the 2D sideband method. The MSTW08 PDFs are used in the theoretical computation [32].

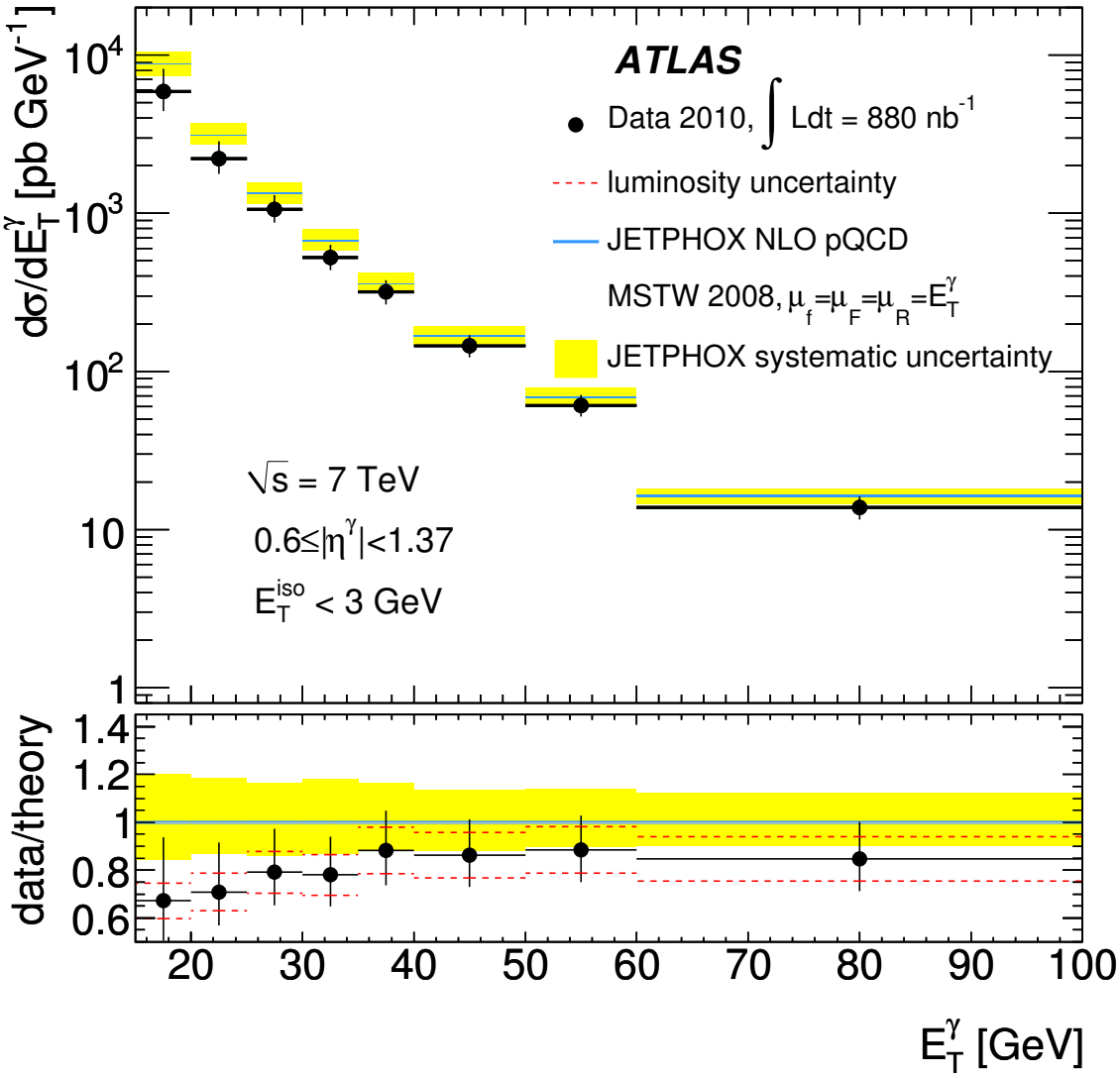


Figure 8.10: Measured vs expected inclusive prompt photon production cross section, for photons with transverse energies above 15 GeV and in the pseudorapidity range $0.6 \leq |\eta^{\gamma}| < 1.37$. Results with the 2D sideband method. The MSTW08 PDFs are used in the theoretical computation [32].

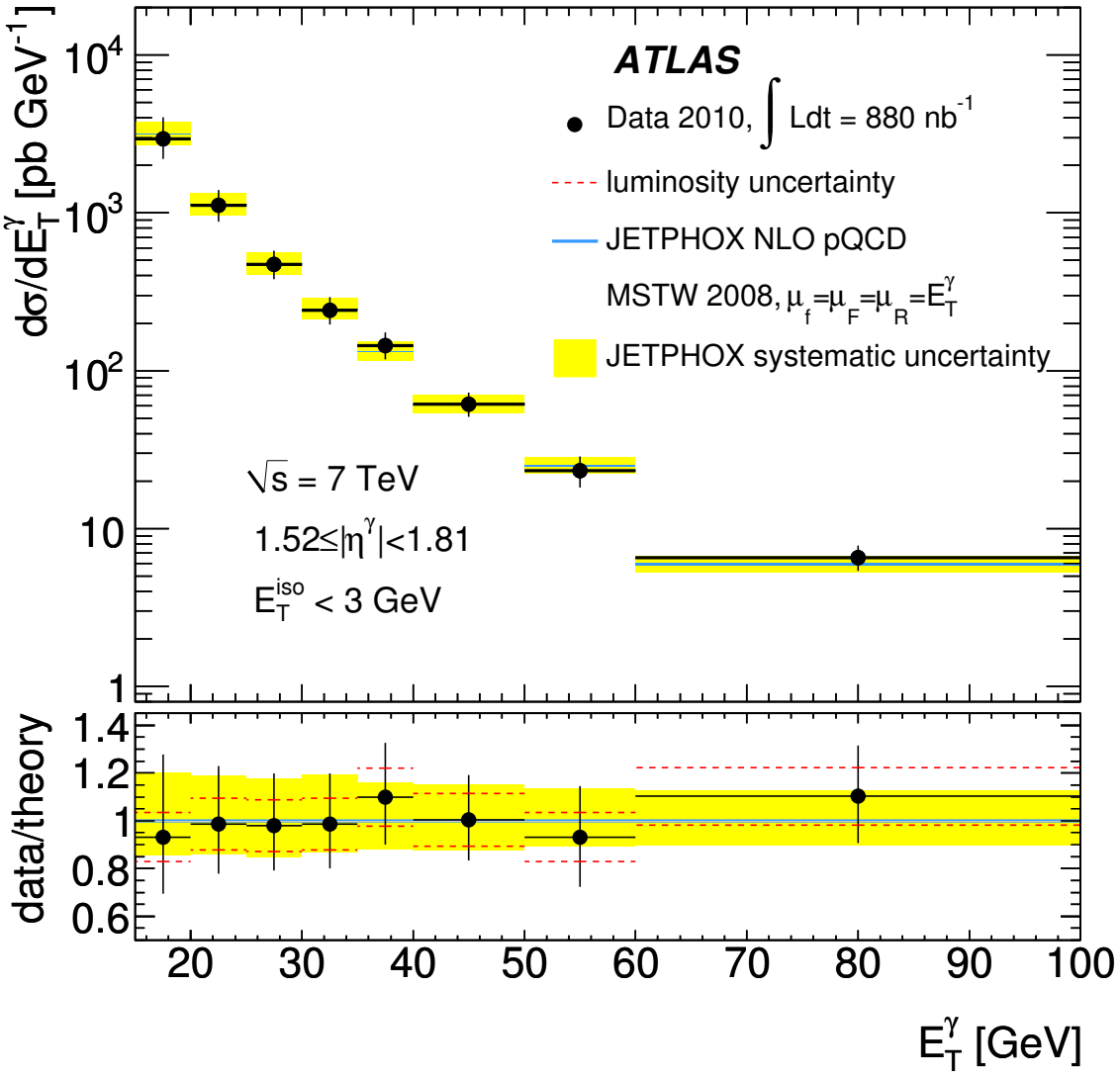


Figure 8.11: Measured vs expected inclusive prompt photon production cross section, for photons with transverse energies above 15 GeV and in the pseudorapidity range $1.52 \leq |\eta^{\gamma}| < 1.81$. Results with the 2D sideband method. The MSTW08 PDFs are used in the theoretical computation [32].

Chapter 9

Prompt photons analysis with full 2010 data LHC runs and comparison with CMS

In this chapter, the results corresponding to the isolated prompt photon cross-section analysis obtained with the full data sample collected by the ATLAS detector during the year 2010 (which is equivalent to an integrated luminosity of 35.5 pb^{-1}) are presented [36, 70]. Moreover, the procedure used to re-optimize of the selection criteria will be quickly described, which was possible because we have recovered the part of the identification at high pseudo-rapidity [1]. Indeed, compared to the previous analysis the full rapidity range up to 2.37 was used after re-optimization of the photon identification cuts. Then, this chapter ends, with a short comparison between ATLAS and CMS results.

9.1 Re-optimization of photon selection criteria

As discussed at the end of the Section 6.5, a re-optimization for the tight selection criteria should be performed in order to recover the high pseudo-rapidity regions ($1.81 \leq |\eta| < 2.37$) for the future analysis and to take advantage of the full acceptance for photons provided by the ATLAS detector.

The first thing to do, is to check how the signal efficiency looks like when the reconstructed photon candidates pass the loose selection criteria, with a $E_T > 20$ GeV and the energy of isolation lower than 3 GeV. If some problems are present in cuts on the discriminating variables on the second layer affecting the signal efficiency, they are identified at this level . On Figure 9.1 one sees an efficiency loss (with respect to others η regions) is found in the outer barrel ($0.6 \leq |\eta| < 1.15$). Moreover, larges differences for efficiencies nominal and corrected (by MC-Data shifts) are found in the outer end-caps ($1.81 \leq |\eta| < 2.37$).

[1] Remember that high η regions were excluded in the first cross section measurement shown in Chapter 8 and [19].

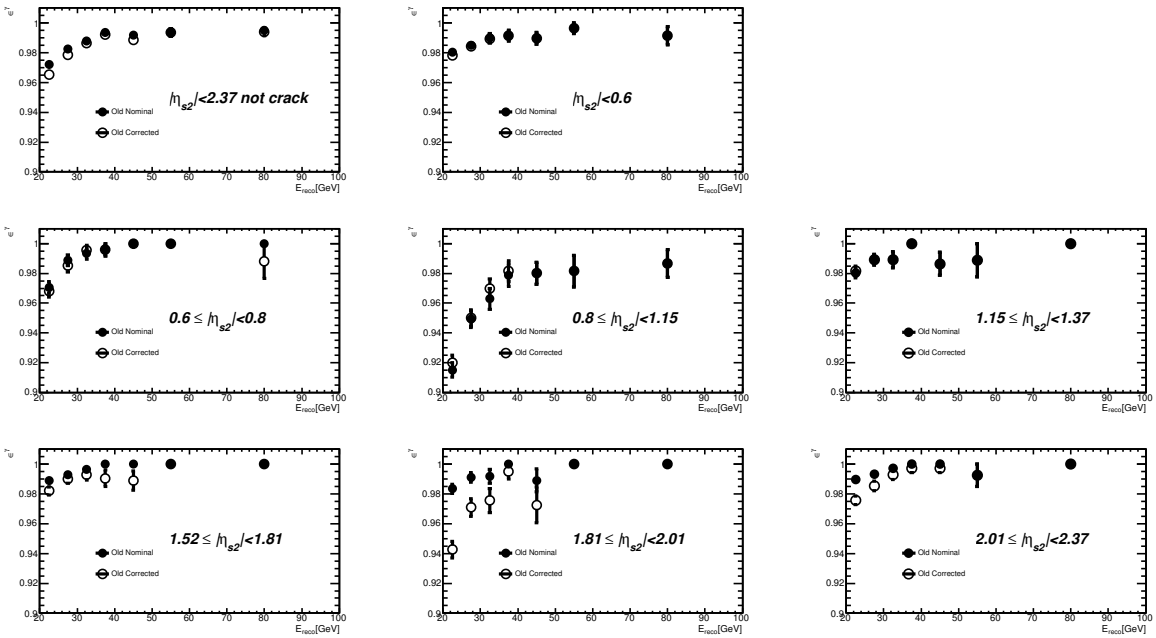


Figure 9.1: Signal efficiency for loose photons (loose is defined here in Table B.1 - it is the one used for the analysis described in Chapter 8 [19]) from the `PYTHIA` Monte Carlo sample JF17. Values used are those shown in Table B.1. Close and open circles represent the nominal and corrected (by the fudge factors defined in Appendix B) efficiencies, respectively.

The strategy followed kept the same criteria than the precedent optimizations, which are listed below:

- Selection cuts are independent of the transverse momentum ($E_T > 20$ GeV is fixed as threshold).

- In general, selection cuts are optimized in the following intervals in pseudo-rapidity

$$|\eta| = \begin{cases} [0.00-0.60), [0.60-0.80), [0.80-1.15), [1.15-1.37) & \text{, } \textbf{barrel} \\ [1.52-1.81), [1.81-2.01), [2.01-2.37) & \text{, } \textbf{end-caps} \end{cases}$$

- The tight selection criteria classifies photons between unconverted and converted (in the loose selection criteria photons are considered as a single object, because this menu is adapted to trigger cuts).

- The main idea of this re-optimization is to try to reach high signal efficiencies and large background rejections, but always looking how it is possible in data and ensure the cuts will be safe and robust in data.

  – *For loose:*
  Try to be safe in the signal efficiency (ϵ^{γ}) , which means reducing the differences

when ϵ^{γ} are computed using the nominal and the corrected (by the fudge factors corresponding to MC-Data shifts) approaches.

  * $\epsilon^{\gamma} > 96 \sim 98\%$ at low p_T and ϵ^{bkg} lower than ≈ 80 to 85% at high p_T (*after having applied the isolation requirement.*)

– *For tight:*
After fixing the new loose criteria, which are then used as benchmark, the re-optimization is performed into two steps (remember the tight cuts are subsets of the loose ones) :

1. Second layer cuts: the goal is to find $\epsilon^{\gamma} \sim 95\%$ [2] at $E_T = 40$ GeV.
2. First later cuts + fixed cuts on the second layer: the idea is to find $\epsilon^{\gamma} \sim 90\%$ at $E_T = 40$ GeV.

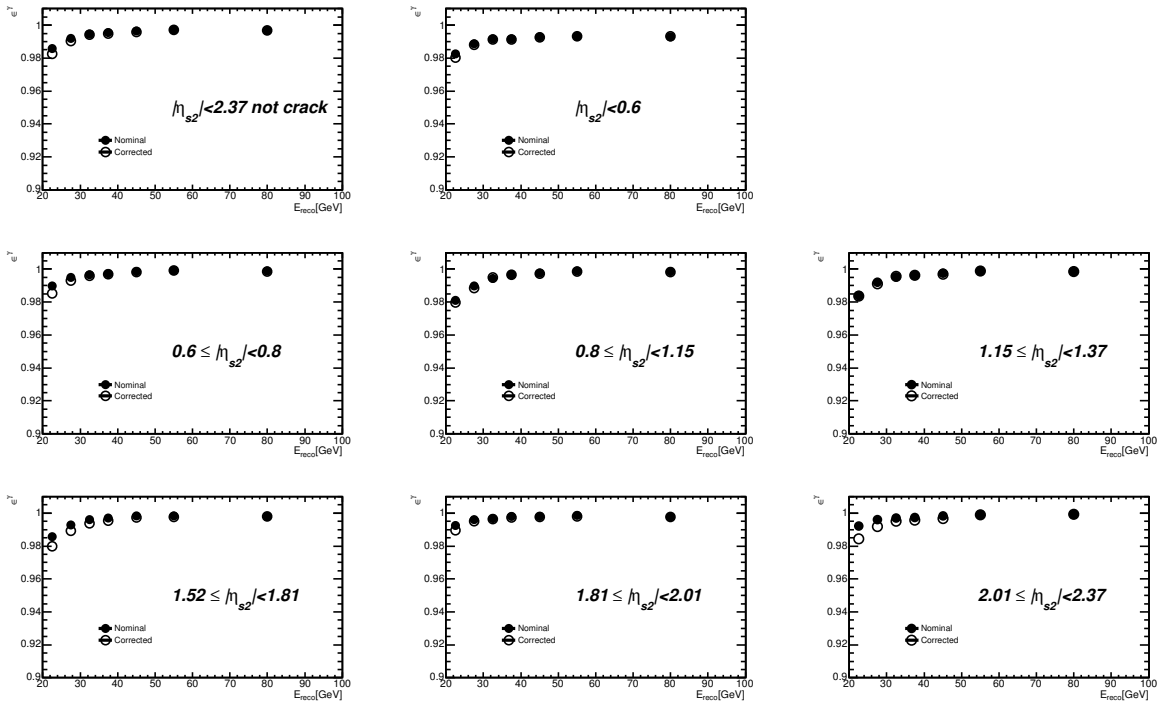


Figure 9.2: Signal efficiency for loose photons (here loose is defined in Table B.5) from the `PYTHIA` Monte Carlo sample γ-jet 17. Values used are those shown in Table B.1. Close and open circles represent the nominal and corrected (by the fudge factors defined in Appendix B) efficiencies, respectively.

After a detailed study, the new loose photons selection was fixed. These cuts were subsequently used in the trigger and offline reconstruction. The values of the cuts are

[2] In order to be consistent with efficiencies found in the other pseudo-rapidity regions.

shown in Table B.5 (they have been changed in four η bins, in particular the large decrease at low E_T on Figure 9.1 was due to non optimal selection criteria). Figure 9.2 shows the efficiency (ϵ^{γ}) with this new selection.

In addition, for the tight selection, criteria were re-optimized [3] leading to new tight menu, whose cut values are shown in Table B.6, which modify the values of Table B.3 . With this new menu systematic effects were mitigated. The ϵ^{γ} (ϵ^{bkg}) was increased (decreased/remained similar) or remained similar (decreased) compared to the previous optimization, depending of the pseudo-rapidity region and the category of the photons.

However looking in detail at 2010 data [4] , some further differences were found between data and Monte Carlo and the cuts were changed for the variable $w_{s\,3}$. The new cuts are in Table B.7. Further details can be found in Appendix B. These are (roughly) the selections used currently in the 2011 runs.

9.2 Isolated prompt photon cross section with 34.6 pb^{-1}

A measurement of the differential cross-section for the inclusive production of isolated prompt photons in pp collisions at a centre-of-mass energy $\sqrt{s} = 7$ TeV is presented, using the same techniques to compute efficiencies, purities and unfolding coefficients shown previously in Chapters 6, 7 and 8, respectively . The measurement covers the pseudorapidity ranges $|\eta| \leq 1.37$ and $1.52 \leq |\eta| < 2.37$, in the transverse energy range $45 \leq E_T < 400$ GeV. The results are based on an integrated luminosity of (34.6 ± 1.2) pb^{-1} , collected with the ATLAS detector at the LHC (here the integrated luminosity is computed using [75], see comment in Figure 3.2).

9.2.1 Collision data

Events are triggered using the `g40_loose` high-level calorimeter trigger [5]. This was the lowest-threshold unprescaled photon trigger during this run period. The integrated efficiency in the plateau region $E_T > 45$ GeV and all η bins is measured to be $(99.4 \pm 0.6)\%$.

9.2.2 Efficiency results

Photon reconstruction and selection

For the results presented here, converted and unconverted photons are treated together in one sample. In the lower η regions (barrel) [6] about 25% of the photons are converted,

[3] Using Release 15 software.
[4] Using the first version of the Release 16 software
[5] The nominal transverse energy threshold of the `g40_loose` trigger is 40 GeV
[6] $|\eta| < 1.37$

rising to $> 33\%$ in the higher η regions (endcap) [7]. After the preselection [8] about 816,000 candidates remain in the data sample. Moreover, after applying the tight identification criteria 290,000 photon candidates remain. Nine photon candidates remain with reconstructed transverse energies above 400 GeV. In the following, all photon candidates with reconstructed isolation energies lower than 3 GeV are considered as experimentally "isolated". Then, after applying this isolation criterion, 174,000 photon candidates remain in the data sample ($\sim 60\%$ of the sample after the tight identification cuts).

Reconstruction efficiencies

The average efficiency of the reconstruction algorithms for isolated direct photons with the transverse energies and within the pseudorapidity ranges mentioned in the beginning of this Section 9.2 and before any further selection is around 97 (92)% in the barrel (endcap) region, dominated by the inefficiency at low E_T. Due to inoperative readout links in the calorimeter, the efficiency above is reduced by around 10% in the inner barrel $\eta < 0.6$ and the outer endcap $1.81 \leq |\eta| < 2.37$ regions, and by around 6% in the pseudorapidity region $0.6 \leq |\eta| < 1.81$. It is further reduced by the experimental isolation requirement by about 14% in the pseudorapidity interval $1.51 \leq |\eta| < 1.81$ and by about 5% in the rest of the acceptance region.

The main source of systematic uncertainties is related to the knowledge of the material in front of the calorimeter. This leads to an uncertainty in the reconstruction efficiency ranging from 1% to 4% depending on the photon candidates η and E_T. The systematic uncertainty on the reconstruction efficiency from the experimental isolation requirement has been found to vary from 3% in the inner barrel to 4% in the inner endcap. All the other sources of systematic uncertainties (hard-process/fragmentation-photon relative composition; differences between the MC generators; the imperfect simulation of acceptance losses due to inoperative readout links in the calorimeter) add $< 2\%$ in total to the reconstruction efficiency uncertainty.

Offline efficiency estimation

The offline efficiency has been estimated in the same way as was presented in Section 6.5. Several sources of systematic uncertainty which affect the precision:

- Intrinsic precision of the correction method for the shower-shape variables: depending on the η region, this uncertainty ranges between 1 and 3%.

- Choice of photon candidate sample to estimate the correction factors: the photon identification efficiencies evaluated for different sample selections (e.g. using different photon shower shape variables) agree within 0.5%.

[7] $1.52 \leq |\eta| < 2.37$

[8] $E_T > 45$ GeV + `g40_loose` + $|\eta| < 1.37$ or $1.52 \leq |\eta| < 2.37$ + quality checks remaining similar to the first γ analysis.

- Knowledge of the material in front of the calorimeter: this uncertainty is estimated to be $< 1\%$ in the barrel regions and $< 2\%$ in the endcap regions. One should note that the impact of the distorted geometry on the efficiency has diminished compared to what was done in the previous paper [19]. Indeed the distorted geometry used now has less ID material than the one used in [19] (this is due to additional work done by tracking experts).

- Hard-process/fragmentation-photon relative composition: varying the sample composition of the two types of photons by as much as 100% affects the global identification efficiencies by $< 1\%$. An additional 1% is assigned if one uses a different MC generator.

- Classification between converted and unconverted photon candidates: the impact of the classification between converted and unconverted photon candidates is studied varying the efficiency of correctly classifying converted photon candidates in the simulation. A loss of less than 1% on the overall efficiency is found for a -10% change in the efficiency to classify correctly converted photons.

The total systematic uncertainties on the photon identification efficiency are $< 2\%$ at low η, and $< 3\%$ at large η. Figure 9.3 shows the identification efficiencies in the different η regions as a function of the photon candidate E_T together with the corresponding systematic uncertainties, obtained with 34.6 pb^{-1} of total integrated luminosity.

9.2.3 Purity results

In the same spirit, the background estimation and signal extraction for this new measurement was computed using the "two-dimensional sidebands" method (Chapter 7, Section 7.1). The corresponding purity are displayed in Figure 9.4.

Systematic uncertainties associated with this method are listed below.

- Photons in background control regions failing varying definitions of non-tight selection: the systematic uncertainty on the signal yield is up to 5% depending on the pseudorapidity and transverse energy bin.

- Photons in background control regions failing varying definitions of the isolation criterion: the effect on the signal yield is estimated to be less than 1% in all pseudorapidity bins.

- Signal leakage into background control regions: the effect of this variation on the photon yield estimate ranges from 2% to 8%. Varying the mixture of hard-scattering and fragmentation photons between the extreme conditions of pure hard photons and pure fragmentation photons adds another 1% to 7% to the systematic uncertainty with the higher values corresponding to the lower transverse energy bins.

- Background correlations: the uncertainty on the photon yield estimate is evaluated to be up to 4% in the high transverse energy bins independent of the pseudorapidity bin.

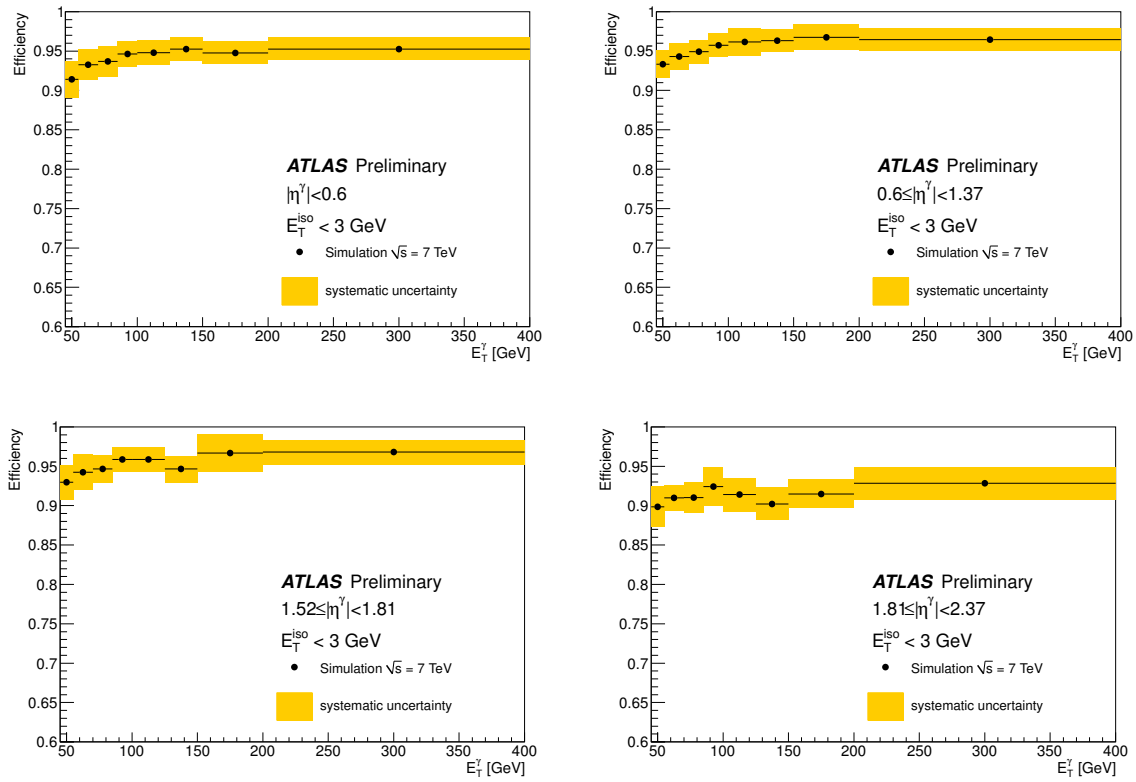


Figure 9.3: Photon offline selection efficiency as a function of the reconstructed photon transverse energy [72]. Top left: $|\eta| < 0.6$. Top right: $0.6 \leq |\eta| < 1.37$. Bottom left: $1.52 \leq |\eta| < 1.81$. Bottom right: $1.81 \leq |\eta| < 2.37$.

- Photon energy scale: the systematic uncertainty on the yield varies between 2% to 8%. One can note that, since there have been some extensive studies on the energy scale using Z's [5] since the previous paper [19] the systematic uncertainty is now smaller.

- Material effects: these are found to contribute less than 1% in the photon signal estimation uncertainty in all pseudorapidity bins.

- Soft-jet energy density: the systematic uncertainty ranges from 3% to 7%.

- Shower transverse energy leakage: the systematic uncertainty is increasing with the photon transverse energy from 1% to 4%.

- MC generator dependence: the corresponding systematic uncertainty $\sim$ 1% for all pseudorapidity bins.

The fraction of electrons that have been misidentified as photons has also been estimated. It is measured by studying the invariant mass spectrum of $e^{\pm}\gamma$ combinations in the $Z-$mass range. The electron contamination has been found to range from 1.2% (1.7%) at low E_T in the barrel (endcap) to around 1% at high E_T in the full η range.

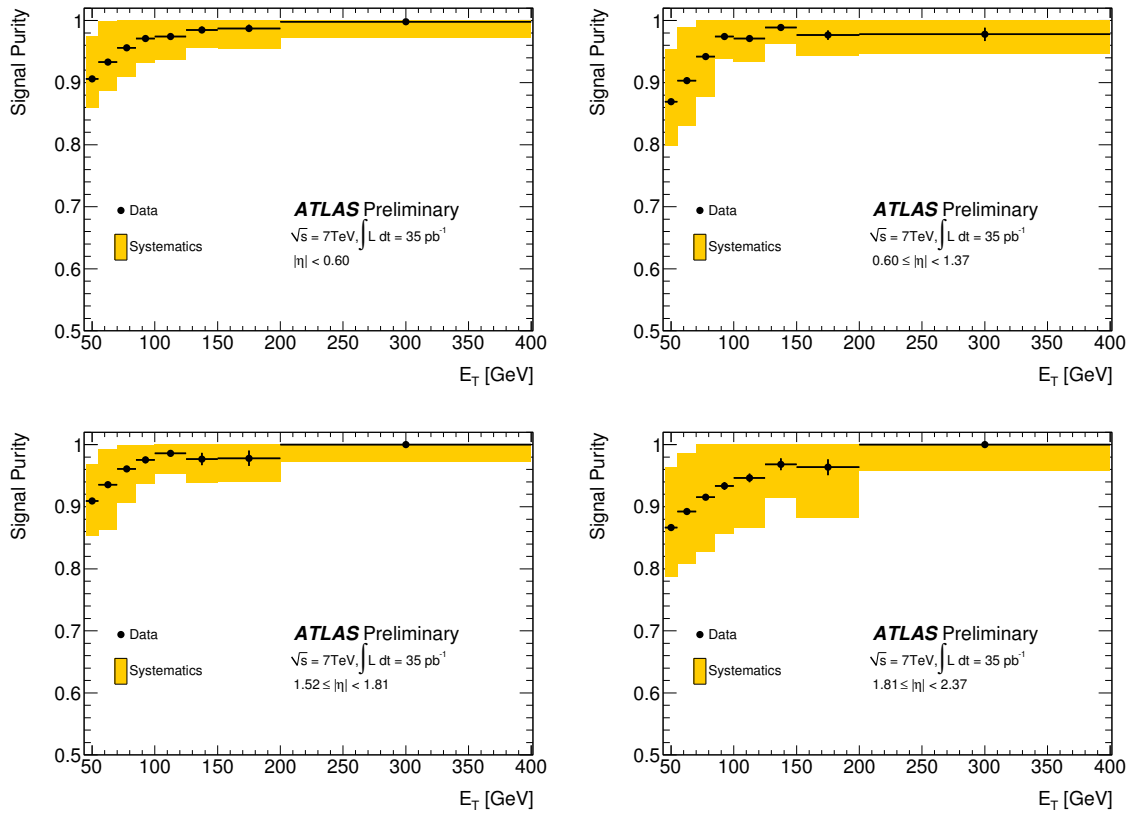


Figure 9.4: Photon purity with statistical errors as a function of E_T [72], for each η region, from two-dimensional sidebands. The yellow band represents the total systematic error.

9.2.4 Cross section measurements

The cross section measurement was computed following the same recipe presented in Chapter 8 (using Equation 8.1 to get results). These are shown in Figures 9.5 and 9.6 together with the theoretical predictions superimposed, which have been computed with `JETPHOX` using the PDFs CTEQ6.6 and MSTW08, respectively. Some comparison with the first analysis [19] is also shown. One can note [5] that there have been some corrections to the energy scale of the liquid Argon Calorimeter between the two analyses that have not been taken into account (for instance the energy scale of the end-cap decreased by $\approx 2\%$ which translates in a change of the cross section of [19] by $\approx -7\%$).

The full list of systematic uncertainties that enter the final uncertainty in the estimated cross-section is summarized in Table 9.2.4.

The theoretical systematic uncertainties on the QCD cross-sections are estimated in the following way:

- The scale uncertainty has been evaluated by varying the three scales following the constraints:
  - $\mu_R = \mu_F = \mu_f \in [0.5\,E_T, 2.0\,E_T]$;

– $\mu_R \in [0.5\,E_T, 2.0\,E_T]\,, \mu_F = \mu_f = 1.0\,E_T$

– $\mu_F \in [0.5\,E_T, 2.0\,E_T]\,, \mu_R = \mu_f = 1.0\,E_T$

– $\mu_f \in [0.5\,E_T, 2.0\,E_T]\,, \mu_R = \mu_F = 1.0\,E_T$

This leads to a change of the predicted cross-section between 20% at low E_T and 12% at high E_T with the contribution from the renormalization scale uncertainty being the largest in most cases.

- The uncertainty on the cross-section from the PDF uncertainty has been obtained by varying the PDFs within the 68% C.L. intervals. The corresponding uncertainty on the cross-section varies between 5% and 2% as E_T increases between 45 and 400 GeV.

- The uncertainty on the parton-level isolation cut has been evaluated by varying the cut between 2 and 6 GeV. This change the predicted cross-section by 2% at most.

Systematic	Reco. Eff.	ID Eff.	Yield	Unfolding	Theory
Finite Statistics per bin				$< 2\%$	
Generator	1%	$< 1\%$	$\sim 1\%$	3%	
E_T Resolution				$< 1\%$	
Photon ID			$< 5\%$		
Photon Isolation			$< 1\%$		
Signal Leakage			$2\% - 8\%$		
Background Correlations			$< 4\%$		
Energy Scale			$2\% - 8\%$		
Material	$1\% - 4\%$	$1\% - 2\%$	$< 1\%$		
Soft-jet Energy Density			$3\% - 7\%$		
Transverse Energy Leakage			$1\% - 4\%$		
Hard/Brem Composition	1%	$< 1\%$	$1\% - 7\%$		
OTX	0.2%				
Photon Isolation Cut	$3\% - 4\%$				
Intrinsic Precision		$1\% - 3\%$			
Photon Sample Selection		0.5%			
Conv/Unconv. Photon Ratio		$< 1\%$			
Scale uncertainty					$10\% - 20\%$
PDFs					$2\% - 5\%$
Parton level Isolation					$< 2\%$

Table 9.1: List of systematic uncertainties used for the cross-section estimation. Correlated sources of systematic uncertainties have been consistently treated. The last column lists the uncertainties on the theoretical predictions that are used to compare the measured cross-section to.

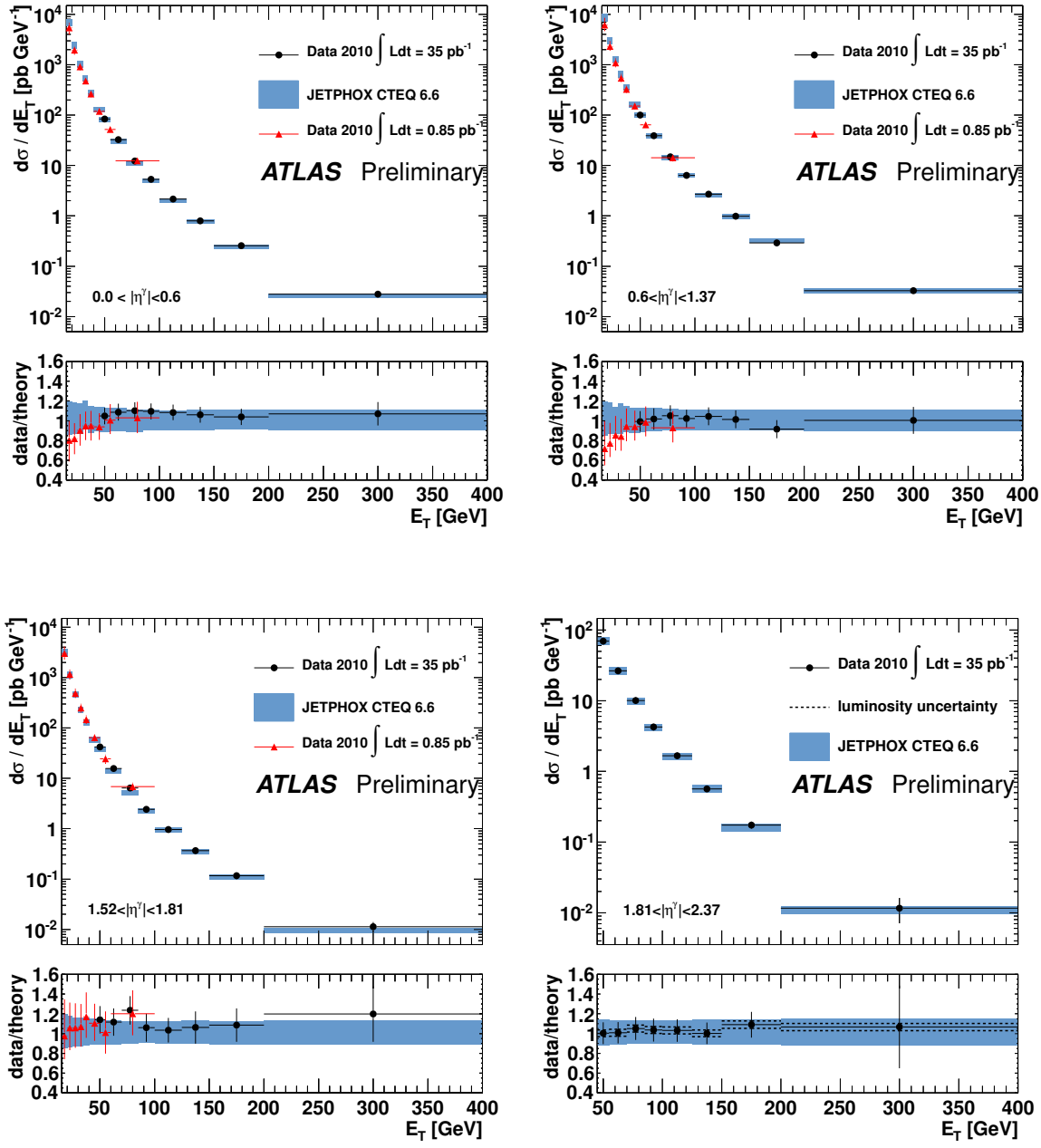


Figure 9.5: Measured vs expected inclusive prompt-photon production cross-section, for photons with transverse energies above 45 GeV in the pseudorapidity range $|\eta| < 0.6$ (top left), $0.6 \leq |\eta| < 1.37$ (top right) and $1.52 \leq |\eta| < 1.81$ (bottom left). The CTEQ6.6 PDFs are used in the JETPHOX theoretical computation. The previous cross-section measurement [19] is also shown (rescaled by the new luminosity central value, i.e. divided by 0.964) extending the overall energy coverage down to 15 GeV. The experimental values are placed at the center of each energy bin. The width of the horizontal bars indicates the size of the bin [72].

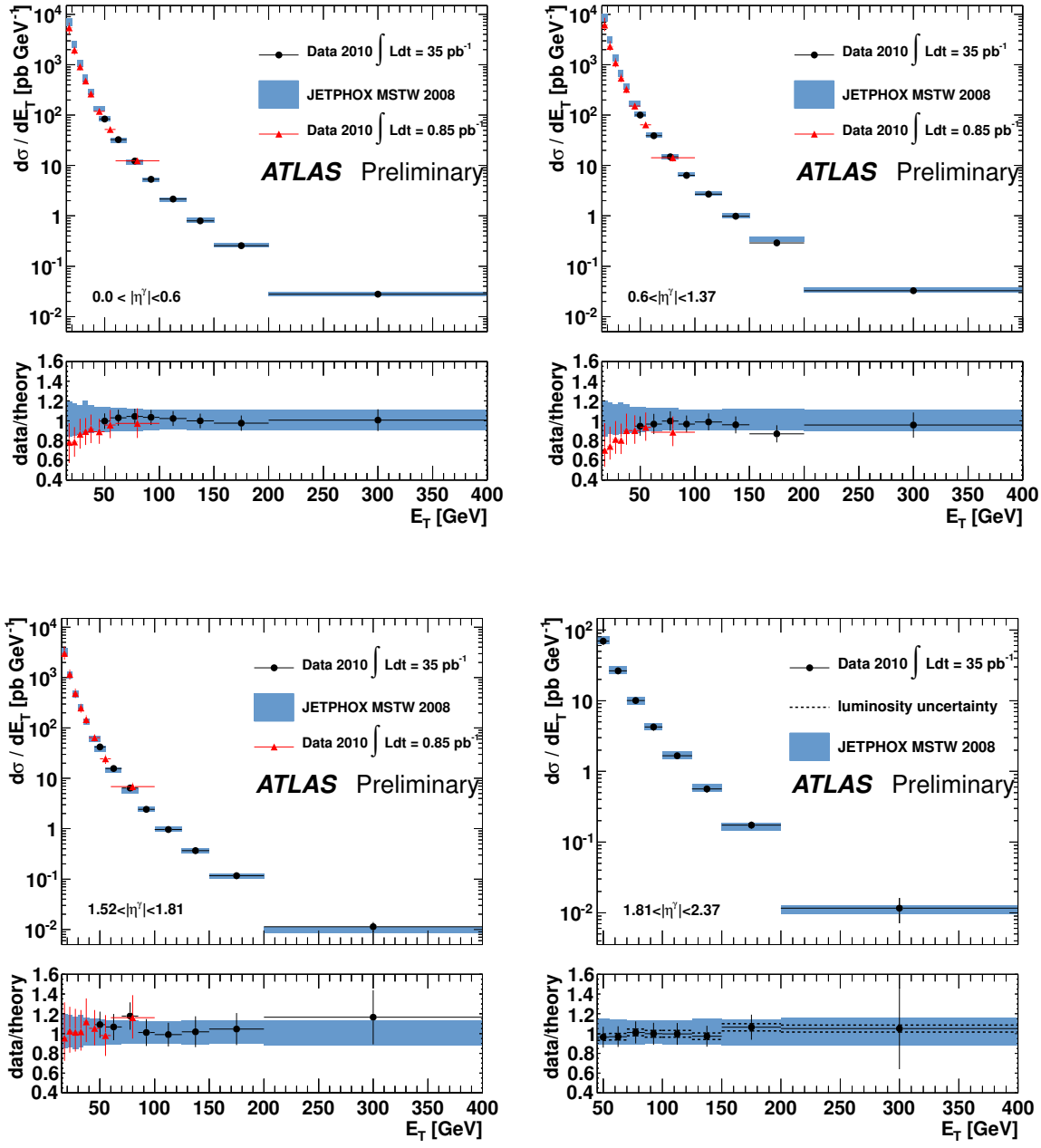


Figure 9.6: Measured vs expected inclusive prompt-photon production cross-section, for photons with transverse energies above 45 GeV in the pseudorapidity range $|\eta| < 0.6$ (top left), $0.6 \leq |\eta| < 1.37$ (top right) and $1.52 \leq |\eta| < 1.81$ (bottom left). The MSTW08 PDFs are used in the JETPHOX theoretical computation. The previous cross-section measurement [19] is also shown (rescaled by the new luminosity central value, i.e. divided by 0.964) extending the overall energy coverage down to 15 GeV. The experimental values are placed at the center of each energy bin. The width of the horizontal bars indicates the size of the bin [72].

9.2.5 Conclusion

A measurement [72] of the differential cross-section for the inclusive production of isolated, prompt photons with $E_T > 45$ GeV in pp collisions at a centre-of-mass energy of $\sqrt{s} = 7$ TeV has been performed, using 35 pb^{-1} of 2010 pp collision data collected with the ATLAS detector at the LHC. The results are compared to next-to-leading order theoretical predictions in four pseudorapidity ranges spanning the range $0 < |\eta| < 2.37$. Good agreement between the data and the theoretical predictions is observed.

The current measurement is an extension to higher photon transverse energies and higher pseudorapidity ranges ($|\eta| > 1.81$) of the inclusive cross-section measured in [19]. In the higher transverse-energy regions ($E_T > 150$ GeV), the available statistics becomes rather limited and the resulting uncertainties are higher. This is expected to be remedied with the new LHC runs during 2011-2012 data-taking.

9.3 A short comparison between ATLAS and CMS results

The CMS experiment [112] produced also a measurement of the isolated photon cross section [167] for reconstructed photon candidates in the pseudorapidity range $|\eta| < 1.45$ (barrel region) and $21 \leq E_T < 300$ GeV of transverse energy with a total integrated luminosity of 2.9 pb^{-1} from LHC 2010 pp collision runs.

Here in this Section, some of the main aspects of the CMS measurement of the isolated photon cross section are discussed, based on their published measurement [167], on their photon reconstruction note [110] and on a recent diphoton paper on search for large extra dimensions [105].

9.3.1 Photon identification and isolation

Photon identification in CMS is based on the following variables:

- `H/E` : The fraction of hadronic energy to total electromagnetic energy inside a cone of $\Delta R = 0.15$ is computed from the energy deposition in HCAL (Hadronic calorimeter) and ECAL (Electromagnetic calorimeter). For photons this ratio should be low, while for jets, which carry both hadronic and electromagnetic energy, it will generally be higher.

- $\sigma_{i\eta i\eta}$: The transverse shape of the electromagnetic cluster. This is computed with logarithmic weights and is defined as

$$\sigma^2_{i\eta i\eta} = \frac{\sum^{5\times5} w_i \left(\eta_i - \bar{\eta}_{5\times5}\right)^2}{\sum_i^{5\times5} w_i}, \quad , w_i = \max\left(0, 4.7 + \ln\frac{E_i}{E_{5\times5}}\right) \tag{9.1}$$

where E_i and η_i are the energy and pseudorapidity of the i^{th} crystal within the 5×5 electromagnetic cluster and $E_{5\times5}$ and $\eta_{5\times5}$ are the energy and η of the entire 5×5 cluster.

- Iso_{TRK} : The track isolation is computed as the sum of the transverse momenta of all tracks in a full cone ($\Delta R_0 = 0.4$) centered around a line joining the primary vertex to the cluster. Tracks in an inner cone ($\Delta R_0 = 0.04$) and η-slice ($\Delta\eta = 0.015$) are not included to avoid misidentification of converted photons. In addition, tracks with a transverse (longitudinal) impact parameter above 0.1 (0.2) cm are also not included.

- Iso_{ECAL} : The ECAL isolation is computed as the E_T sum over the energy deposits in a cone ($\Delta R_0 = 0.4$), centered around the super-cluster [9] with a veto cone ($\Delta R_i = 3.5$ crystals) and eta-slice ($\Delta\eta = 2.5$ crystals) to avoid misidentification of converted photons.

- Iso_{HCAL} : The HCAL isolation is computed as the sum of the transverse energy in the HCAL towers in a hollow cone with an inner radius of $\Delta R_i = 0.15$ and an outer radius of $\Delta R_0 = 0.4$, that is centered around the super-cluster.

The values of the cuts adopted for the loose and tight selections are summarized in Table 9.2.

Variable	Loose		Tight	
	Barrel	Endcap	Barrel	Endcap
Iso_{TRK}	2.0 GeV		0.9 GeV	
Iso_{ECAL}	4.2 GeV		2.4 GeV	
Iso_{HCAL}	2.2 GeV		1.0 GeV	
H/E	0.05		0.03	
$\sigma_{i\eta i\eta}$	0.01	0.03	0.01	0.028

Table 9.2: Cut thresholds for the barrel and the endcap regions [110].

9.3.2 Estimation of signal efficiency

To estimate signal efficiency, a data driven technique (so-called "tag-and-probe" [10]) was applied [109]. The efficiency is computed by counting the fraction of reconstructed Z

[9] The barrel ECAL is constructed with lead tungstate crystal that are arranged in a projective geometry. In this region of ECAL, superclusters are formed from the energy sum clustered in a rectangle of crystal 35 wide in ϕ and 5 wide in η.

[10] A well identified electron conventionally defined as the "tag" is required. It is combined with the "probe" photon candidate which matches, together with the tag, the Z mass within a $50 < M_{ee} < 120$ GeV window.

corresponding to the probe photons (passing probe) over the total number of probe events, which is the sum of passing and falling probe Z control sample.

	Loose		Tight	
E_T [GeV]	MC	DATA	MC	DATA
$20-35$	$84.18 \pm 0.20\%$	$86.73 \pm 1.69\%$	$69.38 \pm 0.18\%$	$69.58 \pm 2.80\%$
$35-45$	$87.27 \pm 0.19\%$	$89.28 \pm 1.27\%$	$72.78 \pm 0.18\%$	$71.94 \pm 2.09\%$
$45-\text{inf}$	$88.50 \pm 0.23\%$	$89.04 \pm 1.83\%$	$74.93 \pm 0.22\%$	$72.48 \pm 2.92\%$
TOT	$86.30 \pm 0.12\%$	$88.41 \pm 0.89\%$	$71.90 \pm 0.11\%$	$71.31 \pm 1.47\%$

Table 9.3: Efficiency measured in data and simulation using the $Z \rightarrow e^+e^-$ control sample for the loose and tight photon selections are listed in Table 9.2 (for the ECAL Barrel ($|\eta| < 1.4442$)) [110].

In the first publication of CMS on the isolated photons [11] [167], the photon reconstruction and selection efficiencies were determined from PYTHIA events with prompt photons and are scaled by the factor ρ_ϵ (the efficiency of the isolation criteria is measured in data using the method mentioned above and is found to be higher than in simulation by $\rho_\epsilon = 1.035 \pm 0.017(\text{stat + syst})$), providing an estimation of $\epsilon^\gamma = 0.916 \pm 0.034(\text{stat + syst})$, which does not change appreciably with E_T^γ or η^γ. These values (used in the CMS publication) are quoted for the CMS photon loose selection criteria (see Table 9.2).

On the other hand, ϵ^γ provided by the ATLAS analysis [19], which are computed using the tight selection criteria in the barrel region ($|\eta| < 0.60$ and $0.60 \leq |\eta| < 1.37$) varies between $\sim 73\%$ to ~ 85 for the E_T bins $20 \leq E_T < 25$ GeV and $30 \leq E_T < 35$ GeV, respectively. For the intermediate E_T range ($35 \leq E_T < 40$ GeV and $40 \leq E_T < 50$ GeV) the ϵ^γ for $|\eta| < 0.6$ ($0.60 \leq |\eta| < 1.37$) varies between $\sim 85(89)\%$ to $\sim 89(92)\%$, respectively. Finally, the ϵ^γ for the high E_T ranges ($50 \leq E_T < 60$ and $60 \leq E_T < 100$ GeV) were computed and they are bigger than $91(94)\%$ for $|\eta| < 0.60$ ($0.60 \leq |\eta| < 1.37$).

In general, one can see that in the high E_T range the efficiencies [12] computed by both experiences are largely compatible. For the intermediate and low E_T range, one see small differences between the estimated values (the 'loose' CMS efficiencies being higher), which are due to the fact that in CMS the loose cuts are expected to be looser that those for the tight selection used in ATLAS. The differences between the ATLAS tight cuts and the CMS tight cuts are not studied here. The tight CMS cuts, like the loose CMS cuts have an efficiency varying less with E_T (see Table 9.3). The ATLAS cuts on the first sample are tight and sensitive to variations of the variables (mean value and fluctuations) with E_T.

A better understanding of the effect of the selection cuts should be achieved in the next Subsection 9.3.3, where the method of signal extraction used for CMS is presented and compared with the purity results reported by ATLAS.

[11] About the measurement of the isolated photon cross section

[12] All values of ϵ^γ computed by ATLAS were taken from Table 6.10.

9.3.3 Signal extraction and background estimation

The isolated prompt photon yield is estimated with a binned extended maximum likelihood fit to $\sigma_{i\eta i\eta}$ distribution with the expected signal and background components. The signal component shape is obtained from photon events generated with `PYTHIA 6.420`. The background component shape is extracted from data by taking the $\sigma_{i\eta i\eta}$ distribution of events in a background-enriched isolation sideband defined by requiring $2 < \mathrm{Iso_{TRK}} < 5$ GeV, while keeping all other selection criteria unchanged. This choice provides a sufficient number of events while minimizing the bias to the $\sigma_{i\eta i\eta}$ distribution due to the positive correlation between $\sigma_{i\eta i\eta}$ and $\mathrm{Iso_{TRK}}$. Both signal and background shapes are obtained separately for each E_T bin. Figure 9.7(left) shows the result of the two-component fit. Figure 9.7(right) shows the comparison between the distributions for the background enriched sample obtained from the side-band selection in the track isolation in data and the simulation prediction for the background in the signal region are also included.

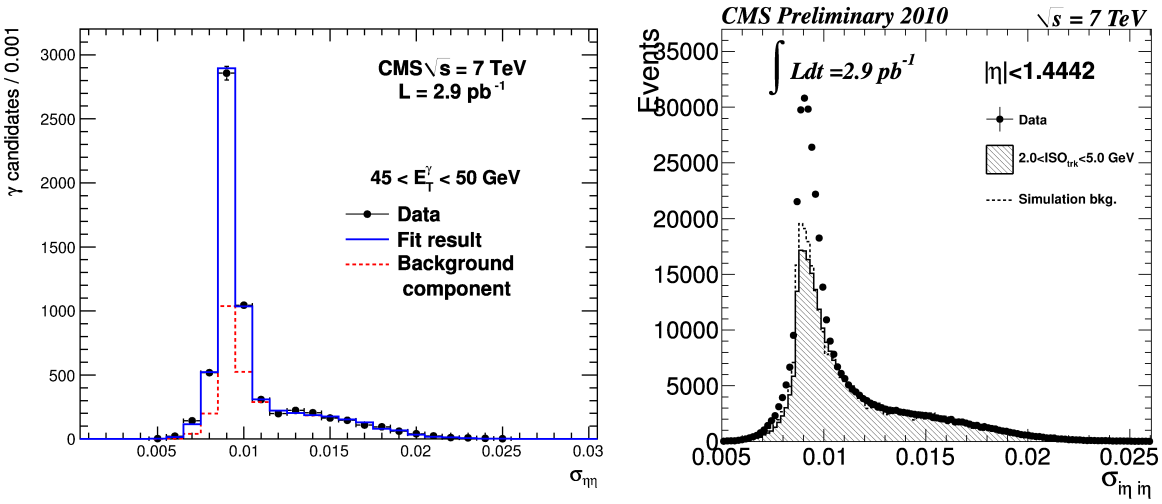


Figure 9.7: Measured $\sigma_{i\eta i\eta}$ distribution (color online) for photons with $45 < E_T < 50$ GeV is shown in left plot. The fit result (solid) and the background component (dashed) are also shown. In the right plot is shown the measured $\sigma_{i\eta i\eta}$ for photons $E_T > 21$ GeV in the barrel. Solid histogram shows the distribution for the side-band selections in the track isolation described in the text. Plates were taken from [167] and [110], respectively.

For $\sigma_{i\eta i\eta} < 0.01$, the fraction of isolated prompt photons in data after full selection increases from 38% at $E_T^\gamma = 25$ GeV to 80% at $E_T^\gamma = 100$ GeV [167]. This corresponds to the purity computed using the loose selection criteria, whose central values are shown in black squares inside red bands in Figure 9.8 [110]. In the same Figure 9.8, the central values corresponding to the purity computed with the tight selection criteria are presented in black triangles inside blue bands. For these, by eye, one can see that the purity increases from $\approx 54\%$ at $E_T^\gamma = 25$ GeV to $\approx 90\%$ at $E_T^\gamma = 100$ GeV.

The central values of the purity computed by ATLAS increases from 66(56)% at $20 \leq E_T < 25$ GeV to 96(91)% at $60 \leq E_T < 100$ GeV in the pseudorapidity range of $|\eta| < 0.60$

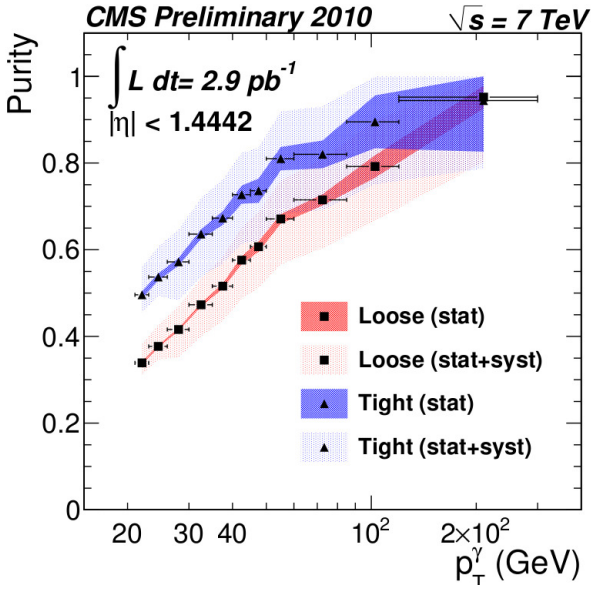


Figure 9.8: Measured purity for the sample defined by the cluster shape method as a function of photon p_T. Plot shows the barrel region. Results for loose and tight photon selections are overlaid. The shadow bands show the statistical only and the quadratic sum of statistical and systematic uncertainties [110].

($0.60 \leq |\eta| < 1.37$), respectively [13]. In addition, in Figure 9.9 are shown the distributions for the isolation, where the difference between tight and normalized non-tight candidates is considered as a measurement of the signal yield [14]. In this both plots, with candidates in the E_T bin of [40-50] GeV purities have been estimated to be bigger than 85% (the exact values of purity could be found in Table 7.2). One can be tempted to compare the purity values of ATLAS with those reported by CMS indirectly in Figure 9.7 and more explicitly in Figure 9.8. For this last, by eye, one sees that using the tight(loose) selection in CMS the purity seems to be close to 80(68)% in the barrel region for the E_T bin of [45,50) GeV.

In general, one can say that when a comparison is performed between central values of purity between ATLAS and CMS a trend was found at low and at the intermediate transverse energy ranges. So, the central values of purity reported by ATLAS are higher than these ones shown by CMS. This differences can be explained, due to the use of the first sampling variables in the tight selection in ATLAS and their powerful capability to reject efficiently the background.

9.3.4 Cross-sections comparison

The measured isolated prompt photon cross section from CMS as a function of E_T , including both statistical and total systematic uncertainties, is reported in Figure 9.10.

[13] ATLAS' purity values were taken from Table 7.2.

[14] In the signal region $E_T^{(R<0.4)} < 3$ GeV.

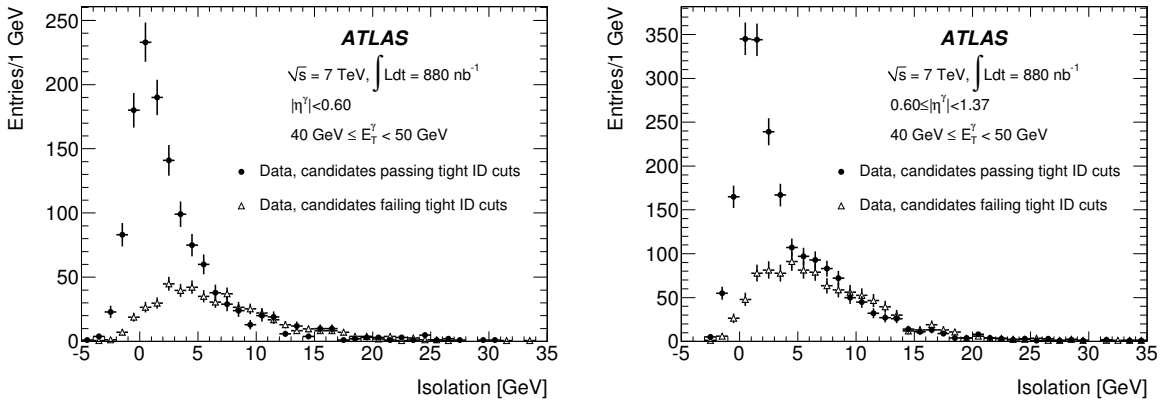


Figure 9.9: The distributions for the calorimetric isolation variable, for tight (dots) and non-tight (triangles) photon candidates, the latter distribution normalized to the former in the non-isolated region $E_T^{(R<0.4)} > 5$ GeV. The left plot corresponds to candidates in the pseudorapidity region $|\eta| < 0.60$ and the right plot for $0.60 \leq |\eta| < 1.37$, both in the E_T bin of [40,50) GeV. The excess of tight candidates over the normalized non-tight candidates in the isolated region $E_T^{(R<0.4)} < 3$ GeV proves the evidence of a signal [30].

The 11% overall uncertainty on the integrated luminosity is considered separately. In Figure 9.10, the data are shown together with the NLO pQCD predictions from `JETPHOX 1.1` [7, 104] and the BFG set II of fragmentation functions (FF) [99]. The renormalization, factorization, and fragmentation scales ($\mu_R, \mu_F,$ and μ_f) are all set to E_T . The hadronic energy surrounding the photon is required to be at most 5 GeV within $R < 0.4$ [15] . To estimate the effect of the choice of theory scales in the predictions, the three scales are varied independently and simultaneously between $0.5\times E_T$ and $2\times E_T$. Retaining the largest variations the predictions change by (+30,-22)% to (+12,-6)% with increasing E_T. It is probably because the three scales are varied independently in CMS, contrary to ATLAS, that this uncertainty is larger in CMS.

The uncertainty on the predictions due to the PDF's is estimated by using three global-fit parametrizations, CT10, MSTW2008 [178] and NNPDF2.0 [86], as recommended by the PDF4LHC Working Group [98]. The theoretical predictions include an additional correction factor $C(E_T)$ to account for the presence of contributions from the underlying event and parton-to-hadron fragmentation, which tend to increase the energy in the isolation cone. Using simulated `PYTHIA` events, C is determined as the ratio between the isolated fraction of the total prompt photon cross section at the hadron level and the same fraction obtained after turning off both multiple-parton interactions and hadronization. The value $C = 0.97 \pm 0.02$ is taken as the correction. Prediction from NLO pQCD are found to be in good agreement with the measured cross sections, as shown in Figure 9.10.

The CMS measurement of the differential cross section for the production of isolated prompt photons with $21 < E_T < 300$ GeV and $|\eta| < 1.45$ [167] can be compared directly

[15] In the analysis of ATLAS, this energy was required to be smaller than 4 GeV [19].

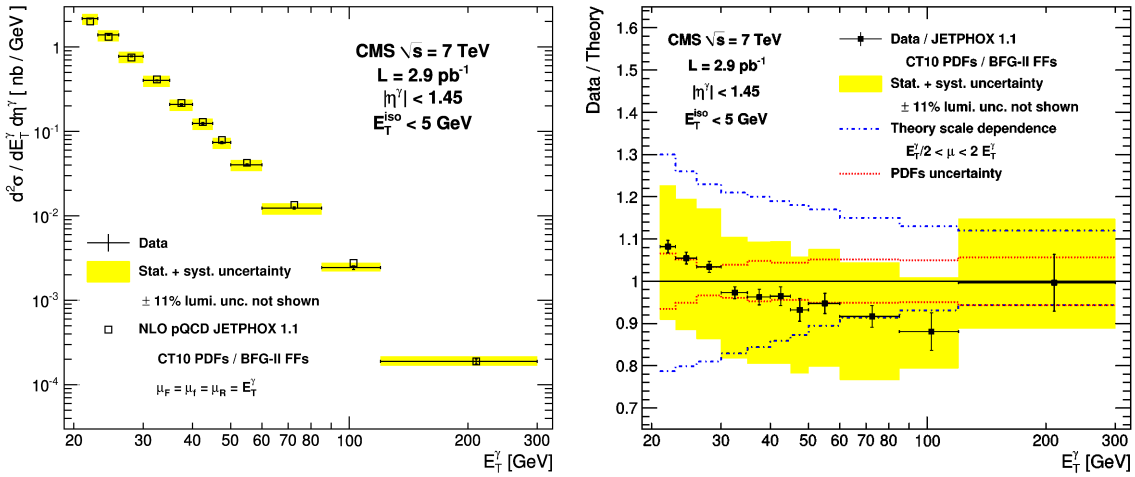


Figure 9.10: In the left plot is presented the measured isolated prompt photon differential cross section and NLO pQCD predictions, as a function of E_T . The vertical error bars show the statistical uncertainties, while the shaded areas show the statistical and systematic uncertainties added in quadrature. The 11% luminosity uncertainty on the data is not included. In the right plot is shown the ratio of the measured isolated prompt photon differential cross setion to the NLO pQCD predictions. The two sets of cursves show the uncertainties on the theoretical predictions due to their dependency on the renormalization, factorization, and fragmentation scales, and on the PDF's [167].

with the same measurement performed by the ATLAS Collaboration [19], in the barrel region (pseudorapidity regions $|\eta| < 0.60$ and $0.60 \leq |\eta| < 1.37$) with $15 \leq E_T < 100$ GeV, as is shown in Figure 9.11. Figure 9.11 shows a good agreement between the measured isolated cross sections of each experiment with some differences at low E_T, despite the different methods used by each collaboration.

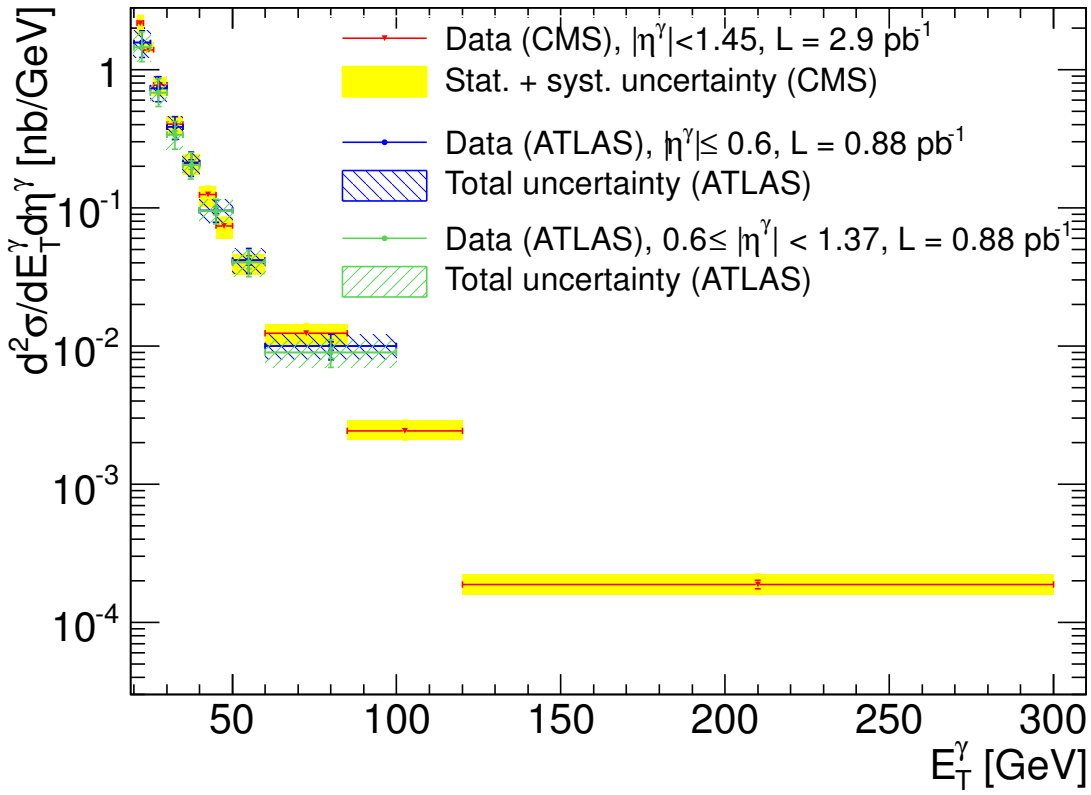


Figure 9.11: Comparison between the mesuared isolated prompt photon differential cross section provided by ATLAS [19] and CMS [167]. The CMS results are in red, while yellow shaded areas represent their statistical and systematic uncertainties, added linearly. The ATLAS results are in blue and green, according the pseudorapidity range ($|\eta| < 0.60$ and $0.60 \leq |\eta| < 1.37$, respectively). In this Figure the ATLAS first point cross-section measurement, E_T bin :$[15-20)$ GeV, is not shown. The statistical and systematic uncertainties are shown by inclined line areas, added linearly.

Chapter 10

Contribution to the data analysis of the SM Higgs boson decaying into two photons

In this chapter the first result of the ATLAS search for the SM Higgs boson (for the mass range of $110 < m_H < 150$ GeV) in the diphoton decay channel with the 38 pb^{-1} of collected data in 2010 at a center-of-mass energy of 7 TeV is presented. The chapter ends showing the results on the observed exclusions. A simulation-based study of signal, incorporating the best current knowledge of the detector performance, is presented and used in the limit setting [35, 70].

10.1 Data and simulated samples

10.1.1 Event selection and reconstruction

The events are selected by a trigger which requires two photon candidates each with transverse energy exceeding 15 GeV. In addition the events have to fulfill the criteria that the detector was fully operational. For the surviving events, at least two photon candidates in the central detector region with $p_T > 25$ GeV, and passing the loose photon identification criterion (whose cuts are shown in Table B.5) are required. The kinematic cuts demanding transverse energy larger than 40 GeV and 25 GeV are applied on the leading and subleading photon candidates respectively. Moreover tight photon identification (from Tables B.5 and B.6) and isolation criteria are applied (with a energy of isolation smaller than 3 GeV). The direction of the photon candidates is measured using the information from the first sampling of the electromagnetic calorimeter and on the measured position of the primary vertex. For events with more than one vertex reconstructed, the vertex associated position with tracks having the highest sum of p_T^2 is used. The invariant mass is then deduced from the two photons with respect to this primary vertex. The final 2010 data sample has 99 events with a diphoton invariant mass between 100 and 150 GeV.

10.1.2 Simulated samples

In order to study the effects of multiple interactions (pile-up), signal samples have been generated with an average number of minimum bias interactions of 2.1 in addition to non pile-up samples.

Background processes can be split into two main categories: those from the production of two isolated photons, which are referred to as *irreducible*, and *reducible* backgrounds coming from events for which at least one of the selected photons is fake. Fake photons are mostly jets where a leading π^0 or η meson resulting from the fragmentation of a quark or a gluon resembles an isolated prompt photon. The `DIPHOX` [94] and `ResBos` [83–85] programs are used to asses the bremsstrahlung contribution. `DIPHOX` includes all processes to order $\mathcal{O}(\alpha_s\alpha^2)$, including the bremsstrahlung contribution with the quasi-collinear fragmentation of quarks and gluons which are computed at NLO.
ResBos includes the Born and box contributions at NLO as well as the bremsstrahlung contribution, but the fragmentation contribution is calculated only at LO. While `DIPHOX` does not include resummation effects, these are included up to NNLL in `ResBos`. Here, `ResBos` with NLO bremsstrahlung taken into account from `DIPHOX` is used as the theoretical prediction of the irreducible background. All the MC samples used in this analysis have been simulated through the ATLAS detector simulation package [13, 42].

10.2 Background composition

The composition of the 2010 data sample is studied by means of a double-sideband method [34, 69], an extension of the technique used to measure the inclusive isolated photon-cross-section [19, 30, 68](see also Chapter 7). In this technique, the photon purity is evaluated by extrapolating to the signal region the background estimated from control regions located in the sideband plane of the identification and isolation variables.

The two photon candidates are considered sequentially as illustrated in Figure 10.1, in a starting sample for which both photons pass the loose identification and isolation criteria. The sidebands method is first applied to the leading p_T photon candidate to extract the N^A events for which it is identified as a photon, and then to the subleading p_T photon candidate to extract the N'^A events for which the subleading p_T candidate is also identified as a photon, knowing that the leading photon is tighly identified and isolated. The number of diphoton, photon-jet, jet-photon and dijet events ($N_{\gamma\gamma}$, $N_{\gamma j}$ and $N_{j\gamma}$, respectively) with both photon candidates in the signal region are obtained by solving the equations of extrapolation from the sidebands to the photon signal regions. The resulting composition in the 2010 data sample is reported in Table 10.1, together with the predictions for the background components made in [71, 73] extrapolated from 10 TeV fully simulated samples [27–29], corrected to take into account the effects of data quality, pile-up and the changes in the selection criteria [1]. The contribution arising from Drell-Yan events is evaluated with a data-driven technique [2], and is not counted in the diphoton component.

[1] with respect to the 10 TeV analysis with fully simulated samples.

[2] Where both electrons are misidentified as photons. Using $Z \to e^+e^-$ events to measure the electron-

Figure 10.2 shows the diphoton invariant mass distribution, together with the predictions for the irreducible (diphoton) and reducible (photon-jets plus dijet) components of the backgrounds, and the composition estimated with the double-sidebands method.

	$N_{\gamma\gamma}$	$N_{\gamma j} + N_{j\gamma}$	N_{jj}	N_{DY}
Data	$75.0 \pm 13.3^{+2.7}_{-3.6}$	$19.6 \pm 7.5 \pm 3.9$	$1.5 \pm 0.7^{+1.8}_{-0.5}$	$2.9 \pm 0.1 \pm 0.6$
Expected	86 ± 23	31 ± 15	1 ± 1	2.7 ± 0.2

Table 10.1: The number of irreducible ($N_{\gamma\gamma}$), reducible ($N_{\gamma j} + N_{j\gamma}$, N_{jj}) and Drell-Yan (N_{DY}) background events to the $H \to \gamma\gamma$ search in the 100-150 GeV mass range. For the measured number of events, the errors are statistical and systematic, respectively. For the expected number of events, the errors on the irreducible and reducible components arise from the theoretical uncertainty on the prediction; for the Drell-Yan component, the corresponding uncertainty arises from the MC statistics.

10.3 Signal modelling

At the LHC, there are several possible Higgs boson production processes, with cross sections calculated at different levels of precision. Monte Carlo samples for each subprocess, produced by the ATLAS detector simulation package, and for values of the Higgs boson mass ranging from 100 to 140 GeV, are used to extract the efficiency of the signal reconstruction and the invariant mass resolution. The MC event samples were produced with a configuration where the average number of interaction per bunch-crossing is equal to 2.2 [3] (with a train structure of 150 ns) .

Table 10.2 summarizes the expected number of events from Higgs signals, as calculted from the Monte Carlo samples. The dominant uncertainties on the expected number of events, discussed in detail in Section 10.4 and summarized in Table 10.3, arise from the photon identification and isolation efficiencies and the theoretical uncertainties on the Higgs boson production cross-section [174].

The probability-density function (PDF) for the signal invariant mass is modeled by a Crystal Ball function (CB) (which takes into account the core resolution and a non-Gaussian tail extending towards lower mass values) added to a small, wider Gaussian component (which takes into account outliers in the distribution). Figure 10.3 shows the invariant diphoton mass distribution for a sample of simulated events with a 120 GeV Higgs decaying into two photons and the PDF used to describe it. The resolution functions for Higgs at masses other than the simulated values are obtained through a linear interpolation of the PDF parameters.

The data points are the output of the MC simulations. To reproduce the behaviour in data the photon energy and resolution corrections described in Section 10.1 are applied

to-photon fake rate.

[3] For the bunch structure and the instantaneous luminosity reached in 2010 this quantity was about 2.

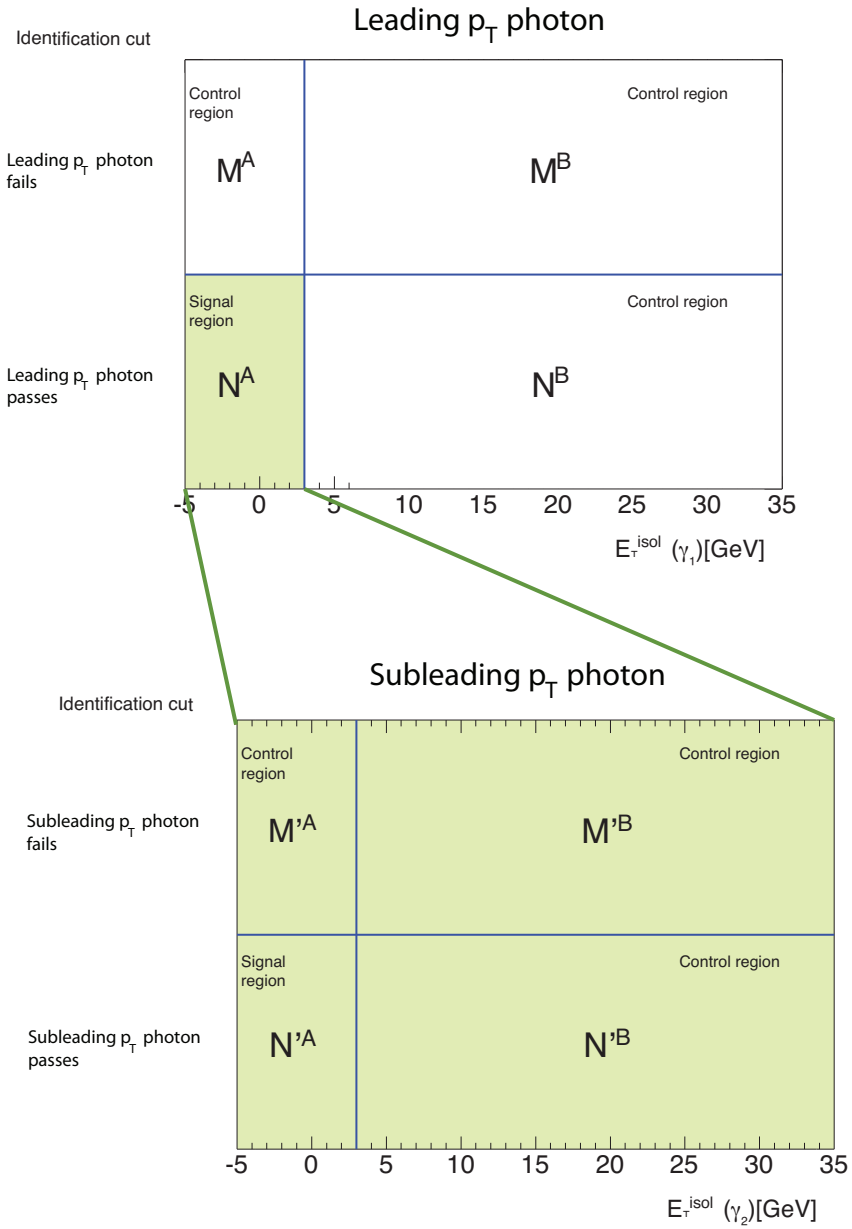


Figure 10.1: Schematic representation of the two-dimensional sidebands method. The top plane is formed with the isolation (x-axis) and tight identification (y-axis) criteria for the leading photon, for all pairs of candidates passing the loose identification criterion. The three background regions are N^C, N^D, N^B and the signal region is N^A. Events form the N^A region are then passed to the bottom plane that works similary to the first plane.

on the invariant mass distribution. Moreover, the fitted curve is shown.

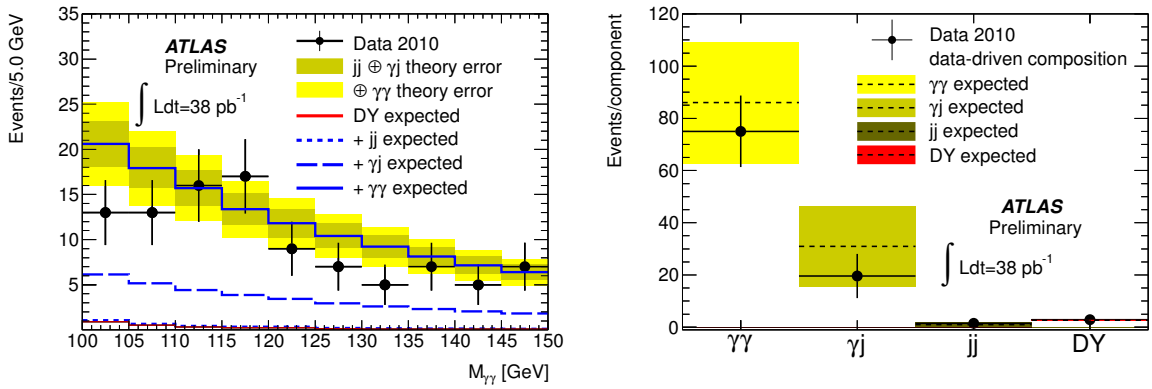


Figure 10.2: Left: the diphoton invariant mass for the 99 events composing the data sample. The overlaid histograms represent the cumulative Drell-Yan (red solid), dijet (blue dotted), photon-jet (blue dashed) and diphoton (blue solid) components of the background, according to the predictions from theoretical models and simulation obtained in [71] and summarized in Table 10.1. The dark yellow band is the uncertainty for the reducible background components, and the yellow band is the total uncertainty on the reducible plus irreducible backgrounds. Right: the results of the double-sideband method for the 99 events composing the data sample. For the diphoton, photon-jet and dijet components, the extracted number of events on data (black dots) are compared with the corresponding predictions (yellow, medium-dark yellow and dark yellow bands, respectively). For the Drell-Yan component, the number of events is compared with the expected number of events predicted from simulation.

10.4 Systematics

The background in the signal region is described with an exponential functional form using two nuisance parameters (a negative exponential coefficient and the overall normalization [4]) which are fitted to the data.

The systematic uncertainties related to the signal can be divided into four main categories, and are summarized in Table 10.3. The first is the uncertainty on the luminosity which is common and correlated among all Higgs decay channels. The second is the

[4] $f(m_{\gamma\gamma}) = \mathcal{N} e^{-\alpha m_{\gamma\gamma}}$

Higgs boson mass [GeV]	110	115	120	130	140
Number of signal events	$0.43^{+0.11}_{-0.09}$	$0.45^{+0.11}_{-0.10}$	$0.45^{+0.11}_{-0.10}$	$0.41^{+0.10}_{-0.08}$	0.31 ± 0.08

Table 10.2: The expected Higgs signal yields for various mass points, for an integrated luminosity of 38 pb^{-1}. The error combines the experimental systematic uncertainties and the theoretical uncertainty on the SM Higgs boson production cross-section [174].

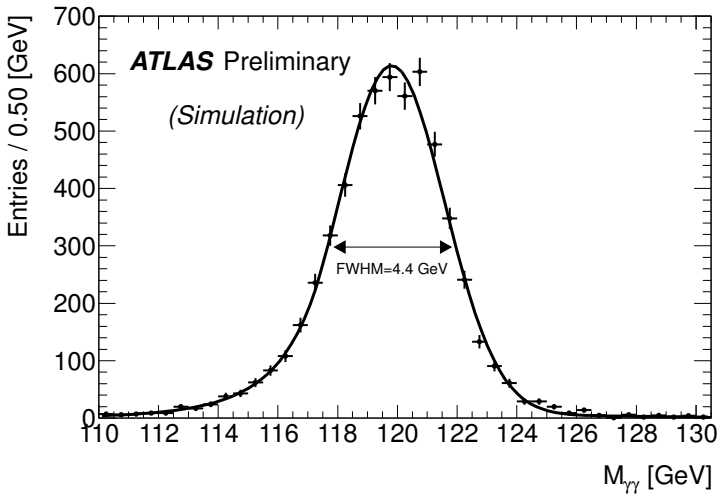


Figure 10.3: The distribution of the diphoton invariant mass for simulated events with a 120 GeV Higgs boson decaying into two photons. The data points are the output of the MC simulations. To reproduce the behaviour in data, the photon energy and resolution corrections described in Section 10.2 are applied on the invariant mass distribution. Furthermore, the fitted curve shows the PDF describing the invariant mass distribution; this represents also the resolution function used in the statistical analaysis described in Section 10.5. The FWHM of the distribution is 4.4 GeV.

	Source	Uncertainty
	Luminosity	$\pm 3.4\%$
Theory	Cross-section (scales)	$^{+20}_{-15}\%$
Efficiency	Photon identification	$\pm 11\%$
	Photon isolation	$\pm 10\%$
	Trigger	$^{+1.1}_{-3.7}\%$
Resolution	Calibration	
	$e \to \gamma$ extrapolation	$\pm 13\%$
	Pile-up	

Table 10.3: Relative systematic uncertainties associated to the signal normalization and invariant mass resolution. For the resolution, the quoted uncertainty is relative to the width of the invariant mass.

theoretical uncertainty on the overall normalization of the signal, dominated by the uncertainty on the computation of the production cross section as estimated in [174](mostly due to scale dependence and uncertainties on the parton density functions). The third category corresponds to uncertainties on the efficiency, whose two main components are

the uncertainty on the photon identification and on the isolation; these uncertainties are estimated from comparisions of data and fully simulated MC samples of photons and electrons. The fourth category of systematic uncertainties is on the invariant mass resolution. The contributions arising from uncertainties on the photon energy resolution are estimated using a fine-grained energy recalibration extracted from Z boson decays to electrons taking into account possible biases from the electron-to-photon extrapolation. An additional contribution arises from the impact of pile-up on the invariant mass resolution.

Systematic uncertainties are treated by adding nuisance parameters and penalty PDFs that reflect the impact of these uncertainties in the likelihood function that is used in the definition of the test statistic. These penalty PDFs are in general simple Gaussian functions, with the exception of the trigger efficiency and theoretical cross-section, for which a double-sided Gaussian function is used.

10.5 Observed sensitivity

The measurement of the inclusive distribution of diphoton events is used to estimate the sensitivity for the $H \to \gamma\gamma$ channel with an integrated luminosity of 38 pb^{-1}. The exclusion sensitivity, as a function of the Higgs boson mass is estimated. The limits are set using a Power Contrained Limit (PCL) method [117]. The procedure uses the profile likelihood ratio [14, 57, 118], with the p-value or CL$_{s+b}$ extracted from the distribution of the profile likelihood ratio by toy MC. To protect against excluding the (signal) null hypothesis in cases of downward fluctuations of the background, the observed limit is not allowed to fluctuate below the -1σ expected limit. This is equivalent to restricting the statistical power of the analysis not go below 16%. This CL$_s$ [192] is also provided as a reference.

Table 10.4 shows the upper bound on the exclusion at the 95% CL, in units of the SM Higgs boson cross-section, as a function of the Higgs boson mass for different methods. The systematic uncertainties introduced in Section 10.4 are taken into account in the limit setting by incorporating the corresponding penalty PDFs in the likelihood function used to model the data sample. On average, the incorporation of systematics degrades the exclusion limiit by up to 10%. With 38 pb^{-1} of data, the obtained limits are mostly driven by statistical uncertainty, which explains the limited impact of systematic uncertainties. As expected, results from the CL$_s$ methods are more conservative than those from CL$_{s+b}$ method.

Figure 10.4 shows the distribution of upper limits expected in the absence of any signal, indicated by the mediam expected limitd and $\pm1\sigma$ and $+2\sigma$ contours, in addition to the observed limit. As the observed limit is constrained not to lie below the -1σ band for the expected limit, the -2σ band is not displayed in plot. For Higgs masses around 127, 132 and 140 GeV, the PCL constraint prevents a false exclusion due to a downwards background fluctuation. With an integrated luminosity of 38 pb^{-1}, this analysis shows that, in the median, cross-sections larger than about 20 times the prediction for the SM Higgs boson may be excluded. This limit already comparable with recent results from Tevatron in the $H \to \gamma\gamma$ channel [185, 204–206]. As a comparison, Figure 10.5 shows

the observed exclusion computed with the CL_s method, for which the limits are around 5 units larger than the corresponding results using the CL_{s+b} method.

m_H [GeV]	Expected limit		Observed limit	
	CL_{s+b}	CL_s	PCL_{s+b}	CL_s
110	22.1	27.9	16.1	24.0
115	20.1	25.5	37.9	39.7
120	19.9	24.4	23.6	27.2
130	19.1	24.0	9.3	18.3
140	23.0	29.9	8.0	20.7

Table 10.4: Upper limits on the cross-section as a function of mass, in units of the SM prediction for the Higgs boson, at the 95% CL for the 38 pb^{-1} of data taken in 2010. PCL_{s+b} means the CL_{s+b} method with Power Constrained Limit technique for the computation of the observed limit. Results using CL_s are also provided as a reference.

Figure 10.5 shows the expected 1σ and 2σ exclusion intervals for the background-only test statistic in addition to the expected and observed exclusion limits. This method gives more conservative results than PCL in the region where the sensitivity to the signal is weak.

10.6 Recent update on Higgs limit

Very recently, new limits were produced by ATLAS [2] with some 2011 data corresponding to 209 pb^{-1} and by the Tevatron with a combination of CDF and DØ [189] . They are shown in Figures 10.6 for ATLAS and 10.7 (top) for Tevatron and compared in Figure 10.7 (bottom).

One can see that the limits of ATLAS are already better than the limits of the Tevatron (see Figure 10.7 (bottom)).

10.7 Future

Figure 10.8 summarizes the limits on the Higgs boson that were expected [71] with 1 fb^{-1}. One could expect to exclude the Higgs boson in the range $130 - 450$ GeV. With current peak luminosity exceeding 10^{33} $cm^{-2}s^{-1}$ one could expect for the $2011 - 2012$ run integrated luminosities up to 10 fb^{-1} for one LHC experiment, with a significant fraction that could be taken at a centre-of-mass energy of 8 TeV. Figure 10.9 shows the expected level of significance as a function of m_H for 5 or 10 fb^{-1} of luminosity at centre-of-mass of 7 and 8 TeV. Very good results can be obtained, even for low mass Higgs.

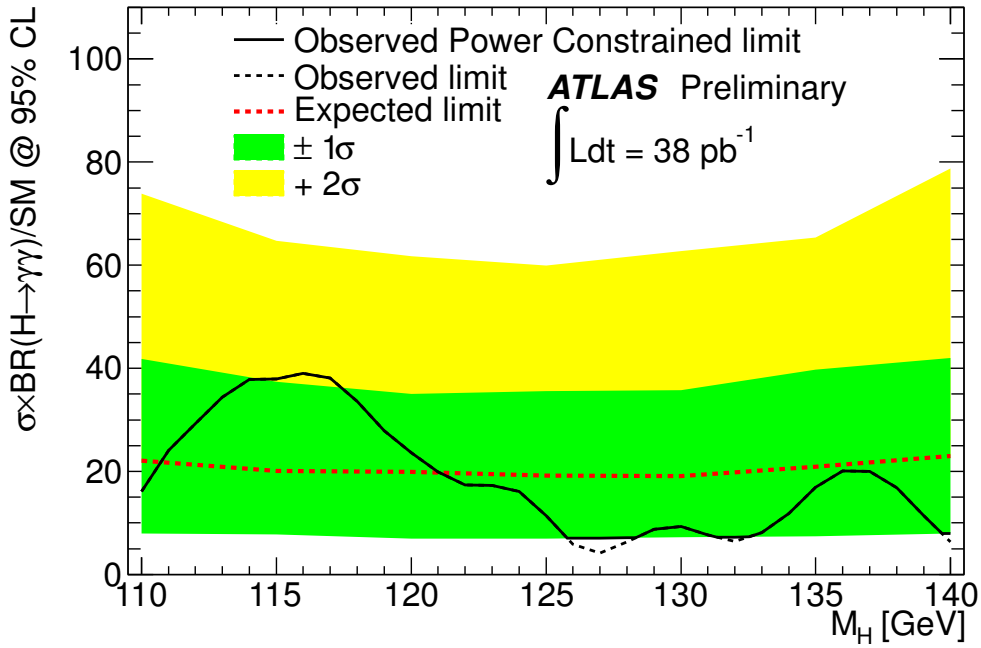


Figure 10.4: The excluded Higgs production cross-section at the 95% CL, normalized by the SM prediction, as a function of the Higgs boson mass with 38 pb^{-1} of data. The black solid line and the red dotted line correspond to the observed limit and expected limit, respectively. The green (yellow) band corresponds to the expected exclusion in the case of a 1σ (2σ) fluctuation of the background. The exclusion results are computed using CL_{s+b} with PCL.

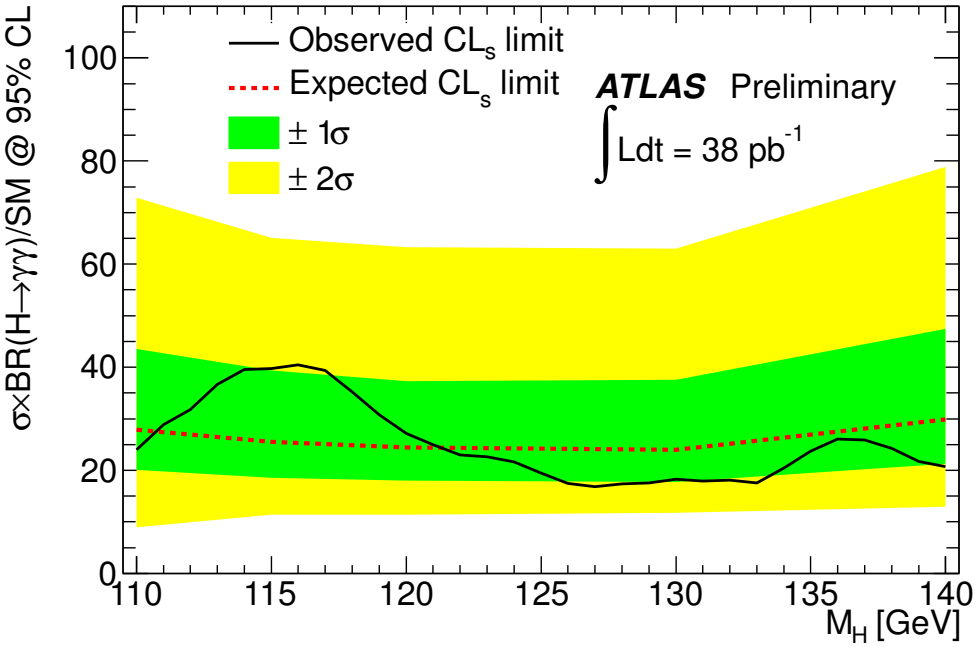


Figure 10.5: The excluded Higgs production cross-section at the 95% CL, normalized by the SM prediction, as a function of the Higgs boson mass with 38 pb^{-1} of data. The black solid line and the red dotted line correspond to the observed limit and expected limit respectively. The green (yellow) band correspond to the expected exclusion in the case of a $\pm 1\sigma$ ($\pm 2\sigma$) fluctuation of the background. The results are computed using the CL$_s$ method.

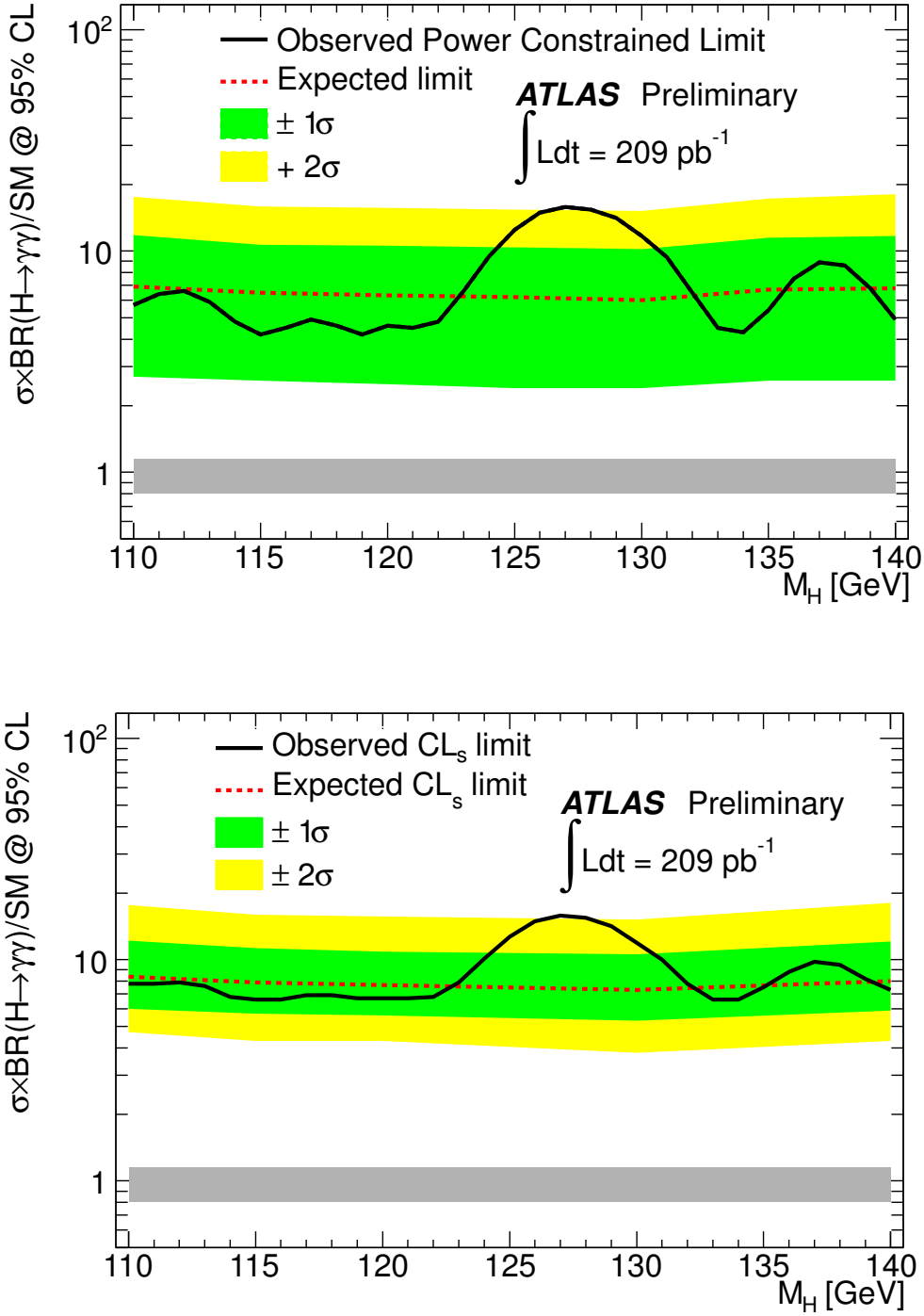


Figure 10.6: Exclusion limits using PCL (top) and CL_s method (bottom) on the production cross section relative to the Standard Model cross section as a function of Higgs mass hypothesis. Figures and caption were taken from [2].

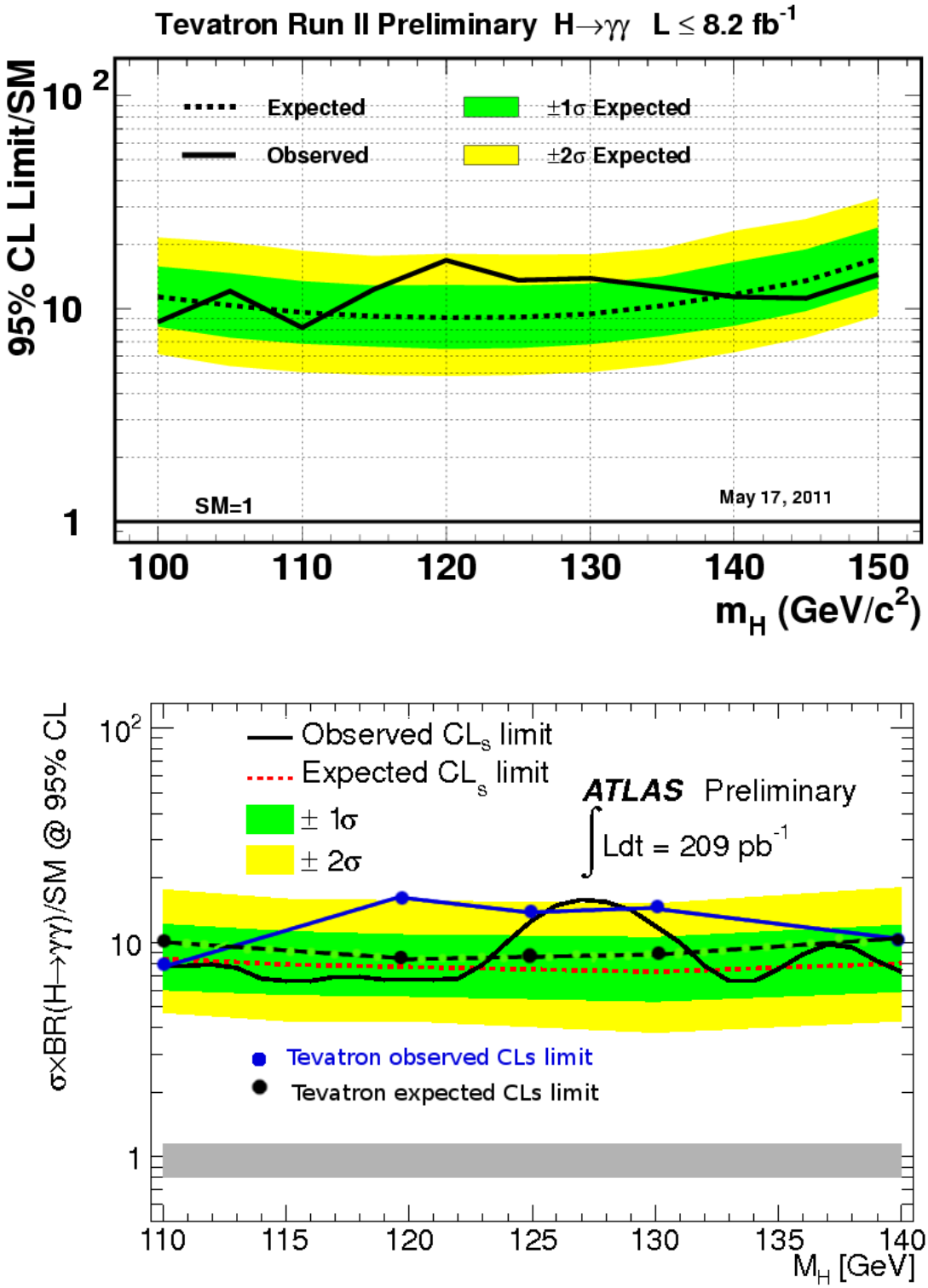


Figure 10.7: Exclusion limits shown by Tevatron [189] (top) and CL_s method reported by ATLAS compared with the Tevatron results (bottom) on the production cross section relative to the Standard Model cross section as a function of Higgs mass hypothesis.

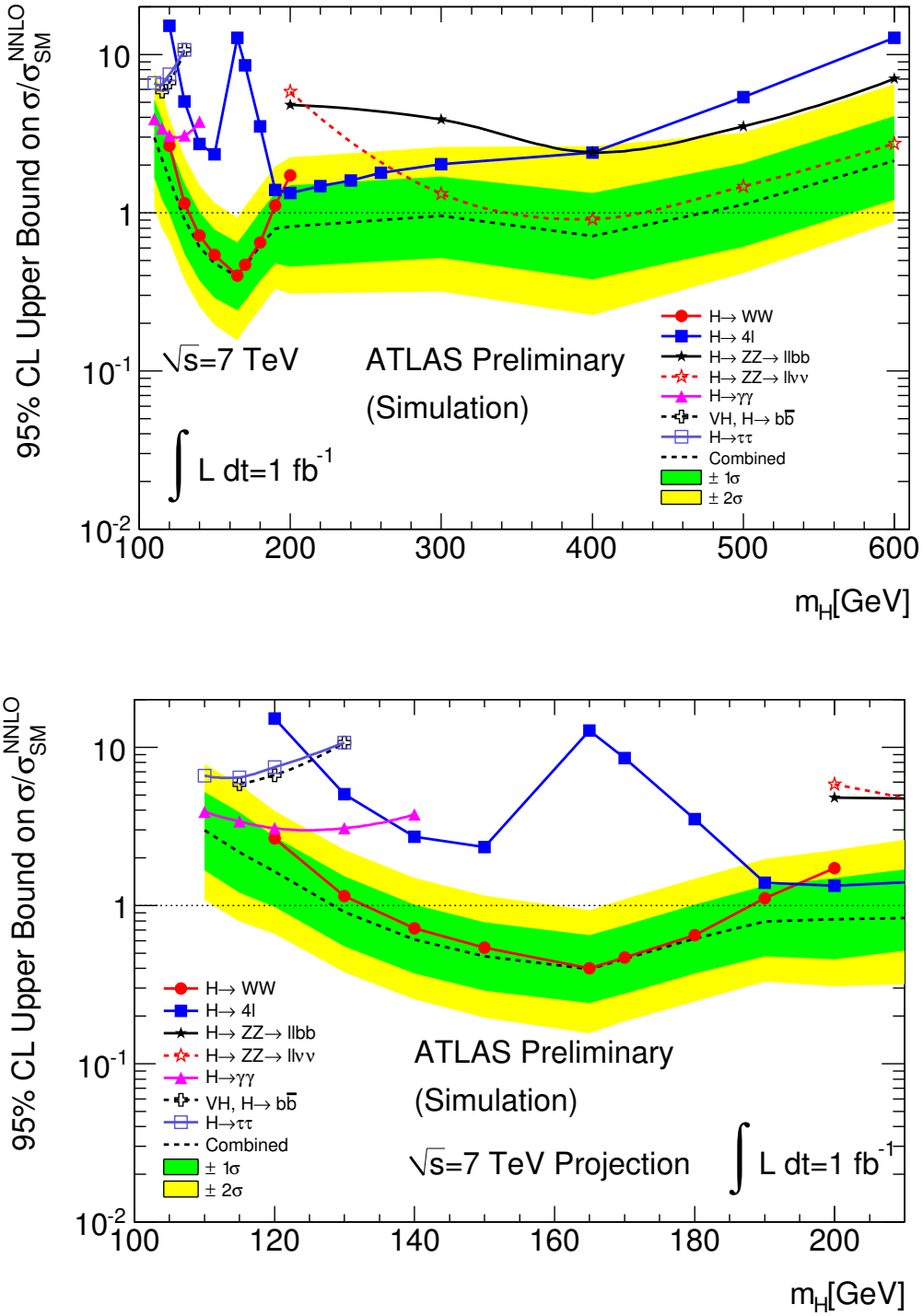


Figure 10.8: Top: The multiple of the cross-section of a Standard Model Higgs boson which can be excluded using 1 fb^{-1} of data at 7 TeV. At each mass, every channel giving reporting on it is used. The plot at the bottom is the same as the top except truncated to 200 GeV. The green and yellow bands indicate the range in which we expect the limit will lie, depending upon the data [71].

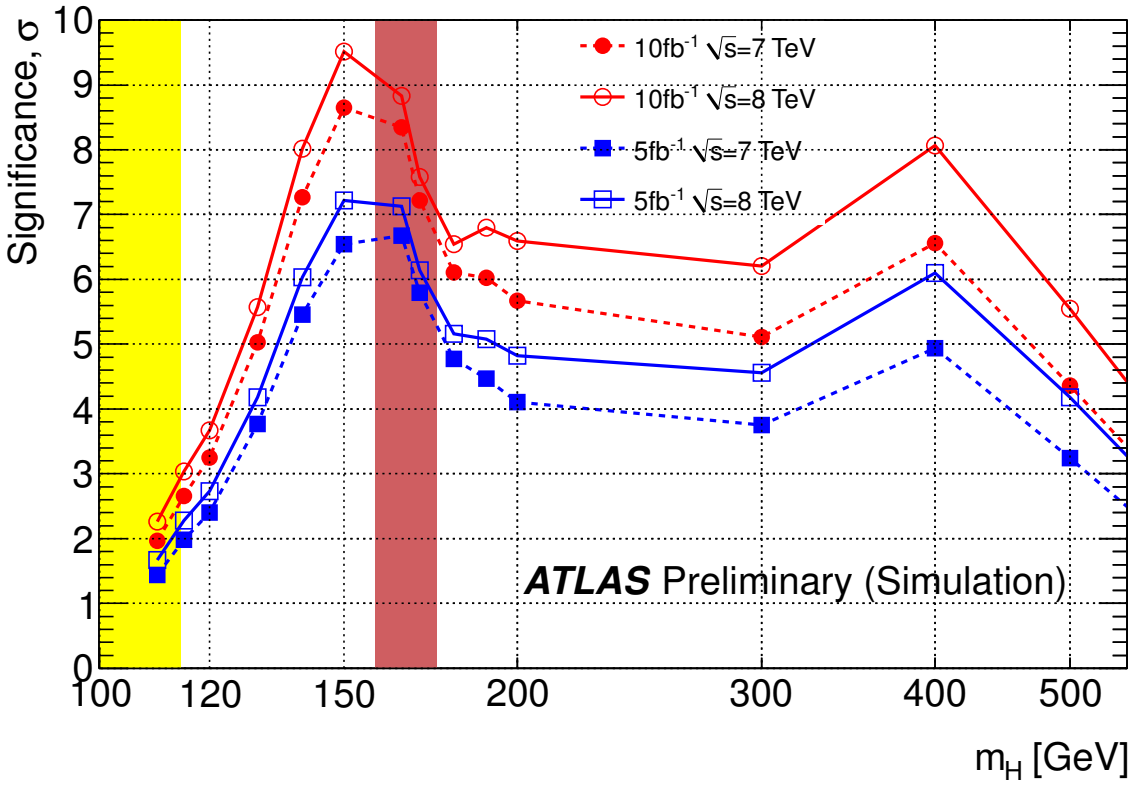


Figure 10.9: The expected level of significance as a function of m_H for 5 or 10 fb^{-1} of luminosity $\sqrt{s} = 7$ or 8 TeV [107].

Chapter 11

Conclusions

The work presented in this thesis is the first measurements of isolated photon studies as well as the preparation to the search for the Higgs boson in the two photons in channel using the early data provided by the LHC during the 2010 data-taking periods.

First, the expected performance of the ATLAS experiment in simulation of the photon reconstruction and identification was presented. For this, the reconstruction and selection efficiencies were measured using fully simulated γ-jet, $H \rightarrow \gamma\gamma$ ($M_H = 120$ GeV) and jet-jet (filtered at $p_T >$17 GeV) samples produced at $\sqrt{s} = 10$ TeV. Efficiencies were computed to be higher than 85 % for $E_T > 25$ GeV with the tight selection. Tight selection provides a background rejection around 5.10^3, which is the rejection needed for the discovery of a possible Higgs boson decaying into two photons (in order to have the background dominated by the "irreducible" photon background). The rejection increases if the isolation criteria are applied (track or calorimeter isolations) which provide a pure sample. These rejections were found to be larger for gluon-jets than for quark-jets. This effect is explained by the characteristics of the parton-shower for each particle (being broader for gluons than for quarks). These results are sensitive to the particle generator used, which implement different parton-shower models. Furthermore, the quality of reconstructed conversion was checked on a $H \rightarrow \gamma\gamma$ ($M_H = 120$ GeV) MC samples produced at $\sqrt{s} = 7$ TeV. In general, photon reconstruction and offline tight selection were found to be highly efficient.

The offline efficiencies were measured in data [1] after having applied shower shapes corrections as a function E_T (range comprising between 15 to 100 GeV) and for three pseudo-rapidity intervals.

A data driven approach to estimate the signal rate in the selected sample [1] for photon candidates, passing the photon identification and isolation criteria $E_T^{R<0.4} < 3$ GeV is given (remember that this a fundamental ingredient for measuring the inclusive prompt photon cross section [19]). With this method "two dimensional sidebands" (see Chapter 7) the signal fraction ("purity") and the signal yields are derived in the pseudo-rapidity regions studied as a function of the energy transverse (eight E_T bins between 15 to 100

[1] with a integrated luminosity of 880 nb^{-1}.

GeV). The main sources of uncertainties are: the errors on the purity range from 5% at high E_T , low $|\eta|$, to $\sim$ 13% for low E_T. The main contributions come from the background control region defined by the reversal of the strips cuts, and from the signal leaking into the non-isolated control region.

These results are used in order to measure the differential cross-section of isolated prompt photons in pp collisions at a centre-of-mass energy $\sqrt{s} = 7$ TeV [1]. The results have been compared with the next-to-leading order theoretical predictions. For $E_T > 25$ GeV the data and theory are in agreement. For $E_T < 25$ GeV, the data appear to favor smaller values of the cross section than those predicted by theory. In this region the experimental measurements have large associated systematic uncertainties, while theoretical predictions are also more difficult at such low values of $x_T = E_T/\sqrt{s}$. The measured prompt-photon cross section is more than a factor of thirty higher than what was measured at the Tevatron, and a factor 10^4 higher than for photoproduction at HERA. The measurement will be extended up to energies of about one TeV in the next two years of data taking at the LHC.

The measurement of the differential cross-section for the inclusive production of isolated prompt photons was updated in the E_T range of $E_T > 45$ GeV and $E_T < 400$ GeV using 34.55 pb^{-1} of collision data [2]. The results obtained are compared with the theory [3] in four pseudo-rapidity ranges spanning the range $0. \leq |\eta| < 2.37$. The pseudo-rapidity bin $1.81 \leq |\eta| < 2.37$ was recovered due to a procedure of re-optimization of the selection criteria. Among the improvements with respect to the first analysis, one could mention: the reduced uncertainty in the luminosity measurements as well as in the systematic uncertainties related to the knowledge of the material in front of the calorimeter [4]. In general a good agreement between data and the theoretical predictions is observed. In the higher transverse-energy regions ($E_T > 150$ GeV), the available statistics becomes rather limited and the resulting uncertainties are higher. This is expected to be solved with increase of the integrated luminosity in the 2011-2012 LHC data-taking.

In addition, a comparison between ATLAS and CMS measured differential cross sections of isolated prompt photons was performed in the barrel regions of each experiment in the E_T range of $15 \leq E_T < 100$ GeV. A good agreement was found with some differences at low E_T.

Finally, first studies of the search for the $H \to \gamma\gamma$ were presented with 38 pb^{-1} data collected at $\sqrt{s} = 7$ TeV collected by the ATLAS experiment in 2010. The background to the $H \to \gamma\gamma$ signal is shown to be dominated by diphoton events. The study of the signal and systematic with current data were described. With the baseline CL$_{s+b}$ method using the Power Constrained Limit technique for the observed exclusion, upper limits at the 95% Confidence Level are set on the cross-section (multiplied by the branching ratio)

[2] 34.55 pb^{-1} corresponding to the total integrated luminosity collected with the ATLAS detector during the 2010 data-taking periods.

[3] as in the previous analysis

[4] Indeed the distorted geometry used here has less Inner Detector material than the one used in the first analysis

for the $H \rightarrow \gamma\gamma$ process, in units of the expectation for the SM, as a function of the Higgs mass in the range 110-140 GeV. The exclusion limit ranges from 8 times the SM at $M_H = 127$ GeV to 38 times the SM cross-section at $M_H = 116$ GeV. The expected limit based on CL_s is comparable with recent results from the Tevatron in this channel. Very recently new limits with 2011 data and an integrated luminosity of 210 pb^{-1} were obtained. They are shown and compared to the Tevatron recent combination.

Bibliography

[1] Combined CDF and DØ Upper Limits on Standard Model Higgs- Boson Production with up to 6.7 fb^{-1} of Data. arXiv:1007.4587 [hep-ex].

[2] Search for the Higgs Boson in the Diphoton Channel with the ATLAS Detector using 209 pb-1 of 7 TeV Data taken in 2011. Technical Report ATLAS-CONF-2011-085, CERN, Geneva, Jun 2011.

[3] CTEQ Group. URL http://www.phys.psu.edu/~cteq/.

[4] public ATLAS egamma plot on conversion. URL http://bit.ly/juV93g.

[5] ATLAS twiki on Energy Scale and ResolutionRecommendations. URL http://bit.ly/jmdlb2.

[6] Gfitter - A Generic Fitter Project fro HEP Model Testing. URL http://project-gfitter.web.cern.ch/project-gfitter/G2HDM/.

[7] JETPHOX. URL http://lapth.in2p3.fr/PHOX_FAMILY/jetphox.html.

[8] The LEP Electroweak Working Group. URL http://lepewwg.web.cern.ch/LEPEWWG/.

[9] *The LHC Study Group CERN/AC/DI/FA/90-06*. CERN, Geneva, October 1990.

[10] MSTW PDF. URL http://projects.hepforge.org/mstwpdf/.

[11] TMVA – Toolkit for Multivariate Data Analysis with ROOT. URL http://tmva.sourceforge.net/.

[12] G. Aad et al. ATLAS Monte Carlo tunes for MC09. *ATL-PHYS-PUB-2010-002*, 2010.

[13] G. Aad et al. The ATLAS Simulation Infrastructure. *ATLAS-SOFT-2010-01-004*, 2010. Submitted to Eur. Phys. J. C.

[14] G. Aad et al. Expected Performance of the ATLAS Experiment - Detector, Trigger and Physics. 2009. URL http://arxiv.org/abs/arxiv:0901.0512.

[15] G Aad et al. Commissioning of the ATLAS Muon Spectrometer with Cosmic Rays. *Eur. Phys. J.*, C70:875–916, 2010. doi: 10.1140/epjc/s10052-010-1415-2.

[16] G Aad et al. Readiness of the ATLAS Tile Calorimeter for LHC collisions. *Eur. Phys. J.*, C70:1193–1236, 2010. doi: 10.1140/epjc/s10052-010-1508-y.

[17] G Aad et al. Performance of the ATLAS Detector using First Collision Data. *JHEP*, 09:056, 2010. doi: 10.1007/JHEP09(2010)056.

[18] Georges Aad et al. Luminosity Determination in pp Collisions at sqrt(s)=7 TeV Using the ATLAS Detector at the LHC. *arXiv:1101.2185 [hep-ex]*, 2011.

[19] Aad, G. et al. (ATLAS Collaboration). Measurement of the inclusive isolated prompt photon cross section in pp collisions at $\sqrt{s} = 7\,TeV$ with the ATLAS detector. *Phys. Rev. D*, 83(5):052005, Mar 2011.

[20] T. Aaltonen et al. Measurement of the inclusive isolated prompt photon cross section in $p\bar{p}$ collisions at $\sqrt{s} = 1.96\,TeV$ using the CDF detector. *Phys. Rev. D*, 80(11): 111106, Dec 2009.

[21] S. Abachi et al. Isolated Photon Cross Section in the Central and Forward Rapidity Regions in $p\bar{p}$ Collisions at $\sqrt{s} = 1.8TeV$. *Phys. Rev. Lett.*, 77(25):5011–5015, Dec 1996.

[22] V. M. Abazov et al. Measurement of the isolated photon cross section in $p\bar{p}$ collisions at $\sqrt{s} = 1.96$-TeV. *Phys. Lett.*, B639:151–158, 2006.

[23] V. M. Abazov et al. Ratio of Isolated Photon Cross Sections in $p\bar{p}$ Collisions at $\sqrt{s}$ =630 and 1800 GeV. *Phys. Rev. Lett.*, 87(25):251805, Nov 2001.

[24] G. Abbiendi et al. Search for the Standard Model Higgs boson at LEP. *Physics Letters B*, 565:61 – 75, 2003.

[25] B. Abbott et al. Isolated Photon Cross Section in $p\bar{p}$ Collisions at $\sqrt{s}$ =1.8 TeV. *Phys. Rev. Lett.*, 84(13):2786–2791, Mar 2000.

[26] F. Abe et al. Precision Measurement of the Prompt Photon Cross Section in $p\bar{p}$ Collisions at $\sqrt{s} = 1.8$ TeV. *Phys. Rev. Lett.*, 74(10):1891–1893, Mar 1995.

[27] H Abreu et al. Prospects for the Exclusion of a SM Higgs Decaying into Two Photons. Technical Report ATL-COM-PHYS-2010-170, CERN, Geneva, Jan 2010.

[28] H Abreu et al. Exclusion Prospects for the Standard Model Higgs Boson Decaying into Two Photons. Technical Report ATL-PHYS-INT-2010-061, CERN, Geneva, Jun 2010.

[29] H Abreu et al. Update of the prospects for the exclusion of a SM Higgs decaying to two photons. Technical Report ATL-COM-PHYS-2010-495, CERN, Geneva, Jul 2010.

[30] H Abreu et al. Purity Estimates for the Inclusive Isolated Photons. Technical Report ATL-PHYS-INT-2011-015, CERN, Geneva, Feb 2011.

[31] H. Abreu et al. Expected photon performance in the ATLAS experiment. Technical Report ATL-PHYS-PUB-2011-007, CERN, Geneva, Dec 2010.

[32] H Abreu et al. Measurement of the inclusive isolated prompt photon cross section in pp collisions at $\sqrt{s} = 7TeV$ with the ATLAS detector. Technical Report ATL-PHYS-INT-2011-013, CERN, Geneva, Mar 2011.

[33] H. Abreu et al. Performance of the electronic readout of the ATLAS liquid argon calorimeters. *JINST*, 5:P09003, 2010. doi: 10.1088/1748-0221/5/09/P09003.

[34] H Abreu et al. Study of the Di-Photon Backgrounds to the $H \to \gamma\gamma$ Search with the ATLAS detector at $\sqrt{s}$= 7 TeV. Technical Report ATL-PHYS-INT-2011-011, CERN, Geneva, Feb 2011.

[35] H Abreu et al. Search for the Higgs boson in the diphoton final state with 38 pb^{-1} of data recorded by the ATLAS detector at $\sqrt{s}$=7 TeV. Technical Report ATL-PHYS-INT-2011-024, CERN, Geneva, Mar 2011.

[36] H Abreu et al. Measurement of the inclusive isolated prompt photon cross section in pp collisions at $\sqrt{s} = 7$ TeV with the ATLAS detector using 35 pb^{-1}. Technical Report ATL-PHYS-INT-2011-037, CERN, Geneva, Apr 2011. Supporting note for inclusive cross section CONF note.

[37] D. Acosta et al. Comparison of the isolated direct photon cross sections in $p\bar{p}$ collisions at $\sqrt{s} = 1.8$TeV and $\sqrt{s} = 0.63$ TeV. *Phys. Rev. D*, 65(11):112003, Jun 2002.

[38] D. Acosta et al. Direct photon cross section with conversions at CDF. *Phys. Rev. D*, 70(7):074008, Oct 2004.

[39] D. L. Adams et al. Measurement of single spin asymmetry for direct photon production in pp collisions at 200 GeV/c. *Physics Letters B*, 345(4):569 – 575, 1995.

[40] S. S. Adler et al. Midrapidity direct-photon production in $p + p$ collisions at $\sqrt{s} = 200\ GeV$. *Phys. Rev. D*, 71(7):071102, Apr 2005.

[41] S. S. Adler et al. Measurement of Direct Photon Production in $p + p$ Collisions at $\sqrt{s} = 200\ GeV$. *Phys. Rev. Lett.*, 98(1):012002, Jan 2007.

[42] S. Agostinelli et al. `GEANT4` - a simulation toolkit. *Nucl. Instrum. Methods A*, 506: 250, 2003.

[43] M Aharrouche et al. $W \to e\nu$ and $Z \to ee$ cross-section measurements in proton-proton collisions at $\sqrt{s} = 7$ TeV with the ATLAS Detector: Support note to publication. Technical Report ATL-COM-PHYS-2010-701, CERN, Geneva, Sep 2010. Back-up note for the W/Z paper.

[44] T. Akesson et al. A comparison of direct photon, π^0 and η production in ppbar and pp interactions at the CERN ISR. *Physics Letters B*, 158(3):282 – 288, 1985.

[45] C. Albajar et al. Direct photon production at the CERN proton-antiproton collider. *Physics Letters B*, 209(2-3):385 – 396, 1988.

[46] J. Alcaraz et al. Precision Electroweak Measurements and Constraints on the Standard Model. 2009. URL http://arxiv.org/pdf/0911.2604v2.

[47] M. Aleksa et al. ATLAS Combined Testbeam: Computation and Validation of the Electronic Calibration Constants for the Electromagnetic Calorimeter. Technical Report ATL-LARG-PUB-2006-003, CERN, Geneva, Apr 2006.

[48] J. Alitti et al. A measurement of single and double prompt photon production at the CERN collider. *Physics Letters B*, 288(3-4):386 – 394, 1992.

[49] G. Altarelli and G. Isidori. Lower limit on the Higgs mass in the standard model: An update. *Physics Letters B*, 337(1-2):141 – 144, 1994.

[50] Guido Altarelli and G. Parisi. Asymptotic Freedom in Parton Language. *Nucl. Phys.*, B126:298, 1977.

[51] L. Alvarez-Gaume and J. Ellis. Eyes on a Prize Particle. *Nature Physics.*, 7:2–3, 2011.

[52] G. Alverson et al. Direct photon production at high p_T in $\pi^- Be$ and pBe collisions at 500 GeV/c. *Phys. Rev. Lett.*, 68(17):2584–2587, Apr 1992.

[53] S Amoruso et al. Study of electron recombination in liquid argon with the ICARUS TPC. *Nucl. Instrum. Methods Phys. Res., A*, 523(3):275 – 286, 2004. ISSN 0168-9002. doi: DOI:10.1016/j.nima.2003.11.423. URL http://bit.ly/hcNZeg.

[54] E. Anassontzis et al. High-p_T direct photon production in pp collisions. *Zeitschrift fr Physik C Particles and Fields*, 13:277–289, 1982.

[55] Charalampos Anastasiou and Kirill Melnikov. Higgs boson production at hadron colliders in NNLO QCD. *Nucl. Phys.*, B646:220–256, 2002.

[56] N. Andari. ATL-COM-PHYS-2010-527. URL http://bit.ly/kVQvLb.

[57] N Andari et al. Exclusion limits and Systematics. Technical Report ATL-COM-PHYS-2010-844, CERN, Geneva, Sep 2010.

[58] P. W. Anderson. Plasmons, gauge invariance, and mass. *Phys. Rev.*, 130(1):439–442, Apr 1963.

[59] A. L. S. Angelis et al. Search for direct single-photon production at large p_T in photon-proton collisions at $\sqrt{s} = 62.4$ GeV. *Physics Letters B*, 94(1):106 – 112, 1980.

[60] A. L. S. Angelis et al. Direct photon production at the CERN ISR. *Nuclear Physics B*, 327(3):541 – 568, 1989.

[61] R. Ansari et al. Direct photon production in proton-antiproton collisions at $\sqrt{s}$ = 630 GeV. *Zeitschrift für Physik C*, 41:395–404, 1988.

[62] L. Apanasevich, C. Balázs, C. Bromberg, J. Huston, A. Maul, W. K. Tung, S. Kuhlmann, J. Owens, M. Begel, T. Ferbel, G. Ginther, P. Slattery, and M. Zieliński. k_T effects in direct-photon production. *Phys. Rev. D*, 59(7):074007, Feb 1999.

[63] L. Apanasevich et al. Evidence for parton k_T effects in high p_T particle production. *Phys. Rev. Lett.*, 81:2642–2645, 1998. doi: 10.1103/PhysRevLett.81.2642.

[64] L. Apanasevich et al. Measurement of direct photon production at Tevatron fixed target energies. *Phys. Rev.*, D70:092009, 2004.

[65] G. Arnison et al. Experimental observation of lepton pairs of invariant mass around 95 GeV/c2 at the CERN SPS collider. *Physics Letters B*, 126(5):398 – 410, 1983.

[66] G. Arnison et al. Experimental observation of isolated large transverse energy electrons with associated missing energy at $\sqrt{s}$ = 540 GeV. *Phys. Lett.*, B122: 103–116, 1983.

[67] Y. Ashie et al. Evidence for an oscillatory signature in atmospheric neutrino oscillations. *Phys. Rev. Lett.*, 93(10):101801, Sep 2004. doi: 10.1103/PhysRevLett.93.101801.

[68] ATLAS Collaboration. Evidence for prompt photon production in pp collisions at $\sqrt{s} = 7$ TeV with the ATLAS detector. Technical Report ATLAS-CONF-2010-077, CERN, Geneva, Jul 2010.

[69] ATLAS Collaboration. Measurement of the backgrounds to the $H \to \gamma\gamma$ search and reappraisal of its sensitivity with 37 pb^{-1} of data recorded by the ATLAS detector. Technical Report ATLAS-CONF-2011-004, CERN, Geneva, Feb 2011.

[70] ATLAS Collaboration. Search for the Higgs boson in the diphoton final state with 38 pb^{-1} of data recorded by the ATLAS detector in proton-proton collisions at $\sqrt{s}$=7 TeV. Technical Report ATLAS-CONF-2011-025, CERN, Geneva, Mar 2011.

[71] ATLAS Collaboration. ATLAS Sensitivity Prospects for 1 Higgs Boson Production at the LHC Running at 7, 8 or 9 TeV. Technical Report ATL-PHYS-PUB-2010-015, CERN, Geneva, Nov 2010.

[72] ATLAS Collaboration. Measurement of the inclusive isolated prompt photon cross section in *pp* collisions at $\sqrt{s}$ = 7 TeV with the ATLAS detector using 35 pb[1]. Technical Report ATLAS-CONF-2011-058, CERN, Geneva, Mar 2011.

[73] ATLAS, Collaboration. ATLAS Sensitivity Prospects for Higgs Boson Production at the LHC Running at 7 TeV. Technical Report ATL-PHYS-PUB-2010-009, CERN, Geneva, Jul 2010.

[74] ATLAS Collaboration. A Search to Randall-Sundrum Gravitons Decaying to Photon Pairs in $\sqrt{s} = 7$ TeV pp Collisions. Technical Report ATLAS-CONF-2011-044, CERN, Geneva, Feb 2011.

[75] ATLAS Collaboration. Updated Luminosity Determination in pp Collisions at $\sqrt{s} = 7$ TeV using the ATLAS Detector. Technical Report ATLAS-CONF-2011-011, CERN, Geneva, Feb 2011.

[76] ATLAS Collaboration. Measurement of isolated di-photon cross section in *pp* collision at $\sqrt{s} = 7$ TeV with the ATLAS detector. Technical Report ATL-COM-PHYS-2011-301, CERN, Geneva, Mar 2011.

[77] ATLAS Collaboration. Measurement of isolated di-photon cross section in *pp* collision at $\sqrt{s} = 7$ TeV with the ATLAS detector. Technical Report ATL-COM-PHYS-2011-379, CERN, Geneva, Apr 2011.

[78] B Aubert et al. Performance of a liquid argon electromagnetic calorimeter with an 'accordion' geometry. *Nucl. Instrum. Meth.*, A309:438–449, 1991. doi: 10.1016/0168-9002(91)90247-N.

[79] B Aubert et al. Performance of the ATLAS Electromagnetic Calorimeter End-cap Module 0. *Nucl. Instrum. Methods Phys. Res., A*, 500(CERN-EP-2002-104):178–201r. 31 p, Nov 2002.

[80] Patrick Aurenche, Michel Fontannaz, Jean-Philippe Guillet, Eric Pilon, and Monique Werlen. A New critical study of photon production in hadronic collisions. *Phys. Rev.*, D73:094007, 2006.

[81] Aurenche, P. and Baier, R. and Fontannaz, M. Prompt photon production at colliders. *Phys. Rev. D*, 42(5):1440–1449, Sep 1990.

[82] P. Bagnaia et al. Evidence for Z0→ e+e- at the CERN antip-p collider. *Physics Letters B*, 129(1-2):130 – 140, 1983.

[83] C. Balazs et al. Photon pair production with soft gluon resummation in hadronic interactions. *Phys. Rev.*, D57:6934–6947, 1998.

[84] C. Balazs et al. Diphoton background to Higgs boson production at the LHC with soft gluon effects. *Phys. Lett.*, B489:157–162, 2000.

[85] C Balazs et al. All-orders resummation for diphoton production at hadron colliders. *Phys. Lett. B*, 637:235–240. 16 p, Mar 2006.

[86] Richard D. Ball et al. A first unbiased global NLO determination of parton distributions and their uncertainties. *Nucl. Phys.*, B838:136–206, 2010.

[87] G. Ballocchi et al. Direct photon cross sections in proton-proton and antiproton-proton interactions at 24.3 GeV. *Physics Letters B*, 436(1-2):222 – 230, 1998.

[88] M. Banner et al. Observation of single isolated electrons of high transverse momentum in events with missing transverse energy at the CERN antipp collider. *Physics Letters B*, 122(5-6):476 – 485, 1983. ISSN 0370-2693.

[89] A. Bazan et al. ATLAS liquid argon calorimeter back end electronics. *JINST*, 2: P06002, 2007.

[90] C. Becot. presentation at the ATLAS SMDP meeting of 2-7-2010. URL http://bit.ly/eqL6xS.

[91] W. Beenakker et al. Higgs radiation off top quarks at the Tevatron and the LHC. *Phys. Rev. Lett.*, 87:201805, 2001.

[92] W. Beenakker et al. NLO QCD corrections to t anti-t H production in hadron collisions. ((U)). *Nucl. Phys.*, B653:151–203, 2003.

[93] T. Binoth, J. P. Guillet, E. Pilon, and M. Werlen. A Full next-to-leading order study of direct photon pair production in hadronic collisions. *Eur. Phys. J.*, C16: 311–330, 2000.

[94] T. Binoth et al. A Full next-to-leading order study of direct photon pair production in hadronic collisions. *Eur. Phys. J.*, C16:311–330, 2000.

[95] B. Blair et al. Theoretical Predictions for Measurements of the Inclusive Isolated Photon Cross Section in pp Collisions at $\sqrt{s} = 7\ TeV$. *ATL-PHYS-INT-2011-016*, 2011.

[96] Paolo Bolzoni, Fabio Maltoni, Sven-Olaf Moch, and Marco Zaro. Higgs production via vector-boson fusion at NNLO in QCD. *Phys. Rev. Lett.*, 105:011801, 2010.

[97] M. Bonesini et al. Production of high transverse momentum prompt photons and neutral pions in proton-proton interactions at 280 GeV/c. *Zeitschrift fr Physik C Particles and Fields*, 38:371–382, 1988.

[98] Michiel Botje et al. (PDF4LHC Working Group). 2011. arXiv:1101.0538.

[99] L. Bourhis, M. Fontannaz, and J.P. Guillet. Quark and gluon fragmentation functions into photons. *The European Physical Journal C - Particles and Fields*, 2: 529–537, 1998.

[100] Bourhis, L. and Fontannaz, M. and Guillet, J. P. and Werlen, M. Next-to-leading order determination of fragmentation functions. *Eur. Phys. J.*, C19:89–98, 2001.

[101] O. Brein, A. Djouadi, and R. Harlander. NNLO QCD corrections to the Higgs-strahlung processes at hadron colliders. *Physics Letters B*, 579:149–156, jan 2004.

[102] D. Buskulic et al. First measurement of the quark-to-photon fragmentation function. *Z. Phys. C*, 69:365–377. 29 p, Jun 1995.

[103] L Carminati et al. Reconstruction and Identification Efficiency of Inclusive Isolated Photons. Technical Report ATL-PHYS-INT-2011-014, CERN, Geneva, Mar 2011.

[104] Catani, S. and Fontannaz, M. and Guillet, J. P. and Pilon, E. Cross-section of isolated prompt photons in hadron hadron collisions. *JHEP*, 05:028, 2002.

[105] CMS Collaboration (Chatrchyan, Serguei et al.). Search for Large Extra Dimensions in the Diphoton Final State at the Large Hadron Collider. 2011. arXiv:1103.4279.

[106] J. Colas et al. Electronics calibration board for the ATLAS liquid argon calorimeters. *Nucl. Instrum. Methods Phys. Res., A*, 593:269–291, August 2008. doi: 10.1016/j.nima.2008.05.031. URL http://adsabs.harvard.edu/abs/2008NIMPA.593..269C.

[107] ATLAS Collaboration. Further investigations of ATLAS Sensitivity to Higgs Boson Production in different assumed LHC scenarios. Technical Report ATL-PHYS-PUB-2011-001, CERN, Geneva, Jan 2011.

[108] ATLAS Collaboration. *Liquid Argon Calorimeter Technical Design Report, CERN/LHCC/96-41.* 15 December 1996.

[109] (CMS Collaboration). Measuring Electron Efficiencies at CMS with Early Data. (CMS Note EGM-07-001), 2007.

[110] (CMS Collaboration). Isolated Photon Reconstruction and Identificaion at $\sqrt{s} = 7$ TeV. (CMS Note EGM-10-006), 2011.

[111] The ATLAS Collaboration. The ATLAS Experiment at the CERN Large Hadron Collider. *JINST*, 3:S08003, 2008.

[112] The CMS Collaboration. The CMS Experiment at the CERN LHC. *JINST*, 3: S08004, 2008.

[113] The LHCb Collaboration. The LHCb Experiment at the CERN LHC. *JINST*, 3: S08005, 2008.

[114] The LHCf Collaboration. The LHCf detector at the CERN Large Hadron Collider. *Journal of Instrumentation,*, 3(08):S08006, 2008.

[115] The TOTEM Collaboration. The TOTEM Experiment at the CERN Large Hadron Collider. *Journal of Instrumentation,*, 3(08):S08007, 2008.

[116] G. Corcella et al. `Herwig` 6.5. *JHEP*, 0101:010, 2001.

[117] Glen Cowan et al. Power-Constrained Limits. 2011. arXiv:1105.3166.

[118] Glen Cowan et al. "asymptotic formulae for likelihood-based tests of new physics". *"Eur. Phys. J. C 71"*, 2011.

[119] C.Seez and J.Virdee, G. Jarlskog and R. Dieter(Eds.). in Large Hadron Collider Worshop, Aachen October 1990, Volume II, report CERN 90-10, ECFA 90-133. page 474.

[120] G. D'Agostini. A multidimensional unfolding method based on Bayes' theorem. *Nucl. Instrum. Methods A*, 362(2-3):487 – 498, 1995.

[121] P. Darriulat et al. Large transverse momentum photons from high-energy proton-proton collisions. *Nuclear Physics B*, 110(4-5):365 – 379, 1976.

[122] S. Dawson, L. H. Orr, L. Reina, and D. Wackeroth. Associated top quark Higgs boson production at the LHC. *Phys. Rev.*, D67:071503, 2003.

[123] R Daya et al. Measurement of electron-photon fake rate in ATLAS official Monte Carlo data using $Z \rightarrow ee$ decays. Technical Report ATL-PHYS-INT-2010-085, CERN, Geneva, Sep 2010.

[124] C. De Marzo et al. Measurement of direct photon production at large transverse momentum in π^-p, π^+p, and pp collisions at 300 GeV/c. *Phys. Rev. D*, 36(1):8, Jul 1987.

[125] A. De Roeck and R. S. Thorne. Structure Functions. 2011. URL http://arxiv.org/abs/1103.0555.

[126] Carolina Deluca Silberberg. *Measurement of the inclusive isolated prompt photon production cross section at the Tevatron using the CDF detector*. PhD thesis, 2009. FERMILAB-THESIS-2009-18.

[127] (DESY for the H1 and ZEUS collaborations) Schilling, F. P. Inclusive diffraction at HERA. 2002. URL http://arxiv.org/abs/hep-ex/0210027.

[128] Abdelhak Djouadi. The Anatomy of electro-weak symmetry breaking. I: The Higgs boson in the standard model. *Phys. Rept.*, 457:1–216, 2008.

[129] Yuri L. Dokshitzer. Calculation of the Structure Functions for Deep Inelastic Scattering and e+ e- Annihilation by Perturbation Theory in Quantum Chromodynamics. *Sov. Phys. JETP*, 46:641–653, 1977.

[130] R. K. Ellis et al. Factorization and the parton model in QCD. *Physics Letters B*, 78(2-3):281 – 284, 1978.

[131] F. Englert and R. Brout. Broken Symmetry and the Mass of Gauge Vector Mesons. *Phys. Rev. Lett.*, 13(9):321–323, 1964.

[132] Escalier, M and Derue, F and Fayard, L and Kado, M and Laforge, B and Reifen, C and Unal, G. Photon/jet separation with DC1 data. Technical Report ATL-PHYS-PUB-2005-018. ATL-COM-PHYS-2005-048. CERN-ATL-PHYS-PUB-2005-018, CERN, Geneva, 2005.

[133] A. A. Glazkov et al. Duoplasmatron-type ion source with improved technical and operational performance for linear accelerator. *Conference Record of the Third European Particle Accelerator Conference*, Vol.2:993–995, 1992.

[134] K. Nakamura et al. Particle Data Group. *J. Phys. G*, 37, 2010.

[135] M. Aharrouche et al. Energy linearity and resolution of the ATLAS electromagnetic barrel calorimeter in an electron test-beam. *Nuclear Instruments and Methods in Physics Research A*, 568:601–623, December 2006. doi: 10.1016/j.nima.2006.07.053.

[136] M. Aharrouche et al. Response uniformity of the ATLAS liquid argon electromagnetic calorimeter. *Nuclear Instruments and Methods in Physics Research Section A: Accelerators, Spectrometers, Detectors and Associated Equipment*, 582(2): 429 – 455, 2007. ISSN 0168-9002. doi: DOI:10.1016/j.nima.2007.08.157. URL http://bit.ly/gv9Q4Y.

[137] Evans, Lyndon, and Bryant, Philip, (eds.). LHC Machine. *JINST*, 3:S08001, 2008. doi: 10.1088/1748-0221/3/08/S08001.

[138] C. Fabjan and F. Gianotti. Calorimeter for particle physics. *Rev. Mod. Phys.*, 75: 1243–1286, 2003.

[139] C. W. Fabjan. *Experimental Techniques in High Energy Physics*. edited by T. Ferbel (Addison-Wesley, Menlo Park), 1987.

[140] Fayard, Louis and Unal, G. Search for Higgs decay into photons with EAGLE. Technical Report ATL-PHYS-92-001, Dec 1992.

[141] D. Fournier. in Large Hadron Collider Worshop, Aachen October 1990, Volume III, report CERN 90-10, ECFA 90-133. page 356.

[142] Fritzsch, H. and Gell-Mann, Murray and Minkowski, P. Vector - Like Weak Currents and New Elementary Fermions. *Phys. Lett.*, B59:256, 1975.

[143] Y. Fukuda et al. Evidence for Oscillation of Atmospheric Neutrinos. *Phys. Rev. Lett.*, 81(8):1562–1567, Aug 1998. doi: 10.1103/PhysRevLett.81.1562.

[144] G. Ballochi et al. (UA6 Collaboration). Determination of α_s and the gluon distribution using direct photon production in pp and $\bar{p}p$ collisions. *Physics Letters B*, 317(1-2):250 – 256, 1993.

[145] S. L. Glashow. Partial Symmetries of Weak Interactions. *Nucl. Phys.*, 22:579–588, 1961.

[146] S. L. Glashow, J. Iliopoulos, and L. Maiani. Weak Interactions with Lepton-Hadron Symmetry. *Phys. Rev.*, D2:1285–1292, 1970.

[147] E. W. N. Glover and A. G. Morgan. Measuring the photon fragmentation function at LEP. *Zeitschrift fr Physik C Particles and Fields*, 62:311–321, 1994.

[148] J. Goldstone. Field Theories with Superconductor Solutions. *Nuovo Cim.*, 19: 154–164, 1961.

[149] Jeffrey Goldstone, Abdus Salam, and Steven Weinberg. Broken Symmetries. *Phys. Rev.*, 127(3):965–970, Aug 1962.

[150] V. N. Gribov and L. N. Lipatov. Deep inelastic e p scattering in perturbation theory. *Sov. J. Nucl. Phys.*, 15:438–450, 1972.

[151] David J. Gross and Frank Wilczek. Asymptotically Free Gauge Theories. I. *Phys. Rev. D*, 8(10):3633–3652, Nov 1973.

[152] David J. Gross and Frank Wilczek. Ultraviolet Behavior of Non-Abelian Gauge Theories. *Phys. Rev. Lett.*, 30(26):1343–1346, Jun 1973.

[153] Guralnik, G. S. and Hagen, C. R. and Kibble, T. W. B. Global Conservation Laws and Massless Particles. *Phys. Rev. Lett.*, 13(20):585–587, 1964.

[154] M. Hance. presentation at the ATLAS SMDP meeting of 11-5-2010. URL http://bit.ly/g9XitM.

[155] Robert V. Harlander and William B. Kilgore. Next-to-next-to-leading order Higgs production at hadron colliders. *Phys. Rev. Lett.*, 88:201801, 2002.

[156] M. Heller. *Mesure de la luminosite absolue et de la section efficace totale proton-proton dans l'expereince ATLAS au LHC*. PhD thesis, Universit de Paris-Sud, Mars 2009.

[157] P. W. Higgs. Spontaneous Symmetry Breakdown without Massless Bosons. *Phys. Rev.*, 145:1156–1163, 1966.

[158] P. W. Higgs. Broken Symmetries and the Masses of Gauge Bosons. *Phys. Rev. Lett.*, 13(16):508–509, 1964.

[159] P. W. Higgs. Broken Symmetries, Massless Particles and Gauge Fields. *Phys. Rev. Lett.*, 12:132–133, 1964.

[160] W. Hollik. Quantum field theory and the Standard Model. 2010. URL http://arxiv.org/abs/1012.3883v1.

[161] Thomas Ivan Hollins. *SCT hybrid testing and the production of direct photons in the ATLAS experiment at the LHC*. PhD thesis, 2006. CERN-THESIS-2007-061.

[162] J Huston. LHC Guide to Parton Distributions and Cross Sections. Technical Report ATL-PHYS-99-008, CERN, Geneva, Apr 1999.

[163] Raphaelle Ichou. *Study of the isolated photon production in proton-proton collisions with the EMCal calorimeter of the ALICE experiment at LHC*. PhD thesis, 2010.

[164] Raphaelle Ichou and David d'Enterria. Sensitivity of isolated photon production at TeV hadron colliders to the gluon distribution in the proton. *Phys. Rev.*, D82: 014015, 2010.

[165] J. Jowett. Chamonix 2011 LHC Performance Workshop. 24-28 January 2011. URL http://bit.ly/hH9w7u.

[166] J.A. Casas, J.R. Espinosa and M. Quiros. Standard model stability bounds for new physics within LHC reach. *Physics Letters B*, 382(4):374 – 382, 1996.

[167] Khachatryan, V. et al. (CMS Collaboration). Measurement of the Isolated Prompt Photon Production Cross Section in pp Collisions at $\sqrt{s} = 7\ TeV$. *Phys. Rev. Lett.*, 106(8):082001, Feb 2011.

[168] T. W. B. Kibble. Symmetry breaking in non-Abelian gauge theories. *Phys. Rev.*, 155:1554–1561, 1967.

[169] A. Kumar et al. Study of parton k_T smearing effects in direct photon production at the Fermilab Tevatron. *Phys. Rev. D*, 68:014017, jul 2003.

[170] H. L. Lai, J. Huston, S. Kuhlmann, F. Olness, J. Owens, D. Soper, W. K. Tung, and H. Weerts. Improved parton distributions from global analysis of recent deep inelastic scattering and inclusive jet data. *Phys. Rev. D*, 55(3):1280–1296, Feb 1997.

[171] W Lampl, S Laplace, M Lechowski, D Rousseau, H Ma, S Menke, and G Unal. Digitization of LAr calorimeter for CSC simulations. Technical Report ATL-LARG-PUB-2007-011. ATL-COM-LARG-2007-008, CERN, Geneva, Sep 2007. This is the calo CSC note calo-5.

[172] W Lampl et al. Calorimeter Clustering Algorithms: Description and Performance. Technical Report ATL-LARG-PUB-2008-002. ATL-COM-LARG-2008-003, CERN, Geneva, Apr 2008.

[173] M. Lechowski. *Test du Modèle du "Petit Higgs" dans ATLAS au LHC & Simulation de la numérisation du calorimètre électromagneétique*. PhD thesis, Universit de Paris-Sud, April 2005.

[174] LHC Higgs Cross Section Working Group, S. Dittmaier, C. Mariotti, G. Passarino, and R. Tanaka (Eds.). Handbook of LHC Higgs Cross Sections: 1. Inclusive Observables. *CERN-2011-002*, CERN, Geneva, 2011. URL http://arxiv.org/abs/1101.0593.

[175] L. N. Lipatov. The parton model and perturbation theory. *Sov. J. Nucl. Phys.*, 20: 94–102, 1975.

[176] Jean-François Marchand. *Etude de la recherche du boson de Higgs en deux photons dans l'expérience ATLAS au LHC et calibration du calorimètre á Argon liquide.* PhD thesis, Université de Savoie, Jun 2009.

[177] Alan D. Martin, R. G. Roberts, W. James Stirling, and R. S. Thorne. Parton distributions: A New global analysis. *Eur. Phys. J.*, C4:463–496, 1998.

[178] Martin, A. and Stirling, W. and Thorne, R. and Watt, G. Parton distributions for the lhc. *The European Physical Journal C - Particles and Fields*, 63:189–285, 2009.

[179] Matteo Cacciari and Gavin P. Salam. Pileup subtraction using jet areas. *Physics Letters B*, 659(1-2):119 – 126, 2008.

[180] Pavel M. Nadolsky et al. Implications of CTEQ global analysis for collider observables. *Phys. Rev.*, D78:013004, 2008.

[181] Y. Nambu and G. Jona-Lasinio. Dynamical Model of Elementary Particles Based on an Analogy with Superconductivity. I. *Phys. Rev.*, 122(1):345–358, Apr 1961.

[182] Y. Nambu and G. Jona-Lasinio. Dynamical Model of Elementary Particles Based on an Analogy with Superconductivity. II. *Phys. Rev.*, 124(1):246–254, Oct 1961.

[183] Yoichiro Nambu. Axial vector current conservation in weak interactions. *Phys. Rev. Lett.*, 4:380–382, 1960.

[184] P. Aurenche and P. Chiappetta and M. Fontannaz and J. Ph. Guillet and E. Pilon. Next to leading order bremsstrahlung contribution to prompt-photon production. *Nuclear Physics B*, 399(1):34 – 62, 1993.

[185] Krisztian Peters. Search for the Higgs boson in the gamma gamma final state at the Tevatron. *PoS*, ICHEP2010:071, 2010.

[186] H. David Politzer. Reliable Perturbative Results for Strong Interactions? *Phys. Rev. Lett.*, 30(26):1346–1349, Jun 1973.

[187] H. David Politzer. Asymptotic Freedom: An Approach to Strong Interactions. *Phys. Rept.*, 14:129–180, 1974.

[188] J. Pumplin et al. New generation of parton distributions with uncertainties from global QCD analysis. *JHEP*, 07:012, 2002.

[189] G. Punzi. presented at the 23rd Rencontres de Blois Particle Physics and Cosmology 30-05-2011. URL http://confs.obspm.fr/Blois2011/index.htm.

[190] Lisa Randall and Raman Sundrum. Large Mass Hierarchy from a Small Extra Dimension. *Phys. Rev. Lett.*, 83(17):3370–3373, Oct 1999.

[191] V. Ravindran, J. Smith, and W. L. van Neerven. NNLO corrections to the total cross section for Higgs boson production in hadron hadron collisions. *Nucl. Phys.*, B665:325–366, 2003.

[192] A L Read. Modified frequentist analysis of search results (the cl_s method). (CERN-OPEN-2000-205), 2000.

[193] K Riesselmann. Limitations of a Standard Model Higgs Boson. Technical Report hep-ph/9711456. DESY-97-222, DESY, Hamburg, Nov 1997.

[194] A. Salam. in Elementary Particle Theory, Stockholm, *Almquist and Wiksell*. 1968.

[195] Marc Sher. Electroweak Higgs potential and vacuum stability. *Physics Reports*, 179 (5-6):273 – 418, 1989.

[196] A. Sherstnev and R. S. Thorne. Parton distributions for lo generators. *Eur. Phys. J.*, C55:553, 2008.

[197] T. Sjöstrand et al. High-Energy-Physics Event Generation with `PYTHIA` 6.1. *Computer Phys. Commun.*, 135:238, 2001.

[198] G. 't Hooft. Renormalizable Lagrangians for massive Yang-Mills fields. *Nucl. Phys.*, B35(1):167 – 188, 1971.

[199] G. 't Hooft and M. Veltman. Regularization and renormalization of gauge fields. *Nuclear Physics B*, 44(1):189 – 213, 1972.

[200] Gerard 't Hooft. Renormalization of Massless Yang-Mills Fields. *Nucl. Phys.*, B33: 173–199, 1971.

[201] Tanaka, J. Study of Systematic Uncertainty of Fake Photon Estimation: Difference Coming from MC Event Generators. Technical Report ATL-COM-PHYS-2009-420, CERN, Geneva, Aug 2009.

[202] The ALICE Collaboration. The ALICE Experiment at the CERN LHC. *JINST*, 3: S08002, 2008.

[203] The CDF and DØ Collaborations and the TEVNPHWG Working Group. Combined CDF and DØ Upper Limits on Standard Model Higgs Boson Production with up to 8.2 fb-1 of Data. 2011. arXiv/1103.3233.

[204] The CDF Collaboration. Search for a SM Higgs Boson with the Diphoton Final State at CDF. *CDF/PUB/EXOTIC/PUBLIC/10065*, .

[205] The CDF Collaboration. Search for a Standard Model Higgs Boson decaying into photons using 7 fb^{-1} of data. *CDF/PUB/EXOTIC/PUBLIC/10485*, .

[206] The DØ Collaboration. Search for the Standard Model Higgs Boson in $\gamma\gamma + X$ final states at DØ using 8.2 fb^{-1} data. *DØ Note 6177-CONF*.

[207] H. Torres. presentation at the ATLAS SMDP meeting of 28-9-2010. URL http://bit.ly/hUbE6G.

[208] M. Tripiana. presentation at the ATLAS e/γ meeting of 16-2-2011. . URL http://bit.ly/fEQpEU.

[209] M. Tripiana. presentation at the ATLAS SMDP meeting of 8-2-2011. . URL http://bit.ly/fDURVJ.

[210] G. Unal. presentation at the ATLAS e/γ meeting of 23-2-2011. URL http://bit.ly/f4NiBn.

[211] Cleland W.E. and E.G. Stern. Signal processing considerations for liquid ionization calorimeters in a high rate environment. *Nucl. Instrum. Methods Phys. Res. A*, 338: 467, 1994.

[212] S. Weinberg. A Model of Leptons. *Phys. Rev. Lett.*, 19(21):1264–1266, Nov 1967.

[213] S. Weinberg. The making of the Standard Model. *Eur. Phys. J. C*, 34:5–13, 2004.

[214] Whalley, M. R. and Bourilkov, D. and Group, R. C. The Les Houches Accord PDFs (LHAPDF) and Lhaglue. 2005. hep-ph/0508110.

[215] M Wielers. Photon Identification with the ATLAS Detector. Technical Report ATL-PHYS-99-016, CERN, Geneva, Mar 1999.

[216] M Wielers. Isolation of Photons. Technical Report ATL-PHYS-2002-004, CERN, Geneva, Nov 2001.

[217] L Yuan et al. Data-driven methods for photon trigger efficiency measurement. Technical Report ATL-COM-PHYS-2010-113, CERN, Geneva, Feb 2010.

[218] J. Zinn-Justin. in From QED to the Higgs Mechanism: A Short Review, Orsay (France), *the Higgs Hunting Workshop*. 2010. URL http://bit.ly/i93VP9.

Appendix A

Optimal Filtering Method

To minimise the influence of electronics noise and the pile-up effect, and to ensure also the condition that a shift on time of the signal will no alter the energy measurement, the ADC samplings are combined using special weights as coefficients, which are calculated by the optimal filtering method [211]. Thus, these coefficients are called *optimal filtering coefficients* (OFC). The OFC method is described in the following paragraphs [171, 173]. The observed signal is expressed as a function of the time:

$$S(t) = Ag(t+\tau) + n(t) \sim Ag(t) + A\tau g'(t) + n(t) \tag{A.1}$$

where A is the amplitude and τ the phase of the signal with respect to the beam crossing clock. $g(t-\tau)$ is the shaper function and g' its derivate. $n(t)$ si the electronic and pile-up capacitive, resistive and inductive noise and is reduced by the RC^2 part of the shaper, the two integrations limiting the bandwidth.

Each signal sample, at a time t_i, is written as:

$$S_i = Ag_i - A\tau g'_i + n_i \tag{A.2}$$

A and τ are extracted by properly combining the signal samples. To minimize the effect of noise a discrete convolution between signal samples and a set of optimal weights is made.

$$U = \Sigma_i a_i S_i, \qquad \langle U \rangle = A \tag{A.3}$$

$$V = \Sigma_i b_i S_i, \qquad \langle V \rangle = A\tau \tag{A.4}$$

The weights a_i and b_i are the so-called **OFC**. Equations A.3, A.4 leads to the set of conditions, considering the noise null in average($< n_i >$):

$$\Sigma_i a_i g_i = 1, \qquad \Sigma_i a_i g'_i = 0 \tag{A.5}$$

$$\Sigma_i b_i g_i = 0, \qquad \Sigma_i b_i g'_i = -1 \tag{A.6}$$

U and V are estimators of A and $A\tau$. Their variance can be written as follow taking into account the auto-correlation of the noise

$$V(U) = \Sigma_{i,j} a_i a_j M_{ij} \qquad V(V) = \Sigma_{i,j} b_i b_j M_{ij} \tag{A.7}$$

M_{ij} are the coefficients of the noise auto-correlation matrix. The OFC are obtained by minimizing the variance of the U and V (assuming A.5), with the use of the Lagrange multipliers method:

$$a = \frac{(g'.Rg')Rg - (g.Rg')Rg'}{(g.Rg)(g'.Rg') - (g.Rg')^2} \qquad \left(R = M^{-1}\right) \tag{A.8}$$

$$b = \frac{(g.Rg)Rg - (g.Rg')Rg}{(g.Rg)(g'.Rg') - (g.Rg')^2} \tag{A.9}$$

The energy deposited in the LAr is the written as :

$$E_{MeV} = C_{ADC \leftrightarrow MeV} \Sigma_i (s_i - p_i) OFC_i\{a_i, b_i\} \tag{A.10}$$

s_i and p_i being respectively the signal and the pedestal amplitude.

Pedestal and Electronic noise

In absence of input signal in the calorimeter, the signal at the output of the electronics chain is called *pedestal*. For each channel, the signal of an event varies from one event to another through a Gaussian distribution, following the effect of the noise produced by the whole read-out electronics chain which treats the signal. This noise, which depends on the shapers gain, is called electronic noise. It is measured through the RMS of the signals of a given channel. Such a measurement is performed only to one pedestal for a given gain. Similarly, the pedestal can be measured by taking this time average value of the signals. Approximatively, it has a value of 1000 ADC counts, allowing the measurement of negative part at the bipolar shape. Pedestal and Electronic noise are defined as the following:

$$Pedestal = \langle E_{ADC} \rangle \tag{A.11}$$

$$Electronic\ noise = \sqrt{\langle E_{ADC}^2 \rangle - \langle E_{ADC} \rangle^2} = \sigma \tag{A.12}$$

Appendix B

Selection cut thresholds

B.1 Cut thresholds

$\|\eta\|$	0-0.6	0.6-0.8	0.8-1.15	1.15-1.37	1.37-1.52	1.52-1.81	1.81-2.01	2.01-2.37	2.37-2.47
$R_{\mathrm{had_1}}$, R_{had}	0.01	0.007	0.006	0.008	0.01	0.025	0.021	0.014	0.019
R_η	0.927	0.912	0.926	0.916	0.750	0.906	0.932	0.913	0.915
w_{η_2}	0.012	0.012	0.013	0.013	0.025	0.015	0.012	0.013	0.012

Table B.1: Values of the photon loose selection cuts for the different discriminating variables in the different $|\eta|$ regions. R_{had} is used for $0.8 \leq |\eta| < 1.37$, $R_{\mathrm{had_1}}$ elsewhere.

$\|\eta\|$	0-0.6	0.6-0.8	0.8-1.15	1.15-1.37	1.37-1.52	1.52-1.81	1.81-2.01	2.01-2.37	2.37-2.47
Unconverted photon candidates									
$R_{\mathrm{had_1}}$, R_{had}	0.0089	0.007	0.006	0.008	–	0.019	0.021	0.0137	–
R_η	0.955	0.946	0.948	0.952	–	0.941	0.948	0.935	–
R_ϕ	0.954	0.95	0.59	0.82	–	0.93	0.947	0.930	–
w_{η_2}	0.0105	0.0112	0.0105	0.0111	–	0.011	0.0111	0.0125	–
F_{side}	0.284	0.36	0.36	0.514	–	0.67	0.211	0.191	–
$w_{s\,3}$	0.66	0.69	0.697	0.81	–	0.73	0.631	0.57	–
$w_{s\,\mathrm{tot}}$	2.95	4.4	3.26	3.4	–	3.8	3.5	1.99	–
ΔE [MeV]	92	92	99	111	–	92	110	380	–
E_{ratio}	0.63	0.84	0.823	0.887	–	0.88	0.65	0.6	–
Converted photon candidates									
$R_{\mathrm{had_1}}$, R_{had}	0.00748	0.00700	0.00489	0.00800	–	0.01490	0.01440	0.01020	–
R_η	0.945	0.933	0.936	0.937	–	0.927	0.938	0.922	–
R_ϕ	0.400	0.426	0.493	0.437	–	0.535	0.479	0.692	–
w_{η_2}	0.0114	0.0111	0.0126	0.0124	–	0.0134	0.0118	0.0125	–
F_{side}	0.32	0.428	0.483	0.51	–	0.508	0.252	0.205	–
$w_{s\,3}$	0.697	0.709	0.749	0.78	–	0.773	0.652	0.624	–
$w_{s\,\mathrm{tot}}$	2.8	2.95	2.89	3.14	–	3.7	2.2	1.6	–
ΔE [MeV]	200	200	122	86	–	123	300	300	–
E_{ratio}	0.908	0.911	0.808	0.803	–	0.67	0.922	0.962	–

Table B.2: Values of the original photon tight selection cuts for the different discriminating variables in the different $|\eta|$ regions, for unconverted and converted candidates. R_{had} is used for $0.8 \leq |\eta| < 1.37$, $R_{\mathrm{had_1}}$ elsewhere.

The values shown in Tables B.2 and B.1 were originally deduced in Reference [31].

$\|\eta\|$	0-0.6	0.6-0.8	0.8-1.15	1.15-1.37	1.37-1.52	1.52-1.81	1.81-2.01	2.01-2.37	2.37-2.47
Unconverted photon candidates									
R_η	0.951	0.940	0.942	0.946	–	0.932	0.939	0.926	–
w_{η_2}	0.0107	0.0115	0.0108	0.0114	–	0.0114	0.0115	0.0129	–
Converted photon candidates									
R_η	0.941	0.927	0.930	0.930	–	0.918	0.932	0.913	–
w_{η_2}	0.0116	0.0114	0.0128	0.0126	–	0.0138	0.0120	0.0129	–

Table B.3: Modified values of the R_η and w_{η_2} photon tight (`Robust tight`) selection cuts in the different $|\eta|$ regions, for unconverted and converted candidates. The rest of the cuts are the same than in Table B.2.

The values shown in Tables B.2 modified by B.3 for tight and B.1 for loose were used for the first photon measurement cross section [19, 103] and for the first note on $H \rightarrow \gamma\gamma$ [69], both done on 2010 data using Release 15 software.

$\|\eta\|$	0-0.6	0.6-0.8	0.8-1.15	1.15-1.37	1.37-1.52	1.52-1.81	1.81-2.01	2.01-2.37	2.37-2.47
R_{had_1}, R_{had}	0.010	0.010	0.010	0.010	0.010	0.025	0.021	0.014	0.019
R_η[1]	0.895	0.900	0.904	0.890	0.730	0.864	0.920	0.906	0.905
R_η[2]	0.900	0.900	0.900	0.900	0.750	0.900	0.900	0.900	0.900
w_{η_2}[1]	0.013	0.014	0.014	0.014	0.025	0.017	0.013	0.014	0.014
w_{η_2}[2]	0.012	0.012	0.013	0.013	0.025	0.015	0.013	0.013	0.013

Table B.4: Values of the photon trigger selection cuts 2010 for the different discriminating variables in the different $|\eta|$ regions. R_{had} is used for $0.8 \leq |\eta| < 1.37$, R_{had_1} elsewhere. The values [1] are those corresponding to `g10_loose` of the beginning of the run, and [2] to `g20_loose` of the end of the run.

$\|\eta\|$	0-0.6	0.6-0.8	0.8-1.15	1.15-1.37	1.37-1.52	1.52-1.81	1.81-2.01	2.01-2.37	2.37-2.47
R_{had_1}, R_{had}	0.01	0.01	0.01	0.008	0.01	0.025	0.019	0.014	0.019
R_η	0.927	0.912	0.921	0.916	0.750	0.906	0.920	0.908	0.915
w_{η_2}	0.012	0.012	0.013	0.013	0.025	0.015	0.013	0.013	0.012

Table B.5: Values of the photon **robust loose** selection cuts for the different discriminating variables in the different $|\eta|$ regions. R_{had} is used for $0.8 \leq |\eta| < 1.37$, R_{had_1} elsewhere.

$\|\eta\|$	R_{had_1}, R_{had}	R_η	R_ϕ	$w_{\eta 2}$	F_{side}	$w_{s\,3}$	$w_{s\,\mathrm{tot}}$	ΔE	E_{ratio}
	Unconverted photon candidates								
1.81 - 2.01	0.019	0.928	0.947	0.011	0.211	0.631	2.4	110	0.710
	Converted photon candidates								
	0.016	0.924	0.479	0.012	0.252	0.652	2.0	80	0.915
	Unconverted photon candidates								
2.01 - 2.37	0.0137	0.924	0.935	0.0125	0.181	0.580	1.64	148	0.780
	Converted photon candidates								
	0.011	0.913	0.692	0.0129	0.215	0.614	1.48	132	0.962

Table B.6: New values on the photon **robust tight** selection cuts in the $|\eta|$ regions 1.81-2.01 and 2.01-2.37, for unconverted and converted candidates, the rest is the same than in Tables B.3 and B.2.

The values shown in Tables B.5 and B.6 were optimised using Release 15 software and are used in the second $H \to \gamma\gamma$ note [70] done on 2010 data using (first version of the) Release 16 software.

However looking in detail at 2010 data using (first version of the) Release 16 software, for the single photon note using all 2010 data [36, 72], some differences were found [208, 209] between data and Monte Carlo and the cuts were changed for the variables $w_{s\,3}$. The new cuts are in Table B.7.

new $w_{s\,3}$ cuts		
$\|\eta\|$	1.81-2.01	2.01-2.37
Unconverted photon candidates	0.651	0.610
Converted photon candidates	0.672	0.644

Table B.7: Modified values of the $w_{s\,3}$ for the `Robust tight` selection cuts at high $|\eta|$ regions, for unconverted and converted candidates. The rest of the cuts are the same than in Table B.6.

Cuts in Table B.6 modified by these presented in Table B.7, are used for the full 2010 single photon note [36, 72] and for the 2010 diphoton notes [76, 77]. For the analysis of 2011 data, the bug was corrected (in the second version of the Release 16 software) [210] but, for safety the change of cut was kept, with some slight difference because the trigger changed in 2011 (see Table B.8, for instance). The new cuts are in Tables B.9 and B.10.

$\|\eta\|$	0-0.6	0.6-0.8	0.8-1.15	1.15-1.37	1.37-1.52	1.52-1.81	1.81-2.01	2.01-2.37	2.37-2.47
R_{had_1}, R_{had}	0.010	0.010	0.010	0.010	0.010	0.020	0.015	0.014	0.014
R_η	0.930	0.930	0.925	0.925	0.750	0.915	0.915	0.900	0.900
$w_{\eta 2}$	0.011	0.012	0.012	0.013	0.025	0.014	0.013	0.013	0.013

Table B.8: Values of the photon trigger selection cuts 2011 for the different discriminating variables in the different $|\eta|$ regions. R_{had} is used for $0.8 \leq |\eta| < 1.37$, R_{had_1} elsewhere.

$\|\eta\|$	0-0.6	0.6-0.8	0.8-1.15	1.15-1.37	1.37-1.52	1.52-1.81	1.81-2.01	2.01-2.37	2.37-2.47
R_{had_1}, R_{had}	0.010	0.010	0.010	0.008	0.010	0.025	0.015	0.014	0.019
R_η	0.927	0.912	0.925	0.916	0.750	0.906	0.920	0.908	0.915
w_{η_2}	0.012	0.012	0.013	0.013	0.025	0.015	0.013	0.013	0.012

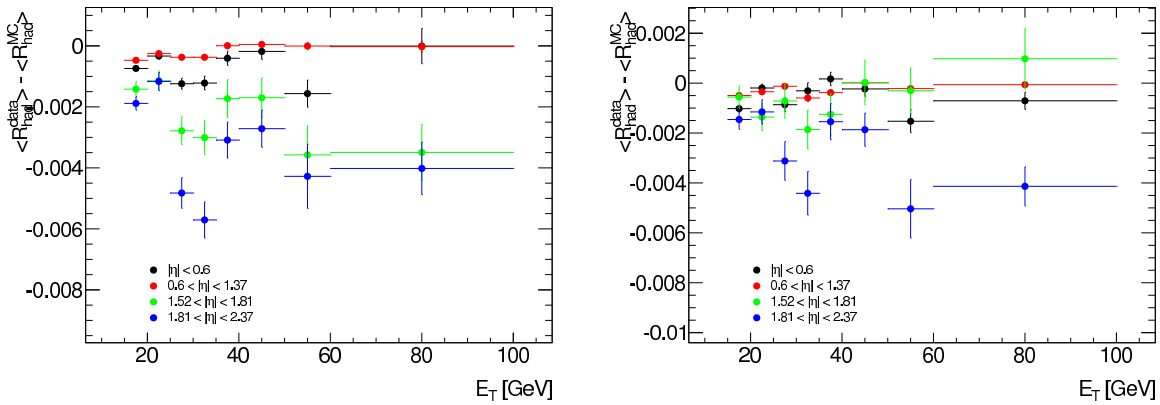
Table B.9: Values of the photon **robust loose 2011 data** selection cuts for the different discriminating variables in the different $|\eta|$ regions. R_{had} is used for $0.8 \leq |\eta| < 1.37$, R_{had_1} elsewhere.

$\|\eta\|$	R_{had_1}, R_{had}	R_η	R_ϕ	w_{η_2}	F_{side}	$w_{s\,3}$	$w_{s\,\mathrm{tot}}$	ΔE	E_{ratio}
	Unconverted photon candidates								
1.81 - 2.01	0.015	0.928	0.947	0.011	0.211	0.651	2.4	110	0.710
	Converted photon candidates								
	0.015	0.924	0.479	0.012	0.252	0.672	2.0	80	0.915
	Unconverted photon candidates								
2.01 - 2.37	0.0137	0.924	0.935	0.0125	0.181	0.610	1.64	148	0.780
	Converted photon candidates								
	0.011	0.913	0.692	0.0129	0.215	0.644	1.48	132	0.962

Table B.10: New values on the photon **robust tight for 2011 data** selection cuts in the $|\eta|$ regions 1.81-2.01 and 2.01-2.37, for unconverted and converted candidates, the rest is the same than in Tables B.3 and B.2.

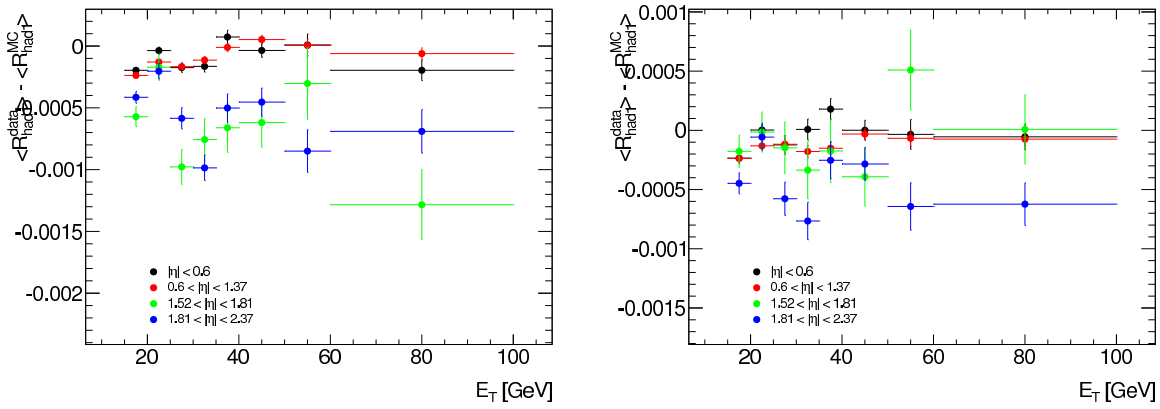
B.2 Data/MC discrepancies on Discriminating Variables

Here are shown [103] the difference of the mean value between data and Monte Carlo, for distributions of the discriminating variables used for the photon identification selection criteria presented in the Section 6.2.1.



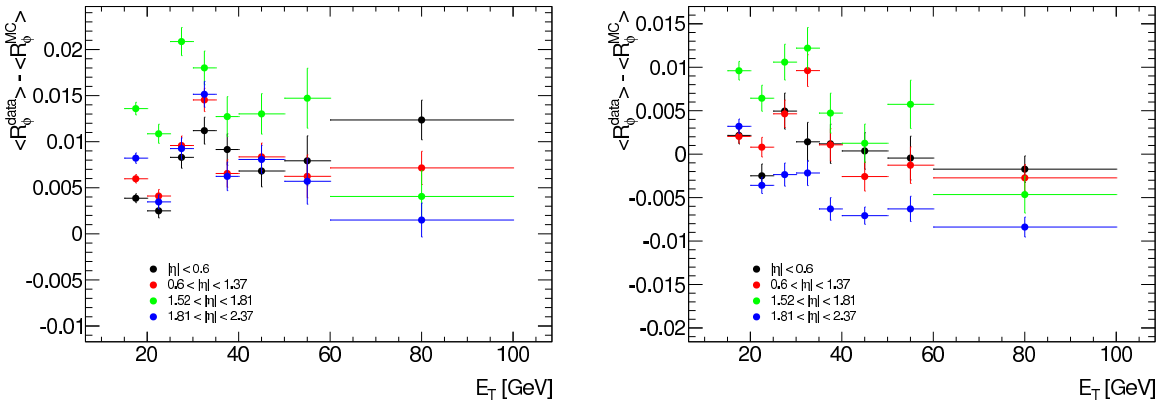
(a) (b)

Figure B.1: Differences $\Delta\mu_{R_{\mathrm{had}}}$ between the means of the R_{had} distributions in data and MC for photon candidates passing the loose (a,b) and tight selections [103].



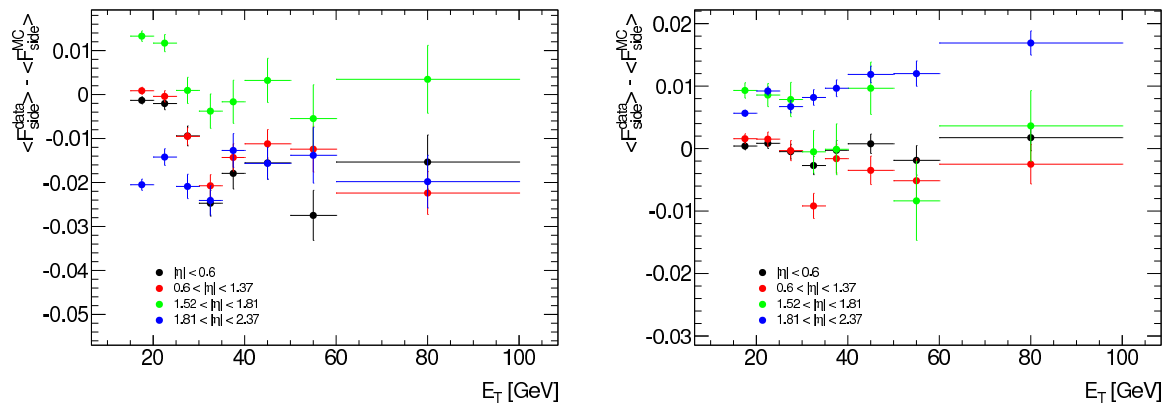
(a) (b)

Figure B.2: Differences $\Delta\mu_{R_{\mathrm{had}_1}}$ between the means of the R_{had_1} distributions in data and MC for photon candidates passing the loose (a,b) and tight selections [103].



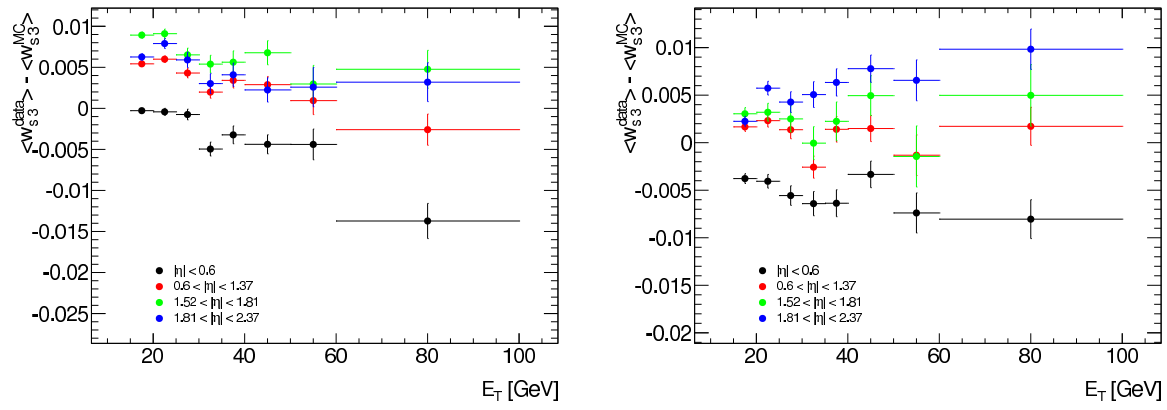
(a) (b)

Figure B.3: Differences $\Delta\mu_{R_{\phi}}$ between the means of the R_{ϕ} distributions in data and MC for photon candidates passing the loose (a) and tight (b) selections [103].



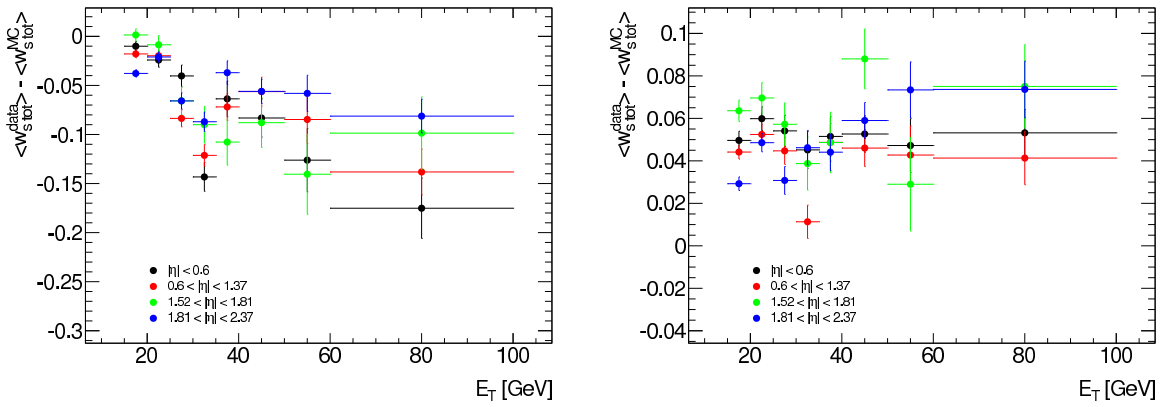
(a) (b)

Figure B.4: Differences $\Delta\mu_{F_{\text{side}}}$ between the means of the F_{side} distributions in data and MC for photon candidates passing the loose (a) and tight (b) selections [103].



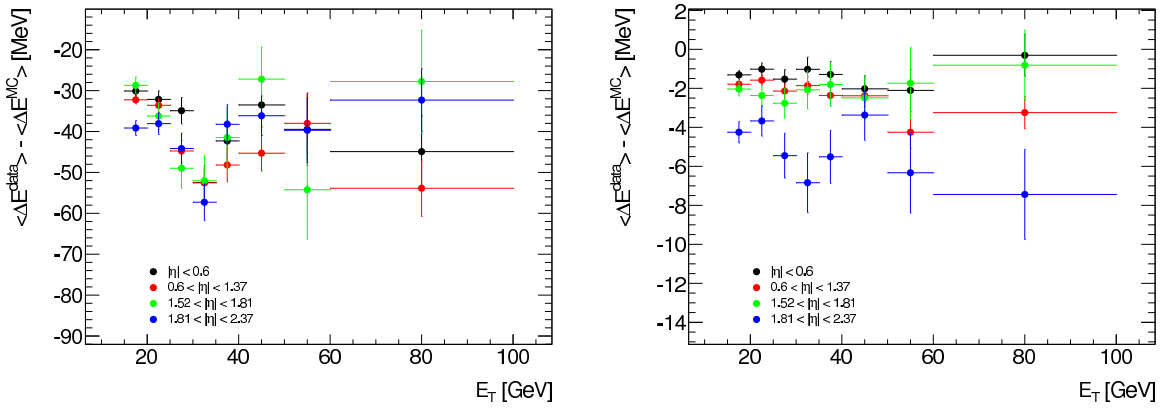
(a) (b)

Figure B.5: Differences $\Delta\mu_{w_{s3}}$ between the means of the w_{s3} distributions in data and MC for photon candidates passing the loose (a) and tight (b) selections [103].



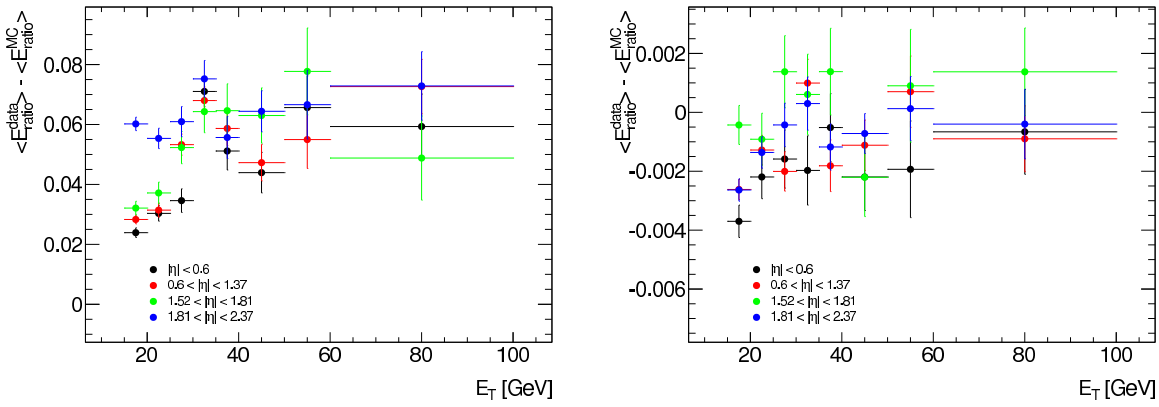
(a) (b)

Figure B.6: Differences $\Delta\mu_{w_{s\,\mathrm{tot}}}$ between the means of the $w_{s\,\mathrm{tot}}$ distributions in data and MC for photon candidates passing the loose (a) and tight (b) selections [103].



(a) (b)

Figure B.7: Differences $\Delta\mu_{\Delta E}$ between the means of the ΔE distributions in data and MC for photon candidates passing the loose (a) and tight (b) selections [103].



(a) (b)

Figure B.8: Differences $\Delta\mu_{E_{\text{ratio}}}$ between the means of the E_{ratio} distributions in data and MC for photon candidates passing the loose (a) and tight (b) selections [103].

Appendix C

Simulated samples and collision data

C.1 Simulated events

To study the characteristics of signal and background events, Monte Carlo samples are generated using PYTHIA 6.4.21 [197], a leading-order (LO) parton-shower MC generator, with the modified leading order MRST2007 [196] parton distribution functions (PDFs). The event generator parameters are set according to the ATLAS MC09 tune [12], and the ATLAS detector response is simulated using the GEANT4 program [42]. These samples are then reconstructed with the same algorithms used for data. More details on the event generation and simulation infrastructure of the ATLAS experiment are provided in Ref. [13]. For the study of systematic uncertainties related to the choice of the event generator and the parton shower model, alternative samples are also generated with HERWIG 6.5 [116]. For a summary of the relevant simulated samples, see Table C.1.

To study background processes, two classes of samples are simulated. In the first one, generated non-diffractive minimum bias events are filtered requiring at least 6 GeV of transverse energy in a 0.18×0.18 region in $\eta \times \phi$ at the truth particle level, mimicking a calorimetric L1 trigger requirement. The events passing this filter, whose efficiency is around 5.3%, are then fully simulated. This filter is found to be unbiased for transverse energies above 10 GeV. The equivalent integrated luminosity of this sample, according to the effective production cross section (including the filter efficiency) $\sigma = 2.58\ mb$ returned by PYTHIA, is 16 nb^{-1}.

Since the E_T spectrum of reconstructed fake candidates decreases rapidly above the filter threshold, a second class of samples, enriched in candidates with higher transverse energies, is used to study fake photon candidates with reconstructed $E_T > 20$ GeV. In these samples, all relevant 2→2 QCD hard subprocesses (see Table C.2). are switched on, the transverse momentum of the hard-scattering products is required to be greater than (at least) 15 GeV, and the same filter as for the minimum bias sample is applied. The filter has a higher threshold than in the minimum bias sample, with cuts at 17 and 35 GeV The sample with a 17 GeV minimum is found to be unbiased for transverse energies above 20 GeV. Its equivalent integrated luminosity, according to the effective production cross section $\sigma = 0.99$ mb computed with PYTHIA (taking into account also the filter efficiency, 8.6%), is 494 nb^{-1}. The sample with a parton-level p_T cut at 33 GeV and a

Data Set	Process	σ [pb]	Filter type	Filter threshold [GeV]	Filter efficiency	Events in tuples	Equivalent luminosity [pb^{-1}]	Generator
105801	QCD	4.845E+10	1 jet	6	5.32E-2	39957193	1.55E-2	PYTHIA
105802	QCD	1.148E+9	1 jet	17	8.62E-2	48931022	4.94E-1	PYTHIA
105807	QCD	5.484E+7	1 jet	35	1.57E-1	4992566	5.79E-1	PYTHIA
105802	QCD	9.162E+8	1 jet	17	8.26E-2	9969117	1.32E-1	HERWIG
105807	QCD	4.396E+7	1 jet	35	1.43E-1	4884587	7.77E-1	HERWIG
115801	QCD	4.911E+10	1 prompt γ	7	9.77E-5	989274	2.06E-1	PYTHIA
115802	QCD	1.147E+9	1 prompt γ	17	1.83E-4	964406	4.60E+0	PYTHIA
115871	QCD	3.924E+10	1 prompt γ	7	1.65E-4	999189	1.54E-1	HERWIG
115872	QCD	9.162E+8	1 prompt γ	17	1.08E-4	927922	9.41E+0	HERWIG
108085	γ-jet	5.015E+6	1 prompt γ	7	2.76E-1	999631	7.21E-1	PYTHIA
108087	γ-jet	2.250E+5	1 prompt γ	17	4.70E-1	4994464	4.72E+1	PYTHIA
108081	γ-jet	1.731E+4	1 prompt γ	35	6.04E-1	1998486	1.91E+2	PYTHIA
108082	γ-jet	1.521E+3	1 prompt γ	70	6.63E-1	999662	9.92E+2	PYTHIA
105830	γ-jet	1.963E+5	1 prompt γ	17	4.66E-1	4988495	5.46E+1	HERWIG
105831	γ-jet	1.478E+4	1 prompt γ	35	6.01E-1	1999395	2.25E+2	HERWIG
108092	γ-jet	1.282E+3	1 prompt γ	70	6.52E-1	998963	1.11E+3	HERWIG

Table C.1: Monte Carlo datasets used in the inclusive photon analysis. All samples contain all relevant signal processes, unless otherwise indicated. The QCD samples contain both prompt photon production events and the most significant sources of background as summarized in Table C.2.

truth-particle-jet filter cut at 35 GeV helps us to extend the reach to higher transverse energies, and corresponds to an integrated luminosities of 579 nb^{-1}.

Process	PYTHIA subcode
$q_i q_j \to q_i q_j$	11
$q_i \bar{q}_i \to q_k \bar{q}_k$	12
$q_i q_i \to gg$	13
$q_i g \to q_i g$	28
$gg \to q_k \bar{q}_k$	53
$gg \to gg$	68
$q_i \bar{q}_i \to Q_k \bar{Q}_k$	81
$gg \to Q_k \bar{Q}_k$	82
$q_i \bar{q}_i \to g\gamma$	14
$q_i g \to q_i \gamma$	29

Table C.2: Elementary QCD processes that are enabled in the QCD PYTHIA samples.

All of these QCD background samples contain "fake" photon candidates (typically from π^0 and η decays), as well as prompt photon signals produced by QED radiation emitted off quarks and by parton fragmentation. The higher energy sample contains also the contribution of the direct LO gamma-jet hard-scattering contributions, either from $q_i \bar{q}_i \to g\gamma$ or $q_i g \to q_i \gamma$. Reconstructed prompt photon candidates are matched to particles in the truth record of the event with the ATLAS McTruthClassifier tool, which uses a combination of ancestry information and ΔR matching to determine whether a candidate

is signal or background. All prompt photon contributions are removed from these samples when studying the background contribution.

Signal-like photons are present in all of the relevant datasets, either as the result of a filter which selects only signal photons at the generator level, or as part of a sample which also contains background processes. For signal-only samples, two types of filters are used. The first class of prompt photon samples consists of simulated leading order γ-jet events, and contains only hard-scattering photons (hard subprocesses $qg \to q\gamma$ and $q\bar{q} \to g\gamma$) with generated transverse momenta above some threshold (7, 17, 35 or 70 GeV thresholds are used in these studies). The equivalent luminosities of these samples range from 71 nb^{-1} (for a 7 GeV threshold) to 1 fb^{-1} (for a 70 GeV threshold). The box-diagram hard subprocess $gg \to g\gamma$ is part of the next-to-next-to-leading order (NNLO) cross section and gives a negligible contribution to the total prompt photon cross section compared to the other two subprocesses. It is therefore not included in the generated samples.

The second class of signal samples contains both hard-scattering photons and photons from QED radiation off quarks, and also includes photons from parton fragmentation. The events generated for this class of samples are similar to those generated for the study of the QCD backgrounds (the same elementary processes of Table C.2 are activated), but the filter applied before the full simulation only retains events that contain reconstructed photons matched to signal photons in the truth record, with generated transverse momenta above some threshold, either 7 GeV or 17 GeV. The equivalent luminosities for those two samples are 206 nb^{-1} and 4600 nb^{-1}, respectively. These samples are used to study the contribution to the prompt photon signal of photons from fragmentation or from the NLO part of the direct process and that are less isolated than those from the LO direct processes. In such studies, all direct LO photon contributions are removed from these samples in the analysis.

C.2 Collision Data

We use the data collected between April and August 2010 which correspond to a total integrated luminosity of 880 ± 100 nb^{-1} collected by the ATLAS detector at the LHC [19].

Trigger Requirements

Events are triggered using the `g10_loose` high-level calorimeter trigger, based on the energy deposits in the electromagnetic and hadronic calorimeters. The `g10_loose` high-level trigger is seeded by a level-1 hardware trigger (`L1_EM5`), which, using a coarser granularity (0.1×0.1 in $\eta \times \phi$) than that of the electromagnetic calorimeter, searches for electromagnetic clusters with fixed size 0.2×0.2 and retains only those whose total transverse energy in two of their four trigger channels is above 5 GeV. The high level trigger exploits the full granularity and precision of the calorimeter to refine the level-1 trigger selection, based on improved energy resolution and detailed information on energy deposition in the calorimeter cells. The nominal transverse energy threshold of the `g10_`-

`loose` trigger is 10 GeV. The selection criteria that are applied by the trigger on the fraction and profile of the energy released in the various layers of the calorimeters are looser than the photon identification criteria applied in the following analysis steps, and are chosen, together with the transverse energy threshold value, in order to reach a plateau of constant efficiency close to 100% for true photons with $E_T > 15$ GeV. More details on trigger efficiency measurements can be found in [217].

Data Quality

Only events where both the calorimeter and the inner detector are fully operational, and have good data quality, are used. In particular, events are required to belong to the $Z \to ee$ e/γ "Good Runs List" (GRL).[1]

Total Integrated Luminosity

The total integrated luminosity of the selected sample, after trigger and GRL requirements, is (880 ± 100) nb^{-1}. A detailed list of all the runs included in this measurement, and the corresponding `g10_loose` integrated luminosities, is available in Table C.3.

Primary Vertex Requirement

For this analysis, events are required to have a reconstructed primary vertex consistent with the average beam spot position and with at least three associated tracks. The efficiency of this requirement is greater than 99.9% both in data and in simulated signal events containing at least one photon candidate with transverse energy above 15 GeV (and lying within the calorimeter acceptance). The total number of selected events is 9.6 million.

Non-Collision Backgrounds

The amount of non-collision background in the data sample is estimated with control samples collected using a dedicated, low-threshold calorimetric trigger. This trigger selects events that either have no proton bunch passing through the interaction region (for cosmic background studies), or in which there is only one bunch corresponding to a single beam (for non-collision beam-induced background studies). The contribution to the final candidate sample was found to be negligible [207].

The list of runs used in the analysis [19] is found below

Run Number	Data Period	Good LB	Bad LB	Luminosity [nb^{-1}]
152166	A	47	48	0.0029
152214	A	43	0	0.0032

Continued on following page

[1] Note that the same quality requirements apply for electrons from Z and photons.

Run Number	Data Period	Good LB	Bad LB	Luminosity [nb^{-1}]
152221	A	163	0	0.0210
152345	A	80	0	0.0161
152409	A	589	1	0.0794
152441	A	359	1	0.0672
152508	A	66	0	0.0109
152777	A	249	1	0.0453
152844	A	55	1	0.0078
152845	A	239	0	0.0262
152878	A	114	1	0.0250
152933	A	128	1	0.0215
152994	A	59	1	0.0053
153030	A	83	0	0.0225
153134	A	42	1	0.0057
153136	A	20	1	0.0021
153159	A	89	1	0.0112
153200	A	36	0	0.0078
153565	B	893	0	0.7653
154810	B	62	0	0.1526
154813	B	128	0	0.2624
154815	B	30	0	0.0618
154817	B	279	0	0.5339
155073	B	318	5	1.1564
155112	B	474	0	3.4111
155116	B	83	0	0.4992
155160	B	263	0	1.3289
155228	C1	16	0	0.0385
155280	C1	16	0	0.0284
155569	C1	240	0	0.9909
155634	C1	186	0	1.0697
155669	C1	54	0	0.4409
155678	C1	68	0	1.1924
155697	C1	240	0	3.4226
156682	C2	105	0	1.3008
158045	D1	61	0	0.7205
158116	D1	413	0	14.4433
158269	D1	75	0	3.4323
158299	D1	71	0	1.3367
158392	D1	212	0	7.6043
158466	D2	16	0	1.6204
158545	D2	23	0	1.3337

Continued on following page

Run Number	Data Period	Good LB	Bad LB	Luminosity [nb^{-1}]
158548	D2	196	0	10.0807
158549	D2	85	0	3.1816
158582	D2	307	0	16.0859
158632	D3	110	0	5.5031
158801	D3	177	0	7.1641
158975	D3	219	0	20.5129
159041	D4	259	0	25.6413
159086	D4	404	0	54.0469
159113	D5	256	0	28.0369
159179	D6	108	0	15.0164
159202	D6	81	0	9.7998
159203	D6	79	0	8.2898
159224	D6	539	0	64.2961
160387	E1	235	0	58.4255
160472	E1	366	0	76.3450
160479	E1	25	0	4.6985
160530	E2	424	0	92.4522
160613	E3	189	0	48.0307
160736	E3	59	0	17.1593
160800	E3	61	1	16.1291
160801	E3	370	0	75.7851
160879	E3	409	0	80.6187
160899	E4	15	0	4.8064
160953	E4	53	0	19.4108
160954	E4	62	1	16.6286
160958	E4	195	0	40.6305
160963	E4	13	0	2.3340
160980	E4	30	0	8.9862
Total	A-E4	12113	65	877.603

Table C.3: Runs used in the inclusive photon analysis, which cover all runs through period E4, except runs 158443 and 160975, which had prescales applied on the g10_loose trigger chain. A lumi block (LB) is bad either if the trigger was disabled, or if the luminosity value for that lumi block in the database is invalid.

C.3 Photon candidates preselection

Photon candidates with calibrated transverse energies (E_T) above 15 GeV are kept for the successive analysis steps. To ensure a proper identification, the cluster barycenter in

the second layer of the electromagnetic calorimeter is required to lie in the pseudorapidity region covered by the very finely segmented first layer: $|\eta| < 1.37$, or $1.52 \leq |\eta| < 2.37$. In addition, for this analysis, photon candidates are selected to be outside regions of the electromagnetic calorimeter where either the presampler, first, or second layers have non working readout optical links: the full 3×7 (in the barrel) or 5×5 (in the end-cap) clusters are required not to overlap with any of these regions. Photon candidates are also rejected if one of the core 3×3 second layer cells does not work properly, or if one of the first layer cells facing the hottest cell in the second layer is non-functional. The `checkOQ.C` egamma object quality tool is used to apply these requirements. The tool makes use of run-dependent maps of dead OTX and inactive channels to remove photon candidates whose cluster overlaps with these bad regions. A summary of the dead OTX maps for the run ranges analysed in this measurement, and the integrated luminosity associated with each map, is presented in Table C.4. These requirements reject 6.4% of the photon candidates reconstructed in collision data.

Run Start	Run End	Dead OTX map	Integrated Luminosity [μb^{-1}]
152166	155227	152166	8552.85
155228	155759	155228	7183.43
155760	158114	155760	2021.34
158115	158642	158115	64622.16
158643	158706	158643	0.00
158707	159039	158707	27677.04
159040	-	159040	767567.89
Total	-	-	877624.71

Table C.4: Run periods, and equivalent luminosities, for the different object quality maps used in the inclusive photon analysis.

In the following, "preselection" is defined as the combination of criteria described in this section and the event-quality criteria defined in the previous sections:

- the event belongs to the e/γ Good Runs List (good inner detector and calorimeter data quality)
- the event passes the g10_loose trigger
- the event contains at least one primary vertex with at least three associated tracks
- the photon candidate has reconstructed $E_T > 15$ GeV and pseudorapidity in the fiducial region ($|\eta^\gamma| < 1.37$ or $1.52 \leq |\eta^\gamma| < 2.37$)
- the cluster of the photon candidate does not contain a bad calorimeter cell (no cell corresponding to a dead OTX in the cluster; no cell with dead HV in the core of the cluster)

After the preselection, 1.3 million photon candidates remain in the data sample. The average multiplicity of photons with $E_T > 15$ GeV and within the pseudorapidity acceptance, in events containing at least one such photon candidate, is 1.02 in collision data.

After the preselection, the candidates are separated in the belonging to four different pseudorapidity regions:

$$\eta \in [0.00; 0.60), \quad \eta \in [0.60; 1.37), \quad \eta \in [1.52; 1.81), \quad \eta \in [1.81; 2.37)$$

chosen according to the detector geometry, and in several E_T intervals [GeV]:

$$[15; 20), \quad [20; 25), \quad [25; 30), \quad [30; 35), \quad [35; 40), \quad [40; 50), \quad [50; 60), \quad [60; 100)$$

where the increase of the interval width at higher E_T values is motivated by the lower candidate statistics.

C.4 Reconstruction and trigger efficiencies

C.4.1 Reconstruction and preselection efficiency

The reconstruction and preselection efficiency, ϵ_{reco}, is computed from simulated events as a function of the true photon transverse energy for each pseudorapidity interval under study. It is defined as the ratio between the number of true prompt photons that are reconstructed - after preselection - in a certain pseudorapidity interval and have reconstructed $E_T^{\text{iso}} < 3$ GeV, and the number of true photons with true pseudorapidity in the same pseudorapidity in the same interval and with particle-level transverse isolation energy lower than 4 GeV.

$$\epsilon^{\text{reco},k}(E^{\gamma}_{T,\text{true}}) \equiv \frac{dN^{\gamma}(\eta_{k,1} \leq |\eta^{\gamma}_{\text{true}}| < \eta_{k,2}, E^{\text{iso}}_{T,\text{true}} < 3 \text{ GeV})/dE^{\gamma}_{T,\text{true}}}{dN^{\gamma}(\eta_{k,1} \leq |\eta^{\gamma}_{\text{true}}| < \eta_{k,2}, E^{\text{iso}}_{T,\text{true}} < 4 \text{ GeV})/dE^{\gamma}_{T,\text{true}}} \tag{C.1}$$

The efficiency of the requirement $E_T^{\gamma} > 15$ GeV for prompt photons of true transverse energy greater than the same threshold is taken into account in the unfolding procedure.

The reconstruction and preselection efficiencies are calculated using a cross-section-weighted mixture of direct photons produced in simulated γ-jet events and of fragmentation photons produced in simulated dijet events. The uncertainty on the reconstruction efficiency due to the difference between the efficiency for direct and fragmentation photons, and the unknown ratio of the two in the final sample of selected signal photons, are taken into account as sources of systematic uncertainty in Section 6.5.

The average reconstruction and preselection efficiency for isolated prompt photons with $|\eta^{\gamma}_{\text{true}}| < 1.37$ or $1.52 \leq |\eta^{\gamma}_{\text{true}}| < 1.81$ is around 82%; the 18% inefficiency is due to the inefficiency of the reconstruction algorithms at low photon transverse energy (a few

%), to the inefficiency of the isolation requirement (5 %) and to the acceptance loss from a few inoperative optical links of the calorimeter readout.

C.4.2 Trigger efficiency

The efficiency of the calorimeter trigger, relative to the photon reconstruction and identification selection, is defined as the probability for a true prompt photon, passing the tight photon identification criteria and with $E_T^{\text{iso}} < 3$ GeV, to pass the trigger selection. It is estimated in two steps. First, using a prescaled sample of minimum bias triggers, the efficiency of a lower threshold(≈ 3.5 GeV) level-1 calorimeter trigger is determined. The measured efficiency of this trigger is 100 % for all photon candidates with reconstructed $E_T^{\gamma} > 15$ GeV passing tight identification criteria. Then, the efficiency of the high-level trigger is measured using the sample of events that pass the level-1 calorimeter trigger with 3.5 GeV threshold.

The trigger efficiency for reconstructed photon candidates passing tight selection criteria, isolated and with $E_T^{\gamma} > 15$ GeV is found to be $\epsilon_{\text{trigger}} = (99.5 \pm 0.5)\%$, constant within uncertainties over the full E_T and η ranges under study. The quoted uncertainty is obtained from the estimation of the possible bias introduced by using photon candidates from data, which are a mixture of signal and background photon candidates. Using Monte Carlo samples the absolute difference of the trigger efficiency for a pure signal sample and for a pure background sample is found to be smaller than 0.5 % for isolated tight photon candidates with $E_T^{\gamma} > 15$ GeV.

In Figure C.1 is shown, a comparison between the high-level trigger efficiency in data and in the background predicted by the simulation.

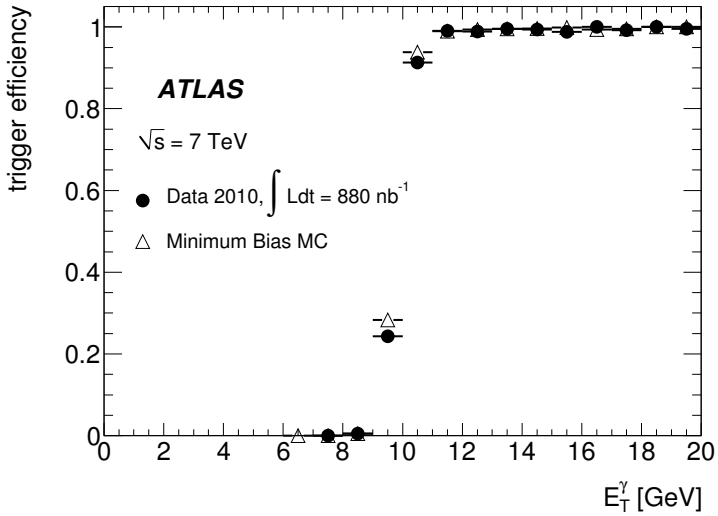


Figure C.1: Photon trigger efficiency with respect to the offline photon selection, as measured in data (circles) and simulated background events (triangles) on photon candidates passing the tight identification criteria and with isolation energy lower than 3 GeV [19].

Acknowledgements

I gratefully acknowledge Monika Wielers and Susan Gascon for having accepted to be the referees of this thesis. I thank Achille Stocchi, Guillaume Unal, José Ocariz and Tejinder Virdee for being part of the jury of this thesis.

I am grateful to Achille Stocchi and Guy Wormser for the support at LAL during my PhD.

I would like to acknowledge all the members of the LAL ATLAS group. You gave me a lot of scientific, technical and human knowledge. I was really lucky with the opportunity of do a thesis in this group, in which the solution to one problem could be found in the next office.

My special thanks to my thesis advisor Louis Fayard for his eternal availability, confidence, friendship, help, support and for all that you could teach me in these years. Actually, I benefit to your experience which allowed me to work efficiently and in a very nice environment.

I would like to thank Guillaume Unal, Marumi Kado, Jean-François Marchand and Marc Escalier for all the fruitful physics discussions and advices.

I want to thank the conveners of the ATLAS notes related to photons where I participed: Leonardo Carminati, Giovanni Marchiori, Mike Hance, Marco Delmastro, Marcello Fanti, Yaquan Fang, Thomas Koffas, Martin Tripiana, Lydia Roos, Francesco Polci, and also the egamma group, in particular Fabrice Hubaut who motivated me.

I would like to thank the administrative and computer sciences teams of the LAL for their help and especially for their infinite patience.

I am very grateful to HELEN and the EIFFEL programs for its financial support during my first years of my PhD thesis. My sincere acknowledgments to José Ocariz for giving us (a bunch of venezuelan physics graduate students) the opportunity to know the exciting world of experimental particle physics.

I want to thank all my friends: Luis Perez, Pietro, Stefania, Rui, Kevin. And also to thanks to much to the Footex LAL team and the PhD LAL students I knew during these time, in particular to my officemate Jean-Baptiste Blanchard, Nancy Andari and Karim Louedec, for your sincere friendship and support.

Thanks to my parents and brothers for having helped me and motivated to go ahead.

Finally, a big thank you to Jeannilet. Thank you for all your love, unconditional support, patience and encouragement. On the difficult days you always persuaded me to look forward. You have made these almost three years, and the five before, fully pleasant and special. Thank you.